The solid state and solution chemistry of selected 3d-transition metal chloride complexes

by

Linda Anna Jacobs

Submitted in partial fulfilment
of the requirements for the degree

Philosophiae Doctor

in the

Faculty of Mathematics and Science
University of Pretoria
Pretoria

September 1988

CONTENTS

	PAGE
ACKNOWLEDGEMENTS	ix
ABBREVIATIONS	x
ABSTRACT	xii
OPSOMMING	xiii
CHAPTER 1	
INTRODUCTION AND OBJECTIVES	
1.1 Introduction	1
1.2 Objectives	10
CHAPTER 2	
THE THEORIES OF SOLID STATE AND SOLUTION CHEMISTRY	
2.1 Introduction	13
2.2 The theory of solid state reactions	13
2.2.1 Introduction	13
2.2.2 Imperfections	14
(a) Point defects	15
(i) Vacancies	15
(ii) Interstitials	16
(iii) Disorder in ordered alloys	16
(b) Line defects	17
(i) Edge dislocations	17
(ii) Screw dislocations	17

PAGE

(c) Planar or surface defects 18

(i) Grain boundaries 18

(ii) Stacking faults 18

2.2.3 Kinetics of solid decomposition 19

(a) The laws of nucleus formation 21

(b) The laws of nucleus growth 28

(c) Kinetic equations of nucleus formation and growth 28

(d) Activation energy and frequency factor 31

2.2.4 Dynamic kinetics 31

2.3 The theory of titration calorimetry 40

2.3.1 Introduction 40

2.3.2 Titration calorimetry 43

(a) Apparatus 44

(b) Thermogram 44

(c) Applicability of the technique 45

(d) Calculation of heats of reactions 45

(e) Non-chemical effects 50

(f) Computer evaluation of the entropy titration data 54

(i) Computer evaluation of calorimetric data 54

(ii) Computer evaluation of the entropy titration method 56

2.3.3 Summary 63

CHAPTER 3

MATERIALS AND EXPERIMENTAL METHODS

3.1 Introduction 64

3.2 Solid State Chemistry 65

3.2.1 Preparation of cobalt(II) chloride complexes 65

PAGE

3.2.2 Preparation of nickel(II) chloride complexes 65

3.2.3 Preparation of manganese(II) chloride complexes 66

3.2.4 Thermogravimetric analysis 67

(a) Dynamic method 67

(b) Isothermal method 68

3.2.5 Differential scanning calorimetry method 69

3.2.6 Electron microscopy 70

3.3 Solution calorimetry 71

3.3.1 Apparatus 71

3.3.2 Solutions 71

3.3.3 Calibrations 72

3.3.4 Data acquisition 73

3.3.5 Calibration runs 73

3.3.6 Calculations 74

CHAPTER 4

STATISTICAL EVALUATION OF THE ENTROPY TITRATION METHOD

4.1 Introduction 75

4.2 Defining the suitable model 75

4.2.1 Systematic error calculations performed on the calculated Q_r values 77

4.2.2 Random and systematic error calculations performed on the ligand concentration 79

4.2.3 Systematic error calculations performed on the metal concentration 82

4.3 Conclusions on systematic error calculations 84

PAGE

CHAPTER 5

THE EFFECT OF SOLVENTS ON THERMODYNAMIC CONSTANTS

5.1 Introduction 90

5.2 The reaction of Ag(I) with tmen 94

5.2.1 The solvent acetone 94

5.2.2 The solvents ethanol and methanol 100

5.2.3 Discussion on the effect of solvent in 1:2 systems 105

5.3 The reaction of Co(II) with tmen 106

5.4 Discussion 109

CHAPTER 6

THE SOLUTION AND SOLID STATE CHEMISTRY OF $CoCl_2$2(py)

6.1 Introduction 111

6.2 Solution Chemistry results 112

6.3 Solid State Chemistry results 115

6.3.1 Dynamic thermogravimetric analysis 115

6.3.2 Isothermal results 120

6.3.3 Electron microscopy results 127

6.3.4 DSC results 133

6.4 Conclusions 137

CHAPTER 7

THE SOLUTION AND SOLID STATE CHEMISTRY OF $CcCl_2$2(quin)

7.1 Introduction 139

7.2 Solution Chemistry results 139

7.3 Solid State Chemistry results 144

7.3.1 Thermogravimetric results 144

PAGE

7.3.2 DSC results 146

7.3.3 Electron microscopy results 150

7.3.4 Dynamic kinetic analysis 156

7.3.5 Isothermal results 158

7.4 Conclusions 163

CHAPTER 8

THE SOLID STATE AND SOLUTION CHEMISTRY OF $CoCl_2 2(\alpha\text{-pic})$

8.1 Introduction 165

8.2 Solid State Chemistry results 165

8.2.1 Dynamic results 165

8.2.2 Isothermal results 171

8.2.3 DSC results 178

8.3 Solution Chemistry 182

8.4 Discussion 184

CHAPTER 9

THE SOLID STATE AND SOLUTION CHEMISTRY OF $CoCl_2 2(\beta\text{-pic})$

9.1 Introduction 186

9.2 Solid State Chemistry results 188

9.2.1 Dynamic results 188

9.2.2 Isothermal results 193

9.2.3 Electron microscopy results 199

9.2.4 The DSC results 202

9.3 Solution Chemistry results 204

9.4 Discussion 207

PAGE

CHAPTER 10

SOLID STATE CHEMISTRY OF $CoCl_2 4(an)$ AND SOLUTION CHEMISTRY OF $CoCl_2 2(an)$

10.1 Introduction 208

10.2 Solid State Chemistry results 209

10.2.1 Dynamic results 209

10.2.2 Isothermal results 218

10.2.3 DSC results 221

10.3 Solution Chemistry results 223

10.4 Discussion 233

CHAPTER 11

THE THERMAL ANALYSIS OF $MnCl_2 2(py)$ and $NiCl_2 2(py)$

11.1 Introduction 235

11.2 Thermogravimetric results 236

11.2.1 Dynamic results 236

11.2.2 Isothermal results 242

11.2.3 DSC results 246

11.3 Conclusions 251

CHAPTER 12

THE THERMAL DECOMPOSITION OF MANGANESE AND NICKEL COMPLEXES CONTAINING PYRIDINE-RELATED LIGANDS

12.1 Introduction 253

12.2 Solid State Chemistry results 254

12.2.1 Dynamic results 254

12.2.2 Isothermal results 265

PAGE

12.2.3 Electron microscopy studies 269

12.2.4 DSC results 269

12.3 Conclusions 277

CHAPTER 13

CONCLUSIONS

13.1 Introduction 279

13.2 Comparisons of complexes in the Solid State 280

13.2.1 Thermogravimetric analysis 280

13.2.2 Kinetic analysis 282

13.2.3 DSC results 289

13.3. Comparisons of complexes in solution 292

REFERENCES 295

To God be all the glory.

ACKNOWLEDGEMENTS

The author wishes to express her gratitude to:

Her promotor, Prof. C.P.J. van Vuuren for his support, unfailing quidance and evaluation of this work. It is difficult to express gratitude to someone who is involved in one's own intellectual development. In this instance the gratitude is sincere.

Mr. A Botha for conducting the electron microscopy experiments.

Dr. S. Chemaly for correcting the grammatical form.

Mrs. E. Baransky for her advice and assistence in the typing and printing of this thesis.

Mr. K. Wagenaar for his assistence throughout this study.

The personnel of the Universities of Pretoria and South Africa for their interest and advice.

My husband, Jaco for his moral support, assistence, patience and encouragement.

Family and friends for their continious interest and encouragement.

ABBREVIATIONS

Solid State Chemistry

M	≡	metal
L	≡	ligand
TG	≡	thermogravimetry
DSC	≡	differential scanning calorimetry
DTA	≡	differential thermal analysis
α	≡	fractional decomposition
t	≡	time
T	≡	temperature
T_p	≡	temperature at peak maximum
T_i	≡	onset temperature
$f(\alpha)$	≡	function describing the rate of solid state reactions
E_a	≡	activation energy
Z	≡	frequency factor
oct.	≡	octahedral
tet.	≡	tetrahedral

$(1-\alpha)^{\frac{1}{2}} = kt$ refers to the contracting area model

$(1-\alpha)^{\frac{1}{3}} = kt$ refers to the contracting volume model

$\alpha = kt$ refers to the linear rate law

Solution Chemistry

β	≡	overall formation constant
ΔH	≡	the change in enthalpy of formation
ΔG	≡	the change in free energy
ΔS	≡	The change in entropy
[L]	≡	free ligand concentration
[M]	≡	free metal concentration
$[L]_i$	≡	initial ligand concentration
$[M]_i$	≡	initial metal concentration
Q	≡	heat

General

tmen	≡	N,N,N^1,N^1-tetramethylenediamine
py	≡	pyridine
quin	≡	quinoline
an	≡	aniline
α-pic	≡	α-picoline or 2-methylpyridine
β-pic	≡	β-picoline or 3-methylpyridine
γ-pic	≡	γ-picoline or 4-methylpyridine
$CoCl_2$2(py)	≡	bis(pyridine)cobalt(II) chloride
$CoCl_2$2(quin)	≡	bis(quinoline)cobalt(II) chloride
$CoCl_2$2(α-pic)	≡	bis(α-picoline)cobalt(II) chloride
$CoCl_2$2(β-pic)	≡	bis(β-picoline)cobalt(II) chloride
$CoCl_2$2(γ-pic)	≡	bis(γ-picoline)cobalt(II) chloride
$CoCl_2$4(an)	≡	tetra(aniline)cobalt(II) chloride

SUMMARY

Comparisons were given for the decomposition reactions of several metal complexes containing ligands related to pyridine. The ligands pyridine, quinoline, aniline, α-, β-, γ-picoline were studied. The metal complexes included the first row transition metal complexes, with special reference to cobalt, nickel and manganese. The effects of the electron-releasing substituents on the kinetic data as well as on the metal-ligand bond was reported. These substituents increased the electron density in the ring and strengthened the σ-bond and weakened the π-bond.

Kinetic models were assigned to the different decomposition reactions. Comparative kinetic data were reported for the analysis of isothermal and dynamic TG curves. It was found that if separate reactions occur the kinetic results of the dynamic TG curve represent the experimental TG curve the best. In addition the electron microscopy studies supported the assigning of the kinetic models.

The enthalpies of formation and the decomposition temperature at peak maximum, obtained from the DSC studies, indicated the strength of the various metal-ligand bonds. The strength of the cobalt(II)-ligand bonds in solution was also studied and if possible, compared to the solid state chemistry.

The strengths of different metal-ligand bonds were investigated by applying various thermogravimetric and physical techniques.

OPSOMMING

Ooreenkomste en verskille is aangetoon vir ontbindingsreaksies van 'n aantal metaalkomplekse wat pyridien verwante ligande bevat. Die ligande piridien, chinolien, anilien, α-, β-, γ-pikolien is bestudeer. Die metaalkomplekse het die eerste ry oorgangs-elemente ingesluit, veral met verwysing na kobalt, nikkel en mangaan. Die effek van die elekronvrystellende substituente op die kinetiese data en die sterkte van die binding tussen die metaal en die ligand is bespreek. Hierdie substituente het die elektrondigtheid van die ring verhoog, die σ-binding versterk en die π-binding verswak.

Kinetiese modelle is aan die verskillende ontbindingsreaksies toegewys. Ooreenkomste en verskille is aangetoon vanuit die kinetiese ontleding van die isotermiese en dinamiese TG kurwes. Dit is gevind dat indien aparte reaksies plaasvind, die kinetiese data verkry vanaf die dinamiese kurwe die eksperimentele TG kurwe die beste verteenwoordig. Bykomend is elektronmikroskopie studies aangewend om die toewysings van kinetiese modelle te ondersteun.

Die vormingsentalpieë en die ontbindingstemperatuur by die piekmaksimum, verkry vanaf die DSC studies, het die bindingsterkte van die verskeie metaal-ligande aangetoon. Die bindingsterkte van die kobalt(II)ligande in oplossing is ook gerapporteer en waar moontlik vergelyk met die resultate verkry vanaf die vastetoestand.

Dus verskeie termogravimetriese en fisiese tegnieke is aangewend om die bindingsterkte tussen die verskillende metale en ligande aan te toon.

CHAPTER 1

INTRODUCTION AND OBJECTIVES

Whatsoever thou takest in hand, remember the end, and thou shalt never do amiss.
Apocrypha, Ecclesiasticus 7:36.

1.1 INTRODUCTION

The majority of all known elements are transition elements. Manganese is relatively abundant, constituting about 0,085% of the earth's crust. In nature it occurs in nodules on the floor of the Pacific together with nickel, cobalt and copper. Cobalt always occurs in association with nickel. The main source of cobalt is the arsenical ores of nickel, copper and lead. The role of transition metals in industry is undeniable and of great importance.

Certain trends are observed for the transition metals, for instance the increased stability of the II state relative to the III state, through the series Ti, V, Cr, Mn, Fe, Co and Ni. The coordination chemistry of the transition metals in the II oxidation state, has been of great interest in the development of chemistry. The cobalt(II) ion forms numerous blue complexes, mostly octahedral or tetrahedral. Most manganese(II) complexes are high spin. The octahedral complexes show spin-forbidden as

well as parity-forbidden transitions, which accounts for the extremely pale colour of such complexes. For tetrahedral complexes, the transitions are still spin-forbidden but no longer parity-forbidden. These transitions are a hundred times stronger and the complexes have a noticeable pale yellow-green colour. Nickel(II) forms a large number of complexes, encompassing coordination numbers 4, 5 and 6, and thus shows all the main structural types viz. trigonal-bipyramidal, octahedral, square-pyramidal, tetrahedral and square.

The coordination chemistry of cobalt(II), manganese(II) and nickel(II) ions in the presence of various π-bonding ligands has been investigated intensively. All of these ligands contain at least one nitrogen atom within an aromatic ring system, and include the following:

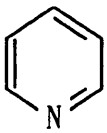

pyridine (py)

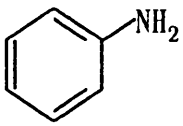

aniline (an)

Aniline is not related to compounds with the pyridine ring system, but some comparisons between aniline and pyridine complexes are possible.

When pyridine, or another hetero-aromatic molecule, forms a complex with a transition metal, the normal σ-bond, L → M, may be

supplemented by an additional π-bond, M → L, which results from the back-donation of electrons from the d-orbitals of the metal to the π^*-antibonding orbitals of the ligand. Substitution of the hydrogens in the pyridine ring by other groups causes a redistribution of electron density. Thus, electron-releasing substituents, e.g. $-CH_3$, cause the electron density in the ring to be raised, strengthening the σ-bond and weakening the π-bond. Another factor contributing to the strength of the bonds is the position of the substituents in the pyridine ring. The following ligands will be considered:

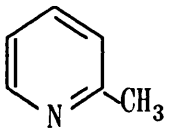

α-picoline (α-pic)

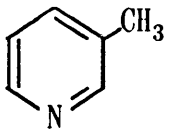

β-picoline (β-pic)

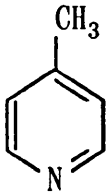

γ-picoline (γ-pic)

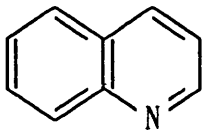

quinoline (quin)

The stabilities of these transition metal complexes are influenced by the delicate balance of several factors. These factors include the basicity of the ligand, steric interactions, π-bonding and the perturbing effect of the ligand field on the energy of the d electrons.

The coordination of transition metal(II) ions, especially the Co(II) ion, in the presence of ligands related to pyridine has been investigated intensively over the last few years [1-6]. Very little information is available on the quantitative aspects of the complex-formation reactions. Once a complex is isolated from a solution, various physical techniques such as X-ray diffraction, infrared and Raman spectroscopy are used to investigate the nature of the solid complex. However, quantitative thermodynamic and kinetic data pertaining the decomposition reactions of the complexes are not available.

The thermal decomposition reactions [7,8] were reported for several Ni(II), Co(II) and Mn(II) complexes containing ligands related to pyridine and include the following possible dissociation reactions:

$MCl_2 4L$ (cryst) → $MCl_2 2L$ (cryst.) + 2L (g) (1)

$MCl_2 2L$ (cryst.) → $MCl_2 L$ (cryst.) + L (g) (2)

$MCl_2 L$ (cryst.) → MCl_2 (cryst.) + L (g) (3)

$3MCl_2 L$ (cryst.) → $M_3Cl_6 2L$ (cryst.) + L (g) (4)

$M_3Cl_6 2L$ (cryst.) → $3MCl_2$ (cryst.) + 2L (g) (5)

$MCl_2 4L$ (cryst.) → MCl_2 (cryst.) + 4L (g) (6)

$MCl_2 2L$ (cryst.) → MCl_2 (cryst.) + 2L (g) (7)

$MCl_2 4L$ (cryst.) → $MCl_2 L$ (cryst.) + 3L (g) (8)

$CoCl_2 2$(py) (cryst.,violet) → $CoCl_2 2$(py) (cryst.,blue) (9)

where L = pyridine, picoline, aniline or quinoline;
and M = Mn, Co or Ni.

The octahedral complex, $CoCl_2 4$(py), decomposes to $CoCl_2 2$(py) according to reaction (1). Two different forms of the complex $CoCl_2 2$(py) exist; the violet form, which is an octahedral complex, and the blue form, which is a tetrahedral complex. Reaction (9) refers to the conversion of the violet form to the blue form. Finally, the formation of the octahedral halogen

compound, $CoCl_2$, is given by the overall reaction (6). The thermochemical decomposition of the complex $NiCl_2 4(py)$ proceeds via reactions (1), (2) and (3). The complex $MnCl_2 2(py)$ decomposes via reactions (2), (4) and (5) and therefore the additional complex, $Mn_3Cl_6 2(py)$, is observed as a stable intermediate.

The thermal decomposition of the complexes $CoCl_2 2(quin)$ and $NiCl_2 2(quin)$ proceeds according to reaction (7). Beech reported that during the first stage of the thermal decomposition of the complex $CoCl_2 2(quin)$, the products dissolve in the liberated quinoline to give a solution which subsequently decomposes to crystalline cobalt(II) chloride and gaseous quinoline. Thus the scheme of thermal decomposition is

$$CoCl_2 2(quin)\ (cryst.) \rightarrow CoCl_2(quin)\ (soln.\ in\ quin) \qquad (10)$$

$$CoCl_2(quin)\ (soln.\ in\ quin) \rightarrow CoCl_2\ (cryst.) + 2(quin)\ (g) \qquad (11)$$

In the study of the complex $NiCl_2 2(quin)$, the decomposition reactions (2) and (3) were observed, but only the heat of the overall reaction (7) was measured. The thermal decomposition of $MnCl_2 2(quin)$ was however, not studied.

The complexes $CoCl_2 2(an)$ and $MnCl_2 2(an)$ decompose according to reaction (7). However, the decomposition of $MnCl_2 2(an)$ takes place in three successive stages and the decomposition reaction therefore shows additional intermediates. The thermal

decomposition of $NiCl_2 2(an)2(EtOH)$ proceeds via reaction (7) as well as an another reaction, which involves the liberation of the ethanol molecules

$$NiCl_2 2(an)2(EtOH)\ (cryst.) \rightarrow NiCl_2 2(an)\ (cryst.) + 2EtOH\ (g)$$

The substituted pyridine complexes, under consideration, include the α- , β- and γ-picoline complexes. The complex $CoCl_2 2(\alpha\text{-pic})$ decomposes according to reaction (7), while the decomposition of $NiCl_2 2(\alpha\text{-pic})$ proceeds via two successive steps, shown in reactions (2) and (3). There is, however, no information available on the decomposition of $MnCl_2 x(\alpha\text{-pic})$, where x is presumably equal to two. The decomposition of the complex $CoCl_2 2(\beta\text{-pic})$ is represented by reaction (7). Additional intermediates were, however, observed for the decomposition of $MnCl_2 2(\beta\text{-pic})$, and this is represented by reactions (2), (4) and (5). Due to the size of the nickel(II) ion, it is possible to prepare a six-coordinate complex, $NiCl_2 4(\beta\text{-pic})$. The stages of dissociation are similar to those for $MnCl_2 2(\beta\text{-pic})$, and are therefore described by reactions (1), (2), (4) and (5). The decomposition of the γ-picoline complexes differ from the other picoline complexes with respect to the intermediates obtained. The complex $CoCl_2 2(\gamma\text{-pic})$ decomposes according to reaction (7), while the decomposition of $MnCl_2 2(\gamma\text{-pic})$ is described by reactions (2), (4) and (5). It is possible to obtain $NiCl_2 4(\gamma\text{-pic})$, similarly to $NiCl_2 4(\beta\text{-pic})$, and its thermal decomposition is characterised by reactions (8) and (3).

The heats of dissociation of $MCL_2 2L$ complexes, obtained for reaction (7), are summarised in Table 1.

Table 1. The heats of dissociation of $MCl_2 2L$, obtained for reaction (7), and the pK_a values of the ligands.

Ligand	pK_a	Enthalpy of formation (kJ mol^{-1})		
		M = Co	M = Ni	M = Mn
py	5,22	119,7	136,4	119,2
α-pic	5,96	109,6	66,11	--
β-pic	5,63	91.63	140,6	134,3
γ-pic	5,98	129,7	--	144,3
quin	4,85	126,8	142,7	--
an	4,58	148,5	135,1	125,9

Factors influencing the enthalpies of formation include the basicity of the ligand and the different charge densities in the pyridine ring. There is a correlation between the strength of the M → L σ-bonds and the basicity of the ligands. A smaller value of the enthalpy of formation is observed for L = α-pic than for L = py. The weaker bonds for L = α-pic is probably due to the steric interaction of the α-methyl group on the metal-donor-N bond. The larger values of the enthalpy of formation for L = γ-pic, compared with L = py, are in agreement with the

greater basicity of the ligand. A similar trend is observed for L = β-pic in the nickel(II) and manganese(II) complexes. However, in the cobalt(II) complexes, a lower heat of formation is observed for L = β-pic than for py. This may be attributed to an additional factor which contributes to the bond strengths, i.e. the different charge densities in the pyridine ring. The Co → L π-bonding will be localised mainly on the 2, 4 and 6 positions. The ligand, β-picoline already carries an excess of charge on these positions, thus inhibiting the π-bonding. However, for L = γ-picoline the positions 2, 4 and 6 are those of the lowest electron density, resulting in favouring of the π-bonding in the complex. Allan [9] observed the following infrared frequencies for the Co-N bonds in the $CoCl_2 2L$ complexes:

LIGAND	FREQUENCY (cm^{-1})
py	243
α-pic	233
β-pic	240
γ-pic	244

In general, higher frequencies represent stronger bonds (as seen for L = py and γ-pic). Previously it was stated that the Co → L π-bonding (for L = β-pic) is encouraged in the β-position, but the inverse is observed for L = α- and β-picoline.

The larger enthalpy values observed for L = quin can be attributed to the more extensive electron delocalisation in quinoline when compared to pyridine. A lower enthalpy value was expected for L = aniline, but this was only observed for the nickel(II) complexes. A possible explanation for the deviation from the expected values in the other metal ions is that for the smaller sized metal ions (Mn and Co) less steric repulsion exists. This is due to the bulky phenyl group being one atom removed from the metal atom and thus allowing in a closer approach of the bonding nitrogen atom. Several other authors have reported the thermal decomposition of the pyridine-related complexes. This will be discussed in detail in the following chapters.

1.2 OBJECTIVES

The aim of this study was to perform a comparative study on several decomposition reactions of metal complexes with ligands related to pyridine. The metals studied were the first row transition metals, specifically manganese, cobalt and nickel. Also the effect of electron-releasing substituents on the π-bond (M → L) and the σ-bond (L → M) were included. This substituents increase the electron density in the ring and therefore a strengthening in the σ-bond and a weakening of the π-bond were anticipated.

The thermal decomposition of these complexes has been

investigated but only the stable intermediates were reported. A fundamental part of the study therefore involved the assigning of kinetic models. This also involved the calculation of activation energies and frequency factors. In order to establish the best representative of the experimental TG curve, comparative kinetic analysis were performed on the isothermal and dynamic TG curves. The analysis of the dynamic TG curves [Section 2.2.4] has been developed recently and the reliability of the analysis method is also under consideration.

Another technique, generally, applied in the determination of the kinetic model is electron microscopy. This technique is especially useful during the initial stages of decomposition.

Information regarding the various metal-ligand bonds can be obtained by performing DSC and DTA studies on the complexes under consideration. The enthalpies of formation for the various decomposition reactions are then obtained by integrating the observed peaks.

Additional thermodynamic data can be obtained by studying the complex-formation reactions in non-aqueous media. This is mainly done to determine the strength of the metal-ligand bonds for comparison with bond strengths obtained in the solid state. However, only the complex-formation reactions of cobalt(II) chloride with various pyridine-related ligands were considered. Various additional equilibria exist for the complex formation of

the metal ion, nickel, and the solution chemistry of the nickel(II) ion was therefore not included in this study. The entropy titration method was selected and it was therefore necessary to evaluate the validity of this method and to compare the results obtained with those given in previous reports. The silver(I) / N,N,N^1,N^1-tetramethylenediamine system in acetone was chosen as a model since the complexes are very stable and the appropriate equilibria are known. Competing reactions were therefore excluded. It was, furthermore, necessary to study a system containing more than one equilibrium, since the complex-formation reactions under investigation involved more than one equilibrium.

Thus the main part of this study involved the investigation of the strengths of various metal-ligand bonds and the assigning of kinetic models, by applying various thermogravimetric and physical techniques.

CHAPTER 2

THE THEORIES OF SOLID STATE AND SOLUTION CHEMISTRY

Professors in every branch of the sciences prefer their own theories to truth; the reason is that their theories are private, but truth is common stock. Lacon (1825),1378.

2.1 INTRODUCTION

In order to achieve the aims stated in the previous chapter, an intensive study of the corresponding theory was initiated. This chapter is concerned with the theory of the different techniques of determination of thermodynamic and kinetic quantities.

2.2 THE THEORY OF SOLID STATE REACTIONS

2.2.1 Introduction

Chemical reactions are the essence of chemistry and thus a treatment of the principles of chemical reactions is essential to a study of chemistry. Reactions in the solid state are concerned with the formation and breakage of chemical bonds. Thermal decomposition reactions involve the addition of heat to crystals in the solid state and this results in the breakage and formation

of bonds in the crystals. Most investigations of decomposition reactions are concerned with the measurement of the fractional decomposition(α) that has occured during a period of time(t), at certain temperatures.

This study involves the following type of irreversible decomposition reactions:

$$A\ (s) \rightarrow B\ (s) + C\ (g)$$

Excellent treatises on solid decompositions have been published [10-15].

2.2.2 Imperfections

Decomposition in the solid state is initiated at certain regions of the crystal only. This initiation occurs in the early stages of decomposition at, or very near, the external crystal surface and at sites where imperfections (defects) are found or disorder exist. Sufficient data have been accumulated during the last forty years to prove this phenomenon [16].

G. Busch [13] and several other workers discussed the different types of imperfections in crystals as well as the effect of imperfections on decomposition. The term lattice defects or imperfections is used to describe all deviations from a strict three-dimensional periodicity of the crystal structure. The first kind of imperfection considered is structural and chemical

imperfections, which may occur in numerous combinations. In imperfections of the second kind, the structural particles have no "ideal" positions and display statistical fluctuations in their positions relative to their nearest neighbours. Imperfections of the second kind will not be considered in the study.

Structural imperfections occur only in stoichiometric crystals without impurities, and include all deviations in the perfect lattice. Thus structural imperfections include all deviations from a perfect arrangement of the crystal building blocks. The three types of structural imperfections are point defects (atomic imperfections), line defects and planar defects.

(a) Point defects

There are several important kinds of lattice defects [17]. Point defects are further subdivided into three types:

(i) Vacancies

These arise if some of the lattice points are unoccupied as a result of the migration of lattice particles to the surface. These defects are also called Scottky defects. The following diagram describes this phenomenon:

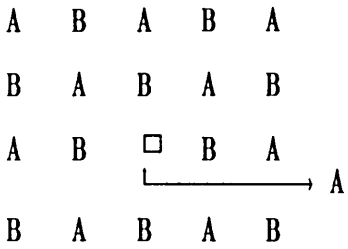

(ii) **Interstitials**

Lattice particles moving from their regular sites, leaving vacancies behind, give rise to the formation of interstitial positions in the lattice. The combination of an interstitial and a vacancy is called a Frenkel defect and is represented by the following diagram:

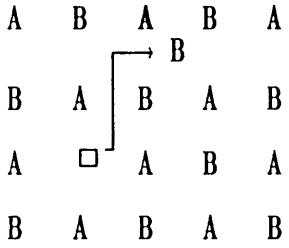

(iii) **Disorder in ordered alloys**

In compounds or ordered alloys lattice sites can be occupied by the "wrong" atoms. This is represented by the following diagram:

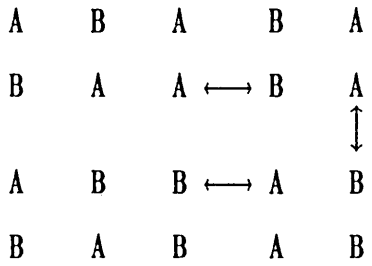

(b) Line defects

According to G. Busch [13] line defects are lattice imperfections along closed lines or open lines which end at the crystal surface. The crystal structure in a volume whose radial extension is of the order of about one atomic separation is disturbed around these lines. These one-dimensional lattice defects are called dislocations. Dislocations are of two general types:

(i) Edge dislocations

A simple way to visualise an edge dislocation is by imagining a plane of atoms inserted only partly into a crystal. Thus a lattice plane which ends inside the crystal will strongly distort the lattice along its boundaries. The lattice forces therefore change, since the lattice particles at the edge of the lattice "half" plane (dislocation line) are different from those in the undisturbed crystal.

(ii) Screw dislocations

They consist of a line of atoms which represents an axis about which the crystal planes are warped, in order to give an effect similar to the threads of a screw. Thus, what would be a round trip about the screw axis, results in a displacement to the crystal plane below. The screw axis is the dislocation line and near it the lattice is strongly distorted.

Dislocations are generally produced when the crystal is growing, but may also result from sufficiently strong external mechanical stress. Etching of metal crytals by acids occurs preferentially

at such points and thus makes the dislocations visible.

The points where edge or screw dislocation lines emerge to the surface of a crystal represent points of strain and enhanced chemical reactivity.

(c) Planar or surface defects

The surface itself is a major defect in the periodicity of the lattice. The reason for this is the discontinuity produced by the surface in the periodic field. Essentially two types of discontinuity, which may also occur in combination, are found:

(i) Grain boundaries

This type of surface defect may be considered to be a series of dislocations. Thus the orientation of the crystal on one side of the surface is different from that on the other.

(ii) Stacking faults

These faults are particularly marked in crystals with close packing. In this type of defect, two lattice planes are mutually shifted by a vector which is not a lattice vector. The plane layers are constructed by arranging equally large spheres as densely as possible.

Tamm [18] suggested that bond levels can exist at such surfaces and that these levels could trap electrons. The role of surface defects in controlling the mechanism of decomposition of solids has been stressed in the photolysis of BaN_6 [19,20].

In addition to the defects arising from structural imperfections defects of a more chemical nature are found. These are associated with the presence of chemical impurities, which may be there accidently or may have been deliberately introduced. Such impurities can drastically change the properties of materials and hence their controlled introduction is being exploited in producing new materials with desirable combinations of properties.

2.2.3 Kinetics of solid decomposition

This review of decomposition of solids includes isothermal as well as non-isothermal methods.

Isothermal methods involve the measuring of α (fractional decomposition) as a function of t (time) at different, constant temperatures. The most general α (t) versus t plot is shown in Figure 1. The decompositions of particular solids may show some or all the the fractions represented in Figure 1. The line AB represents the desorption reaction of physically adsorbed gases and is unrelated to the decomposition reaction. A low activation energy is ussually obtained for this initial rapid gas evolution. An exception exists where a significant surface decomposition takes place and apparently terminates before the main reaction commences. The line BC describes the induction period. This period is characterised by a slow, approximately linear evolution of gas. At point C the acceleratory period begins, during which the rate increases rapidly and monotonicly until the maximum

Figure 1. The most general $\alpha(t)$ versus time plot (isothermal plot).

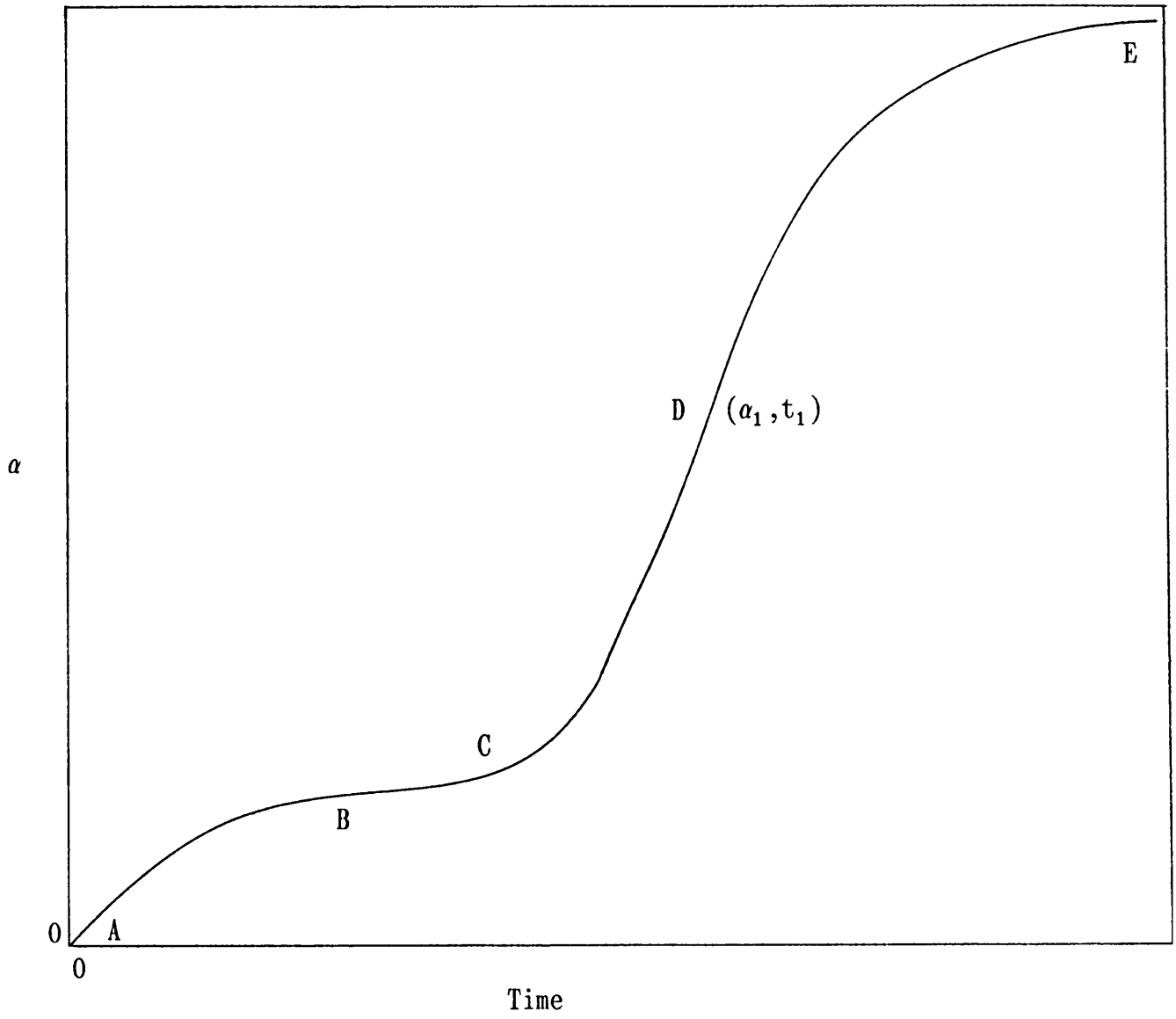

value is reached at the inflection point D. Point D represents also the start of the decay period, which is characterised by a rate decrease to zero, which is reached at the completion of the decomposition at E.

Extensive theoretical as well as experimental studies have been performed on the acceleratory period. The kinetic results are generally fitted to a variety of expressions, which will be discussed later.

The theory regarding the analysis of the sigmoidal curve BE is based on the assumption that the formation of a second product phase is started at certain discrete and energetically favoured positions (nucleus formation sites). The nucleus formation sites rise to the formation of active growth nuclei and the reaction is subsequently confined to the product/reactant interface.

(a) <u>The laws of nucleus formation</u>

A number of sites having defects (imperfections) or highly localised decomposition favour the further decomposition of the solid. The reason for this is that a relatively low activation energy for decomposition is required at these sites. The low energy of activation may be a consequence of a enormous strain energy associated with such sites. These sites are called germ nuclei. They grow to become growth nuclei as decomposition progresses. It is most improbable that a germ nucleus would revert back to its initial stage i.e. undecomposed reactant molecule (observed in phase transformation), since the negative

free energy of the chemical transformation of reactant to product is comparatively large. Thus, in general, all germ nuclei are active growth nuclei.

There are three laws of nucleation. The first law states that a constant number of nuclei exist in the lattice and they grow in size as the reaction progresses. Hannay [12] distinguishes between single-step nucleation and multistep nucleation. The second and third laws are concerned with single-step nucleation and multistep nucleation, respectively.

Single-step nucleation at identical sites assumes a single molecular decomposition in order to produce a stable nucleus that immediately proceeds to grow. The history, chemical nature and form of the crystal determine the number of sites for nucleation. Assuming that the free energy of activation ($\Delta G^{\neq}$) is identical to the transformation of all the initial sites (n_0) to stable nuclei. The number of nuclei present at time t is given by

$$\frac{dn}{dt} = k_1 [n_0 - n(t)]$$

or

$$n(t) = n_0 (1 - e^{-kt})$$

where k is the rate constant and k_1 refers to the rate constant for a single molecular transformation.

In general, it is assumed that $n(t) = 0$ at $t = 0$. The situation may also be considered where $n(t) \neq 0$ at $t = 0$. Previously the assumption was made that the rate constant k_1 is the same for all

n_0 sites which refer to a single molecular transformation. If $\Delta G^{\neq}$ is sufficiently small, and k_1 is thus large, then $n_0 = n(0)$. This refers to the reactant being fully nucleated at room temperature or becoming so within the time period of heating before the reactant decomposes. If the potential sites are well separated, the $\alpha(t)$ versus t plot corresponds to the increasing area of the growing nuclei. If k_1 is sufficiently small ($\Delta G^{\neq}$ is large) then n(t) increases linearly with time and the $\alpha(t)$ versus t plot includes the rate constant of nucleus formation as well as growth.

Single-step nucleus formation at non-identical sites, are usually localities of crystallographic disorder. The specific nature of the disorder, e.g. dislocations, will determine the free energy of activation of the formation of growth nuclei. These dislocations may intersect different external crystallographic planes. A solution for the function of $\Delta G^{\neq}$, $\phi(\Delta G_n)$, with respect to n_t, was developed by Roginski [21], by studying the rate of adsorption of a gas on a non-uniform surface.

Thus the rate of nucleus formation at potential sites for which a free energy ΔG^1 of activation is required, is represented by

$$N^1 - n(t) = C(N^1 - n_t^1)e^{(-\Delta G_n^1/RT)}$$

where N^1 is the total number of potential sites associated with a free energy ΔG_n^1 which varies from ΔG_n^0 (minimum value) to ΔG_n^m (maximum value) and C is a constant. All the sites can be

included by intergration between these two limits, ΔG_n^o and ΔG_n^m.

An explicit solution may be obtained by specifying the simplest distribution, thus

$$\Delta G_n^m = \Delta G_n^o + E(n_t)$$

where $n_t = N_0 B \ln t + D$;
and E, B and D are constants.

In the analysis of single-step nucleation is it essential that the rate of growth does not exceed the rate of nucleus formation appreciably, in order to separate nucleation and growth. This requirement is acceptable, since in single-step nucleation the first molecular decomposition occurs at a different environment than that of all subsequent decompositions of reactant molecules. However, in a multistep nucleation process such a distinction between nucleation and growth may not be evident. It has been found that the multistep process obeys a power law. Barium azide complies to the power law, $n_t = (k_1 t)^3$, as shown by extrapolation of direct microphotographic measurements of the size and number of visible nuclei [22]. This led to the application of photographic sensitivity. It was established that the concentration of germ nuclei and hence the rate of nucleus formation may be altered by changing the conditions of preparation of the material. Alternatively, the sample can be irradiated with UV light or high energy radiation. Acceleration of subsequent decomposition due to prior irradiation has been reported [19,23].

The theory of multistep nuleation involves the formation of a growth nucleus by p successive molecular decompositions at a single site. Nuclei comprising fewer than p product molecules are inactive germ nuclei. These inactive germ nuclei can be converted to growth nuclei by acquiring p product molecules in successive steps. The rate of change of the population of nuclei is given by the following set of coupled differential equations:

$$dn_j/dt = k_{j-i}n_{j-i} - k_jn_j$$

where n_j is the number of nuclei comprising j germ nuclei and k_j is the rate constant for the addition of a germ nucleus to a nucleus comprising j such nuclei.

The following boundary conditions are essential:

(i) At $t = 0$, $n_j = 0$ for $j \lesseqgtr 0$.

(ii) At $t = 0$, $n_0 = N_0$ for $j = 0$.

(iii) At $t = \infty$, $n_0 = N_0$ for $j = 0$.

Thus for p = 0, 1, 2 the values for n_j are

$$n_0 = N_0e^{-k_0t}$$

$$n_1 = [k_0N_0/(k_1 - k_0)](e^{-k_0t} - e^{-k_1t})$$

$$n_2 = \frac{k_1k_0N_0[(k_2 - k_1)e^{-k_0t} - (k_2 - k_0)e^{-k_1t} + (k_1 - k_0)e^{-k_2t}]}{(k_1 - k_0)(k_2 - k_0)(k_2 - k_1)}$$

If $k_j t << 1$ for all j, a condition occuring frequently in practice, the exponential term is expanded to give

$$n_2 = k_0 k_1 N_0 t^2/2!$$

for an active growth nucleus comprising a cluster of two germ nuclei.

Bagdassarian [23] considered the special case where $k_0=k_1....=k_{p-1}$ and $k_p=k_{p+1}$ $....=k_g$. The rate constant of growth, k_g, represents the addition of a germ nucleus to the active growth nucleus, which contains p germ nuclei.

The following approximation applies:

$$n_p = [N_0 (k_0 t)^p/p!]e^{-k_0 t}$$

which for $k_0 t << 1$ reduces to

$$n_p = N_0 (k_0 t)^p/p!$$

The assumption that all k values are equal until the growth nucleus is formed has no justification, since such a nucleus is formed at a selective site by the successive addition of adjacent germ nuclei. Thus, each germ nucleus in the cluster is created in a different crystalline configuration. This is modified by the presence of previously formed germ nuclei. Consequently, the free energy of activation to transform a j cluster to a (j+1) cluster,

will be different for different integral values of j, and therefore $k_0 \neq k_1 \neq \ldots\ldots \neq k_j$. This particular solution is therefore unsatifactory.

Allnatt and Jacobs [24] derived general solutions for two specific cases:

(i) All k_j different.

(ii) k_j different up to $j = p-1$ and all k_j equal to k_g for $j \geq p$.

The solutions are

(i) $n_p = k_{j-1}k_{j-2}\ldots\ldots k_0 N_0 t^p/p!, \qquad k_j t \ll 1$ for all j

and

(ii) $n_p = k^{j-p-2}k_{p-1}k_{p-2}\ldots\ldots\ldots k_0 N_0 t^p/[(j-p-2)!p!],$

$k_g t,\ k_j t \ll 1$

Both equations reduce to the general form in the limit of small values of t

$$n_p = K_p t^p$$

with K_p having different meanings in each case. As soon as the active growth nuclei containing p germ nuclei are formed, no further assumptions about k_j, for $j > p$, are required, since k_j is then determined by the characteristics of the growth process. However, the problem regarding the distinction between nucleus formation and growth remains.

(b) Laws of nucleus growth

Two main theories exist for the mechanism of progression of the reactant/product interface through the solid.

(i) In the interfacial mechanism, the reaction proceeds by successive decomposition of reactant molecules and does not involve the mobility of any species in the reactant matrix.

(ii) In the diffusion-controlled mechanism, the species that ultimately forms the product is assumed to be mobile and diffuse in order to react with the reactant/product interface.

These different types of mechanisms were observed for azide decompositions [12].

(c) Kinetic equations of nucleus formation and growth

The rate of solid state reactions may be finally represented by a function $f(\alpha)$ multiplied by the rate constant(k),

$$\frac{d\alpha}{dt} = kf(\alpha)$$

Thus a decomposition reaction may be sufficiently described when the rate constant and the time law $f(\alpha)$ are given. When using this equation for a particular topochemical model, the temperature in the system must be uniform. For isothermal conditions, i.e. when the decomposition reaction is monitored at a constant temperature, various logical approaches have been developed [25,26]. Rate equations which have found applications in kinetic studies of solid phase reactions are listed in Table 2, as given by Gallagher and Johnson [27,28].

Table 2. The different kinetic rate equations listed by Gallagher and Johnson.

1. Acceleratory rate equations

Power Law: $\alpha^{-n} = kt$ for n = 0,5, 1, 2, 3 and 4

Exponential law: $\ln \alpha = kt$

2. Sigmoid rate equations

Avrami-Erofeev: $[-\ln(1-\alpha)]^{-n} = kt$ for n = 2, 3 and 4

Prout-Tompkins: $\ln[\alpha/(1-\alpha)] = kt$

3. Deceleratory rate equations

3.1 Based on diffusion mechanism

One-dimensional diffusion: $\alpha^2 = kt$

Two-dimensional diffusion: $(1-\alpha)\ln(1-\alpha) + \alpha = kt$

Three-dimensional diffusion: $[1-(1-\alpha)^{-3}]^2 = kt$

Ginstling-Brounshtein: $[1-(2\alpha/3)] - (1-\alpha)^{0.67} = kt$

3.2 Based on geometric models

Contracting area: $1 - (1-\alpha)^{0.5} = kt$

Contracting volume: $1 - (1-\alpha)^{0.33} = kt$

3.3 Based on order with respect to α

First order: $-\ln(1-\alpha) = kt$

Second order: $(1-\alpha)^{-1} = kt$

Third order: $(1-\alpha)^{-2} = kt$

Although rate equations have been developed, greater consequences were observed for the Avrami-Erofeev [29,30] and Prout-Tompkins [31] equations.

Avrami assumed a random distribution of germ nuclei, which are consumed by activation of the germs into growth nuclei, and the promotion of germs into the advancing phase of growth nuclei.

An expression of a similar form has been given by Erofeev [30]. Erofeev has extended the equation of Avrami, by including reactions of solids with different specific surfaces.

This conventional theory of decomposition of solids assumes discrete formation and growth of nuclei. Thus each process is associated with a different rate constant. Allnatt and Jacobs [24] felt that this is a realistic procedure if a nucleus is formed as a result of a single-step reaction. Thus if the nucleus is formed by a single-step and the reaction is auto-catalytic

$$k_{growth} > k_{formation}$$

Alternatively, if the nucleus is formed at a special or unique site, whose geometry or special feature is destroyed during the decomposition, the following applies:

$$k_{growth} < k_{formation}$$

The assigning of kinetic models is simplified by modern computer technology.

(d) Activation Energy and Frequency factor

For the estimation of an activation energy, at least four isothermal experiments are required. For complex processes which possibly yield several fractionally straight lines in the Arrhenius diagram, even six to seven points may not be sufficient.

The activation energy E_a and the frequency factor Z can be expressed as

$$k = Ze^{(-E_a/RT)} \qquad (1)$$

where k is the rate constant, calculated from the expression

$$\frac{d\alpha}{dt} = kf(\alpha) \qquad (2)$$

Previously, isothermal curves have been the only means of determining the kinetic rate equations. Recently, however, Doyle [32] performed kinetic analysis on dynamic TG curves.

2.2.4 Dynamic kinetics

The kinetic analysis of thermogravimetric data involves the deriving of a rate equation for a certain decomposition reaction. For the decomposition reaction, the fractional mass loss (α) can be plotted versus temperature (T) for a sample heated a constant heating rate (q). A dynamic TG curve is thus the equivalent of a number of isothermal curves, and is a rich source of kinetic

data.

Thermogravimetric analysis is performed at a constant heating rate (q), therefore the temperature increases linearly according to the following equation:

$$dT = qdt \qquad (3)$$

Combining equations (1), (2) and (3) gives

$$\frac{d\alpha}{f(\alpha)} = \frac{Z}{q} e^{(-E_a/RT)} \qquad (4)$$

Integration of the equation results in the equations of thermogravimetric curves [32-35].

Several models can be used to deduce the function $f(\alpha)$, which depends upon the mechanism of thermal decomposition. In general the kinetic equation is of the form

$$f(\alpha) = \alpha^a(1-\alpha)^b \qquad (5)$$

where a and b are empirical constants. For more complex processes, the function $f(\alpha)$ should contain additional parameters [36], e.g.

$$f(\alpha) = (1-\alpha)^n[-\ln(1-\alpha)]^p \qquad (6)$$

$$f(\alpha) = c_0 + c_1\alpha + c_2\alpha^2 + \ldots + c_n\alpha^n \qquad (7)$$

which results in an improved fit to the experimental TG data.

Roginski and Schulz [37] considered the simplest law for the decomposition of solids

$$f(\alpha) = (1-\alpha)^b \qquad (8)$$

where $b = \frac{2}{3}$.

His theoretical and experimental methods were used by many other authors [38-40]. The following b values were considered, namely 0, $\frac{1}{3}$, $\frac{1}{2}$, 1 and 2 [41].

Equation 5 with $a \neq 0$ and $b \neq 0$

$$f(\alpha) = \alpha(1-\alpha) \qquad (9)$$

was obtained for the first time by Lewis [42] and was derived theoretically by Prout and Tompkins [31]. Equations of this type have also been discussed for the cases $a < 1$, $b = 1$ and $a = \frac{2}{3}$, $b = \frac{2}{3}$ [41].

Several methods have been suggested for the integration of equation 4. Horowitz and Metzger [43] suggested an asymptotic expansion of T^{-1} at a conveniently chosen temperature, and by neglecting all the terms except the first two, obtained an integrable form of equation 4. When they took the logarithm of

the function, the following equation was obtained:

$$g(\alpha) = \int_0^{\infty} \frac{d\alpha}{f(\alpha)} \qquad (10)$$

which they have found to vary linearly with temperature. The activation energy E_a was calculated from the slope of the straight line. Zsakó [33] showed that the asymptotic expansion was quite justifiable over a temperature range 60^0C to 80^0C. Large errors in the determination of the activation energy were introduced, since the slope of the theoretical curve log $g(\alpha)$ vs T showed an error of approximately 25-30%.

Thus Zsakó [33] and Doyle [32] suggested the accurate integration of equation (4). Equation (4) can be written as

$$\frac{d\alpha}{f(\alpha)} = -[(ZE_a/Rq)(e^{-u}/u^2)]du \qquad (11)$$

where $u = E_a/RT$.

Integration of this equation from a temperature of absolute zero up to the actual temperature of the sample leads to the equation

$$g(\alpha) = -ZE_a/Rq \int_{\infty}^{x} (e^{-u}/u^2)du \qquad (12)$$

where x is the value of u at the temperature of the sample. The integral can also be written as

$$p(x) = -\int_{\infty}^{x} (e^{-u}/u^2)\, du$$

$$= e^{-x}/x - \int_{\infty}^{x} (e^{-u}/u)\, du \qquad (13)$$

Doyle [32] calculated and tabulated $p(x)$ values for x values ranging from 10 to 50. The equation of thermogravimetric curves derived from these values, is given by Doyle as

$$g(\alpha) = (ZE_a/Rq)\, p(x) \qquad (14)$$

The $p(x)$ values are dependent on both temperature and activation energy and this leads to difficulty in applying equation (14). Doyle has suggested a trial-and-error-fitting method for the determination of the activation energy. He considered reactions for which the function $f(\alpha)$ was known and computed $g(\alpha)$ values from the thermogravimetric data. This resulted in the determination of approximate value of E_a from the thermogram and simulated theoretical curves by means of equation (14). The presumed E_a value was then modified until an excellent fit was obtained between the theoretical and experimental curves. The E_a value that conforms to the best fit is taken as the correct value.

Ozawa [44] suggested a graphical method for the determination of the activation energy. Zsakó [33] simplified Doyle's trial-and-error method and found new applications of equation (14).

If the logarithm of equation (14) is taken the following equation is obtained:

$$\log (ZE_a/Rq) = \log g(\alpha) - \log p(x) = B \qquad (15)$$

where B is dependent upon the nature of the compound and the heating rate, but independent of temperature. If $f(\alpha)$ is known, the value of $g(\alpha)$ for a given temperature can be calculated from experimental data. Similarly, $p(x)$ can be obtained for the identical temperature if the activation energy is known. Because of the constancy of the difference $\log g(\alpha) - \log p(x)$ a quantitative method of testing the validity of different kinetic equations of the same type as equation (4) can be used and thus the activation energy can be determined, consistent with a given function $f(\alpha)$.

In Zsakó's method a function $f(\alpha)$ is presumed to be valid and $g(\alpha)$ values are calculated from the thermogravimetric data for different temperatures. By means of a trial-and-error method, the activation energy can be estimated by finding the E_a value. This ensures the the maximum constancy of

$$B = \log g(\alpha) - \log p(x)$$

The fit obtained between the experimental data and simulated data obtained from the presumed E_a value can be characterised quantitatively by the standard deviation of the individual B_i values from the arithmetical mean $\bar{B}$. Thus

$$\delta = \sqrt{(B_i - B)^2/r} \qquad (16)$$

where r is the number of experimental data points used for the calculation of B. The minimum of δ indicates the best E_a value. The minimum value, δ_{min}, is also a measure of the consistency of the decomposition process for a certain function $f(\alpha)$. If the other kinetic equations are presumed and the corresponding δ_{min} values are then calculated, the minimum δ_{min} will indicate the correct function $f(\alpha)$, among all the other functions.

The apparent frequency factor is then calculated from the obtained B value, according to the equation

$$\log Z = B + \log Rq - \log E_a \qquad (17)$$

Šatava and Škvára [45] suggested an alternative graphical procedure, in contrast with the tedious method described by Zsakó. This method involves the graphical comparison of log $g(\alpha)$ and log p(x). The values of -log p(x) vs temperature from 0°C to 1000°C were plotted. The p(x) values were calculated, by applying the Akahira method [46].

The values of log $g(\alpha)$ were calculated for different kinetic equations [47]. The α values at certain intervals and the corresponding temperatures were obtained from the TG curve. The log $g(\alpha)$ values for the various rate processes were plotted on transparent paper against the corresponding temperature values,

on the identical scale as the plot of -log p(x) versus temperature. The plot of log g(α) was placed on top of the log p(x) diagram, while ensuring that the temperature scales coincide. The plot of log g(α) was then shifted along the y-axis until one of the curves fitted on one of the log p(x) curves. From this log p(x) curve, the activation energy could be read. The specific log g(α) curve therefore determines the correct kinetic rate equation. After ensuring that the values on the axis coincide, the values of the quantity B and the subsequent activation energy and the frequency factor can be determined.

The shape of the isothermal decomposition curve depends only on the reaction mechanism. In contrast the shape of the dynamic TG curve depends on:

(i) The temperature, which is dependent on the rate constant, which includes the activation energy and the frequency factor;

(ii) the heating rate q.

Changes in the heating rate and/or the frequency factor result in a shift along the temperature axis. The rate control process, in contrast, affects the shape of the curve. The accuracy of the results depends on the fit of the experimental data on the dynamic TG curve over the whole α-range. In isothermal studies it is even more difficult to obtain a fit over the whole α-range, due to the decomposition of the sample before the preselected temperature is reached and the gradual flattening of the curve in the final decomposition stage.

Šatava [48] later revised the rate constant(k). This involves the inclusion of the change of free energy for the corresponding process. The rate constant is then given by

$$k = Z\ e^{(E_a/RT)}(1 - e^{\Delta G/RT})$$

where ΔG is the change of the free energy corresponding to the given process under consideration. If the equilibrium temperature at which the process proceeds is suffiently different from the equilibrium temperature, then the term $e^{\Delta G/RT}$ becomes negligible and this leads to the normal Arrhenius equation.

Šatava also discussed the effect of heating rate on the decarbonization of calcite. The same decomposition mechanism was obtained by several other authors [49-51]. Šatava reported that the function log $g(\alpha)$ is not linear at low heating rates (e.g. $1^0C\ min^{-1}$). However the function is linear at high temperature rates (e.g. 10 $^0C\ min^{-1}$). It is evident that the use of high heating rates is advantageous in certain studies. Poor distinction between successive reactions is a disadvantage of a high heating rate. In certain studies one factor is more important than the other. In this study, a distinction between the successive reactions was of great importance.

It seems that the analysis of the dynamic TG curve has some definite advantages over the analysis of the isothermal curves. Special applications include cases where rapid reactions occur at high temperatures. Using the dynamic TG curve it is possible to

measure α at each corresponding temperature, since a constant heating rate is applied. Another application is where the product of a reaction becomes the reactant in another reaction at a higher temperature.

A combination of the methods developed by Zsakó and Šatava were used in the analysis of the dynamic TG data. This therefore involves the calculation of δ_{min} for each kinetic expression, providing that the plot of δ versus E_a shows a minimum value over a preselected E_a range. The E_a value obtained at δ_{min} is then the required E_a value for a certain kinetic expression. Therefore, in deciding on a suitable kinetic expression both the minimum δ_{min} and % error of B should be taken into account. The frequency factor Z is then calculated from the quantity B. The parameters $f(\alpha)$, E_a, Z and q are combined to simulate a dynamic TG curve and this is then fitted on the experimental dynamic curve.

2.3 THE THEORY OF TITRATION CALORIMETRY

2.3.1 Introduction

Many experimental methods for the determination of thermodynamic quantities are known. Thermometric titrimetry and titration calorimetry techniques have a variety of applications. In general, titration calorimetry is based on two types of reactions:

(a) A replacement reaction of the form

$$AB + C \rightleftharpoons AC + B$$

(b) An addition reaction of the form

$$A + B \rightleftharpoons AB$$

Metal complexes follow of the addition type of reaction. Consider the following chemical equilibria, which represent the formation of a 1:2 metal-ligand complex

$$M + L \rightleftharpoons ML \qquad K_1 = \frac{[ML]}{[M][L]}$$

$$ML + L \rightleftharpoons ML_2 \qquad K_2 = \frac{[ML_2]}{[ML][L]}$$

where K_i is the stepwise stability constant.

The overall equilibrium is

$$M + 2L \rightleftharpoons ML_2$$

and it is characterised by an overall stability constant

$$\beta_2 = \frac{[ML_2]}{[ML][L]^2} = K_1K_2$$

and $\beta_0 = K_0 = 1$

$\beta_1 = K_1$

The stepwise free energy changes, ΔG_1, ΔG_2 can then be derived from the equilibrium constants by using the following equations:

$$\Delta G_1 = -RT \ln K_1$$

and

$$\Delta G_2 = -RT \ln K_2$$

The enthalpy change ΔH^0 and the entropy change ΔS^0 are related to the free energy change as follows:

$$\Delta G_1 = \Delta H_1^0 - T\Delta S_1^0$$

and

$$\Delta G_2 = \Delta H_2^0 - T\Delta S_2^0$$

The approach of Bjerrum [52] is usually applied in complexation equilibria. It is based on the evaluation of the mean number of ligands coordinated per unit concentration of the metal ion, $\bar{n}$ or the degree of formation of the system

$$\bar{n} = ([ML] + 2[ML_2])/([ML] + [ML_2])$$
$$= (\beta_1[L] + 2\beta_2[L]^2)/(\beta_1[L] + \beta_2[L]^2)$$

where [L] is the concentration of the free ligand.

The degree of formation $\bar{n}$ is also called the average ligand number and it can be evaluated experimentally if the concentration of the free uncomplexed ligand [L] is known. The values of $\bar{n}$ can then be calculated from the following equation:

$$\bar{n} = ([L]_{tot} - [L])/[M]_{tot}$$

where $[L]_{tot}$ = total equilibrium concentration of the ligand;
and $[M]_{tot}$ = total equilibrium concentration of the metal.

The equilibria concentrations are obtained from

$$[M]_{tot} = [M] + [ML] + [ML_2]$$
$$\text{and } [L]_{tot} = [L] + [ML] + 2[ML_2]$$

The degree of formation of the c^{th} momonuclear complex is then

$$\alpha_c = [ML_c]/[M]_{tot}$$

and

$$\sum_{c=o}^{2} \alpha_c = 1$$

Thus the determination of all the thermodynamic quantities can be made using experimental methods. This study is concerned with the titration calorimetry method of determination [53,54].

2.3.2 Titration calorimetry

This technique is mainly concerned with the continuous addition of titrant into the titrated solution. The temperature is measured as a function of the titrant added. An analysis of the data gives the relevant thermodynamic quantities and provides information about the coordination chemistry of the metal.

The shape of the thermometric titration curve is dependent of the equilibrium constants and enthalpy changes for all the reactions involved in the titration. The curve should be suffiently non-linear to allow calculations of log β_i, ΔH_i, ΔS_i and ΔG_i. This entropy titration method has been succesfully applied in many acid-base titrations, which involve a single protonation reaction [55-58].

(a) Apparatus

The apparatus consists of a burette and a reaction vessel in a water bath at a constant temperature of 25,000 ± 0,0003°C. The temperature change caused by the addition is sensed by a temperature sensor T and is converted to a corresponding voltage in a Wheatstone bridge circuit. The temperature of the titrant as well as the titrate is carefully controlled, since they must be the same or the difference must be precisely known. The voltage is then amplified and connected to a Prema Multimeter and a strip recorder. The data is sent via a IEEE bus interface to an Apple Microcomputer and the required calculations are performed.

(b) Thermogram

A thermogram is a plot of the heat liberated from the reaction occuring in the reaction vessel versus moles of titrant added or time of titrant delivery. The thermogram consists of the following four regions:

(1) An initial or lead period where no titrant is added.

(2) This is followed by a reaction period where the change in temperature of the titrant with time is largely the result of one

or more reactions occuring in the reaction vessel.

(3) This is followed by a postreaction period, where the reaction is complete and the temperature changes slightly with the addition of titrant,this region is mainly due to dilution of the titrate.

(4) The last region is the postreaction region where no titrant is added.

(c) Applicability of the technique

The range of applicability depends on the magnitudes of the equilibrium constants (β_i) and the enthalpy of formation (ΔH_i) for the overall reaction. The thermograms of systems where the β values are greater than 10^4 differ only slightly and therefore increase the systematic error. For reactions with a β value less than 0, very little reaction takes place and hence very little heat is evolved.

The following two factors contribute to succesful results [59]; The first factor is that the equilibrium constant should be small enough ($0 < \log \beta_i < 4$) to yield a sufficiently curved thermogram or if two equilibrium constants are present then the difference in the log β values should be approximately 4. The second factor is that the enthalpy change must be large enough so that temperature changes of 0,01% can be observed.

(d) Calculation of heats of reactions

In order to calculate the thermodynamic quantities, the gross heat liberated in the reaction vessel must be determined. This

involves also the calibration of the calorimetric equipment as well as analysis of the thermogram. The calibration of the equipment will be discussed in the following sections.

The analysis of the thermogram consists of the following:
(1) The determination of the initial heat capacity (initial heater calibration) before the addition of the titrant.
(2) The determination of the gross heat liberated in the reaction vessel.
(3) Similarly to (1), the determination of the final heat capacity (final heater calibration) after the addition of the titrant.

The determination of (1) and (2) is similar and they will therefore be discussed together.The heat capacity of the reaction vessel and content (before or after the addition of the titrant) is accurately measured by introducing a constant current through a resistance heater over a measured period of time.

The energy that the resistance heater supplies to the system is

$$Q_c = (HTRV)(HTRI)\Delta t/R \qquad (18)$$

where HTRV = the voltage over the heating element;
HTRI = the voltage over the standard Resistor (100Ω);
Δt = the elapsed time for the heater turned on;
and R = the standard Resistor (100Ω).

Thus the energy equivalent of the reaction vessel plus the contents before the addition of the titrant (initial heat capacity) in J mv^{-1} is

$$C_{pi} = Q_c/[\Delta T - (S_i + S_f)(t/2)] \qquad (19)$$

where Q_c = electrical energy introduced in the reaction vessel measured in Joule;

ΔT = total temperature rise in suitable units (mv);

S_i = initial rate (slope) of the temperature rise due to non-electrical heat contributions (mv s^{-1});

S_f = Final rate (slope) of temperature rise due to non-electrical heat contributions (mv s^{-1});

and t = time elapsed (s).

The energy equivalent of the reaction vessel plus contents (C_{pf}) after the addition of the titrant (final heat capacity), can also be calculated using equation (19).

Then the energy equivalent of the empty reaction vessel is

$$C_v = C_{pi} - V\rho C_p \qquad (20)$$

and $$C_v = C_{pf} - V\rho C_p \qquad (21)$$

where V = volume (cm^3);

ρ = density (g cm^{-3});

and C_p = heat capacity of the solution in the reaction vessel (J/g^0C).

Thus C_v is a constant value for a certain volume, but depends on changes in volume when titrant is added. This is due to the increase in vessel wall and volume contact, as titrant is added.

For a given amount of added titrant, the energy equivalent (heat capacity) of the reaction vessel and the contents is

$$C_p = C_v + (V\rho C_p)_s + (V\rho C_p)_t + (\delta C_{pt}/\delta V)V_t \qquad (22)$$

where $(V\rho C_p)_s$ = total heat capacity of the initial solution in the reaction vessel;

$(V\rho C_p)_t$ = total heat capacity of the titrant added;

$(\delta C_{pt}/\delta V)$ = increase in heat capacity due to the increase in the liquid-wall contact area in the reaction vessel;

and V_t = total volume in reaction vessel.

Therefore the total heat Q_p from the start of the reaction (characterised by a drastic difference in temperature) to any data point p during the reaction period, is given by

$$Q_p = -C_p(T_p - T_x) \qquad (23)$$

where T_p = temperature at point p;

and T_x = initial temperature of the titration.

The change in the bridge voltage E_x at a point x is a function of the bath temperature T_x and therefore

$$E_x = a + bT_x \qquad (24)$$

where a and b are constants.

By combining equations (22), (23) and (24), the following equation is obtained:

$$Q_p = -[C_v+(V\rho C_p)_s+(V\rho C_p)_{t,p}+(\delta C_{pt}/\delta V)V_{t,p}][(E_p-E_x)/b] \qquad (25)$$

where $V_{t,p}$ is the volume titrant added from point x to point p.

Thus

$$Q_p = (C_{p,p})[(E_p - E_x)/b] \qquad (26)$$

where $C_{p,p}$ = heat capacity at point p.

Substituting equation (24) in (26) results in

$$Q_p = (C_{p,p})[T_p - T_x] \qquad (27)$$

But

$$C_{p,p} = C_{p,f}(t_p/t_f) \qquad (28)$$

where $C_{p,f}$ = heat capacity at the end of the reaction period;
t_p = time elapsed up to datapoint p;
and t_f = time elapsed for the complete reaction period.

Substituting equation (28) in (27) results in

$$C_{p,p} = C_{p,f}(t_p/t_f)(T_p - T_x) \qquad (29)$$

Therefore at certain time intervals a set of (T_1, T_2, T_3,...,T_n) is obtained and then converted to a set of (Q_1, Q_2, Q_3,...,Q_n) by using equation (29).

(e) Non-chemical effects

The calculated Q_p values obtained from equation (29) include the heat of the reaction as well as non-chemical effects. These non-chemical effects include heat losses between the reaction vessel and its surroundings, stirring of the solution and resistance heating of the thermistor.

When calculating the non-chemical effects the following assumptions are made:

(1) The energy input from the thermistor and stirrer(w) is constant during the run.

(2) The heat loss is proportional to the temperature difference between the reaction vessel T_p and its surroundings T_j.

(3) The thermal leakage from the reaction vessel k and is constant.

(4) The product kC_p is constant.

Assumption (2) is equivalent to saying that the reaction vessel obeys Newton's law of cooling [60]. Therefore, based on these assumptions the following equations are obtained:

$$-S_i(C_x) = dQ_{h,x}/dt = q_{h,x} = -w - k(T_j - T_x) \quad (30)$$

$$-S_i(C_y) = dQ_{h,y}/dt = q_{h,y} = -w - k(T_j - T_y) \quad (31)$$

where w and k are positive constants and $q_{h,x}$ and $q_{h,y}$ are rates of heat loss at point x and y, respectively. The experimental values of S_i, S_f, T_x, T_y and T_j result in the solution of w and k using equations (30) and (31). Substituting the values of w and k, it is possible to obtain the value of q_h at any point p during the titration

$$q_{h,p} = -w - k(T_j - T_p) \quad (32)$$

In order to eliminate the unknown quantity T_j the equations (30), (31) and (32) can be combined

$$q_{h,p} = q_{h,x} + (q_{h,y} - q_{h,x})[(T_p - T_x)/(T_y - T_x)] \quad (33)$$

Therfore, the total contribution of the non-chemical heat effects from the start of the reaction (point x) to any time during the titration, point p, is given by the following:

$$Q_{h,p} = \int_{t_x}^{t_p} q_{h,i}\, dt \quad (34)$$

Equation (34) may be solved by using equation (33) and assuming that q_h is linear for the time interval (Δt) between the data points. Therefore, equation (34) may be expressed as the sum over all the data points up to point p

$$Q_{h,p} = \sum_{i=0}^{p} (\Delta t_i/2)(q_{h,i} + q_{h,i+1}) \qquad (35)$$

The heat evolved at point p can be simplified to the following equation:

$$Q_{h,p} = (-Q_i + Q_{f,p})\ t_p/2 \qquad (36)$$

where t_p = the time point p is taken;

Q_i = heat loss due to radiation and is calculated by

$$Q_i = S_i C_{pi} \qquad (37)$$

and the other unknown quantity ($Q_{f,p}$) is determined by

$$Q_{f,p} = -S_i C_{pi} + (S_a C_{pf} - S_f C_{pf})(\{T_p - T_x\}\{T_f - T_x\}) \qquad (38)$$

where S_i = initial slope of the titration curve;

S_a = after slope of the titration curve;

S_f = final slope of the titration curve;

T_p = temperature at point p;

T_x = temperature at the beginning of the titration;

and T_f = temperature at the end of the titration.

Combining equations (36), (37) and (38), the heat evolved at point p due to non-chemical effects can be written as

$$Q_{h,p} = (t_p/2)[-2S_i C_{pi} + (S_a C_{pf} - S_f C_{pf})(\{T_p - T_x\}\{T_f - T_x\}) \qquad (39)$$

Another contribution to the reaction is the dilution of the titrant and titrate. The heat due to the dilution of the titrate is negligible, but this is not true for the titrant. The heat contribution due to dilution of the titrant can be measured by titrating titrant into the pure solvent and heat calibrations may be made.

The assumptions made were the following:

(1) The water content of the non-aqeous solvents was between 1% and 2% and therefore the reaction due to hyrolysis was neglected and was assumed not to contribute to the heat evolved.

(2) For reasons of simplicity the activity coefficients of the substances were ignored.

(3) The temperature difference between the titrate and titrant was zero because the solutions were allowed to reach equilibrium before the titration started (the period before the titration was approximately 30 minutes).

The systems under investigation were carefully selected in order to eliminate side reactions.Therefore in addition to equations (29) and (39), the heat evolved due to the reaction alone can be written as follows:

$$Q_r = Q_p - Q_h - Q_{dil} \qquad (40)$$

where Q_{dil} is the heat evolved due to dilution.

(f) Computer evaluation of the entropy titration data

Several methods have been applied to solve the equations involved in the calculations of the desired thermodynamic quantities. In general, an interactive method is used to analyse the evolved heat, during the titration. In the past several interactive calculation methods have been described for the analysis of potentiometric, calorimetric and entropy titration data [61,62,63]. Only the methods decribed by P. Paoletti [62] and J.J. Christensen [63] will be compared and discussed in detail.

(i) Computer evaluation of calorimetric data

Paoletti performed the calculations on calorimetric data obtained in a simple calorimeter. This was done by considering the step-wise formation of a mononuclear complex ML_2, between a metal ion M and ligand L. The equilibria are represented by

$$M + L \rightleftharpoons ML$$

$$M + 2L \rightleftharpoons ML_2$$

The total heat evolved due to the reaction between the metal ion M and the ligand L is given by

$$Q = -V \sum_{i=1}^{2} [ML_i] \Delta H^0_{0-i} \qquad (41)$$

where V represents the volume of the total solution. The values of $[ML_i]$ are dependent on the overall stability constants β_i and the concentration of the free metal ion [M] and free ligand [L],

thus

$$[ML_i] = \beta_i [M][L]^i \qquad (42)$$

The mass balance equations are

$$[M]_{tot} = [M] + [ML] + [ML_2]$$
$$= [M] + \beta_1[M][L] + \beta_2[M][L]^2 \qquad (43)$$

and

$$[L]_{tot} = [M] + [ML] + 2[ML_2]$$
$$= [L] + \beta_1[M][L] + 2\beta_2[M][L]^2 \qquad (44)$$

Thus [L] and [M] depends only on the values of $[M]_{tot}$ and $[L]_{tot}$ and the stability constants of the complexes. A combination of equations (41), (43) and (44) results in an equation for the dependence of the heat evolved (Q) on the enthalpy of formation, overall stability constant, $[M]_{tot}$ and $[L]_{tot}$. Thus if the known β values are combined with the metal and ligand concentrations, the values of [M] and [L] may be found by successive approximation, thus satisfying equations (43) and (44). Consequently, the concentrations of [ML] and $[ML_2]$ may be determined by equation (42). Thus, by performing m (m>2) calorimetric determinations, the best set of ΔH^0_{0-i} values may be obtained by applying the standard least square method, in order to satisfy equation (41).

Since there is a non-linear relationship between β_i, ΔH^0_{0-i}, V, $[M]_{tot}$ and $[L]_{tot}$, it is possible to calculate the values of

unknowns with a simple least squares method. This may be performed by successive approximations. A set of β values are chosen and the corresponding concentrations of the complexes formed are calculated for each measurement, and hence the values of ΔH are obtained.

The error square sum U, which is dependent on the experimental errors, should be close as possible to zero. The error square sum is

$$U = \sum_{j=1}^{m} (Q_j + V \sum_{i=1}^{2} [ML_i]\Delta H^0_{0-i})^2 \qquad (45)$$

This method was successfully applied to the stepwise formation of silver(I)-pyridine complexes [64]. This in agreement with the measurements obtained potentiometrically. This method is also refered to as Pit Mapping, since a fractional relationship is assumed for U and U_{min} as is found by direct differentiation.

(ii) **Computer evaluation of the entropy titration method**

Christensen [63] compared the different interactive methods with the least squares analysis for the enthalpy titration of silver(I) with pyridine. This model system was chosen because the equilibrium constants are expected to be independent of ionic strength.

Consider the equilibria discussed in Section f(i). The heat Q_t liberated at time t during the titration may be calculated from

the following expression

$$Q_t = ([ML]\Delta H^0_{0-1} + [ML_2]\Delta H^0_{0-2})V_{ti} \qquad (46)$$

where V_{ti} is the volume in the reaction flask in the calorimeter at time t_i. Q_t is dependent on the β_i, ΔH^0_{0-i} and [L] values. Thus the combination of equations (46), (42) and (43) results in

$$Q_t = [M]_{tot}V_{ti}([L]\beta_1\Delta H^0_{0-1}+[L]^2\beta_2\Delta H^0_{0-2})/(1+\beta_1[L]+\beta_2[L]^2) \qquad (47)$$

The concentration of the free ligand [L] in solution may be calculated by combining equations (43) and (44). The hydrolysis of the ligand $[HL^+]$ is neglected for simplicity thus

$$[L]_{tot} = [L] +\{[M]_{tot}(\beta_1[L]+2\beta_2[L]^2)/(1+\beta_1[L]+\beta_2[L]^2)\} \qquad (48)$$

In theory [L] can be eliminated from equation (47) and (48) and the resulting equation fitted to the experimental data by the method of least squares. However, in practice the resulting non-linear equations in β_i and ΔH^0_{0-i} cannot be solved directly and some iterative process must be applied.

Using a least squares analysis, the problem may be simplified mathematically. Thus the error square sum over all the data points for the Q_t value calculated from equation (47) is

$$U(\beta_i,\Delta H^0_{0-i}) = \sum_{i=1}^{n} w_i(Q_{ri} - Q_{ti})^2 \qquad (49)$$

where Q_r is the corresponding value of Q_t, which includes the experimentally measured heat corrected for hydrolysis formation of the ligand, titrant dilution and non-chemical contributions such as heat leaks, stirring of the solution and the resistance heating of the thermistor.

The analysis is then carried out in the following sequence: Values for β_1 and β_2 are assumed, using previous reports and if none exist the values are estimated since they are not very critical in the initial determination. The estimation of the ΔH^0_{0-1} and ΔH^0_{0-2} values from the experimental heat data is performed as follows:

The calculation of the heat evolved was described previously. The total volume in the reaction vessel is calculated using

$$V_t = V_i + V_a \qquad (50)$$

where V_t = total volume in the reaction vessel;
V_i = initial volume in the reaction vessel;
and V_a = additional volume of the titrant added.

The additional volume V_a is calculated from the burette delivery rate, thus

$$V_a = (BDR)(\Delta t) \qquad (51)$$

where BDR = burette delivery rate in ml min^{-1};

and Δt = the time elapsed since the burette was turned on.

The enthalpies of formation ΔH^0_{0-1} and ΔH^0_{0-2} are calculated from the following equations:

$$\Delta H^0_{0-1} = Q_{r,1}/\{(V_i + V_{a,1})(M_i)\} \quad (52)$$

$$\Delta H^0_{0-2} = Q_{r,2}/\{(V_i + V_{a,2})(M_i)\} \quad (53)$$

where $Q_{r,1}$ and $Q_{r,2}$ are the heat evolved at the mole ratio metal to ligand 1:1 and 1:2, respectively. $V_{a,1}$ and $V_{a,2}$ are the total volume at a mole ratio metal to ligand 1:1 and 1:2, respectively. The initial metal concentration and the initial volume are represented by M_i and V_i, respectively.

Finally the assumed β_1 and β_2 values are used to calculate the free ligand concentration [L] as a function of titrant added, using equation (48). The weighting terms w_i are taken as unity for the initial concentrations. Thus, by holding the values ΔH^0_{0-1} and ΔH^0_{0-2} constant the β_1 and β_2 values are obtained by calculating the error square sum $U(\beta_i, \Delta H^0_{0-i})$ from equation (49). Substituting the new obtained β_1 and β_2 values, new ΔH^0_{0-1} and ΔH^0_{0-2} are obtained. When the process has been completed the four requirements for the least square fitting of the data

$$\partial U/\partial \Delta H^0_{0-i} = 0$$

and

$$\partial U/\partial \beta_i = 0$$

where i = 1 and 2, have been satisfied.

Thus the problem is finding the minimum value of U i.e. U_{min}. Three different methods have been used previously in order to find U_{min}. The schematic map of $U(\beta_i, \Delta H^0_{0-i})$ involves β_i values varying over a large region and the U_{min} is found by trial-and-error. The computation time for more than one constant is extremely long. Another method is the simultaneous solution of the equations. This involves the direct calculations of β_i and ΔH^0_{0-i} solved simultaneously from four equations similar in form to equation (47). Corrections are made for the activity coefficients and the free ligand concentrations until the results are self-consistent. The assumption is made that the average of the calculated β_i values, from all the possible combinations of data points, corresponds to U_{min}. This assumption can not be verified in this method. The method of Pit Mapping was described in Section f(i) and involves direct differentiation in order to find U_{min}, as well as the assumption of a functional relationship for $U(\beta_i, \Delta H^0_{0-i})$. Paoletti [62] assumed U to be quadratic and explicity independent of ΔH and therefore of the form

$$U = C_{00} + 2 \sum_{r=1}^{n} C_{or} \Delta\beta_r + \sum_{r=1}^{n} \sum_{s=1}^{n} C_{rs} \Delta\beta_r \Delta\beta_s$$

where $\Delta\beta_i$ = deviation of β_i from the initial approximation β_i;
and C_{ij} = coefficients in the expression.

For a system of n reactions, $[(n+1)(n+2)]/2$ sets of $\Delta\beta_i$ values

are required to evaluate [L], [ML] and [ML_2]. U_{min} can then be evaluated, yielding a new approximation for the β_i values. The cycle is repeated until the calculations are self-consistent.

All previously mentioned methods involve the assumption of a functional relationship between $U(\beta_i,\Delta H^0_{0-i})$ and its gradient. A description of the function $U(\beta_i,\Delta H^0_{0-i})$, would result in an actual value of the gradient of $U(\beta_i,\Delta H^0_{0-i})$, rather than an approximated value, which is used in the iterative methods. Davidon [65] developed a computer program, which is a numerical variable metric method of minimization (VMM). The program uses an iterative gradient method in which calculated values of $\partial U/\partial\beta_i$ and approximated values of $\partial^2 U/\partial\beta_i\partial\beta_j$ for various values of β_i are used to find values of β_i for which

$$\partial U/\partial\beta_i = 0$$

and for which the Hession matrix

$$\| \partial^2 U/\partial\beta_i\partial\beta_j \| > 0$$

Thus a U_{min} value can be calculated and a given domain may be explored around this value to determine if it is the only relative minimum in that region.

The schematic map of $U(\beta_i,\Delta H^0_{0-i})$ is an accurate and thorough method, but the computer time required is very long. Simultaneous solutions of equations are not applicable in systems involving

more than one reaction. The VMM method has a larger area of convergence than the Pit Mapping method, but requires 25% more computer time than Pit Mapping.

The Department of Mathematical Statistics of the University of Pretoria developed a least square computer program based on the Gauss-Newton method of analysis. This was used on the heat data in order to obtain the β_i and ΔH^0_{0-i} values. This is similar to the method described by Christensen [63]. The error square sum is the given by equation (49). The free ligand concentration [L] is then calculated using equation (48). This results in a set of β_i and ΔH^0_{0-i} values which best fit the experimental data. These values are then used to determine the degree of formation and then distribution curves are drawn. The change in free energy is the calculated from the following equation:

$$\Delta G_{0-i} = -RT\ln\beta_i \quad \text{for } i = 1,2,.....,n,$$

where T is the temperature of the water bath, therefore 298,15 K.

The change in standard enthalpy for the equilibria under investigation is then given by

$$\Delta S^0_{0-i} = (\Delta H^0_{0-i} - \Delta G_{0-i})/T \quad \text{for } i = 1,2,.....,n.$$

2.3.3 Summary

A variety of valuable techniques is available for the determination of thermodynamic quantities. Titration calorimetry is a widely used technique and has several applications. The apparent heat liberated in a reaction vessel and the heat due to non-chemical heat effects may be determined. Taking into account the correction terms, the overall equilibrium constant and the enthalpy change may be determined. Mathematical equations and techniques are used and assumptions are made in order to calculate the thermodynamic quantities, by applying the Newton Raphson method and the least square method of analysis.

CHAPTER 3

MATERIALS AND EXPERIMENTAL METHODS

However much thou art read in the theory,
if thou hast no practice thou art ignorant.
Gulistan (1258), tr James Ross.

3.1 INTRODUCTION

Experimental measurements are mainly concerned with the intensive study of a chemical reaction. The progresss of the reaction is accompanied by a change in an appropriate measuring quantity which may be observed, detected or followed, using suitable equipment, as a function of time. Decomposition reactions are usually monitored in terms of mass loss as a function of time. In solution chemistry, formation reactions are monitored in terms of products formed and reactants consumed during the titration. Consequently information regarding thermodynamic quantities is obtained.

This study is mainly concerned with the experimental measurement of reaction rates of certain decomposition reactions, but forms part of a more comprehensive investigation undertaken to determine the mechanism of the chemical changes. The observed behaviour is based on data obtained by different but complementary investigative methods. Solution calorimetry is an

important complementary technique.

3.2 SOLID STATE CHEMISTRY

3.2.1 Preparation of cobalt(II) chloride complexes

Anhydrous pyridine, quinoline, aniline, α- and β-picoline were the selected ligands. All the complexes were prepared by a method similar to that described by Ocone [66]. Anhydrous cobalt(II) chloride, 1mmol, (Fluka purum p.a.) was dissolved in absolute ethanol (Merck zur analyse) and 2 mmol of the N-donor ligands, viz. anhydrous pyridine (Merck zur synthese), quinoline (Merck zur synthese), α-picoline (Fluka purum), β-picoline (BDH, Analar grade) and aniline (BDH, Analar grade), were added. The solutions were stirred for an hour, or until the complexes precipitated from the solution. The precipitated complex was filtered off, washed several times with diethyl ether and then dried in air. The residual water was removed by keeping the complexes over P_2O_5 for 24 hours. The complexes were stable up to a few months, if kept under absolutely dry conditions. Violet $CoCl_2$2(py), blue $CoCl_2$2(quin), $CoCl_2$2(α-pic), $CoCl_2$2(β-pic) and $CoCl_2$4(an) crystals were obtained. The complexes were recrystallized from hot absolute ethanol, in order to obtain single crystals.

3.2.2 Preparation of nickel(II) chloride complexes

Anhydrous pyridine, β-and γ-picoline were the preselected ligands. J.R.Allan described two preparative methods [9] for

several nickel(II) complexes. The first method (A) involves the heating of nickel(II) chloride with an excess of the N-donor ligands to produce a solution. The second method (B) involves the addition of ligand to a solution of nickel(II) chloride in ethanol. Method (A) was unsuitable, since no precipitation occured with the selected ligands. A minor modification of method (B) resulted in the precipitation of the desired complexes. An appropriate amount of nickel(II) chloride (Merck zur synthese) was stirred and heated for an hour in absolute ethanol (Merck zur analyse). The undissolved nickel(II) chloride was filtered off and excess ligand was added to the clear solution. In some instances the solutions were heated in order to obtain the desired complexes. The precipitated complex was filtered off, washed with diethyl ether and dried in air. The complexes were kept over P_2O_5 until all the water was removed. The light yellow-green complexes $NiCl_2 2(py)$ and $NiCl_2 4(\beta\text{-pic})$, and the light green complex $NiCl_2 4(\gamma\text{-pic})$, were obtained.

3.2.3 Preparation of manganese(II) chloride complexes

The selected ligands were pyridine, β- and γ-picoline. An appropriate quantity of anhydrous manganese(II) chloride (Hopkin & Williams, Analar grade) was dissolved in absolute ethanol (Merck zur analyse). Excess ligand was added and the solution was stirred until precipitation occured. Only the white-pink complexes, $MnCl_2 2(py)$ and $MnCl_2 2(\gamma\text{-pic})$, and white paper-like complex, $MnCl_2 2(\beta\text{-pic})$, were prepared.

3.2.4 Thermogravimetric analysis

A Stanton Redcraft 780 TG Analyser was used to collect thermogravimetric data. The Simultaneous Thermal Analyser Series is designed to give simultaneous thermogravimetric (TG) and differential thermal analysis (DTA) curves. Platinum sample pans, with a volume of 10 mm^3, were used. Nitrogen was used as the carrier gas, at a flow rate of approximately 40 cm^3 min^{-1}. The main gas flow was from underneath the sample and reference pans, while a "blanket" flow from the top repressed the flow of damaging gases and therefore protected the instrument.

It is known that temperature determines the progress of any chemical reaction. Therefore temperature is an additional dimension in thermogravimetric analysis, which enriches the picture of any chemical event. Two temperature dependent methods were investigated. The first method involves the decomposition of the sample over a certain temperature range and at a certain heating rate (dynamic method). The second method involves the study of the decomposition reaction at certain constant temperatures (isothermal method).

(a) Dynamic method

Approximately 15 mg of the complex was heated from room temperature to 773 K. The rate of the decomposition reaction was measured as the rate of mass loss at a certain temperature.

Kinetic analysis was performed on the TG curves. Different

kinetic equations (Chapter 2.2) were tested and the activation energy and frequency factor calculations were performed on the best descriptive kinetic equation. These parameters were used to simulate a dynamic TG curve.

The dynamic TG curves were used to estimate the appropriate temperature range for the isothermal studies. These temperature ranges were selected in such a way that the decomposition reaction revealed no mass loss before the required temperature was reached, therefore eliminating temperature gradients in the initial stages of the decomposition reaction. The temperature ranges were selected to ensure slow but measurable decomposition rates. For slow decomposition rates, less gas and heat per unit of time is released or consumed and complications are therefore reduced. In order to obtain slow decomposition rates, a relatively slow heating rate was always applied (1 to 5^0C min^{-1}).

(b) Isothermal method

A 15 mg sample was heated rapidly (20^0C) from room temperature to a temperature 50^0C below the required temperature and then a slow heating rate (5^0C) was applied until the required temperature was reached.

During the decomposition reaction mass loss was monitored as a function of time. In order to estimate an activation energy at least four isothermal experiments were conducted. The reason for doing this is that two points always lie on a straight line and the position of the third point on a straight line could be the

result of a combination of an accident and an error in measurement.

If more than one reaction occured in succession, the temperature was held constant until the first reaction was complete and then gradually increased to the next temperature range and mass loss again measured as a function of time. This method is applicable especially when the dynamic studies show that the first product is an unstable intermediate and the first decomposition step continuous almost immediately to the following step.

The data collected were fitted to a variety of kinetic expressions [28]. The linearity of the plots, based on the correlation coefficient and standard deviation, of the calculated $f(\alpha_i)$ versus t expression was taken as a criterion for the identification of the rate equation for each kinetic expression. Activation energies and frequency factors were calculated from the temperature dependence of the rate constant.

3.2.5 Differential scanning calorimetry method

A Du Pont 910 differential scanning calorimeter, controlled by a 910 Thermal Analyser, was used for part of the study. A Perkin-Elmer DTA 1700 System High Temperature Differential Analyser, consisting of the System 7/4 Thermal Analysis Controller (including the Microprocessor Controller) and the DTA 1700 Differential Thermal Analyser, was used for the major part of the study. The instrument was used in the DSC mode, and the

differential temperature changes between the sample and reference materials were measured and then converted to differential heat change. The gas was evolved from a purged tube above the reference and the sample pans, thus removing all the evolved gases. Argon was used as the carrier gas at a flow rate of approximately 40 cm^3 min^{-1}. Aluminium and ceramic sample pans were used. The sample pans contained a 10 mm^3 volume. Peak integration and then the enthalpy calculations were performed using the Du Pont Partial Area Integration data analysis program and the TADS program issued by Perkin Elmer. The melting of pure indium (ΔH_f = 2,84 J g^{-1}) was used to determine the calibration factor. Temperature calibrations were performed on both instruments.

3.2.6 Electron microscopy

Electron microscopy is used as a supplementary technique in the assigning of kinetic models in the isothermal and dynamic studies. The Jeol model JSM-840 scanning electron microscope was used. The surfaces of the crystals were studied by covering the metal(II) complexes with a film of gold under vacuum, in order to enhance conduction. However, it was not possible to perform cross-sections cuts on the crystals, since they are soluble in water.

3.3 SOLUTION CALORIMETRY

3.3.1 Apparatus

The experiments were conducted using a Tronac model 450 isoperibol solution calorimeter. The temperature of the water bath was controlled with a PTC-40 precision temperature controller at a preselected temperature of 25^0C to an accuracy of ± $0{,}0003^0$C. A precision burette of 2 cm^3 capacity and with a 0,1% accuracy was used for the titrations.

3.3.2 Solutions

$CoCl_2$ solutions: Anhydrous $CoCl_2$ (Fluka purum p.a.) was used and stored in a nitrogen filled tank. Acetone, methanol and ethanol (Merck, pro analysi) were used as solvents, without further purification. The solutions were prepared by dissolving a required amount of $CoCl_2$ in acetone, with the concentrations ranging from 0,002 mol dm^{-3} to 0,01 mol dm^{-3}.

Ag(I) solutions: The solutions ranged from 0,002 mol dm^{-3} to 0,01 mol dm^{-3}. The Ag(I) solutions were standardised by extrapolation of the thermogram obtained from the reaction between Ag(I) and tmen. This standardisation method is acceptable, since the ligand tmen is of high purity and therefore a suitable standard. Also, it is known that the complexation reaction is complete and that the complete formation of $Ag(tmen)_2^+$ occurs.

Ligand solutions: The ligands pyridine, quinoline and tmen were obtained from Fluka (Analar grade) and used without further purification. The α-picoline used was Fluka purum. Aniline and β-picoline (Analar grade) were obtained from BDH laboratories. The dark aniline solution was distilled, and the clear fraction which was collected between 165^0C and 168^0C at atmospheric pressure was used. Stock solutions of the ligands (ca. 1,0 mol dm^{-3}) were prepared.

3.3.3 Calibrations

The calibration of the equipment consisted of the calibration of the titrant delivery system as well as the calibration of the temperature device.

The calibration of the titrant delivery system, the burette, involved the weighing of amounts of distilled water delivered over several measured time intervals. A constant delivery rate over the entire period of the run is of the utmost importance.

The calibration of the temperature sensing device was performed by measuring the temperature changes in the reaction vessel by means of a thermistor, incorporated into the Wheatstone bridge circuit. The procedure was performed by placing the thermistor and the thermometer in close proximity in a well controlled constant temperature water bath. The bridge voltage was adjusted until the difference, which was read on the multimeter, was zero.

3.3.4 Data acquisition

The calorimeter was interfaced with an Apple II Europlus microcomputer using a Prema model 5000 integrating digital multimeter, which served as the analog-to-digital converter. The multimeter was equiped with an IEEE 488 bus interface (as a standard feature) which provided the linkage with the microcomputer. Data were collected at a rate of one point per second. An average of 400 points per titration were collected, with 120 points for the initial and final stages of the thermogram.

3.3.5 Calibration runs

In order to determine the heat capacity of the reaction vessel and contents prior to titration, two runs were made by introducing a constant current through a resistance heater, 100,0 ± 0,1Ω, over a measured period of time. The difference in temperature was corrected for non-chemical heat contributions. The calibration procedure was repeated after the titration. For the calibrations, data were also collected at a rate of one point per second and an average of 220 points per calibration was collected. The initial and final slope of the thermogram were obtained by collecting 120 points, and 100 points for the period where a constant current was introduced through the standard resistance heater.

3.3.6 Calculations

Calculations of the heat liberated at each data point of the titration have been described previously. The heat due to the non-chemical effects was substracted from the heat liberated.

Calculations of β_i and ΔH^0_{0-i} values from the experimental data was accomplished by means of the process described in Chapter 2. A least square program based on the Gauss Newton method of analysis was used to calculate the β_i and ΔH^0_{0-i} values. The Newton Raphson method was used to estimate the free ligand concentration, [L], for each set of β values.

CHAPTER 4

STATISTICAL EVALUATION OF THE ENTROPY TITRATION METHOD

If you shut your door to all errors truth
will be shut out. Stray Birds (1916),130.

4.1 INTRODUCTION

Statistical methods form an integral part of all types of analytical investigations. Therefore statistical methods may be seen as a very important aid, in any emperical investigation. Christensen [54] reported that significant deviations in the minimum error square sum may be due to assumed reactions which do not define the system, or may reflect large systematic or random errors present in the data. However, small minimum values do not imply that the system is correctly described. For these reasons it was of the utmost importance to perform an analysis of systematic errors, which were thought to be the most likely under experimental conditions, on an ideal system and study the effect on the thermodynamic quantities.

4.2 DEFINING THE SUITABLE MODEL SYSTEM

The complex formation of Ag(I) and tmen in acetone was chosen as a model. The Ag(I) complexes of tmen are very stable and have the linear structure $L\text{-}Ag\text{-}L^{+}$. The equilibrium constants are

anticipated to be independent of ionic strength. Competing reactions are negligible and more than one equilibrium is present.

Thus, the following equilibria are applicable, with ΔH^0_{0-1} and β_1 at 298K refering to

$$Ag^+ \text{ (soln.)} + \text{tmen (soln.)} \rightleftharpoons Ag(\text{tmen})^+ + \text{soln.}$$

ΔH^0_{0-2} and β_2 at 298K refering to

$$Ag^+ \text{ (soln.)} + 2(\text{tmen}) \text{ (soln.)} \rightleftharpoons Ag(\text{tmen})_2^+ + \text{soln.}$$

The overall formation constants (β_i) and the enthalpy of formation (ΔH^0_{0-i}) were calculated.

For $[Ag(I)]_i = 9{,}334 \times 10^{-3}$ mol dm^{-3} and $[\text{tmen}]_i = 1{,}001$ mol dm^{-3} the following thermodynamic quantities were obtained:

$\log \beta_1 = 4{,}020$
$\log \beta_2 = 8{,}003$
$\Delta H^0_{0-1} = -73{,}74$ kJ mol^{-1}
$\Delta H^0_{0-2} = -198{,}7$ kJ mol^{-1}

Systematic error calculations were performed on fifty-five Q_r values. The Q_r values were obtained from the calculated Q_r values and not the experimental Q_r values, therefore ensuring that no errors were present in the Q_r values.

Systematic error calculations ranging from 0,1 to 1,0% were performed on the calculated Q_r values, as well as the initial concentrations of Ag(I) ($[Ag(I)]_i$) and tmen ($[tmen]_i$).

A new term, log E_i, was defined in order to visualise the magnitude of the random error, where log E_i is taken to be the absolute value of the difference between the log β_i calculated for the ideal system and the new log β_i values obtained after the systematic error calculations were made.

4.2.1 Systematic error calculations performed on the calculated Q_r values

Systematic error calculations of 0,1 % and 1,0% were applied on the Q_r values. The thermodynamic quantities obtained are summarised in Table 3.

Christensen [59] found that a cumulative random error of 0,4% in the experimental heat data as well as a 0,1% random error in the concentrations of the solution and titrant normally caused an error of less than 0,01 units in the value of log K. However, it was observed that a systematic error of ± 0,1%, resulted in an error of less than 0,004 units in the value of log β_i. Large errors in the value of log β_i of up to 0,138 units were obtained if a systematic error of ± 1,0% was made on the Q_r values. Therefore, in order to ensure significant results, the error in the Q_r values should not exceed 1,0%.

Table 3. The thermodynamic quantities obtained when systematic error calculations were performed on the Q_r values. The values in brackets represent the % error.

Systematic error (%)	log β_1	log β_2	log E_1	log E_2	$-\Delta H^0_{0-1}$	$-\Delta H^0_{0-2}$
					kJ/mol	
-0,1	4,024	8,001	0,004	0,002	73,70	199,0
	(0,10)	(0,02)			(0,05)	(0,15)
+0,1	4,022	8,004	0,002	0,001	73,70	199,0
	(0,05)	(0,01)			(0,05)	(0,15)
-1,0	3,967	7,890	0,053	0,113	87,00	179,2
	(1,32)	(1,41)			(18,0)	(9,81)
+1,0	4,102	8,141	0,082	0,138	51,92	217,8
	(2,04)	(1,72)			(29,6)	(9,61)

Large differences are observed in the ΔH^0_{0-i} if the systematic error is 1,0%. When considering the ΔH^0_{0-i} values, the percentage error is very high in ΔH^0_{0-1}, but lower in ΔH^0_{0-2}. Therefore, another factor contributing to the percentage error is the magnitude of the ΔH^0_{0-i} values. Table 3 reflects the greater significance of the systematic error in the lower ΔH^0_{0-i} values.

The different results reported by Christensen [59] may be attributed to the different type of error (random) and the number of the complexation equilibria (1:1) he investigated. Christensen [67] criticised the random errors performed by Cabani and Gianni

[68]. He criticised the evaluation of random errors in the temperature changes in the calorimeter as well as those due to the heat of dilution. Random errors in temperature changes are not included in this study. Christensen reported systematic errors for a 1:1 system by substituting appropriate values for the determination of K and ΔH.

4.2.2 Random and systematic error calculations performed on the ligand concentration

Errors in the preparation of solutions occur easily. The possible errors include the following:

(1) Inaccurate weighing of the sample.

(2) Incomplete transfer of the weighed sample into the volumetric flask.

(3) Temperature differences in the preparation laboratory and the instrumental laboratory.

(4) Inaccurate determination of the concentrations by standardisation methods. This includes incorrect standard concentrations and inaccurate end point determination due to over-titrating and difficulty in seeing the end point.

S. Cabani [68] made suggestions regarding the concentrations of the titrate and titrant. He conducted his experiments by varying the concentration of one reagent and keeping the concentration of the other reagent constant. The ΔH^{0}_{0-i} revealed large systematic errors, although the K values remained the same. In order to

reduce all possible errors he made the following suggestions:

(1) Run a large number of experiments, at widely different concentrations, in order to obtain reasonably large ΔH^0_{0-i} values.

(2) If possible, alternate the order of addition of reagents.

(3) Preferably operate with separate experiments, rather than drawing different points from the obtained curve and therefore decrease the possibility of systematic errors.

(4) Give experiments performed under different conditions a proper weight in the calculations.

(5) If possible, verify K values by other methods.

Since the concentration of the titrate is usually chosen to be approximately 1,0 mol dm^{-3}, the relatively high concentration values are presumed to be free from errors. Several authors have done work on concentrations in order to ensure minimum errors and maximum accuracy. The concentrations used in these titrations were those suggested for optimum results.

The results obtained when systematic error calculations were performed on $[tmen]_i$ are summarised in Table 4. The Q_r values reported in Section 4.2.1 were obtained by combining all the data sets and thus determining the thermodynamic quantities for the average Q_r values. In Table 4, the first set of thermodynamic quantities was obtained by using one data set(error = 0(alone)). The second set represents the thermodynamic quantities for the average Q_r values(error = 0 (comb.)). The separate set is in 1% error of the average set. Systematic errors of ± 0,1% and ± 0,4%

resulted in log E_i values lower than 0,006 units. Even a systematic error of ± 1,0% reflected a small deviation. However, a systematic error of -1,0% resulted in large changes in the ΔH^0_{0-i} values.

Table 4. The thermodynamic quantities obtained when systematic error calculations were performed on the initial ligand concentration. The values in brackets represent the % error.

Systematic error (%)	log β_1	log β_2	log E_1	log E_2	$-\Delta H^0_{0-1}$	$-\Delta H^0_{0-2}$
					kJ/mol	
0 (alone)	3,977	7,965	0,000	0,000	78,76	193,5
0 (comb.)	4,020	8,003	0,043	0,038	73,74	198,7
	(1,08)	(0,48)			(6,37)	(2,69)
-0,1	3,977	7,967	0,000	0,002	78,67	193,6
	(0,00)	(0,02)			(0,11)	(0,05)
+0,1	3,977	7,964	0,000	0,001	78,86	193,4
	(0,00)	(0,01)			(0,13)	(0,05)
-0,4	3,975	7,971	0,002	0,006	78,43	193,7
	(0,05)	(0,07)			(0,42)	(0,10)
+0,4	3,977	7,959	0,000	0,006	79,07	193,3
	(0,00)	(0,07)			(0,39)	(0,10)
-1,0	4,018	8,136	0,041	0,171	56,55	207,2
	(1,03)	(2,15)			(28,2)	(7,08)
+1,0	4,031	7,855	0,054	0,110	77,12	189,0
	(1,36)	(1,38)			(2,08)	(2,32)

Systematic errors have a smaller significance on the ligand concentration than on the liberated heat. This correlates with what is expected from the preselected concentrations, since it was anticipated that high concentrations would minimize errors.

4.2.3 Systematic error calculations performed on the metal concentration

Recently H.C. Smit [69] reported factors influencing the precision of potentiometric strong acid-strong base titrations by data handling using non-linear regression analysis. Once more, it was found that the errors in the substance titrated influenced the values of the equilibrium constants to a great extent.

The results for the systematic errors performed on $[Ag(I)]_i$ are represented in Table 5. Similarly to Section 4.2.1, systematic error calculations of ± 0,1% and ± 0,4% revealed no significant effect on the log β_i values. However, definite % errors were observed for ΔH^0_{0-i} values. This stresses the fact that the experimental values of ΔH^0_{0-i} must be determined accurately.

Table 5. The thermodynamic quantities obtained when systematic error calculations were performed on the initial metal concentration. The values in brackets represent the % error.

Systematic error (%)	log β_1	log β_2	log E_1	log E_2	$-\Delta H^0_{0-1}$	$-\Delta H^0_{0-2}$
					kJ/mol	
0 (alone)	3,977	7,965	0,000	0,000	78,76	193,5
-0,1	3,977	7,964	0,000	0,001	78,92	193,6
	(0,00)	(0,01)			(0,20)	(0,05)
+0,1	3,975	7,968	0,002	0,003	77,01	195,2
	(0,05)	(0,04)			(2,22)	(0,88)
-0,4	3,979	7,961	0,002	0,004	77,18	195,0
	(0,05)	(0,05)			(2,00)	(0,77)
+0,4	3,972	7,972	0,005	0,007	76,89	195,3
	(0,12)	(0,09)			(2,37)	(0,93)
-1,0	4,150	8,024	0,173	0,059	56,14	209,4
	(4,35)	(0,74)			(28,7)	(8,22)
+1,0	3,973	7,998	0,004	0,033	77,37	189,5
	(0,10)	(0,41)			(1,76)	(2,07)

4.3 CONCLUSIONS ON SYSTEMATIC ERROR CALCULATIONS

The effect of systematic errors in the titrant and titrate concentrations and the liberated heat have been investigated. For all the systematic errors, relatively low log E_i values were obtained. Systematic errors of ± 0,1% and ± 0,4% resulted in low % errors. However, a systematic error of -1.0% had a significant effect on the thermodynamic quantities and thus the % error.

Figure 2 is the distribution curve and titration curve of the reaction of Ag(I) with tmen, assuming the presence of only experimental errors, but not systematic errors. Figures 3 to 5 represent the distribution diagrams and the titration curves, if a systematic error of +1,0% was performed on $[Ag(I)]_i$, $[tmen]_i$ and the calculated Q_r values. All the titration curves are in acceptable experimental error. Figure 4 gives the best fit for the experimental data. Thus, according to the titration curves, systematic errors in the titrant concentration and the liberated heat are of great significance.

Table 6 represents the degree of formation for $Ag(tmen)^+$, when a 1,0% systematic error was performed on the concentrations of the titrate and titrant and the liberated heat.

Figure 2. The distribution (A) and titration (B) curves for the Ag(I)/tmen system, assuming only experimental errors.

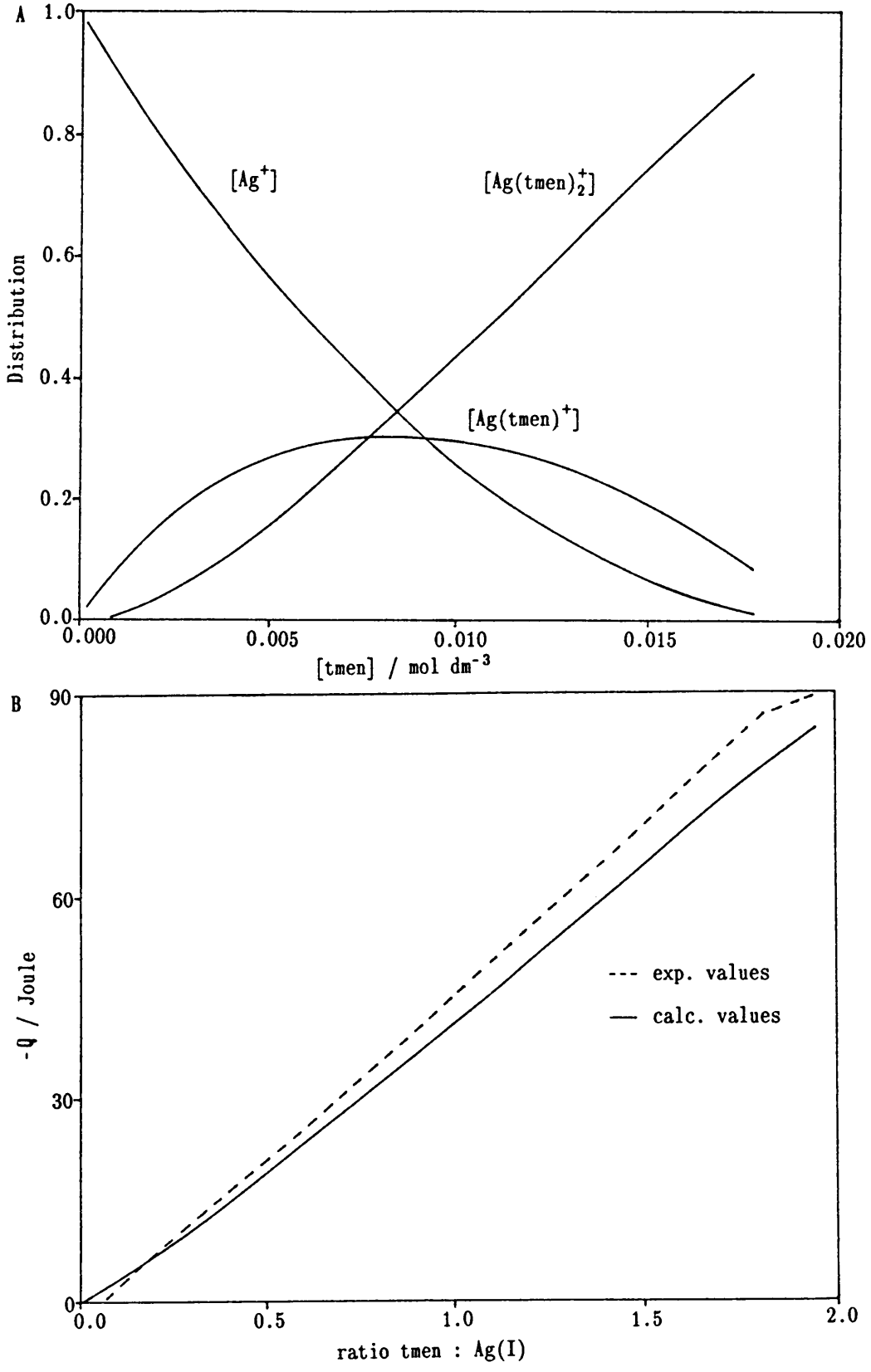

Figure 3. The distribution (A) and titration (B) curves for the Ag(I)/tmen system, when a systematic error calculation of 1,0% was performed on $[tmen]_i$.

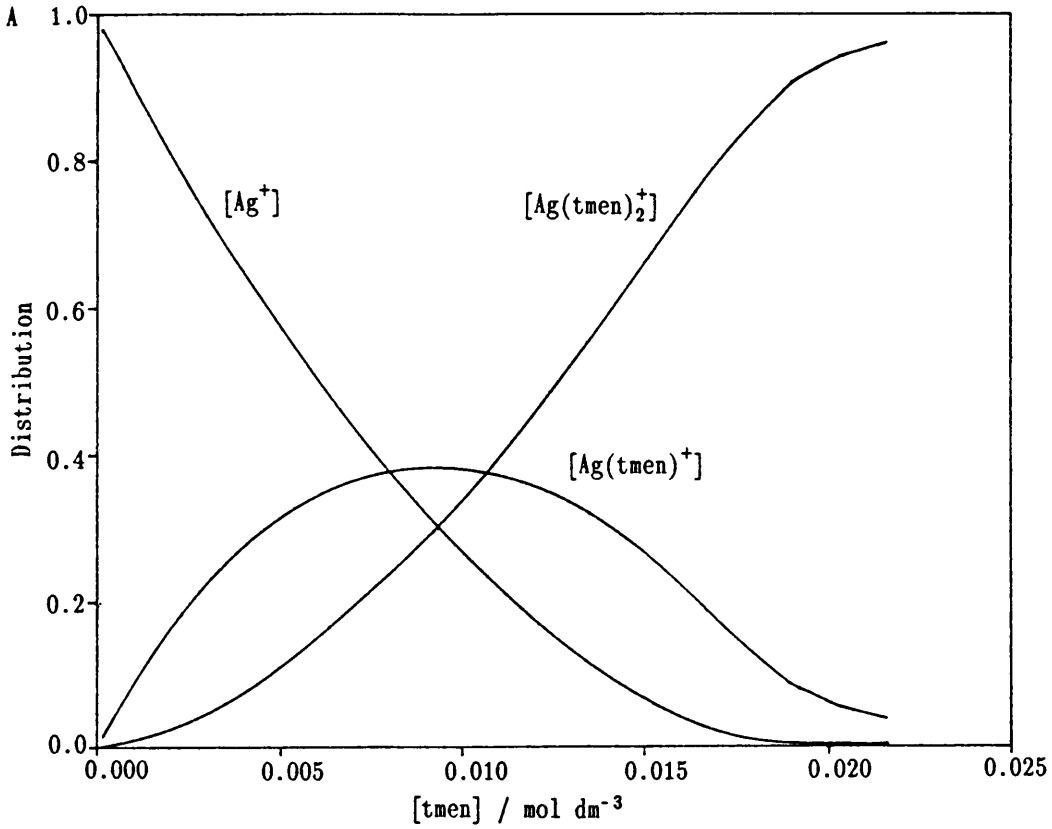

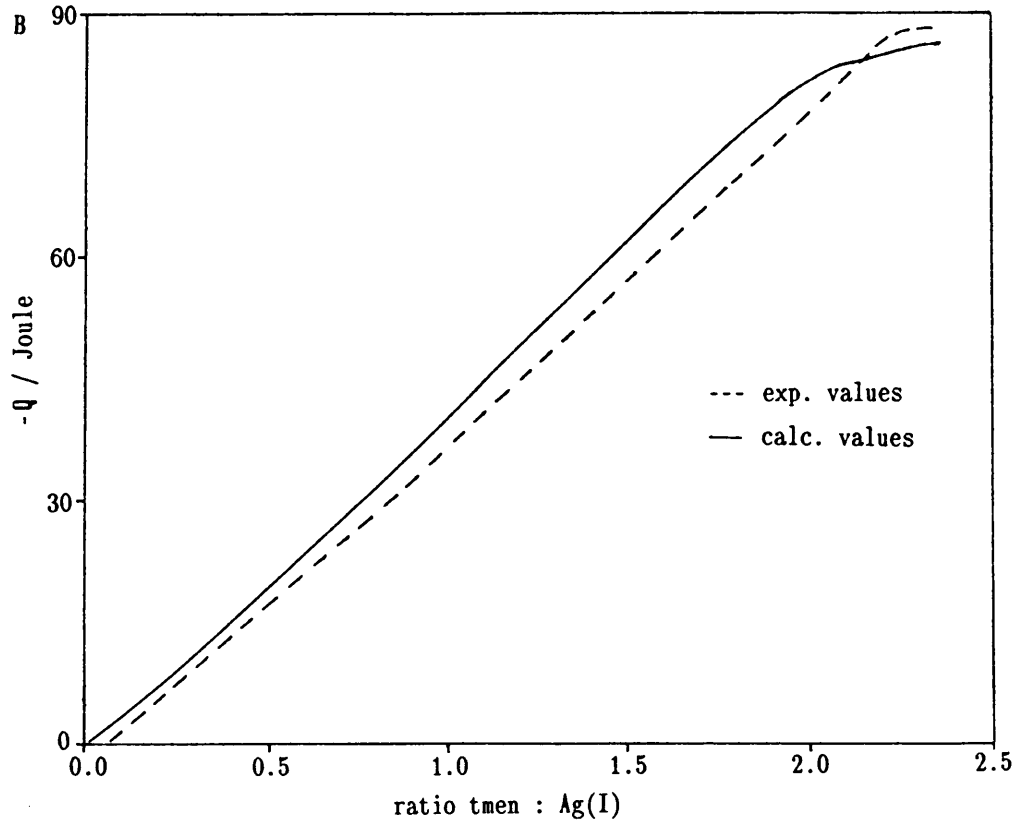

Figure 4. The distribution (A) and titration (B) curves for the Ag(I)/tmen system, when a systematic error calculation of 1,0% was performed on $[Ag(I)]_i$.

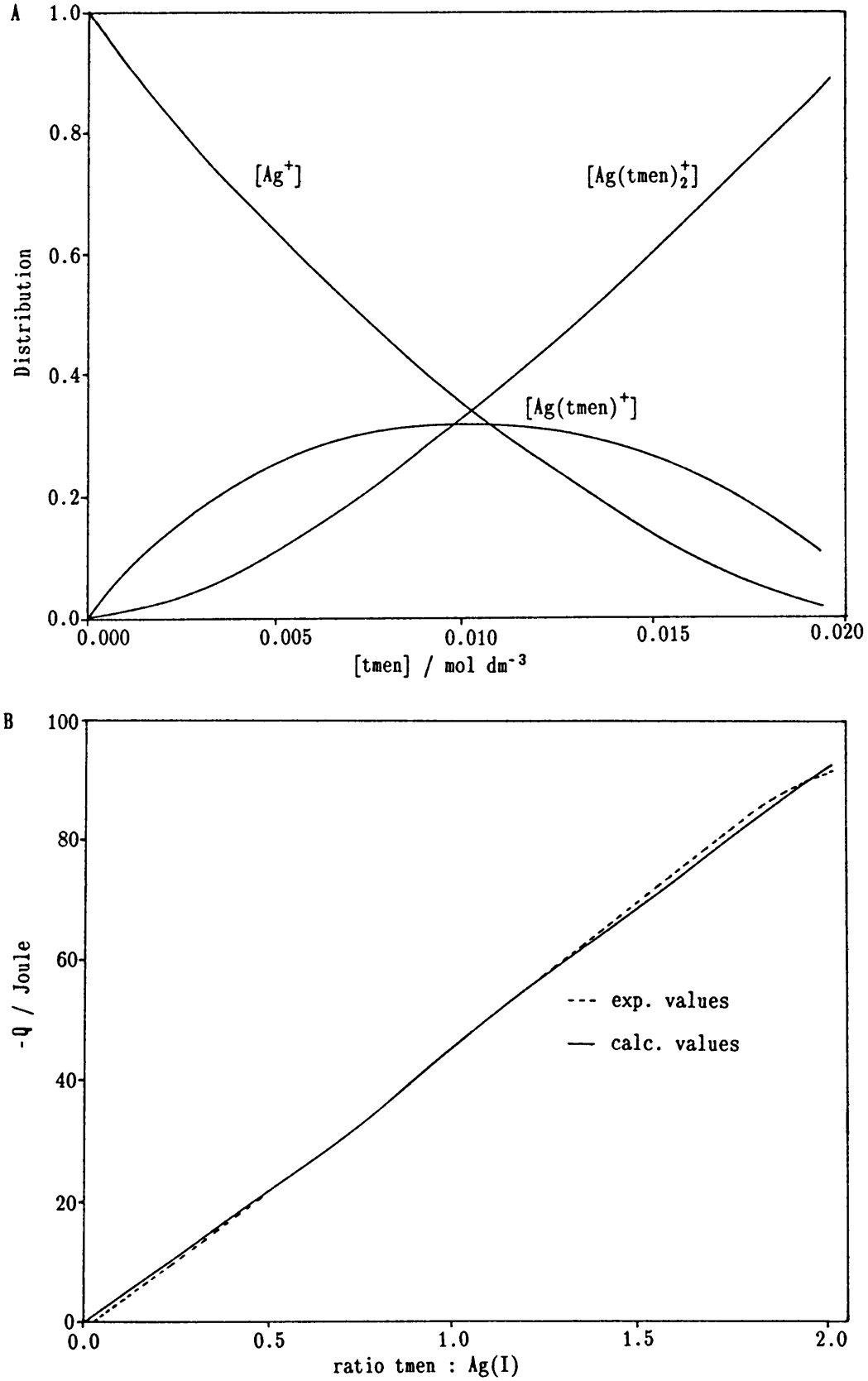

Figure 5. The distribution (A) and titration (B) curves for the Ag(I)/tmen system, when a systematic error calculation of 1,0% was performed on the calculated Q_r values.

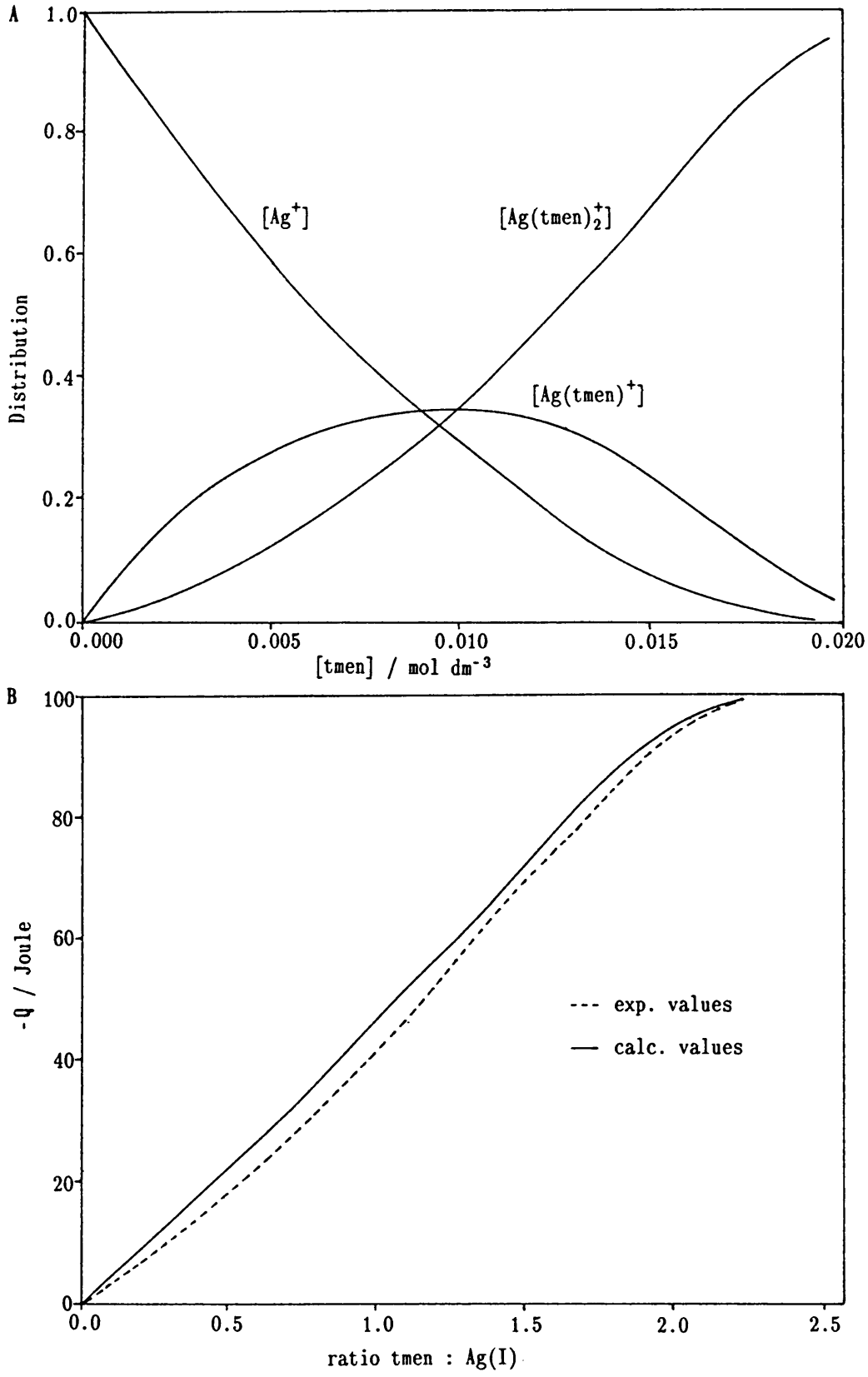

Table 6. The degree of formation for $Ag(tmen)^+$ with various systematic errors.

+1,0% Systematic error in	Degree of formation of $Ag(tmen)^+$ (%)	Figure reference
1. None	30,8	2
2. $[tmen]_i$	39,2	3
3. $[Ag(I)]_i$	31,7	4
4. Q_r values	35,0	5

As seen in the titration curves, similar large deviations are observed in the degree of formation when a systematic error is performed on the liberated heat and ligand concentration. A small change is observed when a systematic error is performed on the metal concentration.

Thus the titration curve and the distribution diagram reflect the dependence of the degree of formation of $Ag(tmen)^+$ on systematic errors. However, the results were all within experimental error.

CHAPTER 5

THE EFFECT OF SOLVENTS ON THERMODYNAMIC CONSTANTS

5.1 INTRODUCTION

The study of solution chemistry has largely been confined to aqueous solutions. Water is cheap, available in excess and is an excellent solvent for most inorganic salts. However, fundamental research in and practical applications of non-aqueous solvents have increased greatly during the last three decades. Non-aqueous solvents, such as acetone, ethanol and methanol, may be defined as media other than water which will dissolve a reasonable number of inorganic compounds and allow the occurence of chemical reactions.

Solvents have been classified on the basis of various criteria. Popovych and Tomkins [70] divided solvents into two broad categories: (1) organic solvents and amphiprotic inorganic solvents; and (2) inorganic aprotic solvents. The first category includes all organic solvents as well as those inorganic solvents that are capable of donating or accepting protons. The second category includes molecular SO_2 and amphoteric inorganic solvents. The first category is of great importance in solution chemistry. This category also differentiates between the following type of solvents:

(1) Amphiprotic solvents, which are subdivided into

(a) protophilic (predominantly basic);

(b) protogenic (predominantly acidic); and

(c) neutral.

(2) Aprotic, solvents which are incapable of transferring protons to any appreciable extent. These solvents are subdivided into

(a) dipolar aprotic; and

(b) inert (non-polar).

The dipolar solvents are further subdivided into solvents which are protophilic (slightly basic) and protophobic (without basic properties).

Acetone is a dipolar aprotic solvent and, therefore, exhibits no tendency to participate in the transfer of protons but is a moderately good solvating and ionising medium due to its dipolar nature. Dipolar aprotic solvents are moderately good solvents for electrolytes. In contrast neutral amphiprotic solvents, such as methanol and ethanol, possess both acidic and basic properties. The acidic and basic properties are roughly balanced and are similar to those of water; thus alcohols can act as proton donors or as proton acceptors, depending on the properties of the solute. They are generally very good solvents for a large number of electrolytes.

Another scheme of classification of solvents is Gutmann's scale of donor numbers [71]. The donor number is defined as the negative enthalpy of the reaction between the solvent and antimony

pentachloride. Thus a scale of Lewis basicity is set up, in which $SbCl_5$ serves as the reference acid. Acetone has a donor number of 17,0 which is similar to the donor number of 18,0 for water. Thus in terms of Lewis basicity, alcohols, which may be considered as derivatives of water, have approximately the same Lewis basicity as acetone. Acetone and alcohols exhibit fairly moderate basic strength, since they are approximately in the middle of the scale.

Although alcohols may be considered as derivatives of water, the amount of hydrogen bridging is smaller than in water, with which they are miscible. The effect of water on non-aqueous solvents has been studied in terms of an acid and base titration [72]. In mixed solvents, competition between the two solvent components for the primary coordination shell of a cation may occur. These studies were performed on various systems, including Ni(II) with ammonia in methanol and water mixtures [73] and Cr(III) with thiocyanate, also in methanol and water mixtures [74].

A water content of 1% to 2% in the solvent may be tolerated in the experimental titrations without exceeding the range for experimental errors. However the presence of water reduces the sharpness of the thermogram, thus resulting in a roundness in the end point. This roundness may also be caused by a slow reaction and it is difficult to obtain a meaningful end point by simple extrapolation.

Non-aqueous solvents are extensivly used as media for the

preparation of coordination complexes. Reactions of these complexes, for example ligand exchange reactions, are normally carried out in non-aqueous solvents. The following is assumed; the metal and ligand accept N solvent molecules and the interaction is very weak compared with the interaction between the metal and the ligand. Thus the heat of solvation is negligible, for both the metal and the ligand. The solvent molecules of the metal are replaced by the solvated ligand, thus forming a metal-ligand bond when the solvent molecules are released.

The aim of this chapter was two-fold. Firstly, a model system was chosen, in order to evaluate the validity of the results from the entropy titration method. Again the complex formation of Ag(I) and tmen in acetone was chosen as the model. A similar Ag(I)/py system was investigated by Christensen [63] and more recently by C.P.J. van Vuuren [64]. A simplified system which involves one equilibrium, the Co(II)/tmen system in acetone, was also included in this study. Secondly, the effect of the concentration of the metal ion was investigated, with reference to the results of Section 4.2.3. The study was extended to include the effect of solvents on the thermodynamic quantities of the Ag(I)/tmen system. Methanol and ethanol were chosen as additional non-aqueous solvents. The small amount of water present in these solvents would have no significant effect on the equilibria, since $[Ag(H_2O)_2]^+$ is very labile [75]. The Co(II)/tmen system was not studied in methanol and ethanol, since a large amount of $[Co(H_2O)_6]^{2+}$ is formed in solution and the amount of this species

thus not negligible. Thus the equilibrium of $[Co(H_2O)_4]^{2+}$ with $[Co(H_2O)_6]^{2+}$ would have to be considered and the complexity of the system would therefore increase.

5.2 THE REACTION OF AG(I) WITH TMEN

5.2.1 The solvent acetone

The titration curve obtained by titrating approximately 0,010 mol dm^{-3} Ag(I) solution with 1,00 mol dm^{-3} tmen in acetone, is given in Figure 6. The curve reflects a sharp end point at a mole ratio Ag(I):tmen of 1:2.

The thermodynamic constants, obtained for the stepwise formation of $Ag(tmen)^+$ and $Ag(tmen)_2^+$ at different initial Ag(I) concentrations ($[Ag(I)]_i$), are listed in Table 7. The formation of $Ag(tmen)^+$ as well as the $Ag(tmen)_2^+$ species is enthalpy driven. A significant change in the ΔH^0_{0-1} values is observed. The $-\Delta H^0_{0-1}$ values decrease with a decrease in $[Ag(I)]_i$. The following expression represents the relationship:

$$-\Delta H^0_{0-1} = 8{,}33 \times 10^3 [Ag(I)]_i - 2{,}59$$

with a correlation of 0,9999.

The ΔH^0_{0-1} values are more dependent than the ΔH^0_{0-2} values on $[Ag(I)]_i$.

Figure 6. The titration curves for Ag(I) ($1,0x10^{-2}$ mol dm^{-3}) with tmen (1,0 mol dm^{-3}) in A: ethanol and B: acetone.

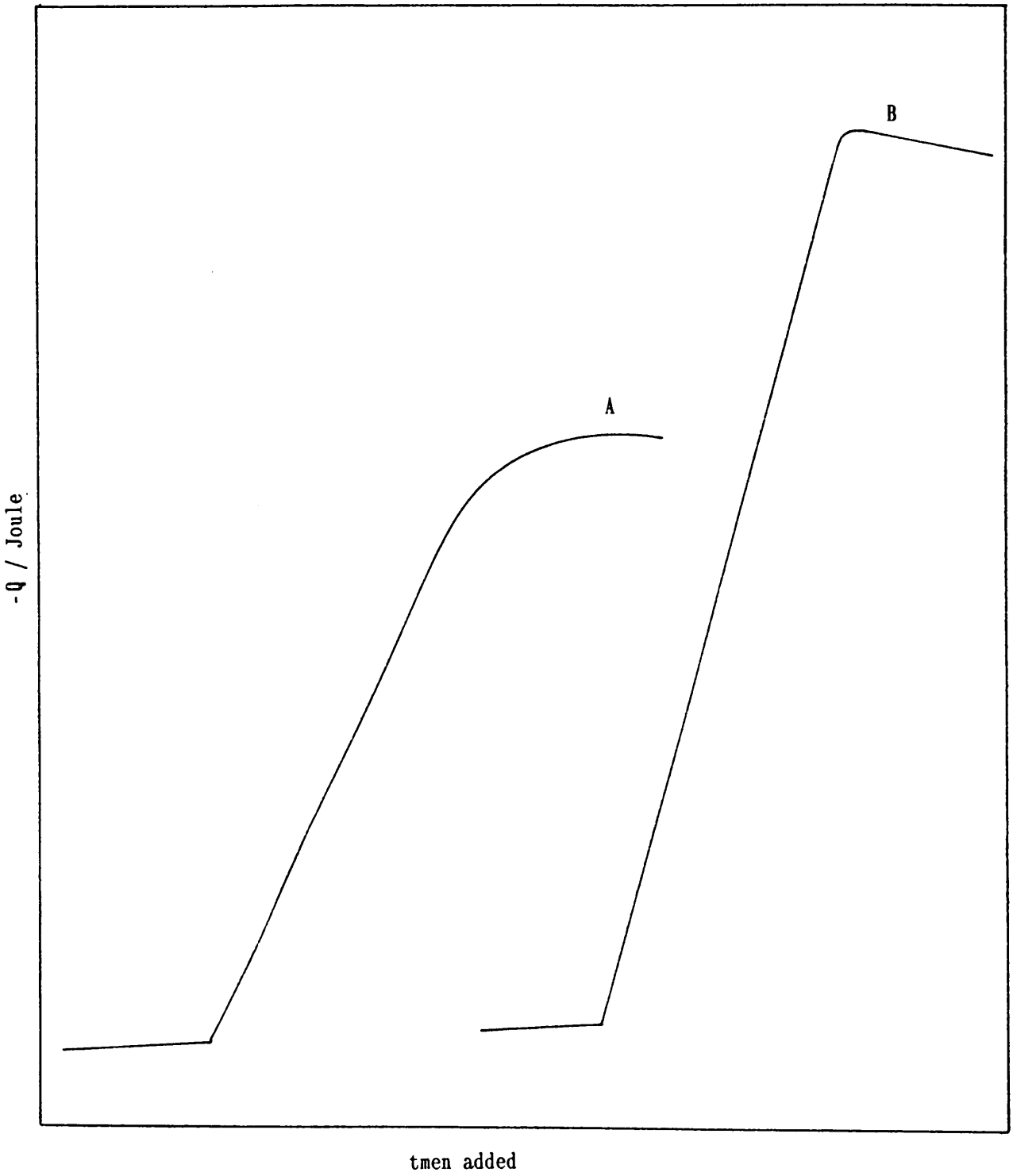

Table 7. The effect of $[Ag(I)]_i$ on the thermodynamic constants, using acetone as solvent. $[tmen]_i$ = 1,00 mol dm^{-3}.

Thermodynamic parameters	$[Ag(I)]_i$		
	$9{,}33 \times 10^{-3}$ mol dm^{-3}	$4{,}67 \times 10^{-3}$ mol dm^{-3}	$2{,}800 \times 10^{-3}$ mol dm^{-3}
log β_1	4,03	4,02	3,35
log β_2	8,00	8,18	8,44
ΔG_{0-1} (kJ mol^{-1})	-23,02	-22,94	-19,10
ΔG_{0-2} (kJ mol^{-1})	-45,69	-46,71	-48,18
ΔH^0_{0-1} (kJ mol^{-1})	-75,11	-36,56	-20,55
ΔH^0_{0-2} (kJ mol^{-1})	-198,07	-166,04	-199,66
ΔS^0_{0-1} (J $mol^{-1}K^{-1}$)	-174,71	-45,68	-4,86
ΔS^0_{0-2} (J $mol^{-1}K^{-1}$)	-511,08	-400,23	-508,07

Christensen [54] mentioned that different concentrations should have no significant effect on the thermodynamic quantities in a 1:1 system, this contradicts the observed results for a 1:2 system. However, the detection limit of the instrument contributes to experimental errors. In order to obtain significant results, sufficient heat must be evolved. Decreasing the $[Ag(I)]_i$ resulted in a decrease in liberated heat and thus an increase in the experimental error. The contribution of the solvent increased with a decrease in the $[Ag(I)]_i$.

A significant change in log β_i values is observed if $[Ag(I)]_i = 2{,}800 \times 10^{-3}$ mol dm^{-3}. A decrease in log β_1 value and an increase in the log β_2 value is observed with a decrease in $[Ag(I)]_i$. This influences the degree of formation of $Ag(tmen)^+$ at a mole ratio of Ag(I) to tmen of 1:1. The degree of formation of $Ag(tmen)^+$ decreases from approximately 34% to an extremely low value of 0,60% if the $[Ag(I)]_i$ is decreased (Table 8 and Figure 7). At a mole ratio 1:2 the formation of $Ag(tmen)_2^+$ decreased with decreasing $[Ag(I)]_i$.

Table 8. The degree of formation of $Ag(tmen)^+$ in various solvents.

Degree of formation	$[Ag(I)]_i$ (mol dm^{-3})	log β_1	Solvent
33,8%	$9{,}33 \times 10^{-3}$	4,03	Acetone
29,4%	$4{,}67 \times 10^{-3}$	4,02	Acetone
0,60%	$2{,}80 \times 10^{-3}$	3,35	Acetone
19,5%	$1{,}06 \times 10^{-2}$	3,74	Methanol
52,1%	$5{,}32 \times 10^{-3}$	3,77	Methanol
22,9%	$1{,}07 \times 10^{-2}$	3,82	Ethanol
40,7%	$5{,}36 \times 10^{-3}$	4,19	Ethanol

Figure 7. The distribution diagrams for the Ag(I)/tmen system in acetone, with different $[Ag(I)]_i$ concentrations.

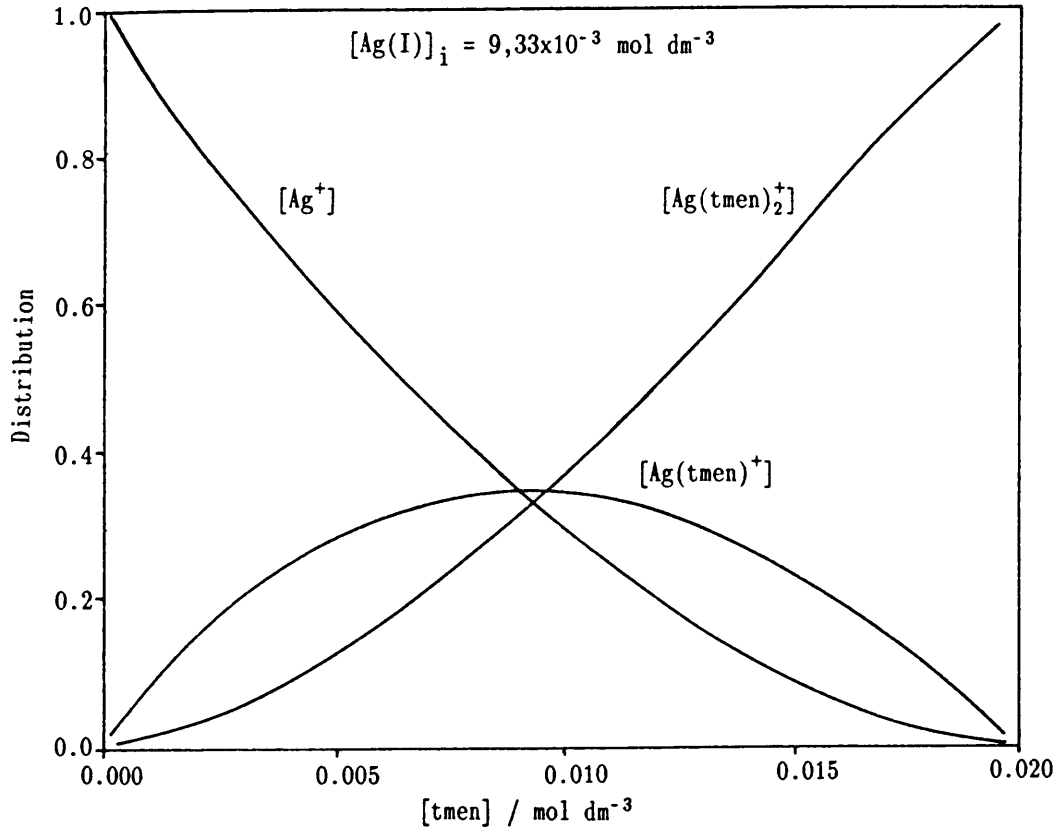

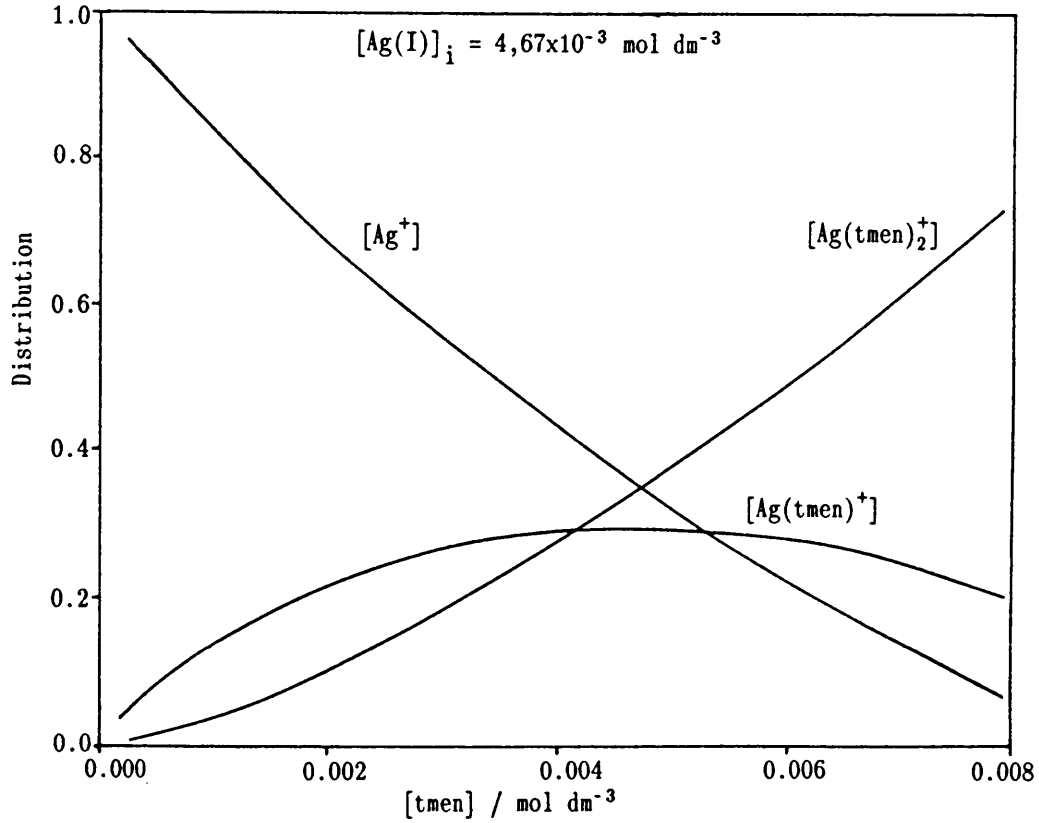

Figure 7 continues.

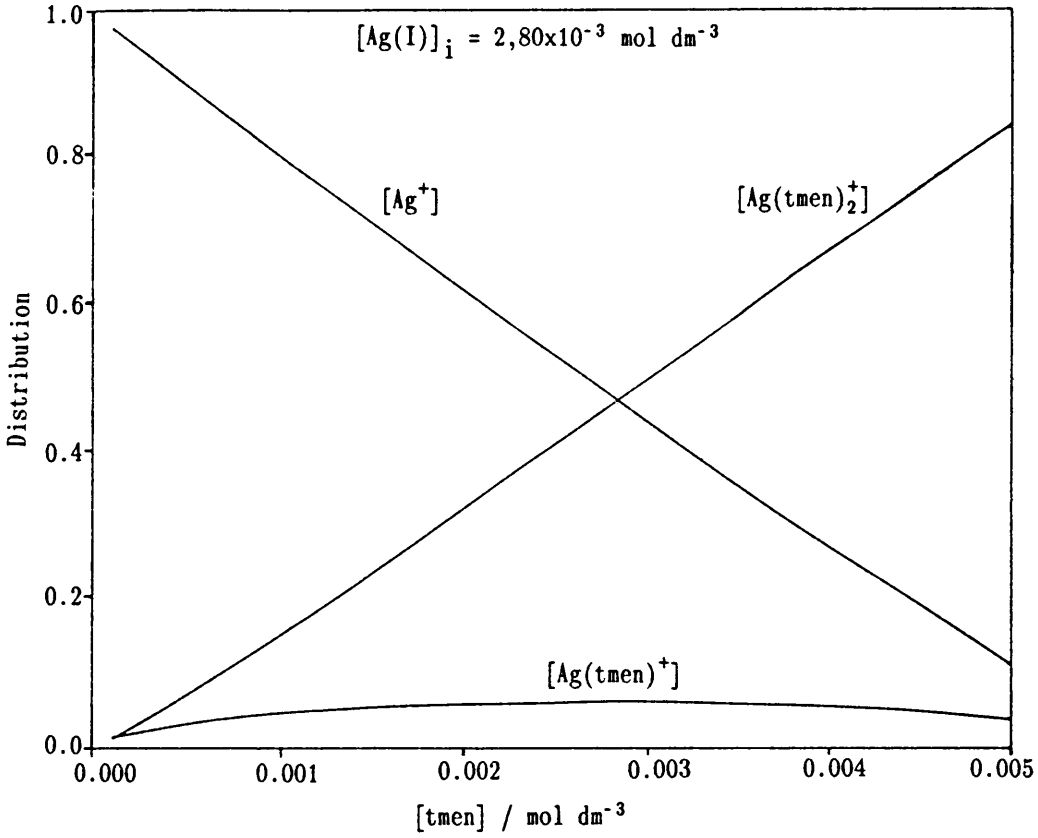

The differences in the thermodynamic quantities may be attributed to additional simultaneous equilibria, occuring in the initial stages of the reaction. No rigorous measures were employed to exclude water from the reaction. The ionic strengths were also not controlled during the titrations.

5.2.2 The solvents ethanol and methanol

The titration obtained by titrating a 0,010 mol dm^{-3} solution of Ag(I) with 1,0 mol dm^{-3} tmen in ethanol is shown in Figure 6. The solvent methanol gave a similar titration curve. The curve indicates that Ag(I) and tmen react in the mole ratio of 1:2 in both solvents. A roundness in the end point of the titration curve can be attributed to a slow reaction, or the presence of water and makes it difficult to determine the end point by simple extrapolation. The form of the curve suggests smaller formation constants for the reactions in both solvents. This phenomenon is reflected in the results summarised in Table 9. The β_1 value decreased, but the β_2 value remained the same if $[Ag(I)]_i$ = 0,01 mol dm^{-3}.

The degree of formation of $Ag(tmen)^+$ was similar in methanol and ethanol, but significantly different from the observed value in acetone. The $Ag(tmen)_2^+$ specie in acetone was more dominant from the beginning of the titration compared to what was observed for the other two solvents.

Table 9. The thermodynamic constants for the Ag(I)/tmen system in various different solvents. $[Ag(I)]_i$ = 0,01 mol dm^{-3} and $[tmen]_i$ = 1,00 mol dm^{-3}.

Thermodynamic parameters	Acetone	Methanol	Ethanol
log β_1	4,03	3,74	3,82
log β_2	8,00	8,09	8,09
ΔG_{0-1} (kJ mol^{-1})	-23,02	-21,33	-21,82
ΔG_{0-2} (kJ mol^{-1})	-45,69	-46,19	-46,17
ΔH^0_{0-1} (kJ mol^{-1})	-75,11	-39,82	-25,30
ΔH^0_{0-2} (kJ mol^{-1})	-198,07	-97 39	-88,24
ΔS^0_{0-1} (J $mol^{-1}K^{-1}$)	-174,71	-62,02	-11,67
ΔS^0_{0-2} (J $mol^{-1}K^{-1}$)	-511,08	-171,72	-141,10

The results for the dilution of the $[Ag(I)]_i$ are reported in Tables 10 and 11. In general, the dilution of $[Ag(I)]_i$ gives rise to no significant differences in the thermodynamic constants compared with those obtained in acetone. A large deviation was, however, observed in the β_2 value when methanol was used as solvent. This was also observed in the different entropy values obtained in ethanol.

Table 10. The effect of $[Ag(I)]_i$ on the thermodynamic constants using ethanol as solvent. $[tmen]_i$ = 1,00 mol dm^{-3}.

Thermodynamic parameters	$[Ag(I)]_i$	
	1.07×10^{-2} mol dm^{-3}	$5,37 \times 10^{-3}$ mol dm^{-3}
$\log \beta_1$	3,82	4,19
$\log \beta_2$	8,09	8,08
ΔG_{0-1} (kJ mol^{-1})	-21,82	-23,90
ΔG_{0-2} (kJ mol^{-1})	-46,17	-46,09
ΔH^0_{0-1} (kJ mol^{-1})	-25,30	-29,24
ΔH^0_{0-2} (kJ mol^{-1})	-88,24	-74,33
ΔS^0_{0-1} (J $mol^{-1}K^{-1}$)	-11,67	-17,91
ΔS^0_{0-2} (J $mol^{-1}K^{-1}$)	-141,10	-94,72

Table 11. The effect of $[Ag(I)]_i$ on the thermodynamic constants using methanol as solvent. $[tmen]_i$ = 1,00 mol dm^{-3}.

Thermodynamic parameters	$[Ag(I)]_i$	
	$1.07x10^{-2}$ mol dm^{-3}	$5,33x10^{-3}$ mol dm^{-3}
log β_1	3,74	3,77
log β_2	8,09	6,82
ΔG_{0-1} (kJ mol^{-1})	-21,33	-21,49
ΔG_{0-2} (kJ mol^{-1})	-46,19	-38,93
ΔH^0_{0-1} (kJ mol^{-1})	-39,82	-40,53
ΔH^0_{0-2} (kJ mol^{-1})	-97,39	-91,84
ΔS^0_{0-1} (J $mol^{-1}K^{-1}$)	-62,02	-63,86
ΔS^0_{0-2} (J $mol^{-1}K^{-1}$)	-171,72	-177,46

When using the solvents methanol and ethanol, dilution of $[Ag(I)]_i$ caused an increase in the degree of formation of $Ag(tmen)^+$ (Table 8 and Figures 7 and 8.). The distribution diagrams in the solvent ethanol are similar to the distribution diagrams obtained in methanol.

Figure 8. The distribution diagrams for the Ag(I)/tmen system using ethanol as solvent (methanol similar) and at different $[Ag(I)]_i$.

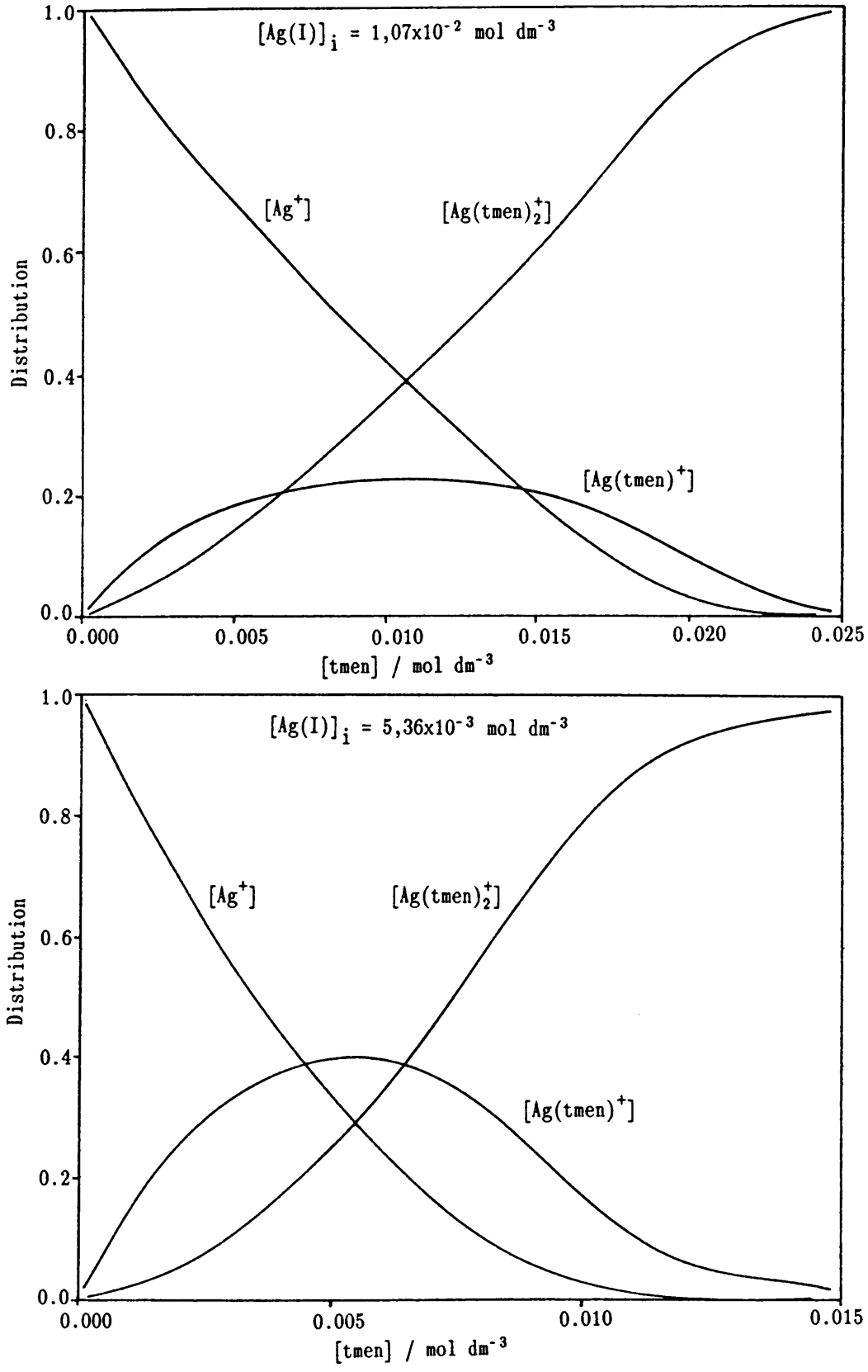

5.2.3 Discussion on the effect of solvent in the 1:2 system

In general, the formation constant β_2 was similar in all three solvents at $[Ag(I)]_i$ = 0,010 mol dm^{-3}. Decreasing the $[Ag(I)]_i$ in acetone and ethanol had little effect on the log β_2 value. A value of 6,82 was however obtained in methanol. The formation constant β_1 represents the reaction

$$Ag^+ \text{ (solv.)} + \text{tmen (solv.)} \rightleftharpoons Ag(\text{tmen})^+ + \text{solv.}$$

and decreases for the various solvents in the order:

acetone > ethanol > methanol.

The formation of $Ag(tmen)^+$ and $Ag(tmen)_2^+$ is enthalpy driven in all three solvents. The values obtained reflect the fact that the reaction in acetone is more enthalpy driven than in methanol and ethanol. The enthalpy of formation for $Ag(tmen)_2^+$ ($-\Delta H^0_{0-2}$) is more than twice as great as that for $Ag(tmen)^+$ ($-\Delta H^0_{0-1}$) in all three solvents. The enthalpy values are more exothermic in acetone than in methanol and ethanol. The enthalpy values for methanol and ethanol solutions are, however, similar. Large negative entropy values were observed in all three solvents. However, the entropy values in methanol and ethanol are more positive compared to those in acetone. Thus the coordination of the solvent to the metal contributes to the order or disorder in the structures.

In the initial construction of this part of the study, it was anticipated that the thermodynamic constants would remain the

same on dilution of the solutions. This only applied when the solvents ethanol and methanol were used.

5.3 THE REACTION OF CO(II) WITH TMEN

The titration of a 0,010 mol dm^{-3} $CoCl_2$ solution with a 1,00 mol dm^{-3} solution of tmen in acetone gave a sharp end point at a mole ratio of Co(II) to tmen of 1:1. The distribution diagram is shown in Figure 9. Thus the complexation reaction is

$$Co^{2+}\ (solv.) + tmen \rightleftharpoons Co(tmen)^{2+} + solv.$$

Small deviations in the overall formation constant and the free energy change were observed if the $CoCl_2$ solution was diluted (Table 12). The reaction is enthalpy driven at all concentrations. However, a slight increase in the enthalpy of formation was observed when the concentration of the $CoCl_2$ solution was decreased. This phenomenon was also reflected in the Ag(I)/tmen system in acetone. A further decrease in the $CoCl_2$ concentration resulted in low reproducibility, especially if the concentrations exceeded $3,0 \times 10^{-3}$ mol dm^{-3}.

Attempts were made to study the reaction in methanol and ethanol, but the presence of the $Co(H_2O)_6^{2+}$ ion resulted in an additional equilibrium. Round end points and an endothermic reaction were observed. Due to the unreproduciblity, the study was not extended to include the effect of solvent on the 1:1 system.

Figure 9. The distribution curve for the $CoCl_2$/tmen system in acetone.

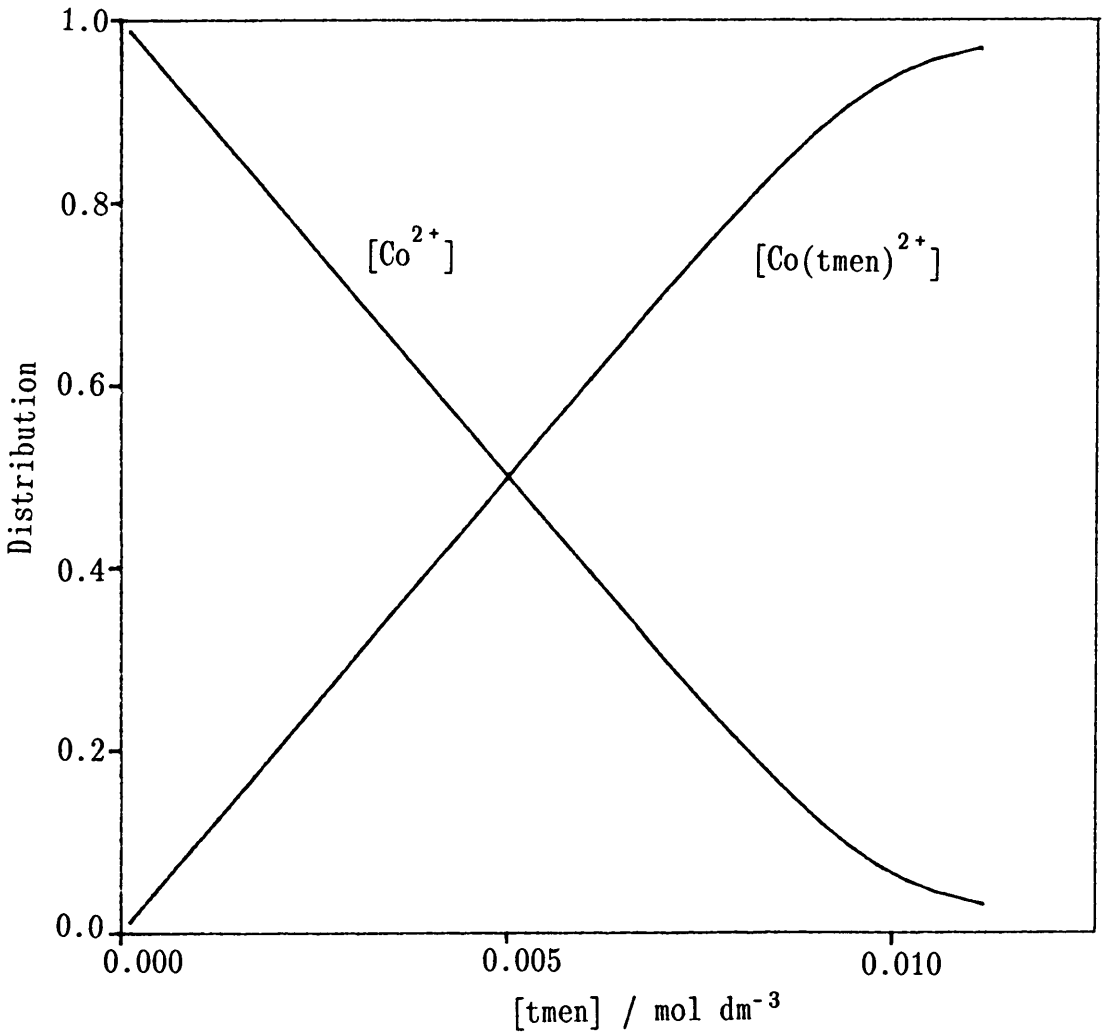

Table 12. The effect of $[CoCl_2]_i$ on the thermodynamic quantities, using the solvent acetone. $[tmen]_i$ = 1,00 mol dm^{-3}.

Thermodynamic parameters	$[CoCl_2]_i$		
	$1,00x10^{-2}$ mol dm^{-3}	$5,01x10^{-3}$ mol dm^{-3}	$3,01x10^{-3}$ mol dm^{-3}
$\log \beta_1$	4,29	4,30	4,04
ΔG_{0-1} (kJ mol^{-1})	-24,5	-24,5	-23,1
ΔH^0_{0-1} (kJ mol^{-1})	-90,0	-82,4	-82,6
ΔS^0_{0-1} (J $mol^{-1}K^{-1}$)	-219,8	-194,3	199,7

5.4 DISCUSSION

Decreasing the $[CoCl_2]_i$, in the experimentally reproducible range, resulted in a small deviation in the thermodynamic constants. Therefore a 1:1 system reflects the independence of the thermodynamic quantities of the titrant concentration. This is in agreement with the results published by Christensen [54]. However, the thermodynamic quantities are not independent of the titrant concentration in a 1:2 system.

Different structures can be expected for the complexes, since the Ag(I) (d^{10}) and Co(II) (d^7) ions reflect different coordination numbers depending on the type of ligand. The Co(II) ion forms numerous complexes, mostly either octahedral or tetrahedral, but five-coordinated and square species are also known. More tetrahedral complexes of Co(II) are known than for any other transition metal ion.

The ligand tmen contains two amino groups which are available for coordination. This leads to the formation of a tetrahedral complex between Co(II) and tmen. Sacconi [76] studied the reaction between Co(II) and polyethylene polyamines, which form a 1:1 complex. He deduced that in $Co(penten)^{2+}$, where penten = N,N,N^1,N^1-tetra- (2-aminoethyl) ethylenediamine, either six atoms are bonded, since 6 amino groups are available for coordination. These bonds are very weak and both five- and six-coordinate species may exist in equilibrium. Sacconi reported an ethalpy change of -28 kJ/mol for the formation of $[Co(en)]^{2+}$, where

en = ethylenediamine. This is close to the value obtained for $[Co(tmen)]^{2+}$.

A large variety of Ag(I) complexes exists in both solid state and in solution. The most stable Ag(I) complexes have a linear structure, $L\text{-}Ag\text{-}L^{+}$. This may be due to the relatively small energy difference between the filled 4d orbitals and the unfilled 5s orbitals, which permits extensive hybridisation of the d_{z^2} and s orbitals. The electron pair initially in the d_{z^2} orbital occupies $\Psi_1 = 1/\sqrt{2}\,(d_{z^2} - s)$, giving a circular region of relatively high electron density from which the ligands are somewhat repelled, and regions above and below the ring in which the electron density is relatively low. Ligands are attracted to the latter region. By further mixing of $\Psi_2 = 1/\sqrt{2}\,(d_{z^2} + s)$ with the p_z orbital, two hybrid orbitals siutable for forming a pair of linear covalent bonds are obtained.

CHAPTER 6

THE SOLID STATE AND SOLUTION CHEMISTRY OF BIS(PYRIDINE) COBALT(II) CHLORIDE

6.1 INTRODUCTION

The thermal decomposition of cobalt(II) complexes containing pyridine-related ligands has been investigated since 1891 [7,66,77-80]. The decomposition products are known, but no quantitative kinetic parameters have been reported for the decomposition reaction of $CoCl_2 2(py)$.

The complex $CoCl_2 2(py)$ has two isomers; the blue form, which is a tetrahedral monomer, and the violet form, which is an octahedral polymer [77]. The change-over from the blue form to the violet form is autocatalytic and is accelerated by the presence of moist air. Once the violet octahedral complex has formed, it remains stable for several months under dry conditions.

Kinetic data obtained from dynamic and isothermal studies of the thermal decomposition of $CoCl_2 2(py)$ were investigated and compared and are reported in this chapter. Additional thermodynamic data were obtained from the $CoCl_2$/py system in acetone.

6.2 SOLUTION CHEMISTRY RESULTS

The values of $\log \beta_i$, ΔH^0_{0-i}, ΔG_{0-i} and ΔS^0_{0-i} (for i = 1 and 2) for the stepwise formation of the complexes are given in Table 13. The ΔH^0_{0-i} values refer to the overall enthalpy of formation of the complex,

i.e. ΔH^0_{0-1} (298,15K) refers to the reaction

$$CoCl_2 \text{ (solv.)} + \text{py (solv.)} \rightarrow CoCl_2\text{(py)} + \text{solv.}$$

and ΔH^0_{0-2} (298,15K) refers to

$$CoCl_2 \text{ (solv.)} + 2\text{(py) (solv.)} \rightarrow CoCl_2 2\text{(py)} + \text{solv.}$$

Table 13. The thermodynamic quantities of the $CoCl_2$/py system in acetone.

$\log \beta_1$	= 4,919
$\log \beta_2$	= 8,407
ΔG_{0-1}	= -28,08 kJ mol^{-1}
ΔG_{0-2}	= -47,99 kJ mol^{-1}
ΔH^0_{0-1}	= -37,47 kJ mol^{-1}
ΔH^0_{0-2}	= -79,81 kJ mol^{-1}
ΔS^0_{0-1}	= -31,49 J mol^{-1} K^{-1}
ΔS^0_{0-2}	= -106,7 J mol^{-1} K^{-1}

The formation of $CoCl_2 2(py)$ and of $CoCl_2(py)$ was found to be enthalpy-driven. From the ΔH^0_{0-i} values, the enthalpy for the reaction

$$CoCl_2(py) + py \rightarrow CoCl_2 2(py) \qquad \Delta H^0_2 = -42{,}34 \text{ kJ mol}^{-1}$$

was calculated. Thus, a slightly stronger interaction exists between $CoCl_2(py)$ and py, than between $CoCl_2$ and py.

Logachev and co-workers [2,3] reported the thermodynamic quantities for the 1:1 as well as the 1:2 cobalt(II) chloride/pyridine complexes, in different solvents. In acetone, they obtained the following values for $CoCl_2 2(py)$: $K_2 = 4{,}8 \times 10^{-6}$, $\Delta H_{0-2} = -44{,}77$ kJ mol^{-1}, $\Delta G_{0-2} = -30{,}54$ kJ mol^{-1} and $\Delta S_{0-2} = -47{,}70$ kJ mol^{-1}. For the complex $CoCl_2(py)S$, where S represents a molecule of the solvent, the following values were obtained: $K_1 = 7{,}50 \times 10^{-4}$, $\Delta H_{0-1} = -21{,}33$ kJ mol^{-1}, $\Delta G_{0-1} = -17{,}99$ kJ mol^{-1} and $\Delta S_{0-1} = -11{,}30$ kJ mol^{-1}.

The distribution diagram of the species present during the titration, as calculated from the β_i values obtained, is given in Figure 10. The distribution diagram indicates that the $CoCl_2(py)$ species forms to an extent of 73% and that $CoCl_2 2(py)$ only reaches a maximum of 83% during the titration. The formation of $CoCl_2(py)$ reaches a maximum at approximately half way through the titration, i.e. at a mole ratio of py:$CoCl_2$ of 1:1. The $CoCl_2(py)$ species is dominant during the titration and is therefore a very stable complex in solution.

Figure 10. The distribution diagram of the $CoCl_2$/py system in acetone.

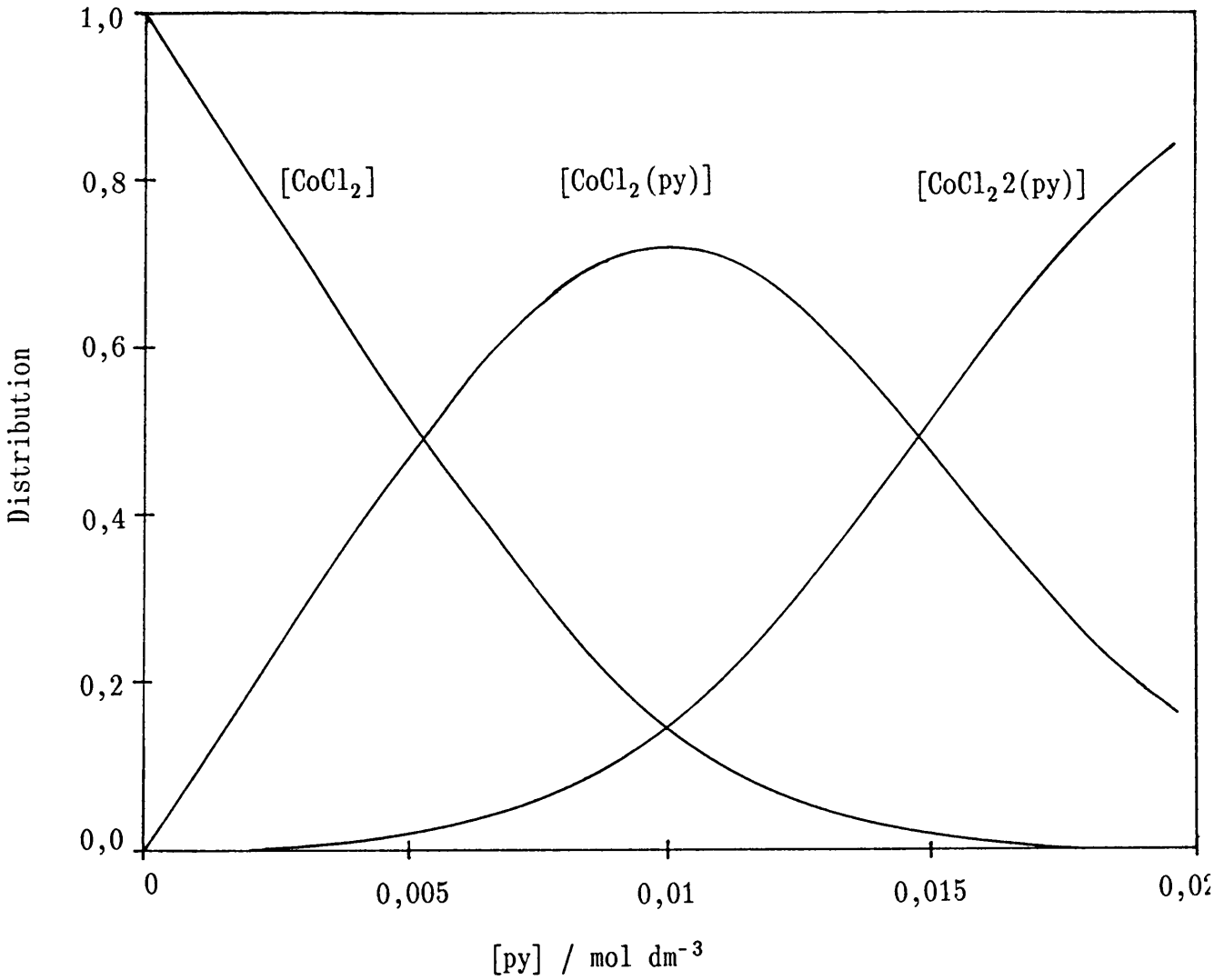

The method applied by Logachev [2,3] was developed by Murygina and resulted in more positive values if compared to the results listed in Table 13. In this method, an ampoule containing the ligand is broken into the reaction vessel. In this method the assumption is made that $CoCl_2 2(py)$ is formed completely and no traces of $CoCl_2(py)$ are present. The distribution diagram (Figure 10) reflects the existence of approximately 17% $CoCl_2(py)$ at the end of the titration. This contradicts the assumption that no $CoCl_2(py)$ is present and could account for the differences from the expected distribution diagram.

6.3 SOLID STATE CHEMISTRY RESULTS

6.3.1 Dynamic thermogravimetric analysis

The dynamic TG curve indicates three successive sigmoidal curves (Figure 11). Trace A represents the decomposition of the violet powder and trace B of the single crystals. The larger crystals decompose relatively more rapidly than the powder. This behaviour may be attributed to the enhanced nucleation in the larger particles, due to strain. A shift in the DTA trace is also observed.

Figure 11. The DTA and TG traces recorded for $CoCl_2 2(py)$. The broken line represents the powder and the solid line the single crystals.

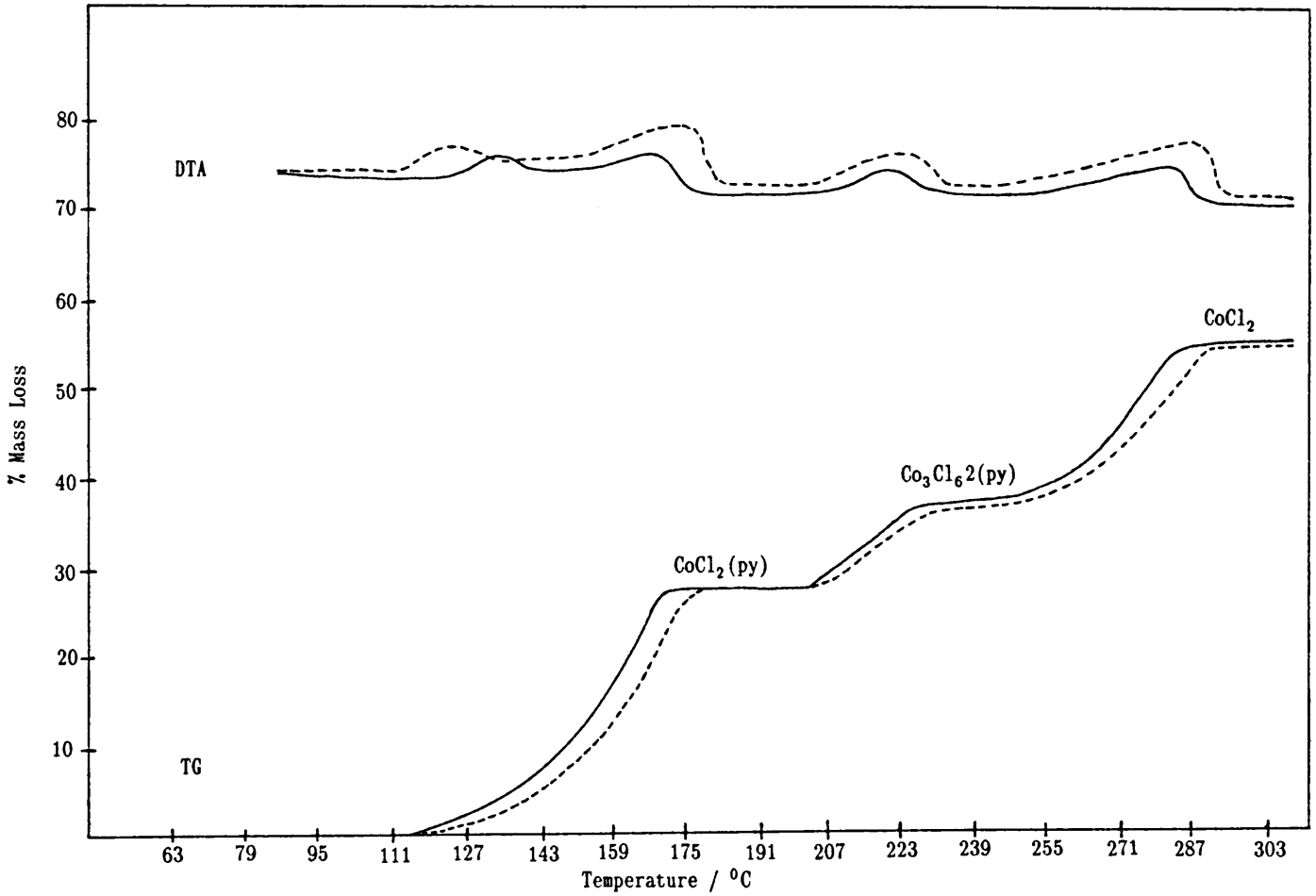

The complex, $CoCl_2 2(py)$, decomposes over the temperature range 121^0C to 370^0C to yield the stable intermediates, according to the following reactions:

$$CoCl_2 2(py)\ (s) \rightarrow CoCl_2(py)\ (s) + py\ (g) \qquad (1)$$

$$3CoCl_2(py)\ (s) \rightarrow Co_3Cl_6 2(py)\ (s) + py\ (g) \qquad (2)$$

$$Co_3Cl_6 2(py)\ (s) \rightarrow 3CoCl_2\ (s) + 2(py)\ (g) \qquad (3)$$

The experimental temperatures (Table 14) observed are similar to the temperatures obtained by Ocone [66]. The difference from the values obtained by Allan may be attributed to the difference in sample atmosphere and the different preparation of the thermal products [78].

Table 14. The temperatures and mass losses obtained for the decomposition of $CoCl_2 2(py)$.

Reaction	Mass loss (%)		$^*T_i$ (^0C)		
	Exp.	Theor.	This work	Ocone	Allan
1	27,4	27,5	97	102	210
2	13,0	12,6	235	233	250
3	28,9	28,8	281	284	350

$^*T_i$ is the onset temperature.

The experimental mass losses obtained correspond extremely well with the calculated theoretical mass losses (Table 14).

The kinetic results obtained from the dynamic TG trace are summarised in Table 15. The three reactions were separated and calculations were performed on the individual reactions.

Table 15. The results of the kinetic analysis performed on the dynamic curve of $CoCl_2 2(py)$ (violet powder). All the reactions conform to the contracting area model.

Reaction	E_a (kJ mol^{-1})	ln Z (ln min^{-1})	Standard deviation
1	99,00	25,82	0,0543
2	217,0	51,97	0,0425
3	194,0	40,50	0,0465

The contracting area model, $1-(1-\alpha)^{\frac{1}{2}} = kt$, describes all three of the decomposition reactions (Table 15). The activation energy of reaction (1), which involves the loss of one pyridine, is considerably less than the activation energies calculated for the other two reactions. These data were used to simulate a dynamic TG curve. A comparison of the simulated curve with the experimentally obtained TG curve shows an excellent fit over the whole α-range (Figure 12).

Figure 12. Plots of the simulated dynamic curve (---) and the experimental dynamic curve (—).

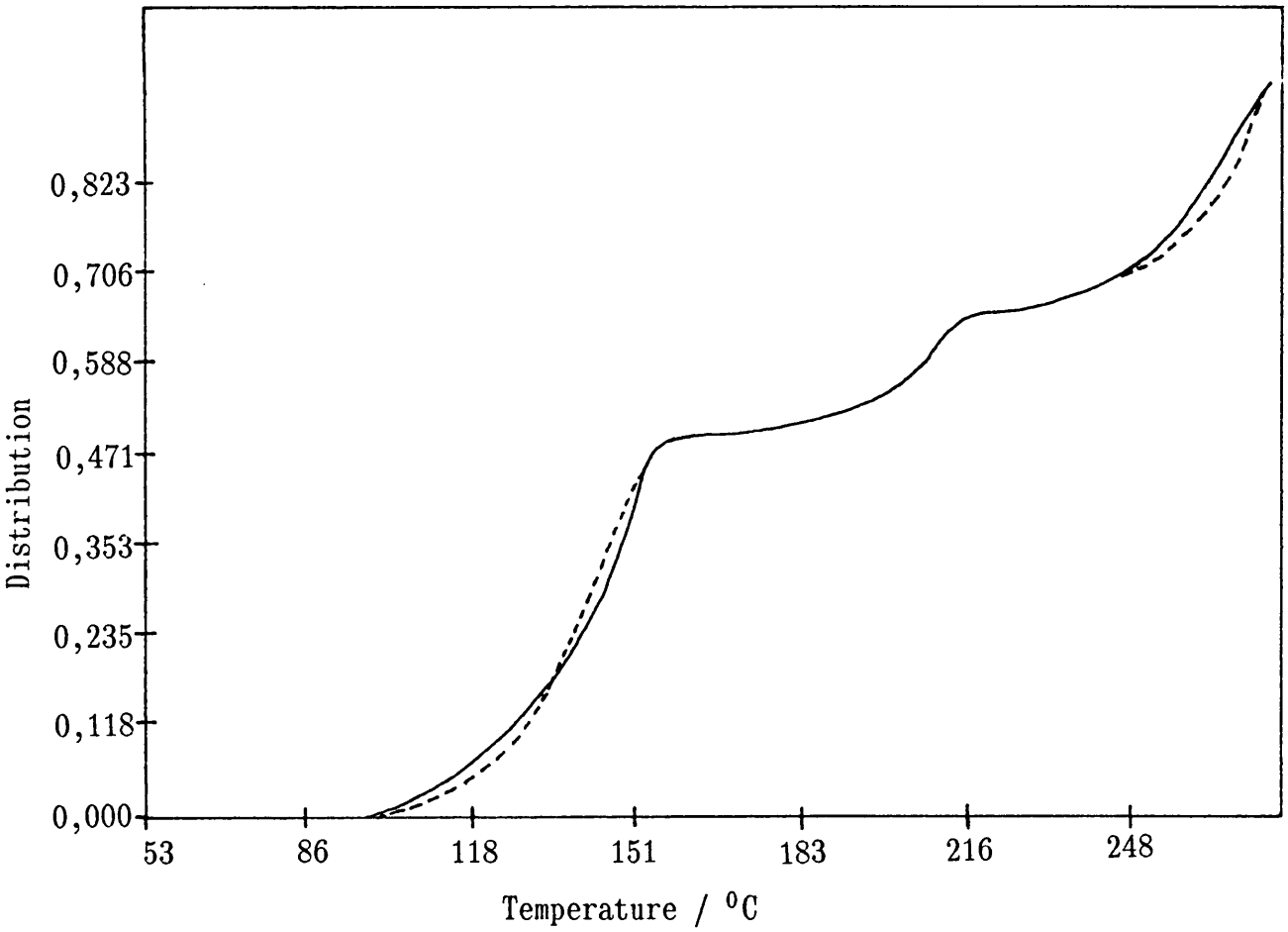

The results obtained from the analysis of the dynamic curve obtained from the single crystals are summarised in Table 16.

Table 16. The results of the kinetic analysis performed on the dynamic curve of the single crystals of $CoCl_2 2(py)$. All the reactions conform to the contracting area model.

Reaction	E_a (kJ mol^{-1})	ln Z (ln min^{-1})	Standard deviation
1	98,00	25,89	0,0322
2	243,0	58,39	0,0544
3	228,0	48,27	0,1030

An excellent fit was obtained for the first part of the decomposition and is also reflected in the similar values obtained. However, poorer fits were obtained for reactions (2) and (3). Larger E_a and ln Z values were obtained from the analysis of the single crystals. This was anticipated, since a shift to the left was observed for the dynamic curve (Figure 10), and results in larger values.

6.3.2 Isothermal results

The studies were performed on the single crystals and the powder of the violet isomer of $CoCl_2 2(py)$. The results for the violet isomer are summarised in Table 17. All three reactions conform to

the contracting area model and are thus similar to the results obtained in the kinetic analysis of the dynamic curve.

Table 17. The isothermal results for the analysis of $CoCl_2 2(py)$. All the reactions conform to the contracting area model.

Reaction	Temperature range (^0C)	α-range	E_a (kJ mol^{-1})	ln Z (ln min^{-1})
1	97 - 109	,09 - ,87	66,8	15,38
2	235 - 256	,00 - ,30	95,9	20,91
3		,37 - ,95	82,5	14,49
3	281 - 294	,07 - ,91	159,3	31,59

Reaction (2) was studied by heating $CoCl_2 2(py)$ dynamically until a mass loss of 27,5%, which corresponds to the formation of $CoCl_2(py)$, was observed and then the temperature was held constant at a preselected value in the range 235^0C to 256^0C. A mass loss of 12,6% was expected; instead the reaction continued up to a mass loss of 41% (Figure 13). This suggests that the decomposition of the intermediate, $Co_3Cl_6 2(py)$, overlapped with the decomposition reaction of $CoCl_2(py)$. For this reason, it was not possible to fit a single rate equation over the whole α-range of the experimental data, but with careful consideration of the data the results were obtained which are given in Table 17.

Figure 13. The isothermal decomposition of $CoCl_2 2(py)$ at 256^0C (solid line) and 285^0C (broken line).

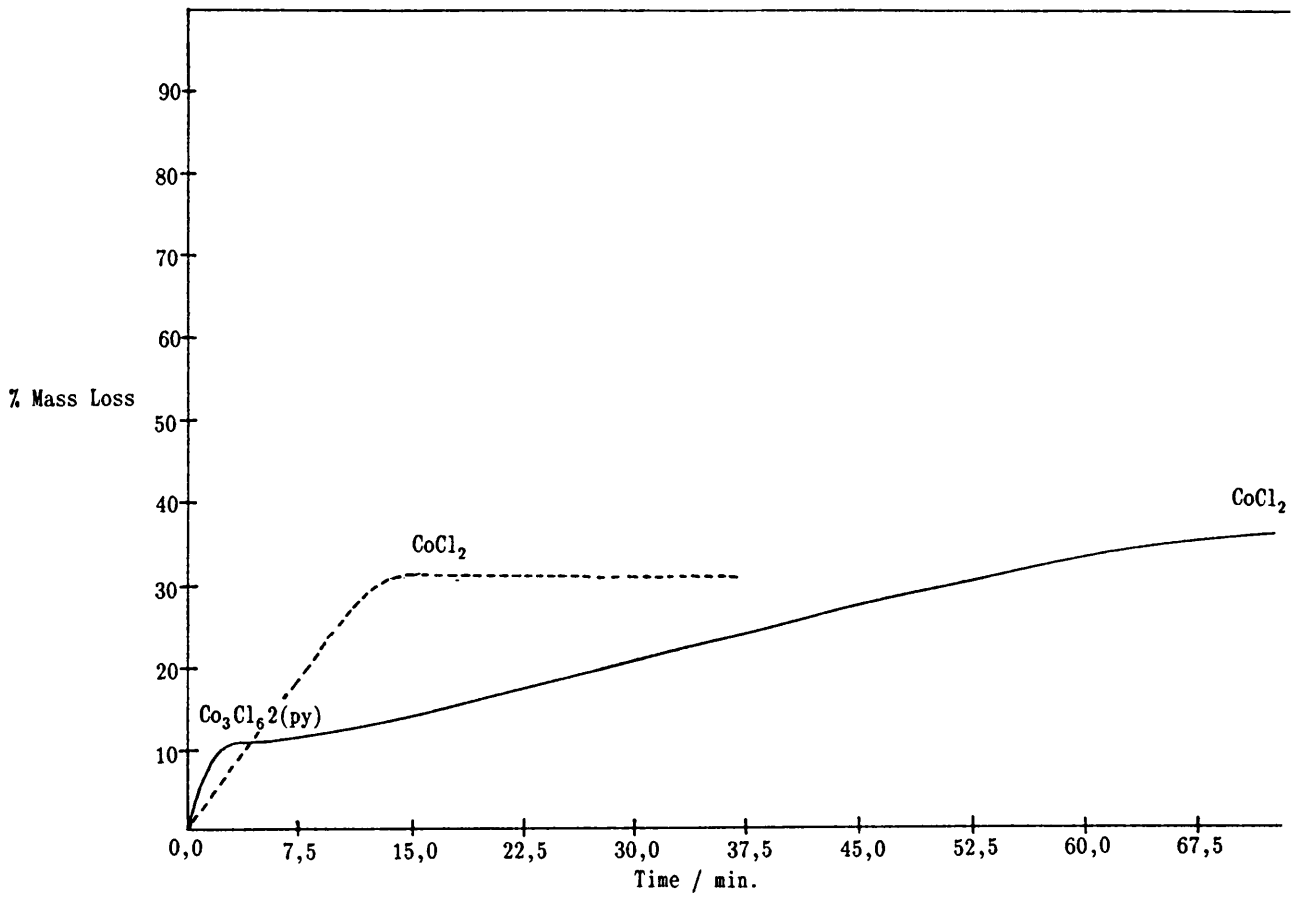

In order to obtain improved results for reaction (3), $Co_3Cl_6 2(py)$ was prepared *in situ* by heating $CoCl_2 2(py)$. The results obtained are found in Table 17. These values differ from the values obtained at a lower temperature range and seem to suggest that, whenever overlapping processes occur, each should be treated separately. These values must obviously be treated with suspicion, since overlapping processes can give rise to inaccurate results.

The parameters were used to simulate a dynamic TG curve, assuming an identical heating rate of $2^0C\ min^{-1}$. Although the decomposition reaction is described by the same kinetic rate equation, a poor fit was obtained (Figure 14). The kinetic rate equations obtained do not describe the decomposition reaction over the entire α-range. This is acceptable, since during the initial stages of the reaction, the sample temperature had not reached the oven temperature. The final stage of decomposition exhibits different flattening curves, resulting in a poor fit at very high α-values. Therefore, new kinetic calculations were performed on the isothermal data for $0,10 < \alpha < 0,90$. In Table 18 the parameters obtained from this calculation were compared with the previous values over the whole α-range.

Figure 14. Plots of the simulated dynamic curve(---) obtaincd form the isothermal parameters and the experimental dynamic curve (—).

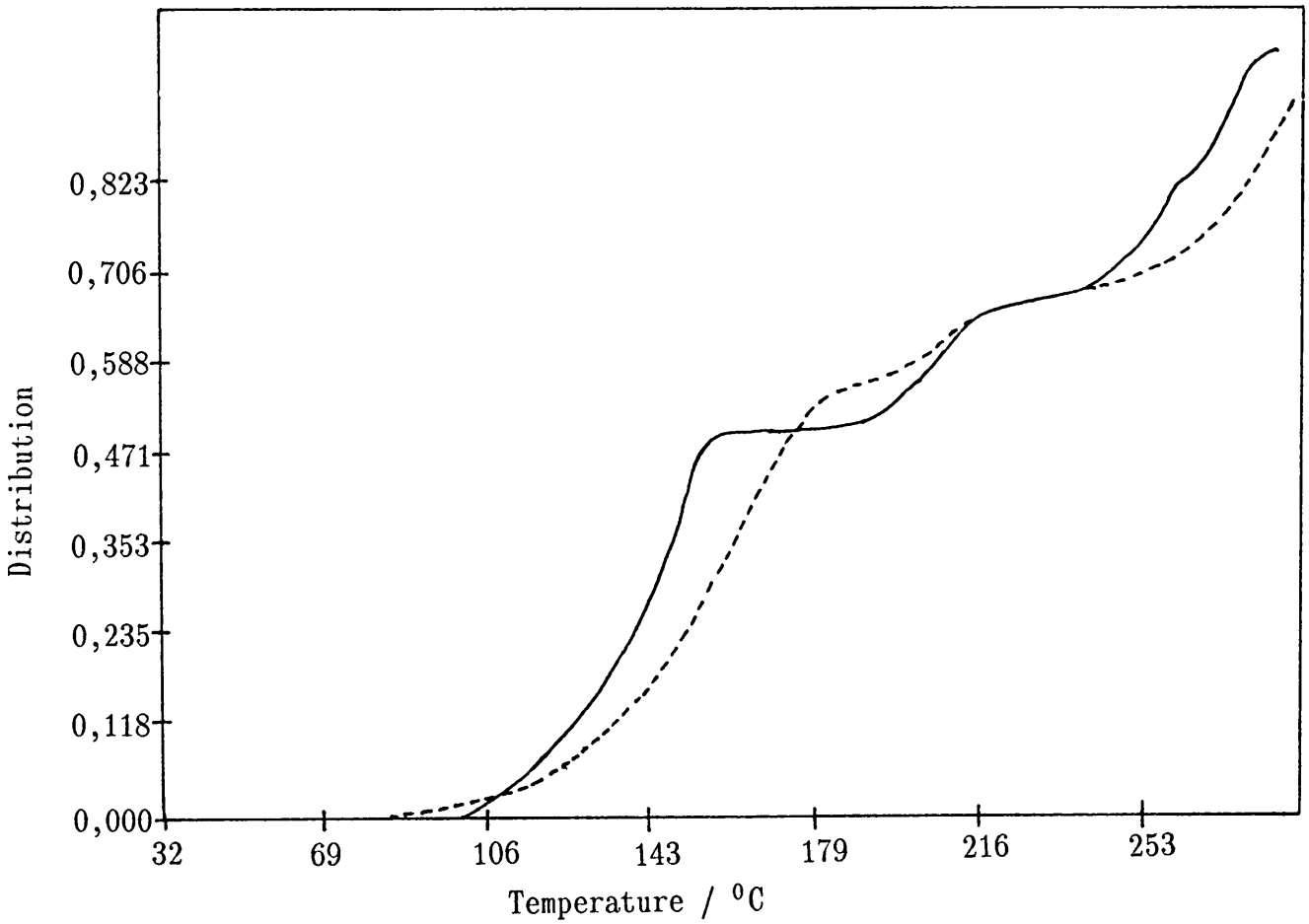

Table 18. Isothermal results obtained for the preselected α-ranges.

Reaction	α-range	E_a (kJ mol^{-1})	ln Z (ln min^{-1})	Standard deviation
1	,00 - 1,0	66,8	15,4	0,066
	,10 - ,90	64,6	14,6	0,051
2	,00 - 1,0	95,9	20,9	0,007
	,10 - ,90	95,9	20,9	0,007
3	,00 - 1,0	159,3	31,6	0,014
	,10 - ,90	97,1	18,3	0,005

The activation energy for reaction (1) decreased slightly, but it remained unchanged for reaction (2). Reaction (3) revealed a significant decrease in the activation energy. The new value is closer to the value obtained at lower temperatures, and therefore more acceptable. The simulated dynamic TG curve results in an improved fit (Figure 15).

Isothermal studies were also performed on the single crystals. Again, it was found that the contracting area model described all three reactions. This is similar to the results obtained for the powder.

Figure 15. Plots of the simulated curve (---) (obtained from the isothermal studies in the preselected α-range) and the experimental dynamic curve (—).

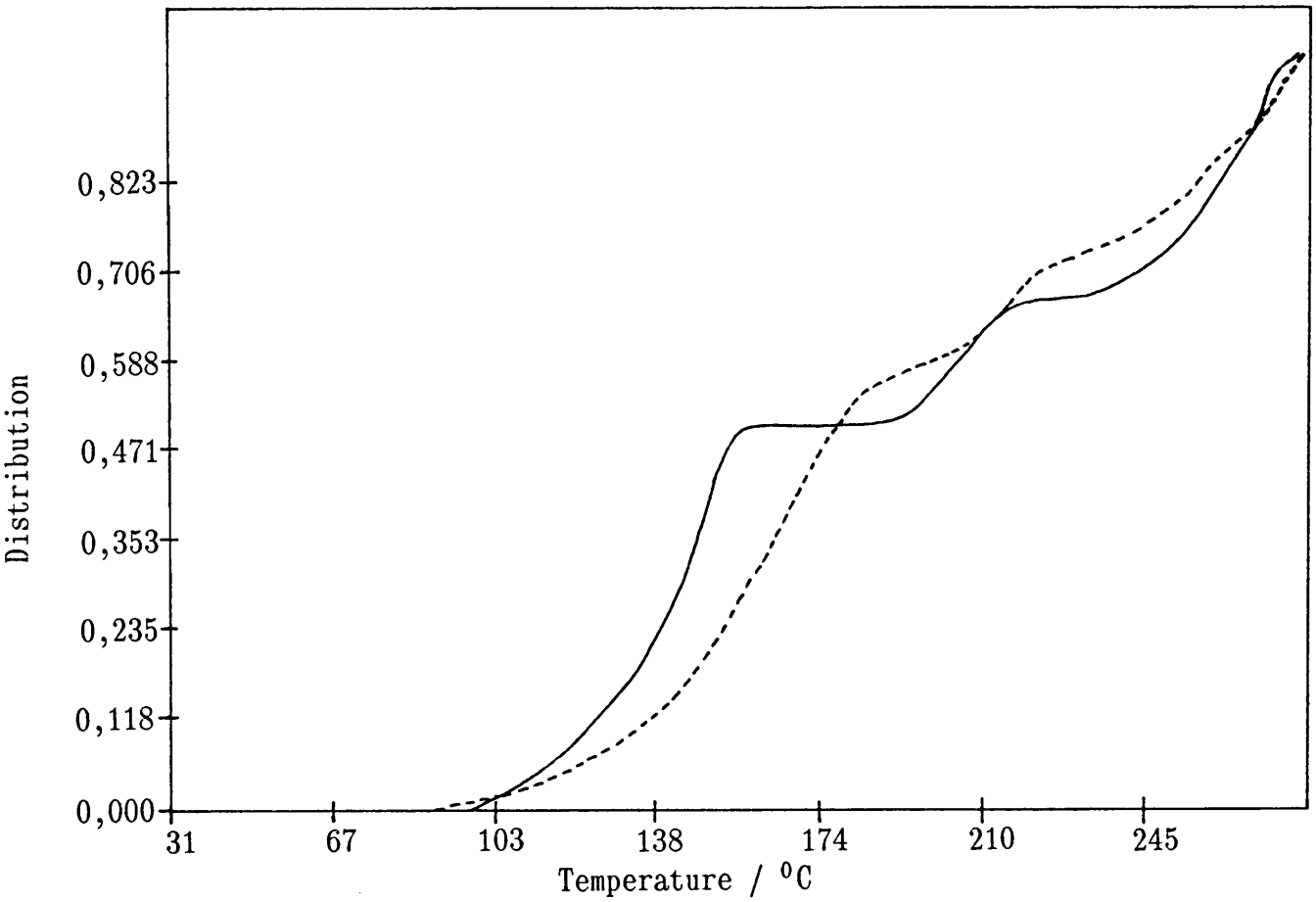

6.3.3 Electron microscopy studies

Micrographs 1 and 2 represent the crystals of $CoCl_2 2(py)$ before decomposition. The surface shows points of imperfection, which may act as active points where decay can start. If 1% of the $CoCl_2 2(py)$ is decomposed to form $CoCl_2(py)$, the surface reveals areas of decomposition (Micrograph 3).

Micrograph 4 reveals the complete decomposition of $CoCl_2 2(py)$ to $CoCl_2(py)$. Complete decomposition is visible on the surface of the crystals. Thus, if it is assumed that the decomposition continues into the crystal after being initiated on the surface of the crystal (i.e. decomposition in two dimensions), excellent agreement with the isothermal studies is obtained. Cross-section cuts would have revealed this phenomenon more clearly, but the complexes are soluble in water and therefore the method could not be applied. A layer-like structure is observed in Micrograph 5. It seems that the decomposition continues in layers and gives rise to a breakage of the crystals in certain layers, from which the pyridine may evolve.

If 1% of the $CoCl_2(py)$ is decomposed to $Co_3Cl_6 2(py)$, cracks are observed as well as an increase in the decomposition area (Micrograph 6). Micrograph 7 shows an increase in decomposition for the intermediate, $Co_3Cl_6 2(py)$.

Micrographs 8 and 9 represent the final decomposition product $CoCl_2$. The crystals are porous but still intact.

Micrograph 1. The surface of a $CoCl_2$2py crystal before decomposition. (Magnification x2500).

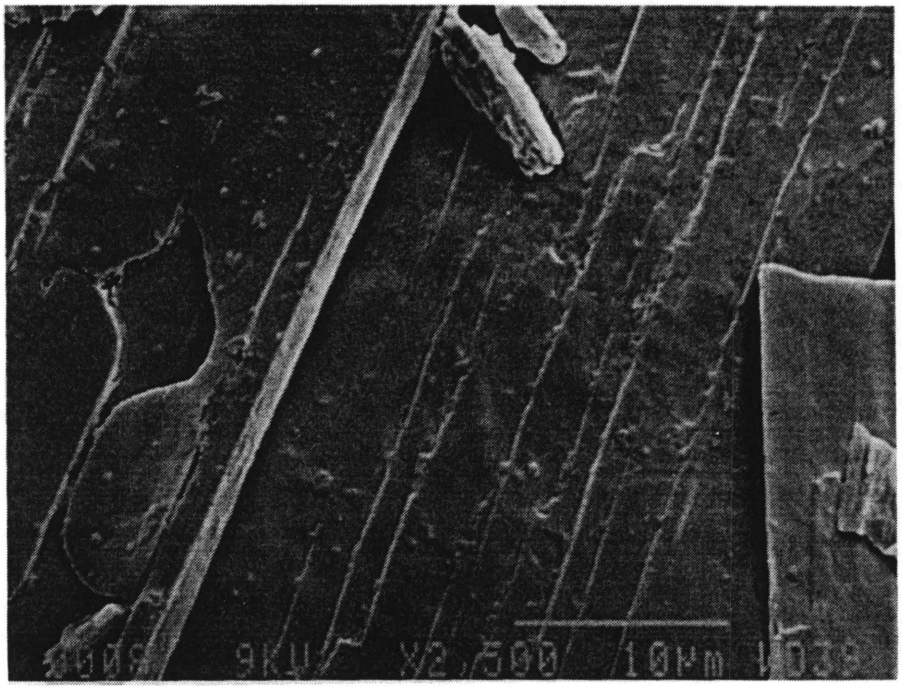

Micrograph 2. The surface of a $CoCl_2$2py crystal before decomposition. (Magnification x2500).

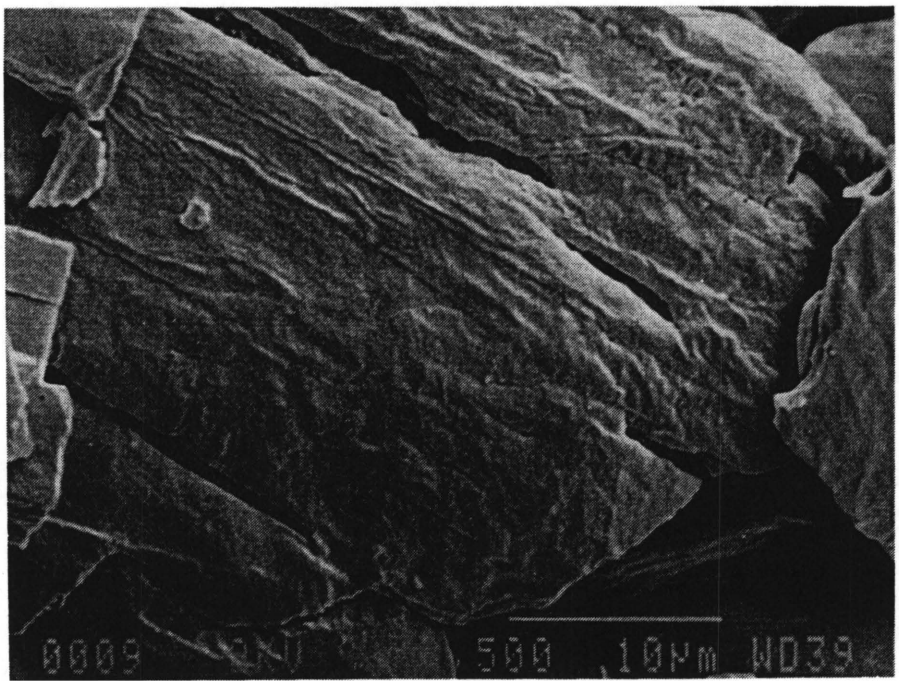

Micrograph 3. The initial decomposition (1%) of $CoCl_2 2py$ to $CoCl_2 py$. (Magnification x3500).

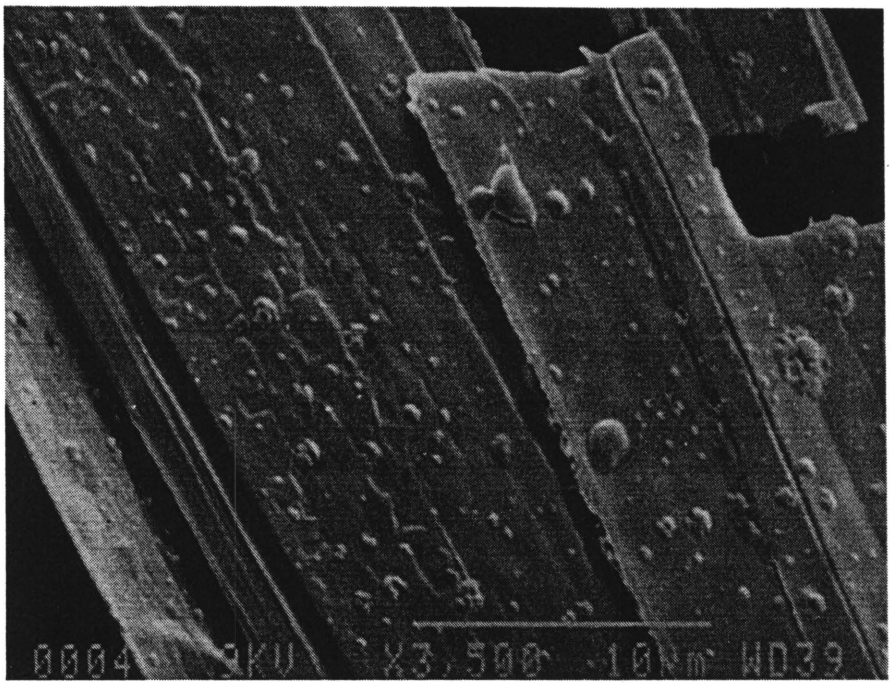

Micrograph 4. The surface of the decomposition intermediate, $CoCl_2py$. (Magnification x5000).

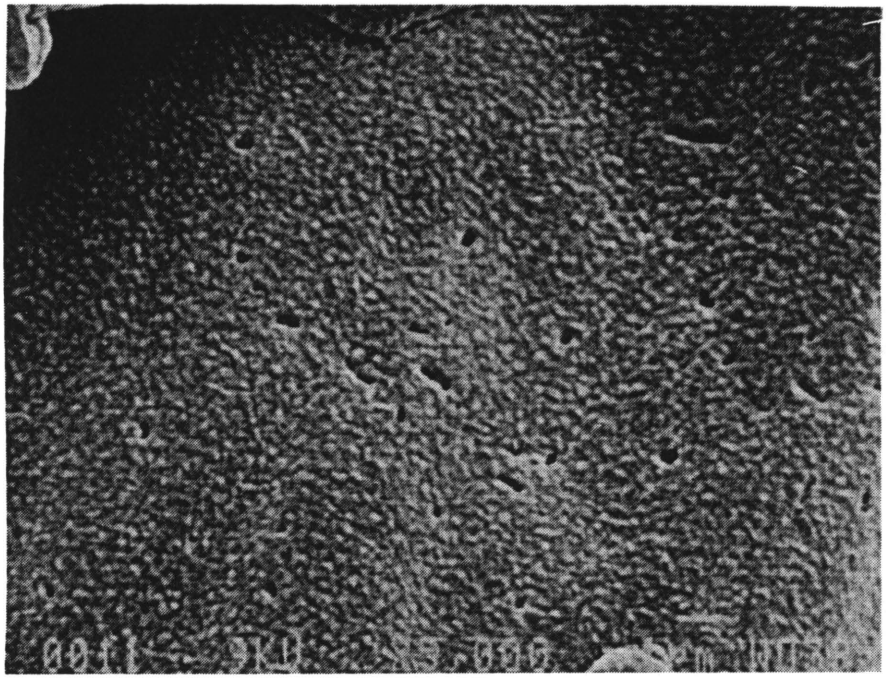

Micrograph 5. The layerlike structure observed for the decomposition intermediate, $CoCl_2py$. (Magnification x5000)

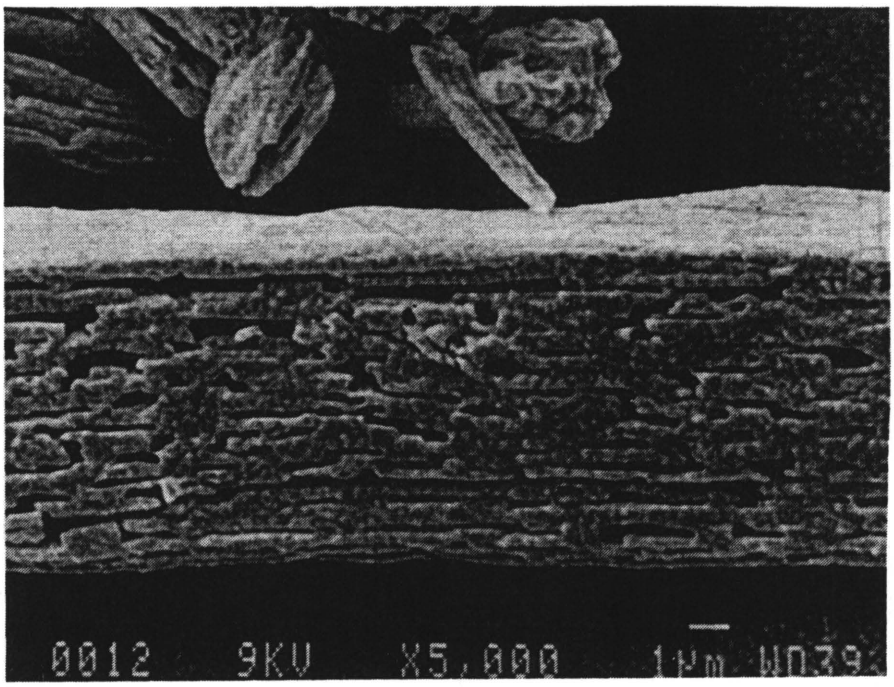

Micrograph 6. The initial decomposition (1%) of $CoCl_2py$ to $Co_3Cl_6 2py$. (Magnification x5000).

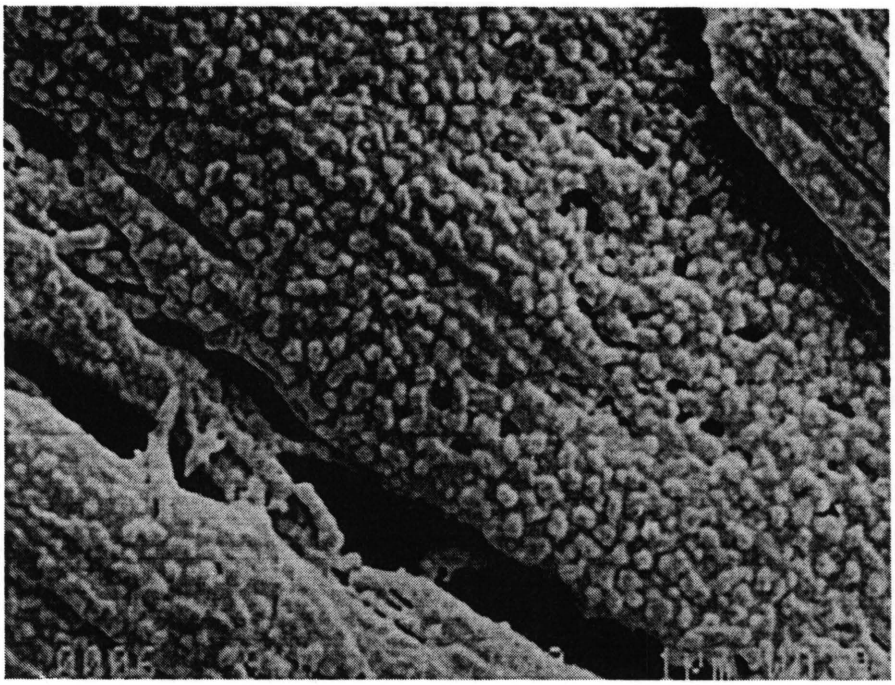

Micrograph 7. The surface of the decomposition intermediate, $Co_3Cl_6 2py$. (Magnification x2500).

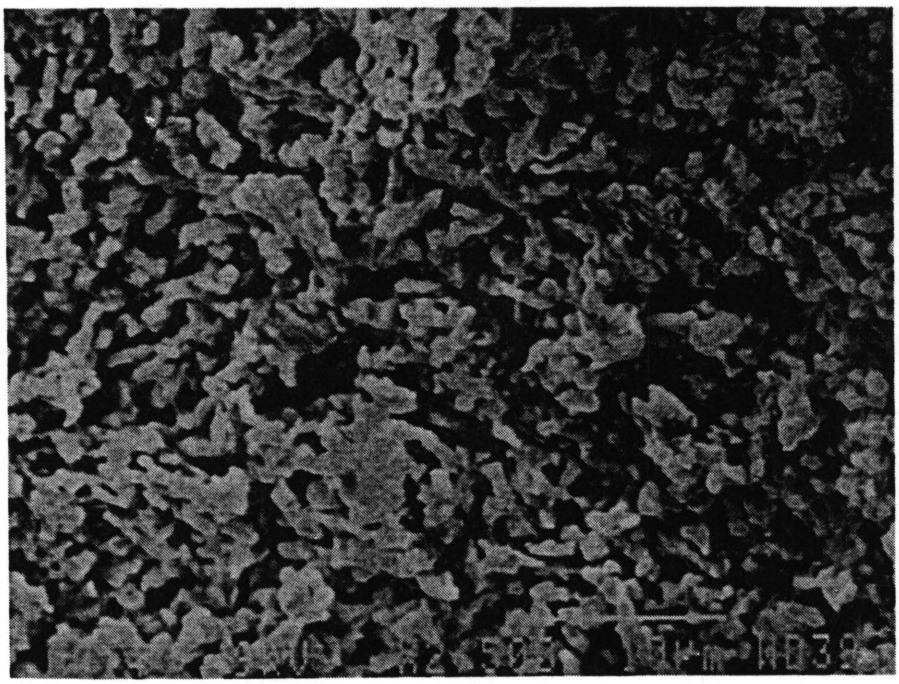

Micrograph 8. The single crystals of the final decomposition product, $CoCl_2$. (Magnification x250).

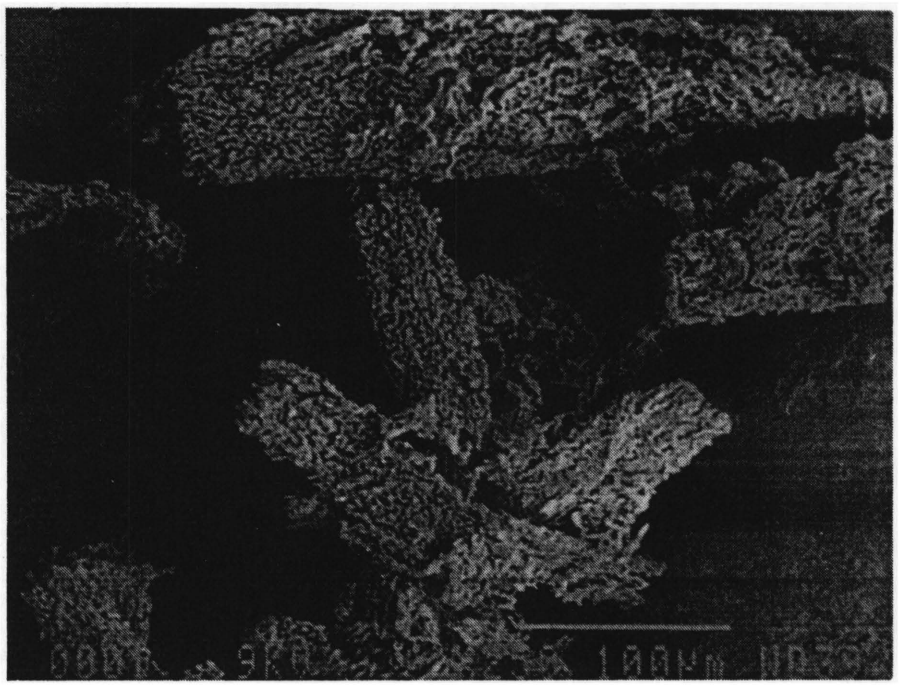

Micrograph 9. The surface of the final decomposition product, $CoCl_2$. (Magnification x2000).

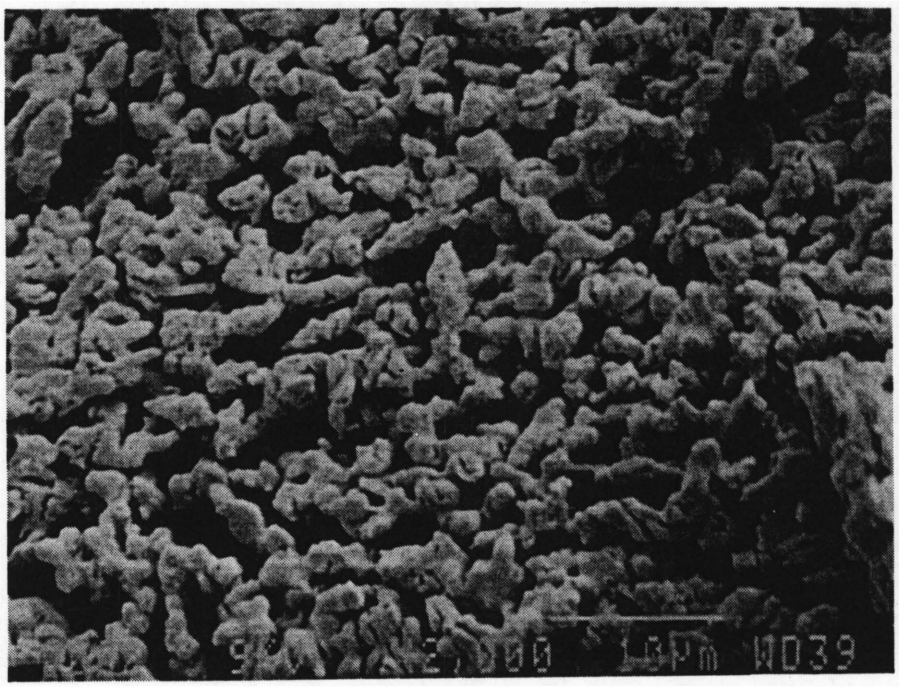

6.3.4 DSC results

The studies were performed in open and sealed sample pans.

The DSC traces from the studies in the open pans revealed four well-defined endothermic peaks, with the first two overlapping (Figure 16).

Wendlandt [81] reported the conversion of the distorted octahedral polymer to the tetrahedral monomer at a temperature of 119^0C. This is in agreement with the results obtained.

Thus, structural assignments show that the scheme of decomposition is

$3CoCl_2 2(py)$ oct. → $3CoCl_2(py)$ tet. → $3CoCl_2(py)$ oct. →
$Co_3Cl_6 2(py)$ oct. → $3CoCl_2$ oct.

The structure of the thermal products was discussed by Gill [77].

Thus, the first peak at 121^0C can be assigned to the change-over of the violet form (octahedral) to the blue form (tetrahedral). The second peak at $160,2^0$C represents the loss of one pyridine, while the peak at $217,1^0$C is due to the formation of $Co_3Cl_6 2(py)$ from $CoCl_2(py)$. The last peak at $282,9^0$C can be assigned to the formation of $CoCl_2$ from the complex $Co_3Cl_6 2(py)$. The calculated values of enthalpy of formation are summarised in Table 19.

Figure 16. The DSC trace of $CoCl_2 2(py)$ in open sample pans.

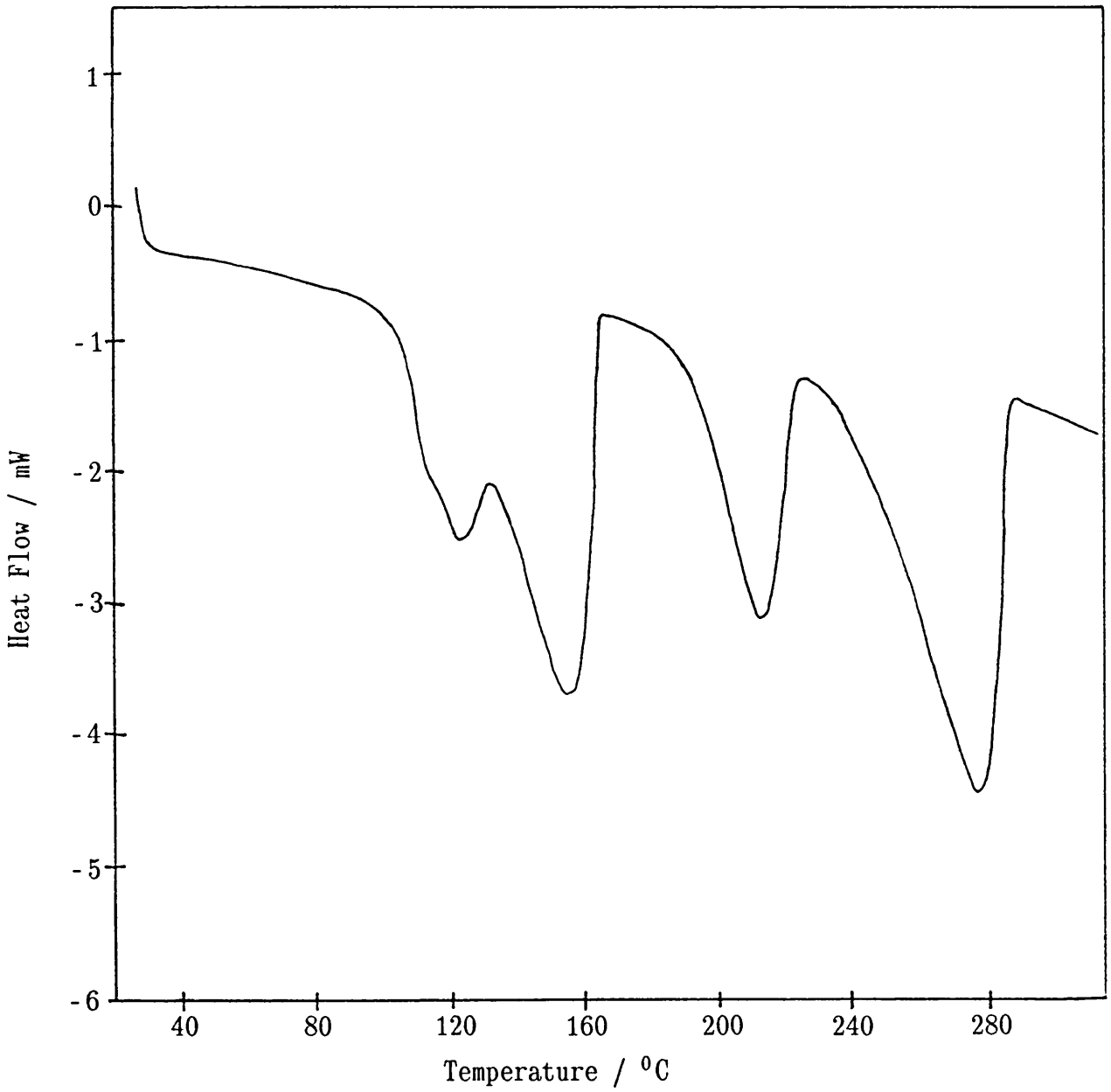

Table 19. The thermal transitions for $CoCl_2 2(py)$.

Sample pans	Reaction	$^*T_p$ (^0C)	ΔH (kJ mol^{-1})
open	$CoCl_2 2(py)oct. \rightarrow CoCl_2 2(py)tet. \rightarrow CoCl_2(py)oct.$	160,2	66,8
	$3CoCl_2(py)oct. \rightarrow Co_3Cl_6 2(py)oct.$	217,1	22,8
	$Co_3Cl_6 2(py)oct. \rightarrow 3CoCl_2 oct.$	282,9	55,4
sealed	$CoCl_2 2(py)oct. \rightarrow CoCl_2 2(py)tet.$	114,9	15,4
	$CoCl_2 2(py)tet. \rightarrow CoCl_2(py)oct.$	204,5	32,8

$^*T_p$ is the temperature at the peak maximum.

The DSC traces for the studies performed in the sealed pans, resulted in two well-defined peaks below 220^0C (Figure 17). The peaks above 240^0C were not reproducible, due to the high pressure built up in the sample pans when pyridine molecules were evolved.

Figure 17. The DSC trace of $CoCl_2 2(py)$ in sealed sample pans.

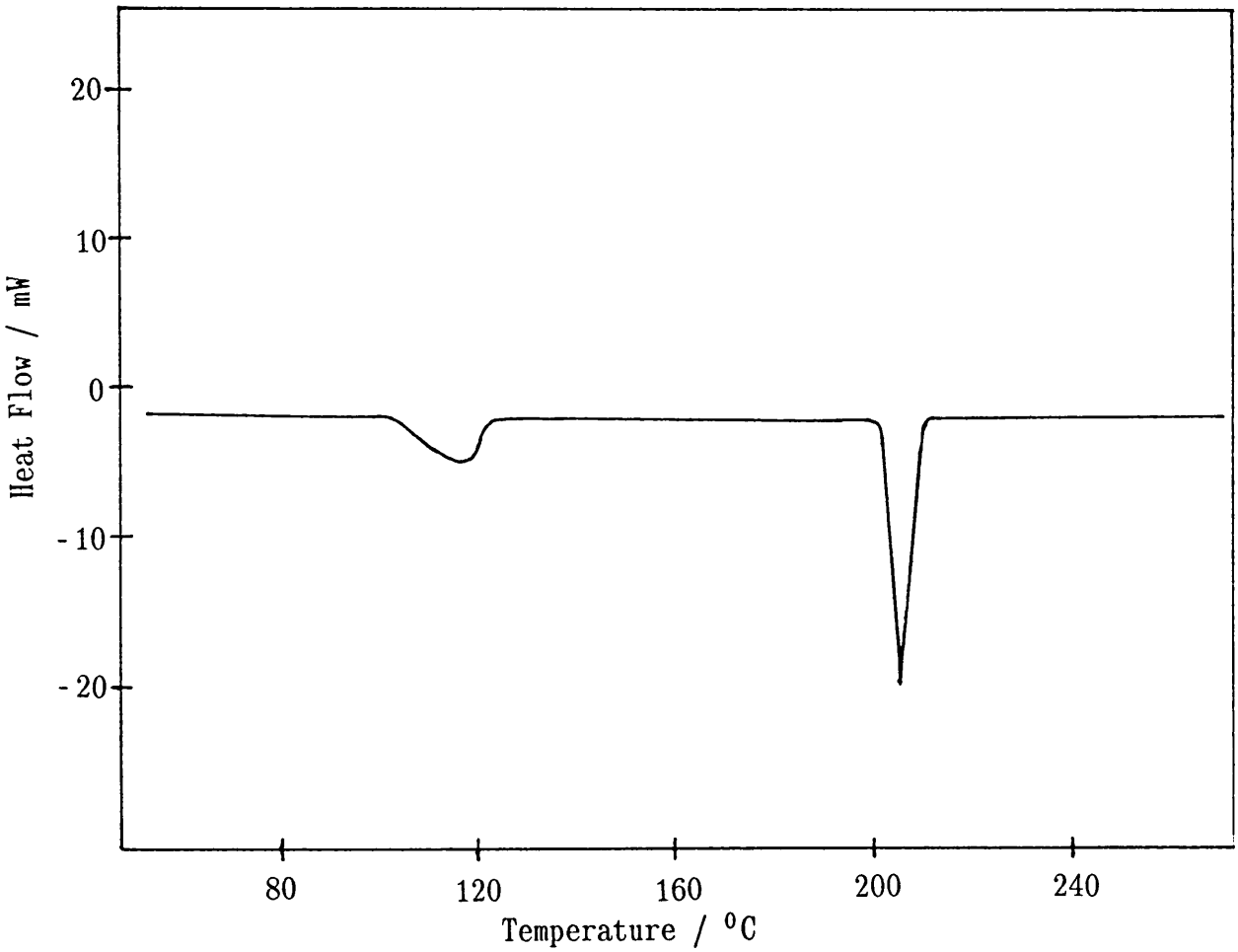

In the sealed pans, the change-over from the violet form to blue form is separated and the loss of one pyridine is observed at a higher temperature (204,5^{0}C) (Table 19). The higher temperature is due to the difficulty in breaking the Co-py bonds at high pressures. The heat of transition for the change-over from the violet to the blue form is 15,4 kJ mol^{-1}, compared with the values of 13,4 and 12,6 kJ mol^{-1} reported by Wendlant and Beech, respectively.

The total enthalpy for the change-over and the loss of one pyridine is 48,2 kJ mol^{-1}, compared with the value of 66,8 kJ mol^{-1} in the open sample pans. This suggests that the reaction is incomplete.

6.4 CONCLUSIONS

Analysis of the dynamic curve and isothermal curves is a useful method of testing the validity of different kinetic equations, especially if the same rate equations are applicable. This was studied in the decomposition of $CoCl_2$2(py). The parameters obtained from the analysis of the dynamic curve described three reactions perfectly over the whole α-range. In contrast, the parameters obtained from the isothermal studies revealed only a partial fit over the α-range.

The analysis of the dynamic curve has many advantages over the analysis of several isothermal curves. The reasons for this is that the dynamic curve represents the fractional decomposition

over a certain temperature range. The isothermal method may result in decomposition of the sample before the constant temperature is reached, which will result in less accurate E_a and ln Z values. Thus, the analysis of the dynamic curve results in a smaller error in the parameters and it is especially applicable in instances where the product of a reaction becomes the reactant in another reaction, at a higher temperature.

The blue form of $CoCl_2$2(py) is a tedrahedral momomer in solution. It is, therefore, not possible to compare the results obtained from the decomposition reaction of $CoCl_2$2(py) with the formation enthalpy of the $CoCl_2$/py system. However, valuable information regarding the Co-py bond was obtained. It was observed that with the decomposition of the solid, the last pyridine is evolved with greater ease than the first pyridine. This was also reflected in the solution chemistry, where a stronger interaction exists between the $CoCl_2$(py) and py, than between the $CoCl_2$ and py species.

CHAPTER 7

THE SOLUTION AND SOLID STATE CHEMISTRY OF BIS(QUINOLINE) COBALT(II) CHLORIDE

7.1 INTRODUCTION

The effects of metal ions and ligands on the thermal stability of some metal amine complexes have been studied extensively over the last few years [7,66,77,78,79,80,82]. Pyridine and pyridine-related ligands were studied in terms of the basic strength of the ligand and of metal-ligand bonds. In the previous chapter, the thermodynamics of the formation in non-aqueous solution and the decomposition of bis(pyridine)cobalt(II) chloride, $CoCl_2 2(py)$, were reported. It was therefore of interest to extend the study to other pyridine-related complexes, in order to gain comparative thermodynamic and kinetic data. In this chapter, bis(quinoline)cobalt(II) chloride, $CoCl_2 2(quin)$ is reported.

7.2 SOLUTION CHEMISTRY RESULTS

V. Logachev and his co-workers reported the thermodynamic quantities of $CoCl_2(quin)$ [3] and $CoCl_2 2(quin)$ [2] in different solvents. They used a method developed by Murygina, which involves the breaking of an ampoule containing the ligand into the reaction vessel, which contains $CoCl_2$ solution. Christensen

developed a more accurate method, the entropy titration method, and it was therefore of interest to study the $CoCl_2$/quin system in acetone and compare results.

The values of log β_i, ΔH^0_{0-i}, ΔG_{0-i} and ΔS^0_{0-i} for the stepwise formation of the complexes are given in Table 20.

Table 20. The thermodynamic quantities for the $CoCl_2$/quin system in acetone.

Thermodynamic quantities	$CoCl_2$ concentration	
	0,0100 mol dm^{-3}	0,00502 mol dm^{-3}
log β_1	4,255	4,316
log β_2	8,570	8,838
ΔG_{0-1} (kJ mol^{-1})	-24,3	-24,6
ΔG_{0-2} (kJ mol^{-1})	-48,9	-50,4
ΔH^0_{0-1} (kJ mol^{-1})	-30,2	-22,6
ΔH^0_{0-2} (kJ mol^{-1})	-41,5	-36,1
ΔS^0_{0-1} (J $mol^{-1}K^{-1}$)	-19,9	+6,78
ΔS^0_{0-2} (J $mol^{-1}K^{-1}$)	+24,8	+48,0

The ΔH^0_{0-i} values refer to the overall enthalpy of formation of the complex in the solution, i.e.

ΔH^0_{0-1}(298,15K) refers to the reaction

$CoCl_2$(solv.) + quin (solv.) ⇌ $CoCl_2$(quin) + solv.

and ΔH^0_{0-2} (298,15K) refers to the reaction

$CoCl_2$(solv.) + 2(quin) (solv.) ⇌ $CoCl_2$2(quin) + solv.

The formation of $CoCl_2$(quin) and $CoCl_2$2(quin) is enthalpy driven, but in addition to this also entropy driven at the lower $CoCl_2$ concentration. The enthalpy of formation for the reaction

$CoCl_2$(quin) + quin(solv.) ⇌ $CoCl_2$2(quin) + solv.

was calculated at -11,3 kJ mol^{-1} and -13,5 kJ mol^{-1} for the 0,0100 mol dm^{-3} and 0,00502 mol dm^{-3} $CoCl_2$ solutions, respectively. Therefore, a stronger interaction exists between $CoCl_2$ and quinoline than between $CoCl_2$(quin) and quinoline. A decrease in concentration of the $CoCl_2$ solutions resulted in a decrease in the exothermic enthalpy value. A slightly improved fit was obtained if the metal concentration was 0,0050 mol dm^{-3}. However, it was not possible to decrease the $CoCl_2$ concentration further, since the experiments became less reproducible, causing a large error in the results.

A decrease in the $CoCl_2$ solutions resulted in an increase in the log β_1 and log β_2 values. The increase in log β_1 and log β_2 values was therefore also reflected in the distribution diagrams (Figures 18 and 19), which indicates a very low maximum (32%) for

Figure 18. The distribution diagram of 0,0100 mol dm^{-3} $CoCl_2$ solution with 1,00 mol dm^{-3} quinoline in acetone.

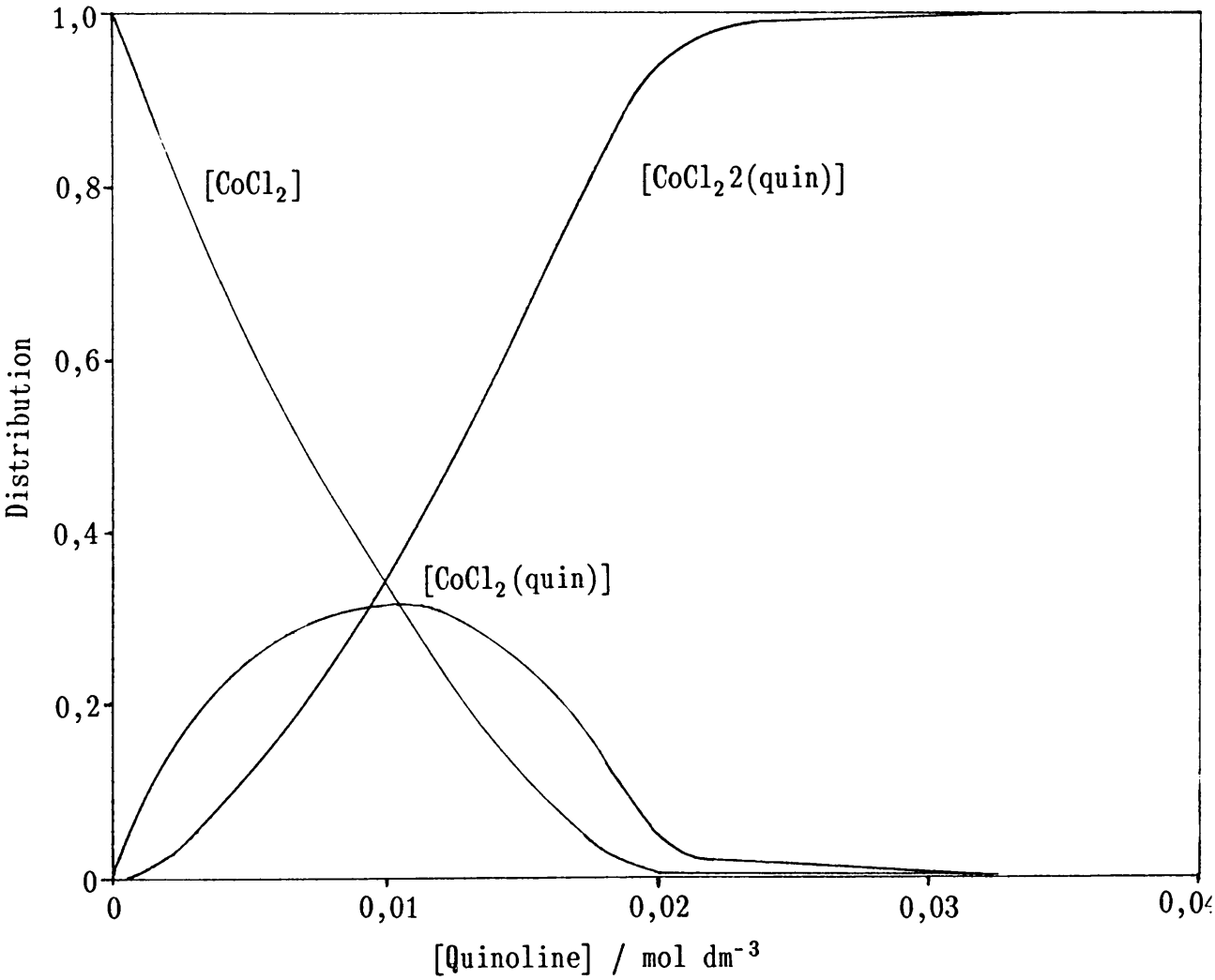

Figure 19. The distribution diagram of 0,00502 mol dm^{-3} $CoCl_2$ solution with 1,00 mol dm^{-3} quinoline in acetone.

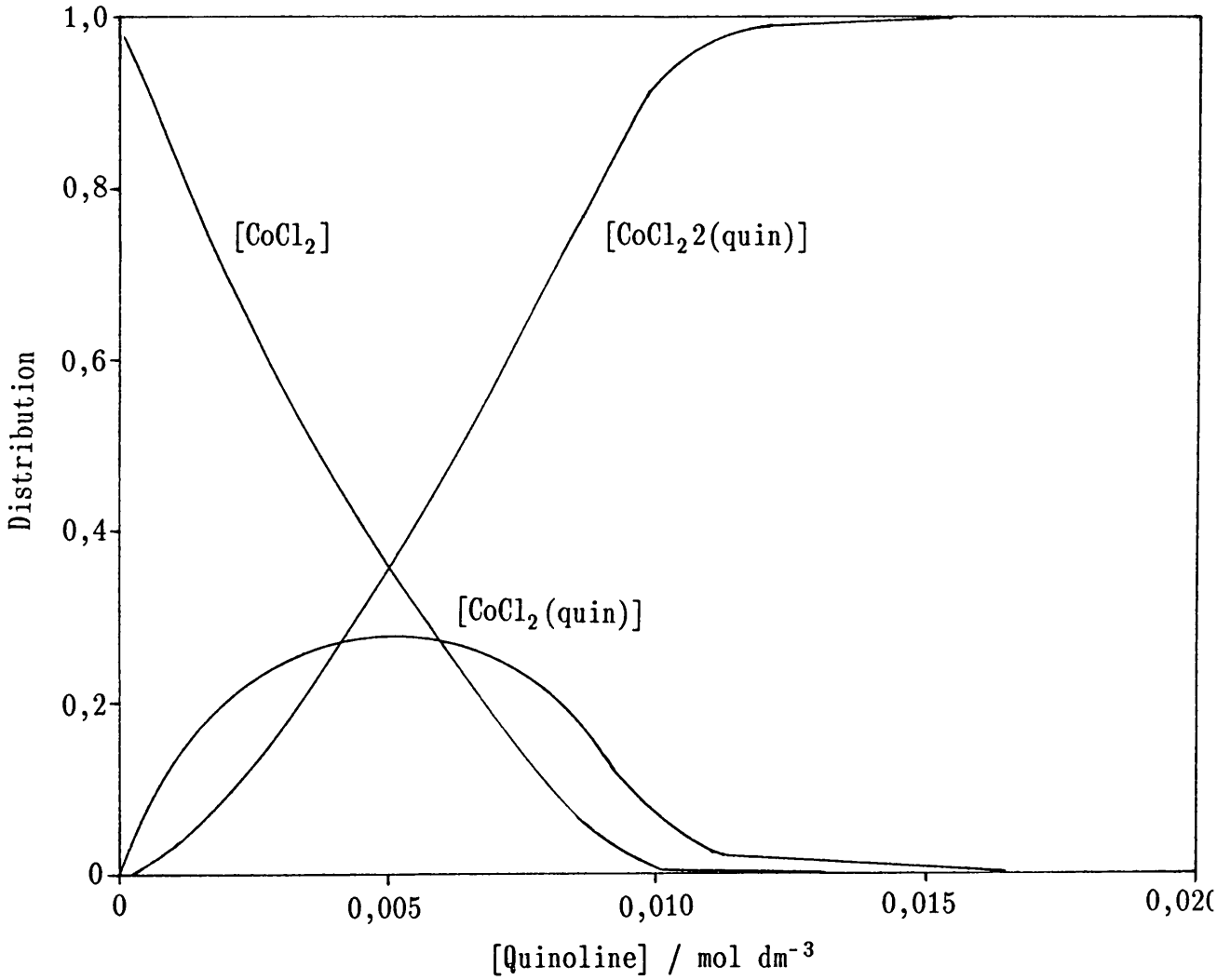

the formation of $CoCl_2$(quin) if the concentration of $CoCl_2$ was 0,0100 mol dm^{-3} and even lower if the concentration was 0,00502 mol dm^{-3} (29%).

7.3 SOLID STATE CHEMISTRY RESULTS

7.3.1 Thermogravimetric results

Figure 20 represents the TG trace obtained for the powder and the single crystals of $CoCl_2$2(quin). The $CoCl_2$2(quin) powder revealed a more rapid decomposition process and a difference in mass loss.

The complex $CoCl_2$2(quin) decomposes over the temperature range 170^{0}C to 340^{0}C, according to the following dissociation reactions:

$$CoCl_2\,2(quin)\ (s) \rightarrow CoCl_2(quin)\ (s) + quin\ (g) \qquad (1)$$

$$CoCl_2(quin)\ (s) \rightarrow CoCl_2\ (s) + quin\ (g) \qquad (2)$$

The decomposition temperatures of the powder are well in agreement with the values observed by D. Brown [82]. Also, an excellent comparison between the experimental and theoretical mass losses was obtained.

Figure 20. The TG trace of $CoCl_2 2(quin)$, where the broken line represents the crystals and the solid line the powder. Heating rate = $5^0C\ min^{-1}$.

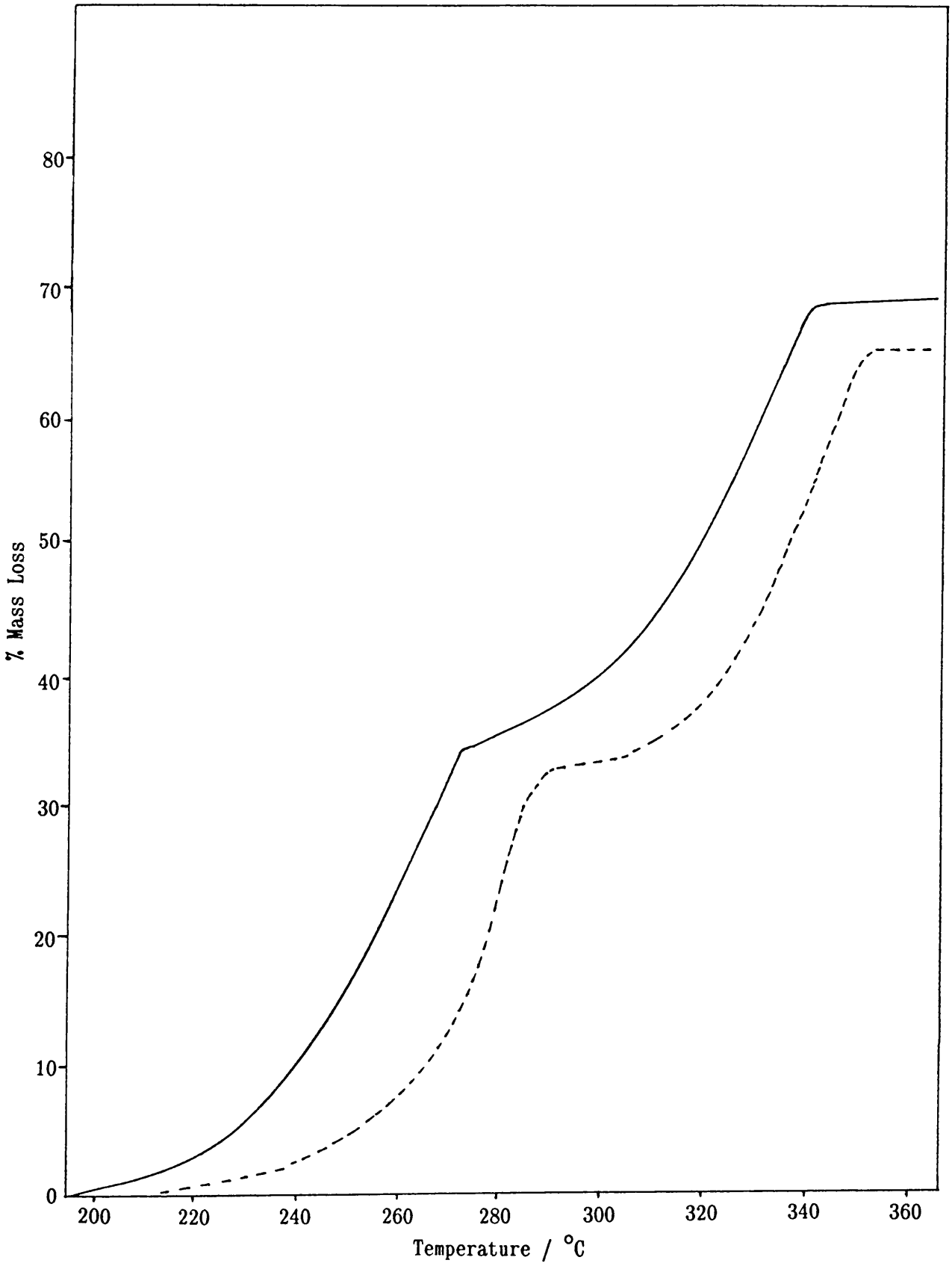

7.3.2 DSC results

The DSC studies were performed in both sealed and open sample pans.

The DSC traces from the studies performed in the open sample pans revealed two endothermic peaks (Figure 21). Since the two peaks are not well-defined, the peaks were integrated together. This resulted in an average enthalpy value for reaction (1) and (2) of 214 kJ mol^{-1}.

The average enthalpy value is less than the sum of the values obtained from the integration of the DTA curve. Values of ±105 kJ mol^{-1} and ±115 kJ mol^{-1} were estimated for the two reactions, respectively. However, the values obtained from the DSC analysis can be taken as the correct values, since it is a more accurate method of determination.

A small shoulder is observed on the first peak. This is not the result of a phase-change, since the electron microscopy studies revealed no phase-change. This may be due to an additional reverse equilibrium, existing between $CoCl_2$2(quin) and $CoCl_2$(quin).

Figure 21. The DSC trace of $CoCl_2$2(quin) in open sample pans.

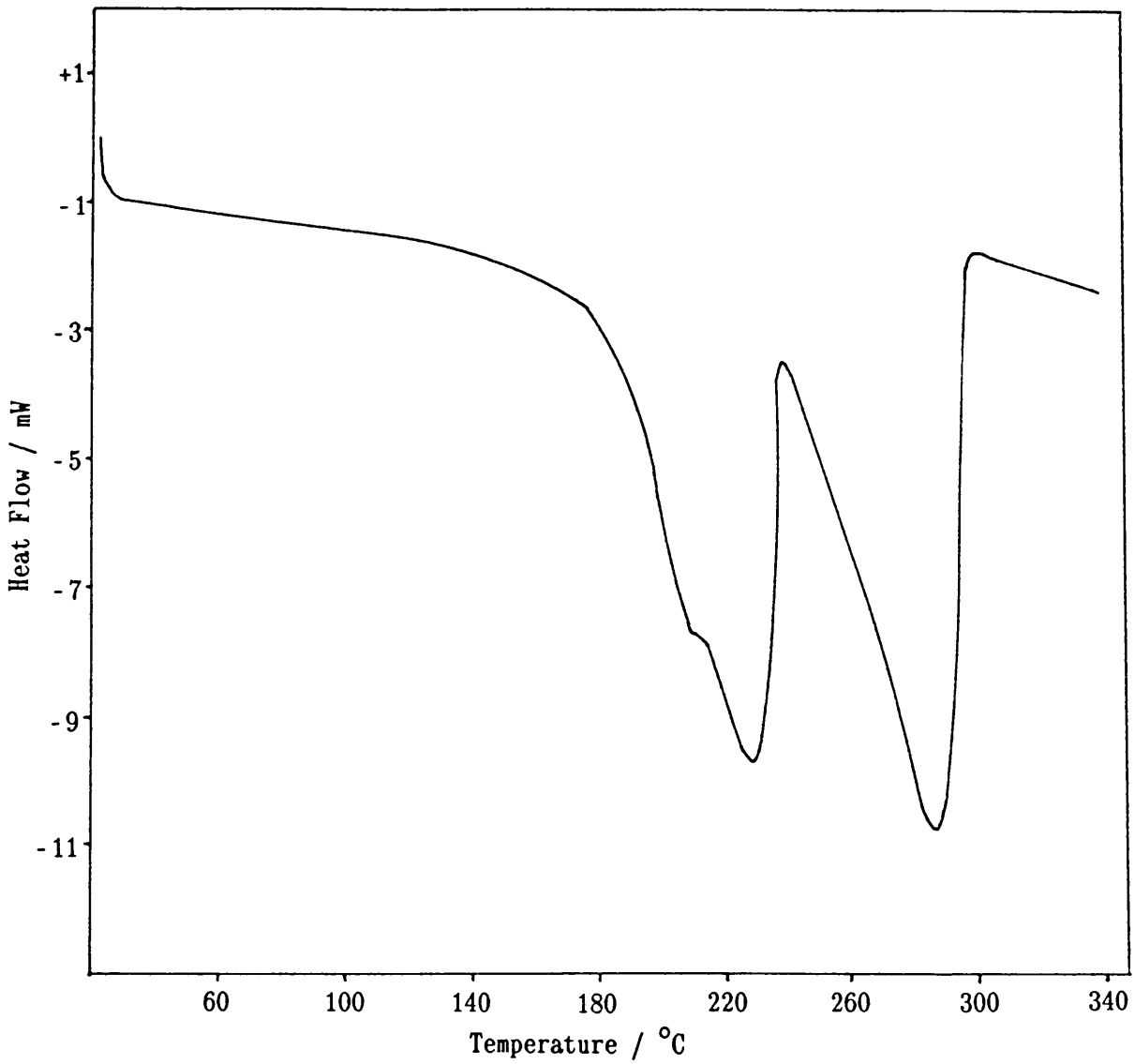

The DSC traces from the studies performed in the sealed pans revealed a well-defined endothermic peak below 270^0C (Figure 22). The peaks above 270^0C were not reproducible, due to the high pressure build up and eventual perturbing of the pans.

The sharp endothermic peak at $256,4^0$C may be assigned [82] to the following reaction:

$CoCl_2 2(quin)$ tet. → $CoCl_2(quin)$ tet. + quin

The average enthalpy value was calculated to be 53,1 kJ mol^{-1}. The increase in temperature is due to the high pressure build up from the evolution of quinoline molecules which, possibly, favours the reverse reaction. Thus, the $CoCl_2 2(quin)$ changes from a monomeric tetrahedral form to a dimeric or polymeric tetrahedral form, $CoCl_2(quin)$ [82]. The enthalpy value for this reaction is low when compared with the values reported previously.

Figure 22. The DSC trace of $CoCl_2 2(quin)$ in sealed sample pans.

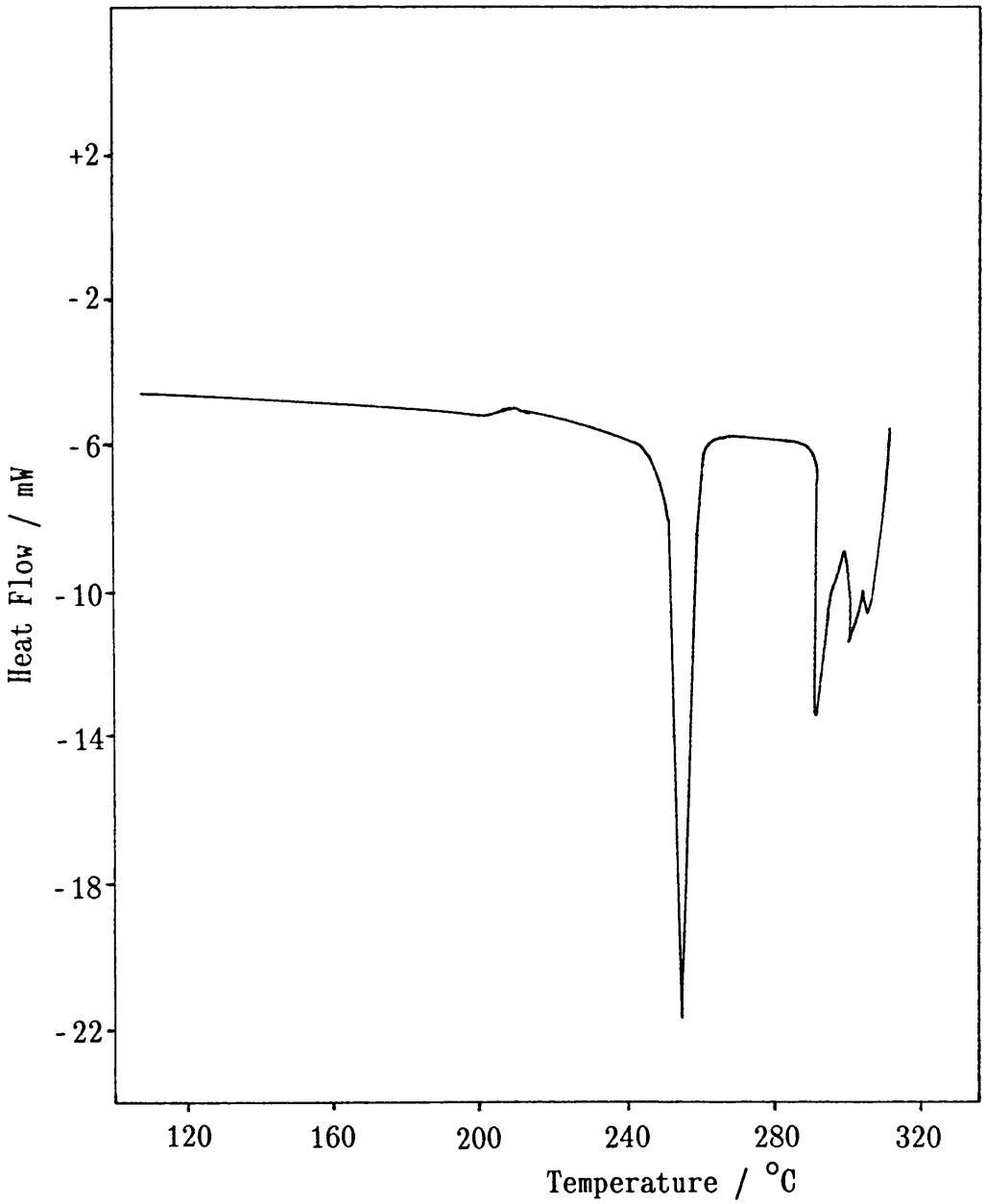

7.3.3 Electron microscopy results

According to G. Beech [7] the thermal decomposition of $CoCl_2 2(quin)$ is accompanied by the dissolution of the products in the liberated quinoline. Thus the scheme of decomposition involves the following steps:

$CoCl_2 2(quin)$ (cryst.) → $CoCl_2(quin)$ (soln. in quin)
$CoCl_2(quin)$ (soln. in quin) → $CoCl_2$ (cryst.) + 2(quin) (g)

This led to an electron microscopy study of the initial decomposition reaction. Micrographs during the initial stages of the decomposition reaction as well as of the final decomposition products were taken.

Micrograph 10 represents the crystals of $CoCl_2 2(quin)$ before decomposition. Interstitials are visible on the surface (magnification x80). The surface of the crystals before decomposition shows possible points of imperfection and thus active points (Micrograph 11). A 1% decomposition of $CoCl_2 2(quin)$ to $CoCl_2(quin)$ results in decomposition on the surface in certain areas of the crystals (Micrograph 12). The decomposed areas seem to have a porous structure. It seems, however, that no dissolution of the products and the reactant has occured.

Crystals of $CoCl_2 2(quin)$ completely decomposed to $CoCl_2(quin)$, reveal cracks in all the crystals, at a small magnification (x95) (Micrograph 14), while a larger magnification (x2500) shows the

Micrograph 10. The single crystals of $CoCl_2$2quin before decomposition. (Magnification x80).

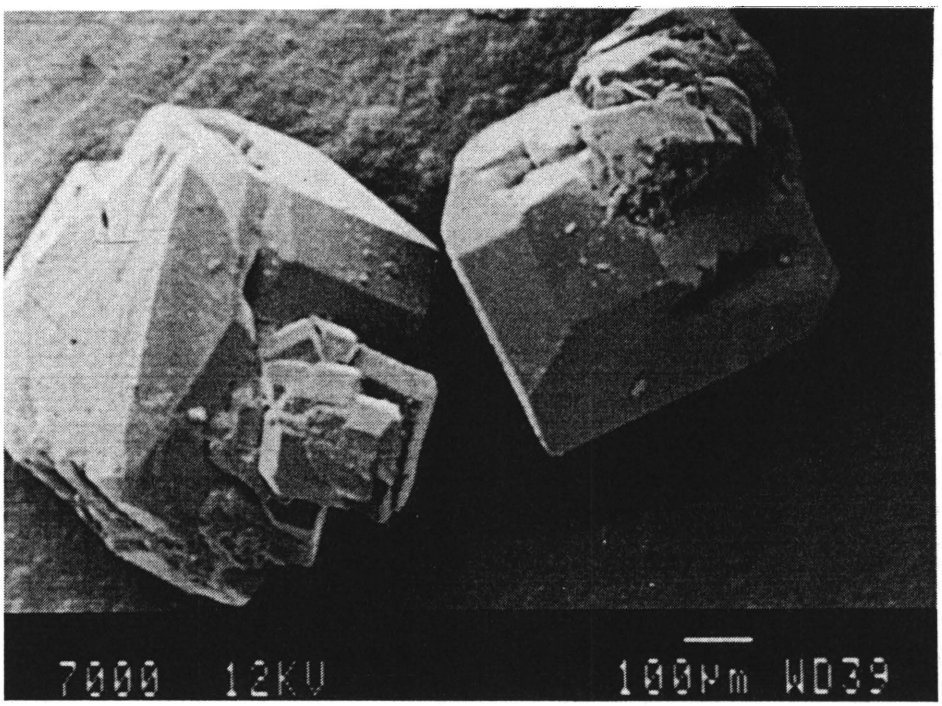

Micrograph 11. The surface of the $CoCl_2$2quin crystals before decomposition. (Magnification x1500).

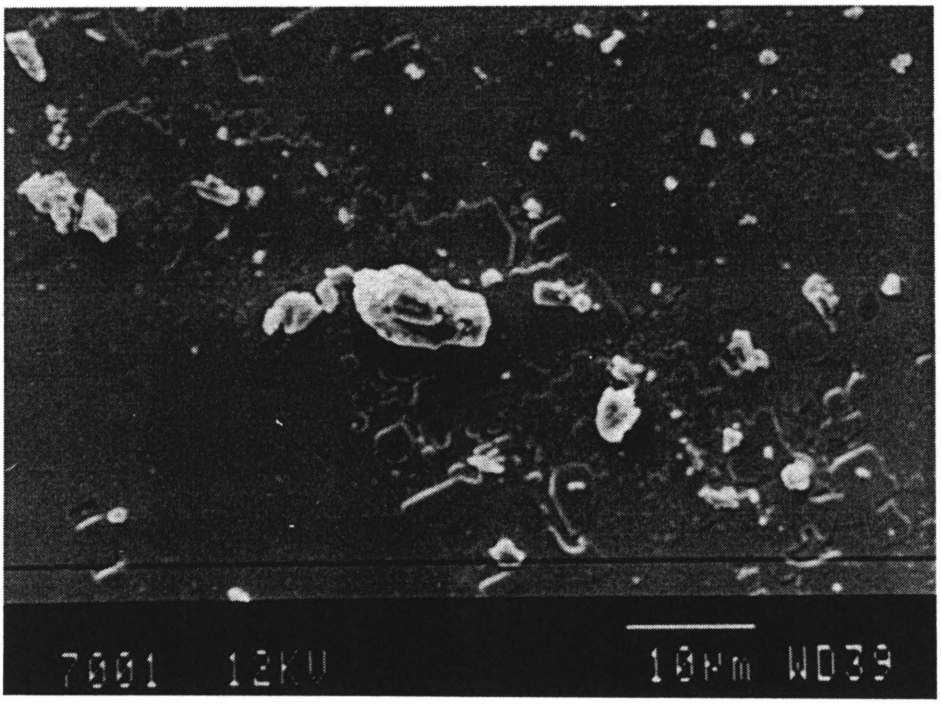

Micrograph 12. The initial decomposition (1%) of $CoCl_2$2quin to $CoCl_2$quin. (Magnification x5000).

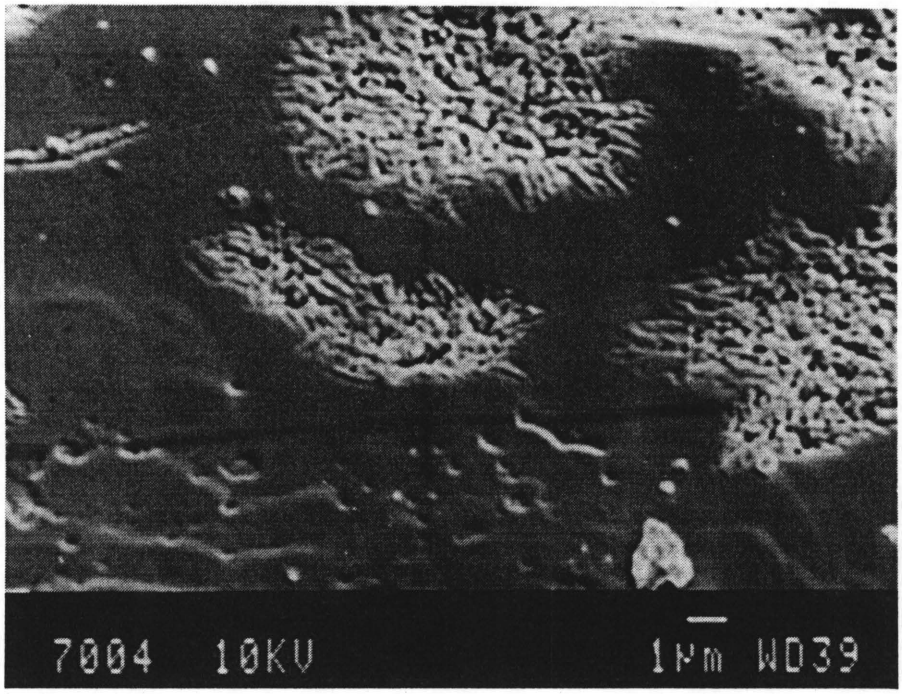

Micrograph 13. The final decomposition (32%) of $CoCl_2$2quin to $CoCl_2$quin. (Magnification x2500).

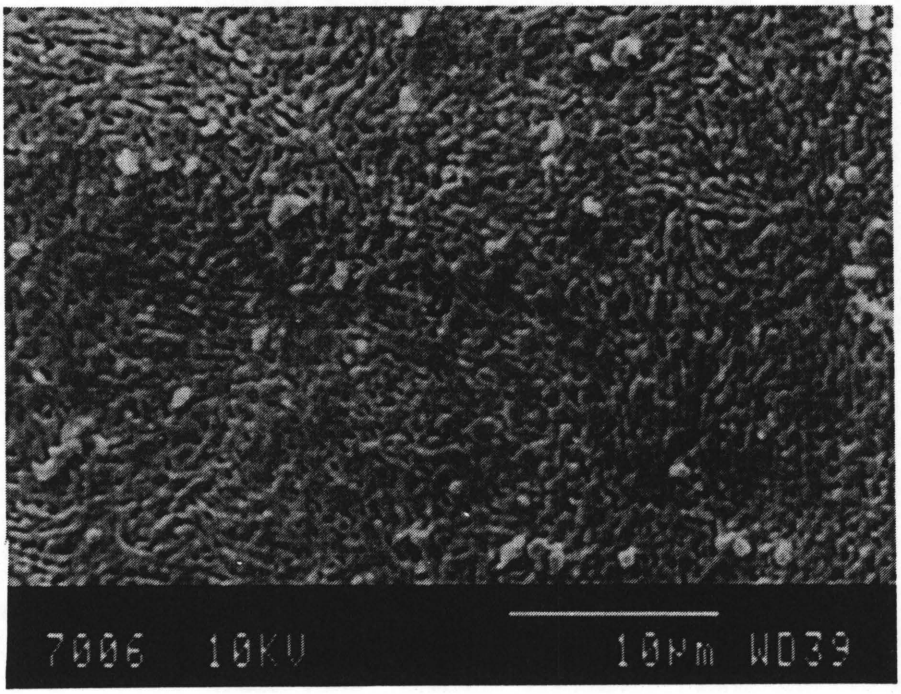

Micrograph 14. The single crystals of the final decomposition intermediate, $CoCl_2$quin. (Magnification x95).

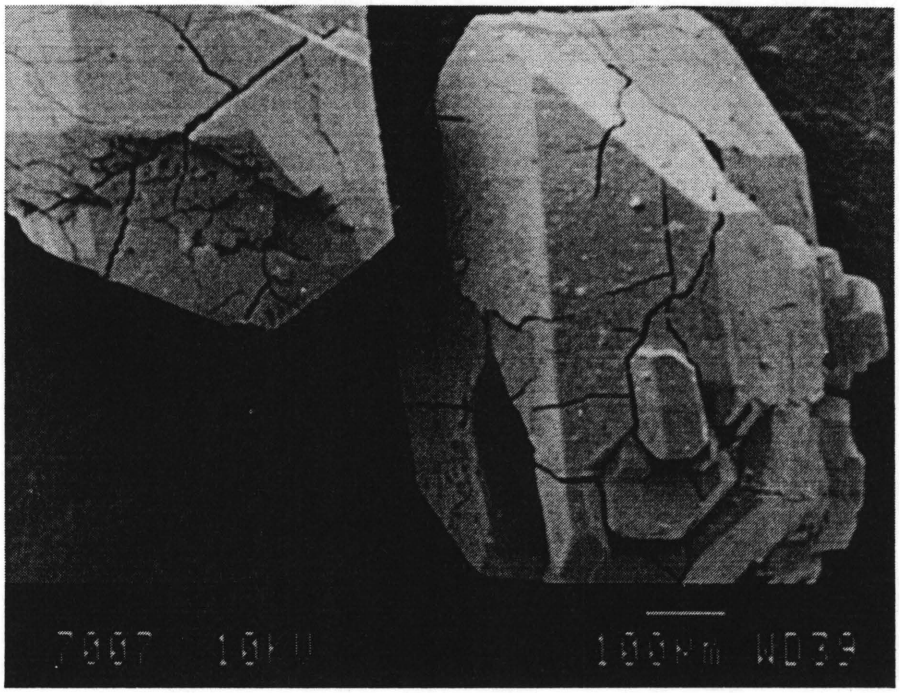

Micrograph 15. The surface of the decomposition intermediate, $CoCl_2$quin. (Magnification x5000).

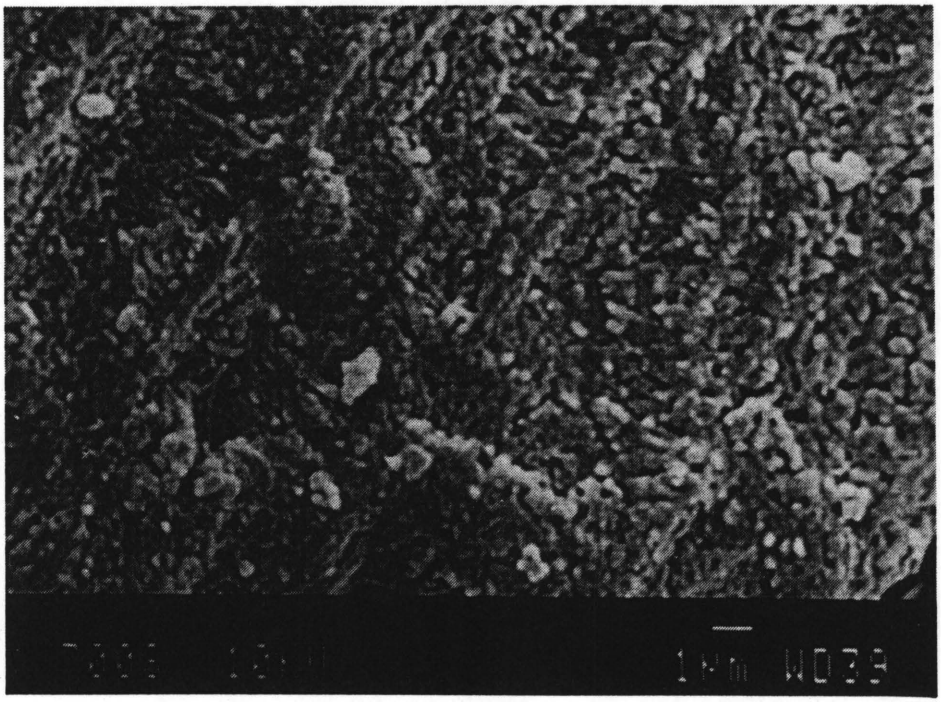

entire surface decomposed (Micrograph 15).

Micrograph 16, which shows the initial decomposition (1%) of $CoCl_2$(quin) to $CoCl_2$, reveals further decomposition on the surface.

The crystals of the final decomposition product $CoCl_2$ were completely decomposed and porous, but still intact.The surface of the decomposed intermediate was completely decomposed with the impurities still remaining on the surface. The impurities are therefore not active nuclei (Micrograph 17).

Thus, the decomposition on the surface of the crystals seems to be in agreement with the contracting area model, which was obtained from the kinetic analysis (see later). However, the electron microscopy studies revealed no formation of a solution during the formation of $CoCl_2$(quin). The crystals remained crystalline and intact throughout the entire decomposition reaction.

Micrograph 16. The initial decomposition (1%) of $CoCl_2$quin to $CoCl_2$. (Magnification x2500).

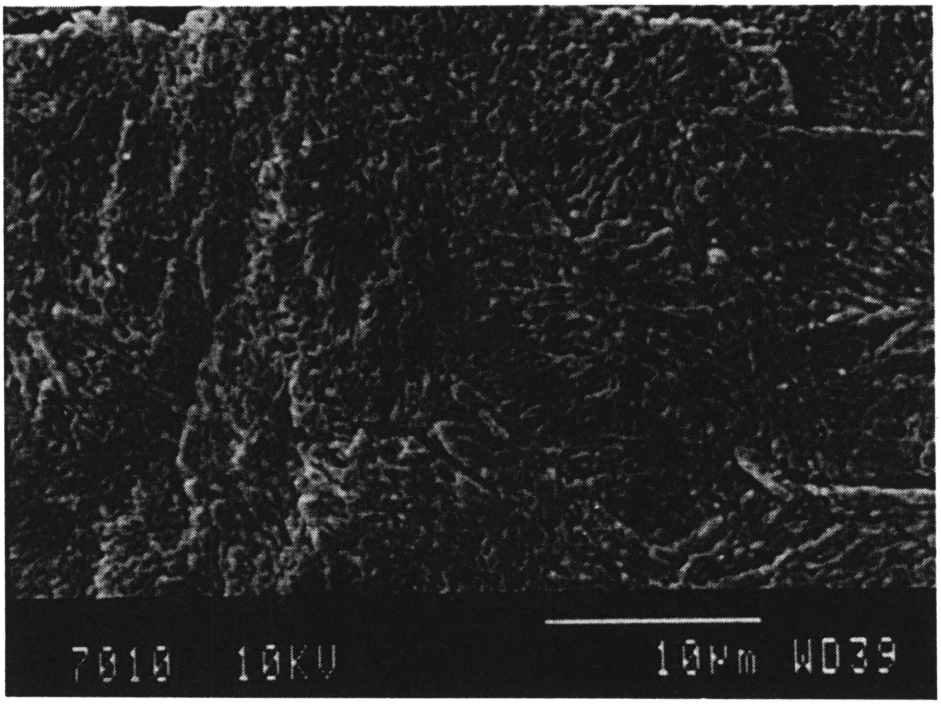

Micrograph 17. The surface of the final decomposition product, $CoCl_2$. (Magnification x2500).

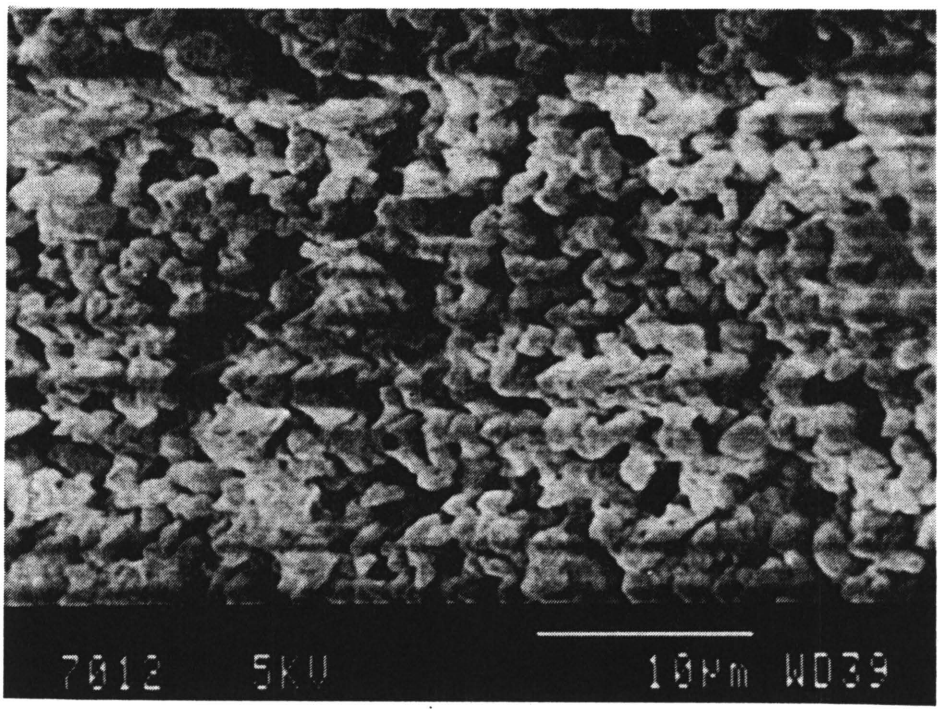

7.3.4 Dynamic kinetic analysis

Kinetic analysis was performed on the dynamic curves obtained using the powder form as well as those obtained using the single crystals of $CoCl_2$2(quin).

The following results were obtained for the powder form. The formation of $CoCl_2$(quin) (reaction 1), is the best described by the contracting area model, $1-(1-\alpha)^{\frac{1}{2}} = kt$, where E_a = 135,00 kJ mol^{-1} and ln (Z/min) = 31,21. The formation of $CoCl_2$ (reaction 2) also conforms to the contracting area model, with E_a = 192,00 kJ mol^{-1} and ln (Z/min) = 40,52. The simulated curve shows an excellent fit over the entire α-range (Figure 23).

The kinetic analysis of the single crystals gave results which fitted the contracting area model for both reactions. E_a values of 127,00 kJ $mol^{-1}$and 191,00 kJ mol^{-1} were obtained for reactions (1) and (2), respectively and the ln Z values for reactions (1) and (2) were 28,56 and 39,38, respectively. A slight decrease in the ln Z values is observed if the parameters are compared with the parameters obtained from the powder form. This is in agreement with the shift to the right observed in the dynamic curve for the single crystals. An excellent fit was obtained over the whole α-range if the parameters were used to simulate a dynamic curve.

Figure 23. The simulated dynamic curve (---), obtained from the kinetic studies performed on the dynamic curve, and the experimental curve (—).

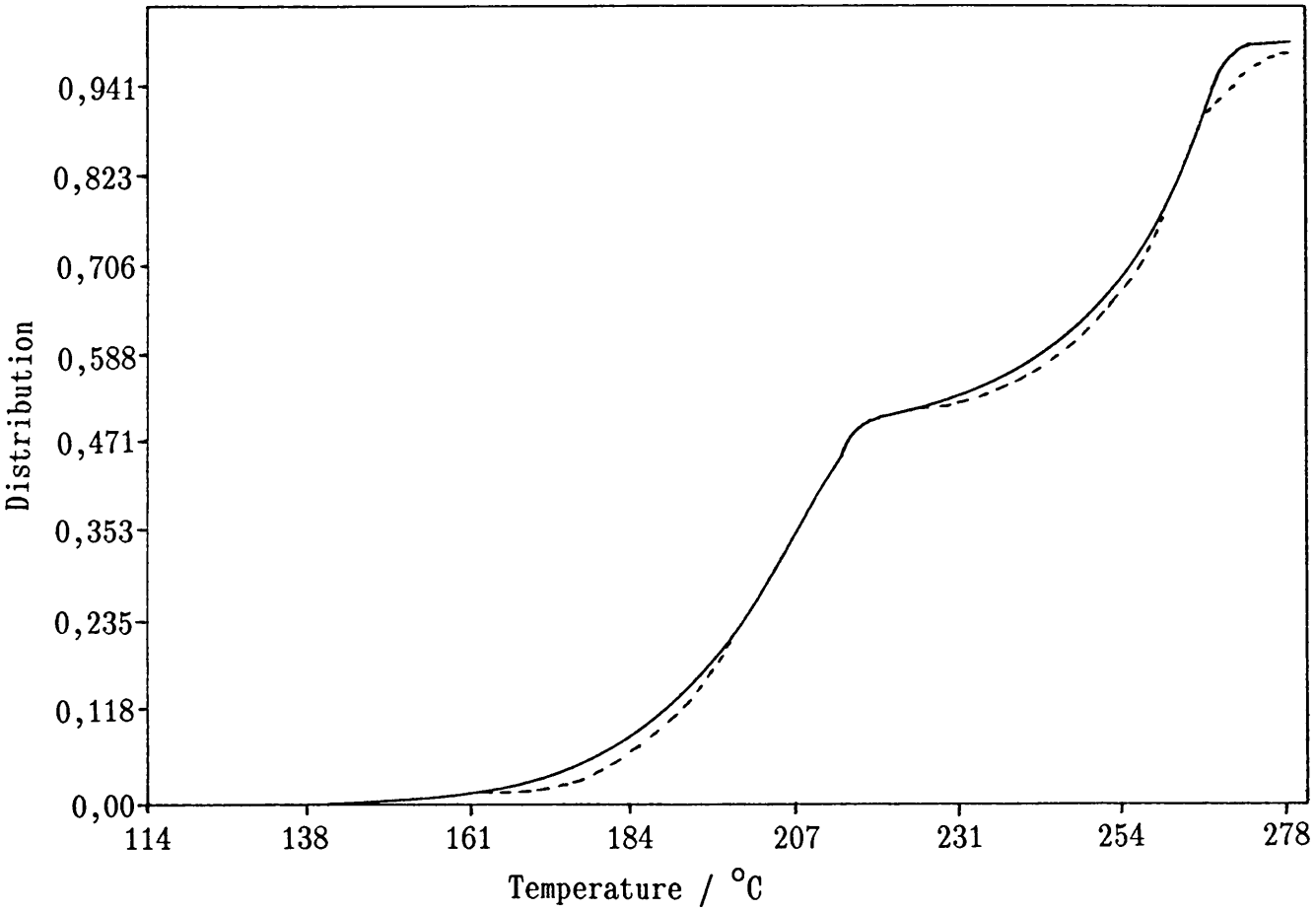

7.3.5 Isothermal results

The temperature range 167^{0}C to 182^{0}C, represents the loss of one quinoline (reaction 1). This reaction mechanism conforms to the contracting area model over the temperature range $0 < \alpha < 0,90$ with E_a = 107,7 kJ mol^{-1} and ln Z = 23,69. Reaction (2), the loss of the second quinoline, was studied in the temperature range 239^{0}C to 248^{0}C. This reaction again conforms to the contracting area model for $0,15 < \alpha < 0,88$ with E_a = 69,3 kJ mol^{-1} and ln Z = 11,92. These parameters were used to simulate a dynamic curve which was compared with the experimental curve (Figure 24). The results obtained from the kinetic analysis of the TG curve differ very much from these values (isothermal), especially for reaction (2).

Figure 24. The simulated dynamic curve (---), obtained from the isothermal results, and the experimental curve (—).

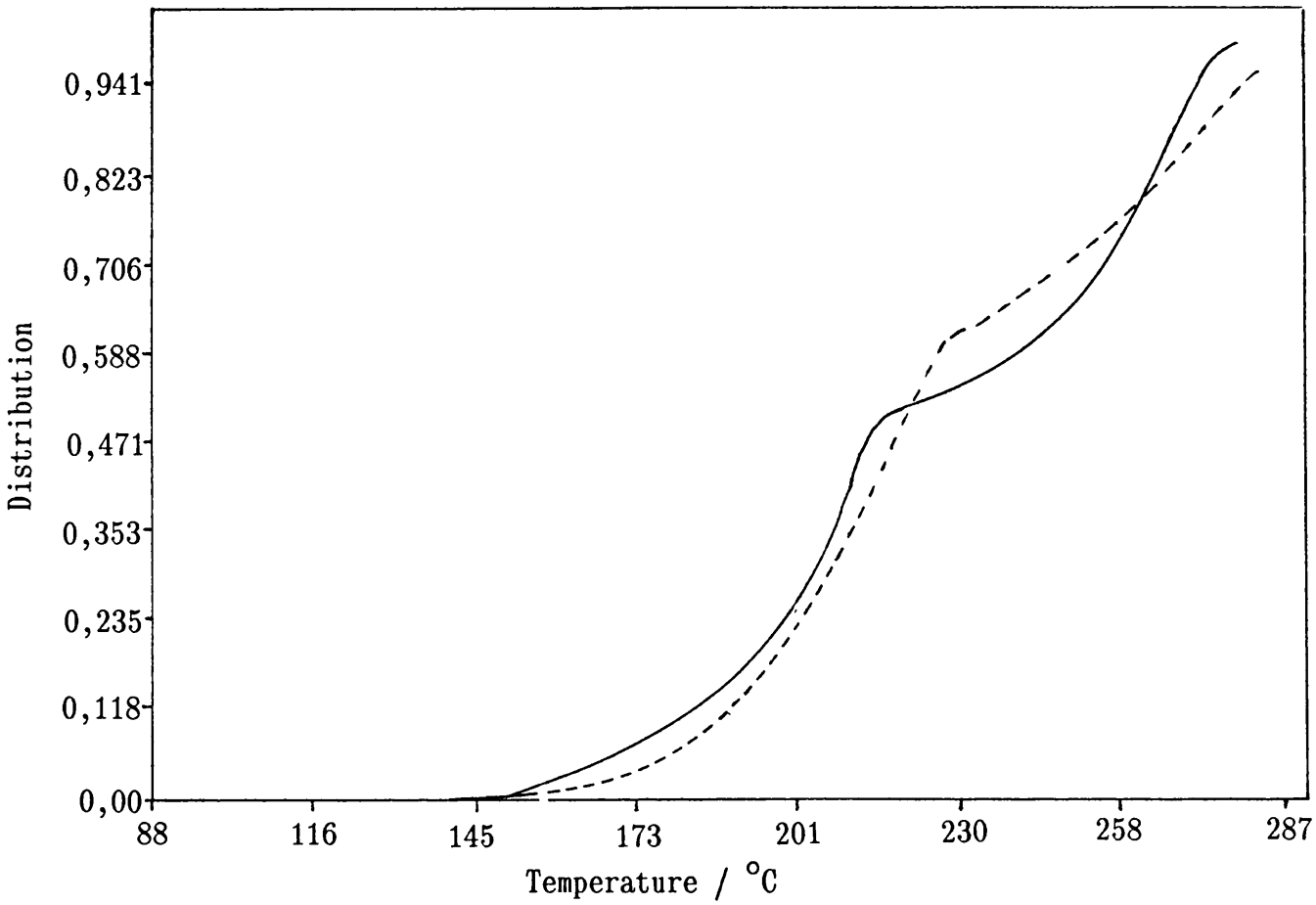

If the kinetic calculations on $CoCl_2 2(py)$ were performed on a preselected α-range, a distinct increase in the fit with the experimental TG curve was observed. Thus, since the rate equations were not applicable over the whole α-range, it was decided to repeat the kinetic calculations for reaction (1) over the α-range 0,20 to 0,80 and for reaction (2) over the α-range 0,20 to 0,87. For the last range, a fit with the experimental TG curve was expected up to approximately 1,00, but this was obtained only up to 0,87. This discrepancy could be due to the different flattenings of the curves obtained at different temperatures. These results, again, fitted the contracting area model when describing reaction (1), with E_a = 111,65 kJ mol^{-1} and ln Z = 24,66 ln min^{-1}, as well as reaction (2), with E_a = 74,37 kJ mol^{-1} and ln Z = 12,41. In contrast to the results for $CoCl_2 2(py)$, an even less accurate fit (Figure 25), than the fit obtained from the parameters over the whole α-range was found (Figure 24). In addition, it was found that reaction (2) is also described by the linear rate law, $\alpha = kt$, with E_a = 76,33 kJ mol^{-1} and ln Z = 13,71. A slightly better fit than that found in Figure 25 was obtained (Figure 26).

Figure 25. The simulated dynamic curve (---),obtained from the isothermal results over the preselected α-range, and the experimental curve (—). Reaction (2) conforms to the contracting area model.

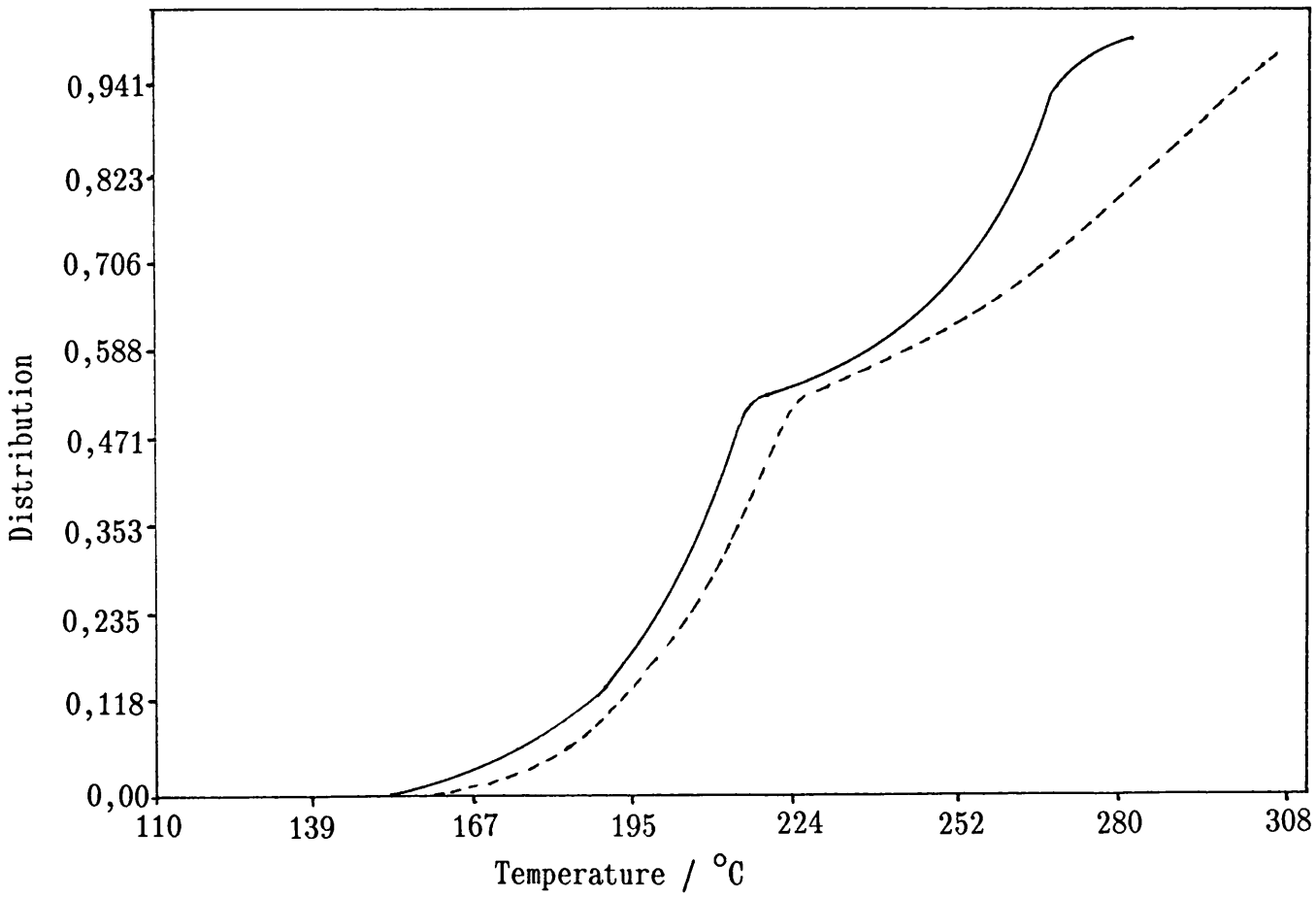

Figure 26. The simulated dynamic curve (---),obtained from the isothermal results over the preselected α-range, and the experimental curve (—). Reaction (2) conforms to the linear rate law.

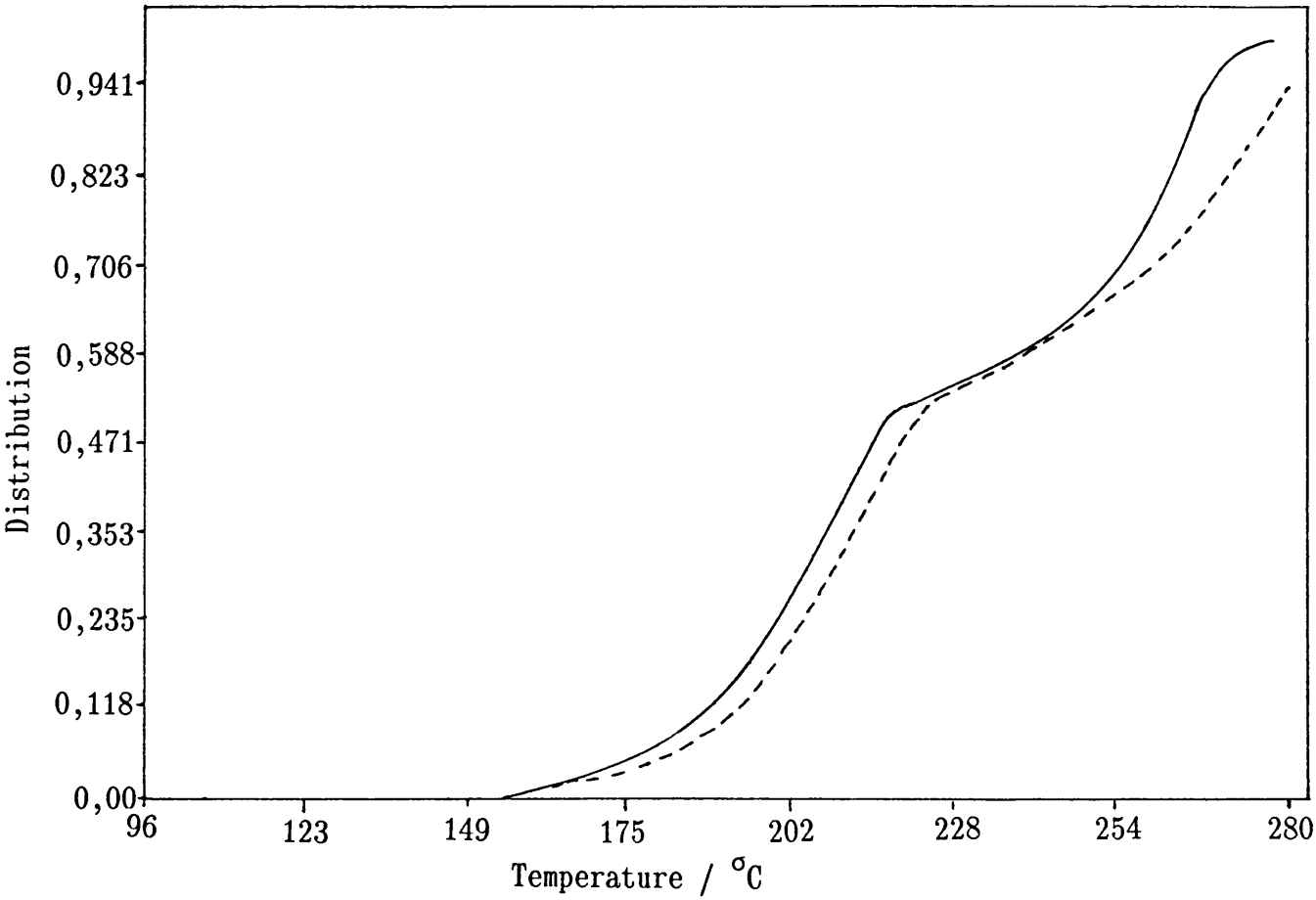

The kinetic analysis performed on the isothermal studies, obtained from the larger crystals, showed that both reactions can be described by the contracting area model.

7.4 CONCLUSIONS

It can be concluded from the preceding results that the kinetic values obtained from the dynamic curve describe the experimental TG curve better than the isothermal parameters. The thermodynamic studies performed on $CoCl_2 2(py)$ also showed a better fit with the parameters obtained from the analysis of the dynamic TG curve.

The DSC studies revealed that the liberation of both quinolines occurs as an overlapping process. Thus, the dynamic curve may represent two reactions which occur simultaneously. In contrast, the isothermal reactions represent a single process. This may be a reason for the different results obtained using the two methods. However, the results obtained from the isothermal studies are more significant.

Studies in solution showed that there is a stronger interaction between $CoCl_2$ and quinoline than between $CoCl_2(quin)$ and quinoline. The kinetic analysis of the dynamic curve revealed a stronger interaction between $CoCl_2$ and quinoline than between $CoCl_2(quin)$ and quinoline. In contrast, the isothermal studies revealed a stronger interaction between $CoCl_2(quin)$ and quinoline than between $CoCl_2$ and quinoline. This difference in the results obtained by the two methods may be attributed to the occurence of

overlapping processes.

Thus, studies in solution of the complex-formation reaction and in the solid state of the decomposition reaction of $CoCl_2 2(quin)$ may result in valuable information with respect to the cobalt-quinoline bonds.

CHAPTER 8

THE SOLID STATE AND SOLUTION CHEMISTRY OF $CoCl_2$2(α-pic)

8.1 INTRODUCTION

Several complexes of CoX_2 (X = Cl, Br, I and NCS) with two or four pyridine-related molecules have been prepared. In Chapter 6 it was stated that $CoCl_2$2(py) exists as an octahedral complex. It is known that the replacement of pyridine by 2-methylpyridine (α-picoline) results in the formation of a tetrahedral complex, presumably due to the steric interference of the methyl group [83]. Allan [78] suggested that the presence of a substituent α to the nitrogen atom results in the formation of complexes which contain fewer molecules of base (ligand) for each metal atom.

An extended, intensive study on the mixed picolinecobalt(II) chloride complexes was undertaken. The effect of the methyl substituent on the metal-donor-N bond as well as on the thermodynamic quantities was investigated. This chapter deals mainly with the complexes of cobalt(II) chloride with α-picoline.

8.2 SOLID STATE CHEMISTRY RESULTS

8.2.1 Dynamic results

The thermal decomposition of the blue complex, $CoCl_2$2(α-pic)

reflects two successive and deceleratory processes (Figure 27).

The complex, $CoCl_2 2(\alpha\text{-pic})$, decomposes over the temperature range 108^0C to 222^0C according to the following dissociation reactions:

$$CoCl_2 2(\alpha\text{-pic})\ (s) \rightarrow CoCl_2(\alpha\text{-pic})\ (s) + (\alpha\text{-pic})\ (g) \qquad (1)$$

$$CoCl_2(\alpha\text{-pic})\ (s) \rightarrow CoCl_2\ (s) + (\alpha\text{-pic})\ (g) \qquad (2)$$

The ligand, α-picoline, is evolved as gaseous molecules. Reactions (1) and (2) correspond to the calculated mass losses of 29,5% and 58,9%, respectively. The experimental decomposition temperatures, obtained from the dynamic TG curve recorded at $2^0C\ min^{-1}$, are summarised in Table 21. This is in excellent agreement with the temperatures recorded previously.

Table 21. Thermal decomposition products and corresponding decomposition temperatures.

Reaction	Resulting compound	Decomposition temperatures	
		Observed	Reported
1	$CoCl_2(\alpha\text{-pic})$	169^0C	160^0C [80]
2	$CoCl_2$	220^0C	220^0C [78]

Figure 27. The TG (solid line) and DTA (broken line) traces recorded for $CoCl_2 2(\alpha\text{-pic})$ at $2^0C\ min^{-1}$.

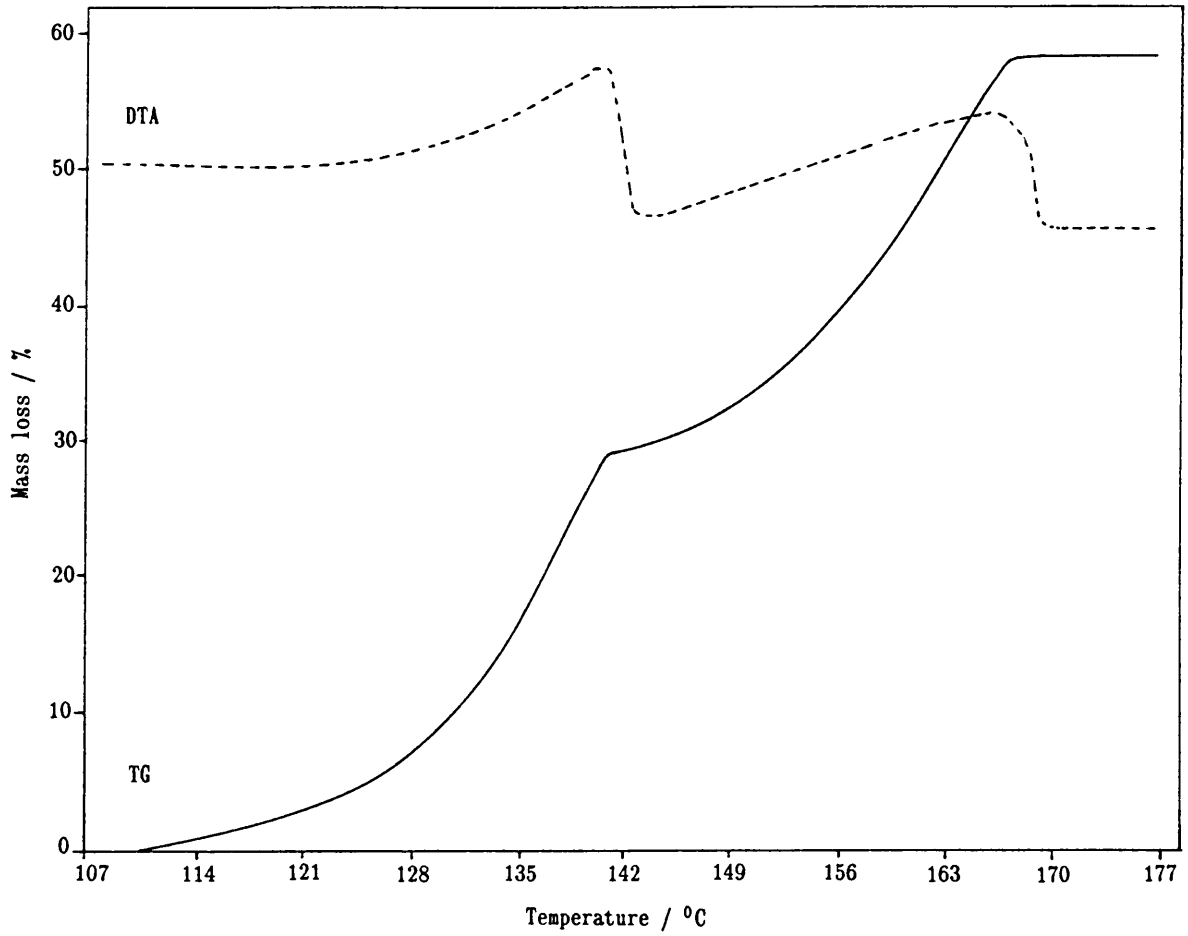

Kinetic analysis was performed on the dynamic TG curve recorded at $2^0C\ min^{-1}$. Reaction (1) conforms to the contracting area model, with E_a = 116,00 kJ mol^{-1} and ln Z = 29,82. The α-temperature data collected for reaction (2) were best described by the contracting area model, with E_a = 198,00 kJ mol^{-1} and ln Z = 47,39. However, a poor fit was obtained for the second part of the decomposition reactions (Figure 28). The percentage contribution of both reactions was calculated at 50%.

Reaction (2) was separated into an induction period and a dominating deceleratory period. For $\alpha < 0,18$ the Avrami-Erofeev equation, $[-\ln(1 - \alpha)]^{0.25} = kt$ applied, with the values of E_a = 100,0 kJ mol^{-1} and ln Z = 24,31. The deceleratory period, $\alpha > 0,18$, conforms to the Avrami-Erofeev equation $[-\ln(1-\alpha)]^{0.67} = kt$, with the values of E_a = 160,00 kJ mol^{-1} and ln Z = 38,33. An improved fit was obtained (Figure 29).

The percentage contribution for both reactions was 50%, with the second reaction comprising the initial period of 9% and a deceleratory period of 41%. Thus, the kinetic analysis of the dynamic curve gave rise to the separation of the induction period and the deceleratory period, which resulted in an improved fit.

Figure 28. Plots of the simulated dynamic curve (---), obtained from the dynamic studies, and the experimental dynamic curve (—).

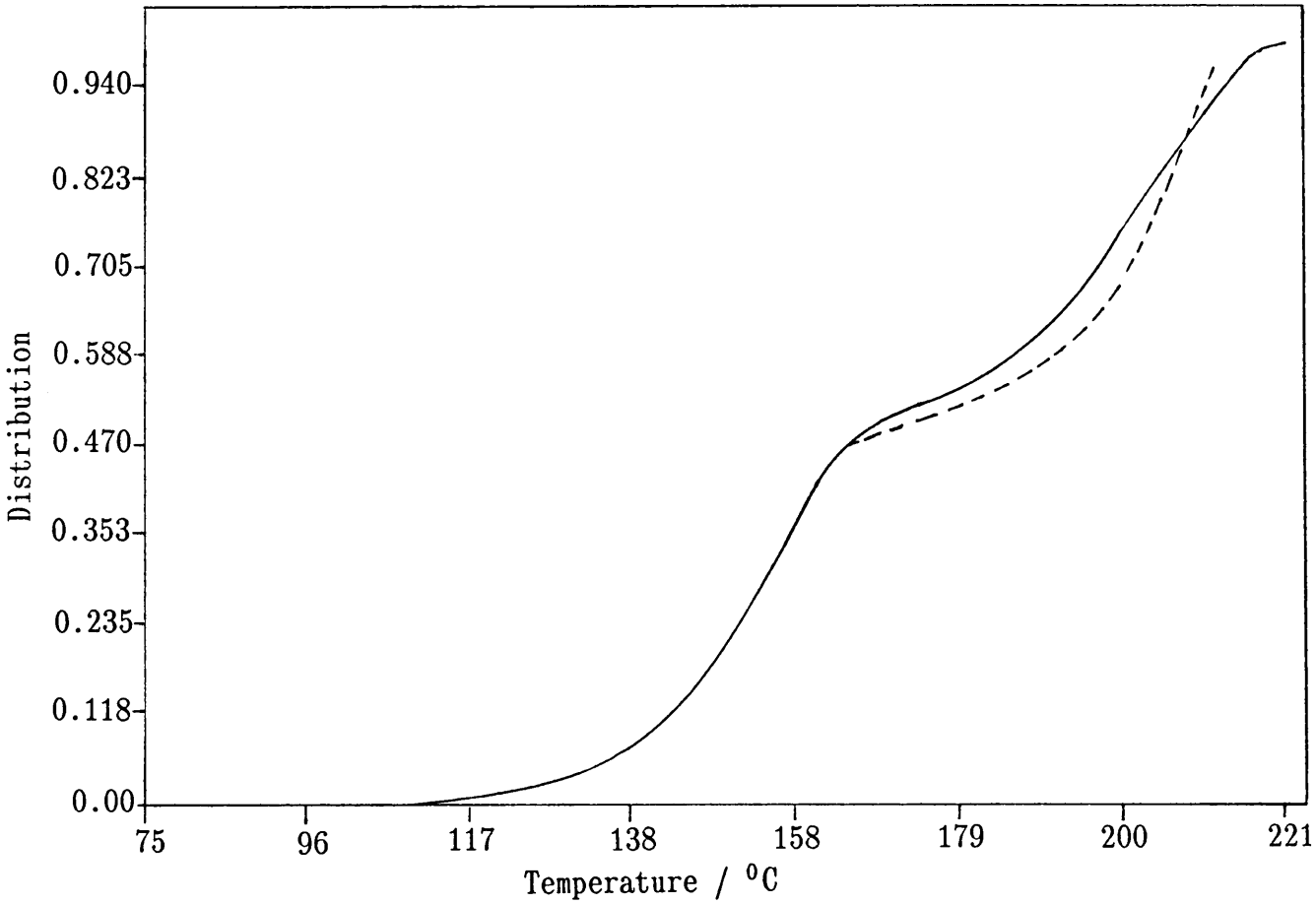

Figure 29. Plots of the simulated dynamic curve (---), obtained from the dynamic studies (reaction (2) separated), and the experimental dynamic curve (—).

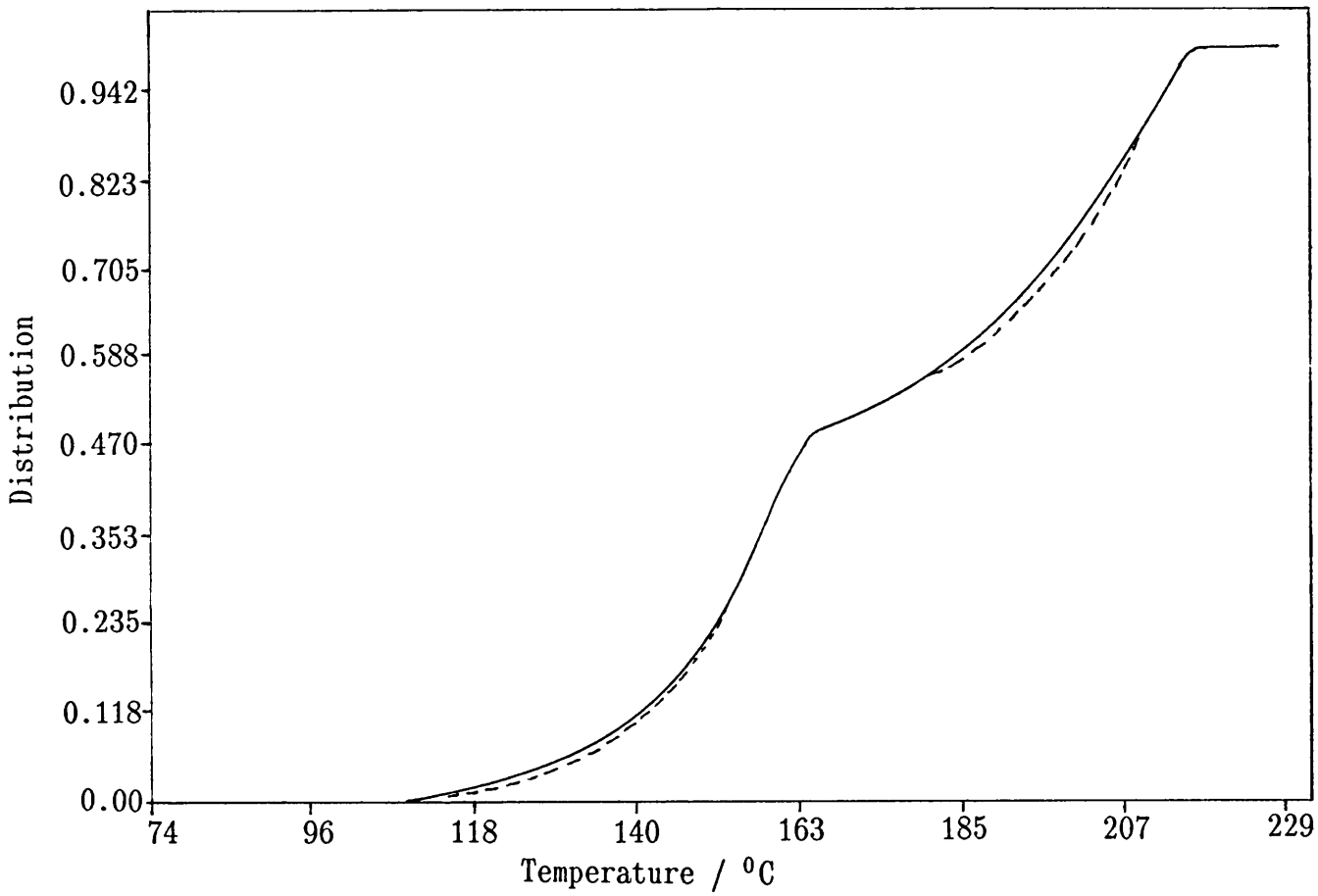

8.2.2 Isothermal results

In the temperature range 105^{0}C to 121^{0}C, reaction (1) conforms to the contracting area model, with E_a = 117,7 kJ mol^{-1} and ln Z = 30,73. This is in excellent agreement with the kinetic studies. An average experimental mass loss of 30,5% was obtained (calculated mass loss = 29,5%).

The temperature range 163^{0}C to 179^{0}C yielded two possible kinetic rate equations, the linear rate law (kt = α) and the contracting area model. When the contracting area model was used, a slighty improved fit was obtained between the theoretical and experimental α-time curves. An average fit was observed for the α-range 0,14 to 0,87. An E_a value of 72,87 kJ mol^{-1} and a ln Z value of 14,92 were calculated.

In Chapters 6 and 7, the isothermal results were applied to obtain a fit between the simulated dynamic curve and the experimental curve. The percentage contributions of the reactions were calculated from the mass losses, which correspond to 50% for both reactions. The simulated dynamic curve is given in Figure 30. Although the shape of the experimental curve corresponds to that of the simulated curve, a shift is observed and it was therefore necessary to vary the percentage contribution. The percentage contribution of reaction (2) was increased to 54%, resulting in 46% for reaction (1). An improved fit was obtained (Figure 31). An even better fit was obtained by increasing the percentage contribution of reaction (2) to 59% and decreasing it

Figure 30. Plots of the simulated dynamic curve (---), obtained from the isothermal studies, and the experimental curve (—). Contribution of both reactions is 50%.

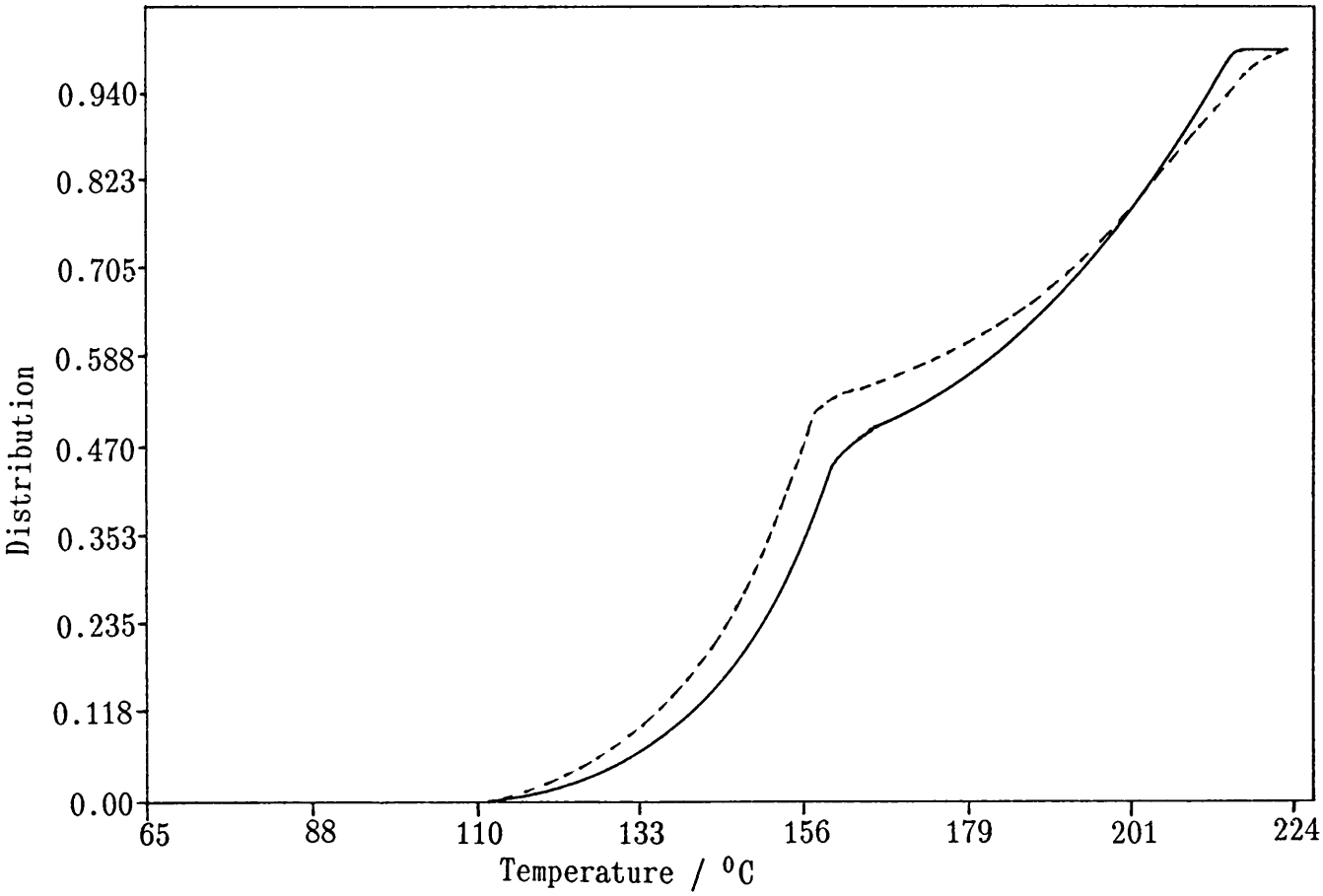

Figure 31. Plots of the simulated dynamic curve (---), obtained from the isothermal studies, and the experimental curve (—). Contribution of reactions (1) and (2) is 46% and 54%, respectively.

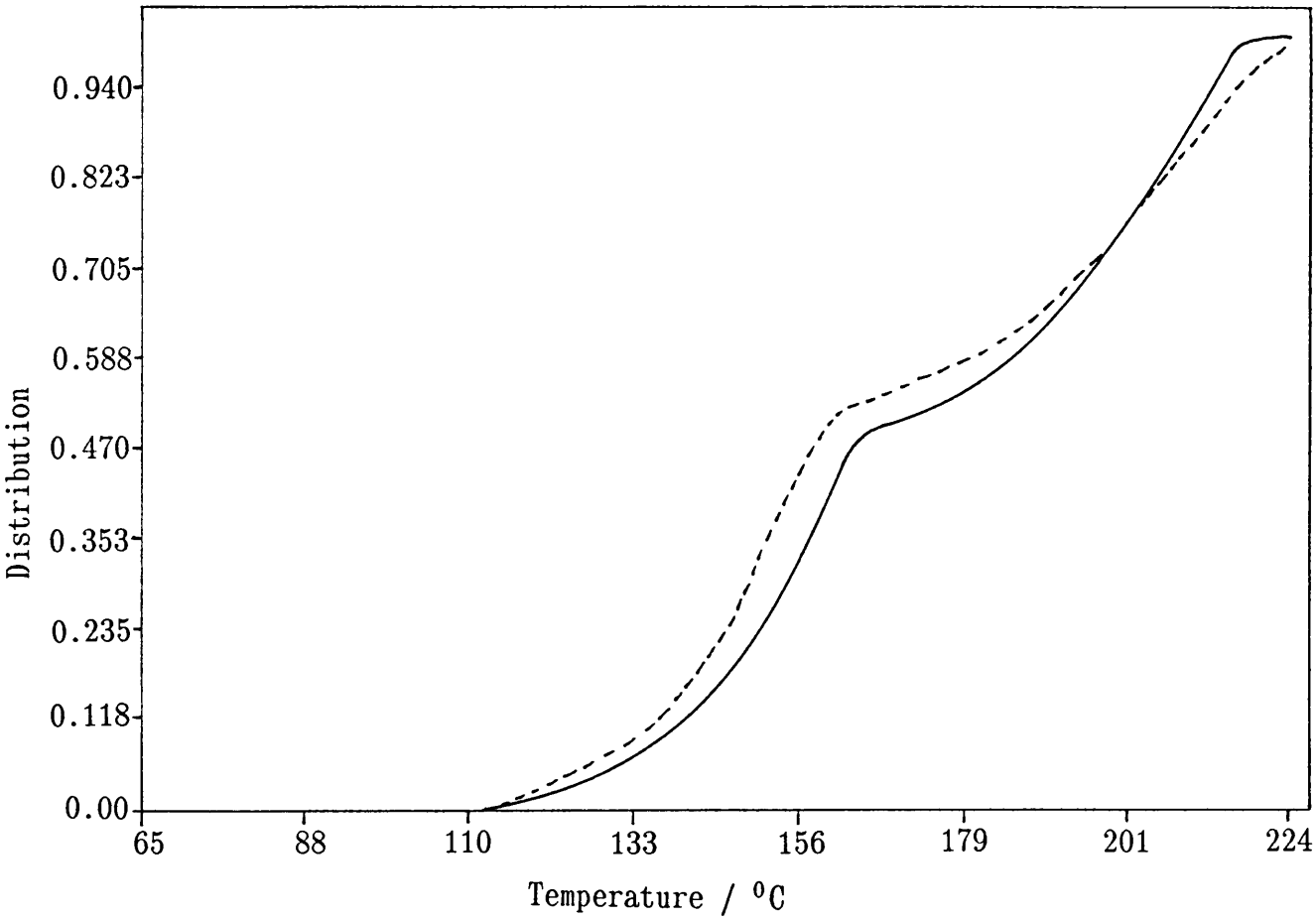

to 41% for reaction (1) (Figure 32). Thus, by varying the percentage contribution of reactions (1) and (2), it was possible to obtain a relatively good fit between the experimental dynamic curve and the simulated curves.

Two steps were separated for the second reaction, by performing kinetic analysis on the dynamic TG curve. Calculations on the isothermal studies were repeated for $0 < \alpha < 0,1$ and $0,10 < \alpha < 1,0$. Separate steps were only revealed when the isothermal studies were performed at high temperatures. This gives rise to the linear rate law which describes the first part of reaction (2) and gives E_a = 64,95 kJ mol^{-1} and ln Z = 13,00. The linear rate law was also obtained for the second part of reaction (2) with values of E_a = 207,81 kJ mol^{-1} and ln Z = 54,15. However, an extremely poor fit was obtained if these data were used to simulate a dynamic curve (Figure 33). The percentage contribution for reaction (2) was taken as 9% and 41% for the first and second part, respectively.

Figure 32. Plots of the simulated dynamic curve (---), obtained from the isothermal studies, and the experimental curve (—). Contribution of reactions (1) and (2) is 41% and 59%, respectively.

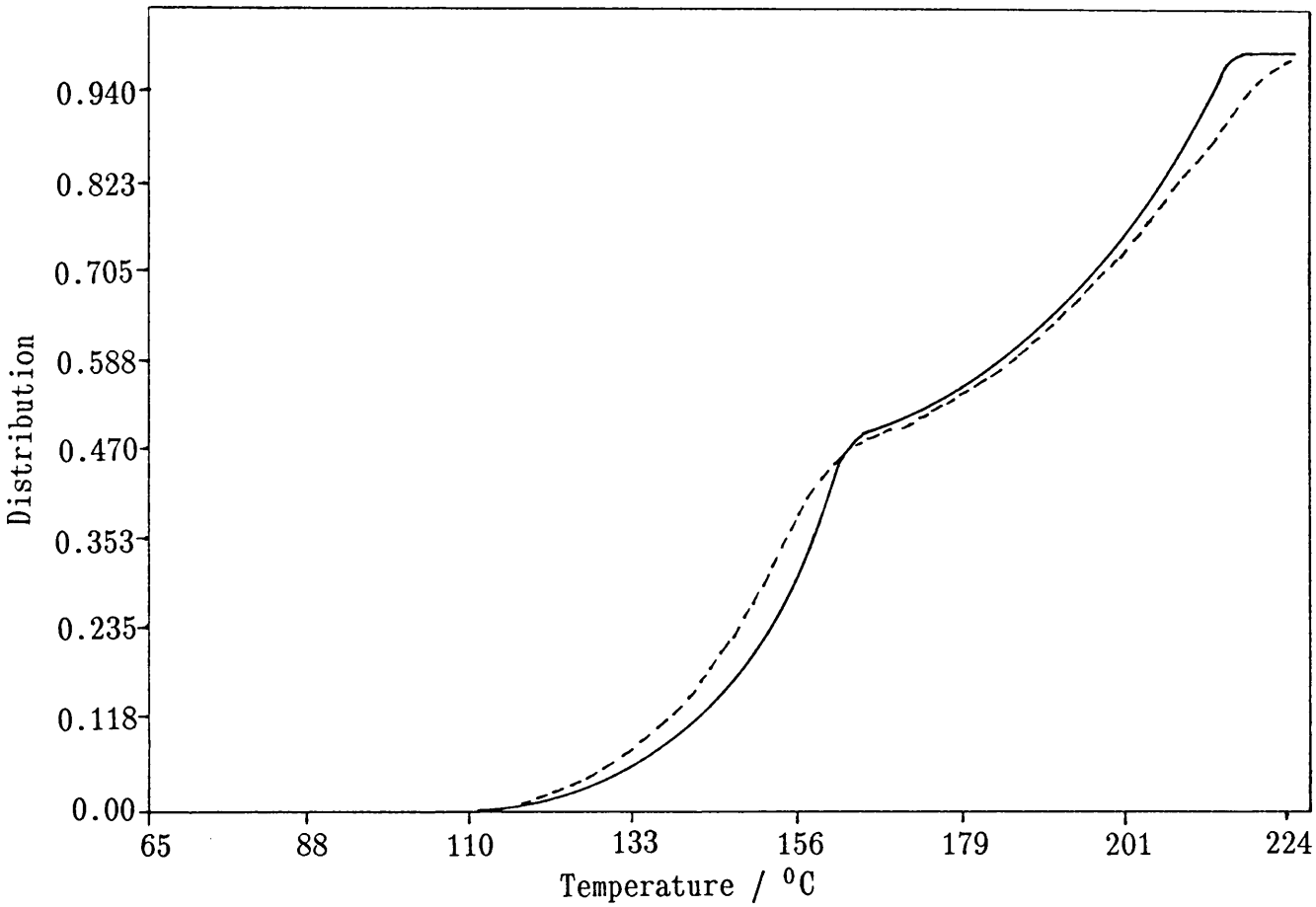

Figure 33. Plots of the simulated dynamic curve (---), obtained from the isothermal studies (reaction (2) separated), and the experimental curve (—).

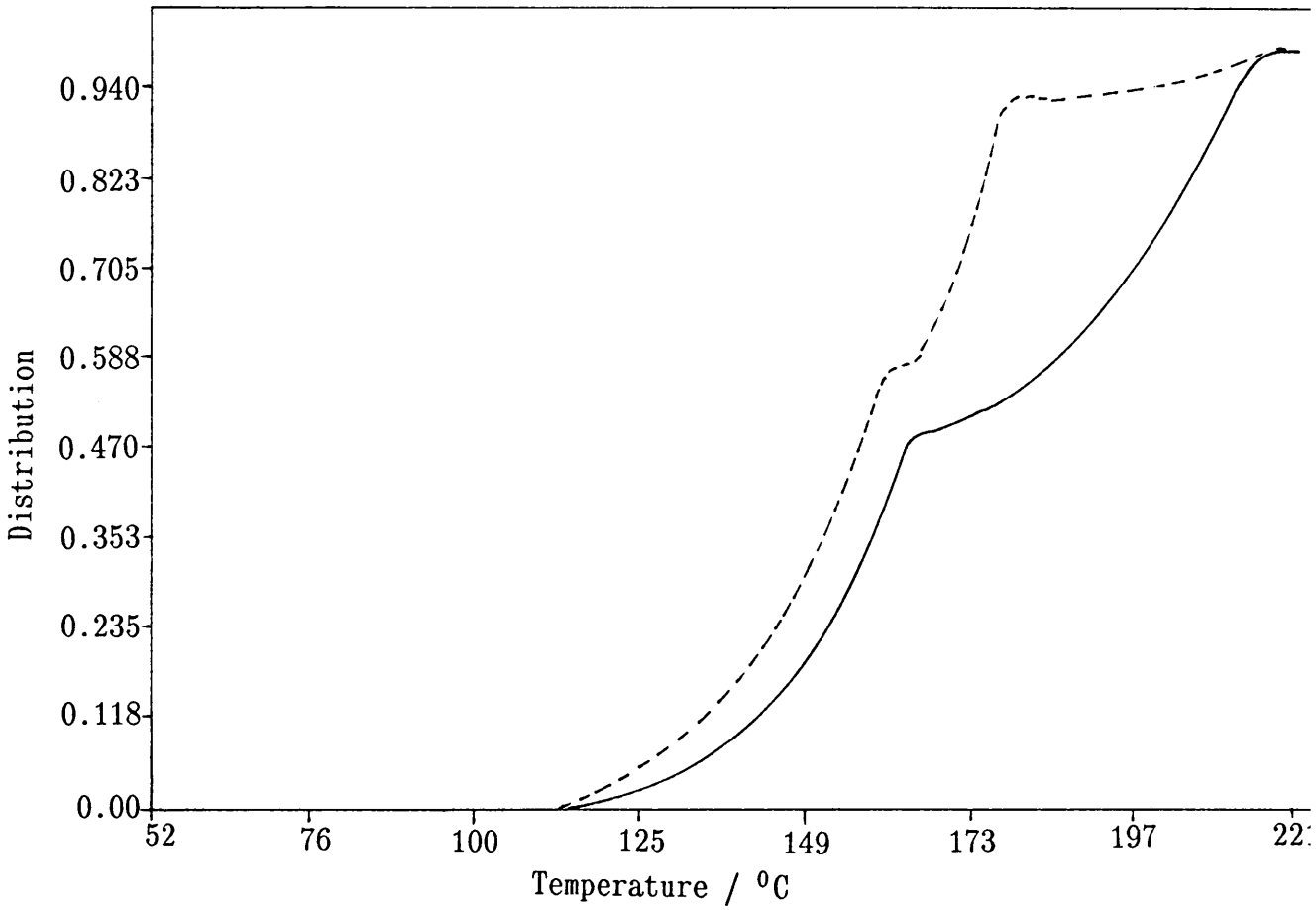

Thus, it may be concluded that the kinetic results of the dynamic curve are not always applicable to the isothermal curve. No problems were encountered with reaction (1) and an excellent correlation between the results of the isothermal and dynamic studies was obtained. The discrepancies observed for reaction (2) may be attributed to the simultaneous occurence of more than one reaction, thus the existence of overlapping processes, and it seems to be difficult to separate these reactions. However, an improved fit was obtained if the percentage contribution of the second reaction was increased. Thus, although the dynamic curve flattens approximately half way through the decomposition reaction, a small part of the $CoCl_2$(α-pic) molecules may be converted to $CoCl_2$. Overlapping processes were observed in the DTA and DSC studies (see later). It may, therefore, be concluded that the dynamic and isothermal curves cannot be reconciled when more than one reaction occurs simultaneously.

Allan [78] investigated the spectroscopic properties and thermal decomposition of several complexes of cobalt(II) halides with substituted pyridine ligands. He reported, that only the product $CoCl_2$ was formed, at a temperature of 220^0C. Liptay [80] reported the formation of mixed complexes at approximately 160^0C for the complex $CoCl_2 2(\alpha$-pic). This corresponds with the excellent results, obtained in this study, at temperatures lower than 160^0C.

8.2.3 DSC results

The DSC studies were performed in open and sealed pans.

The DSC trace observed in the open sample pans is given in Figure 34. The two endothermic peaks observed below 240^0C represent the decomposition of $CoCl_2 2(\alpha\text{-pic})$ to $CoCl_2$. The curve indicates that two successive processes occur simultaneously. This corresponds to the results expected from the kinetic studies. An average enthalpy value of 155 kJ mol^{-1} was observed, with peak maxima at $153{,}2^0$C and $207{,}8^0$C. The continuous deceleratory process may be attributed to the melting of small quantities of $CoCl_2 2(\alpha\text{-pic})$ and the formation of cobalt oxide at approximately 424^0C.

G. Beech [7] reported a lower enthalpy change of 110 kJ mol^{-1} and an enthalpy of fusion of 32 kJ mol^{-1}. This difference between the values may be due to the difficulty in determining the baseline because of the large negative slope and the high heating rate (16^0C min^{-1}) applied by Beech.

Once structural assignments have been made, the scheme of thermal decomposition is

$$CoCl_2 2(\alpha\text{-pic})\ \text{tet.} \rightarrow CoCl_2(\alpha\text{-pic})\ \text{oct.} \rightarrow CoCl_2\ \text{oct.}$$

The tetrahedral environment of the cobalt(II) in the $CoCl_2 2(\alpha\text{-pic})$ complex was deduced from its spectroscopic properties [78] and is typical of pyridine-substituted cobalt

Figure 34. The DSC trace observed for $CoCl_2 2(\alpha\text{-pic})$ at $5^0C\ min^{-1}$ in open sample pans.

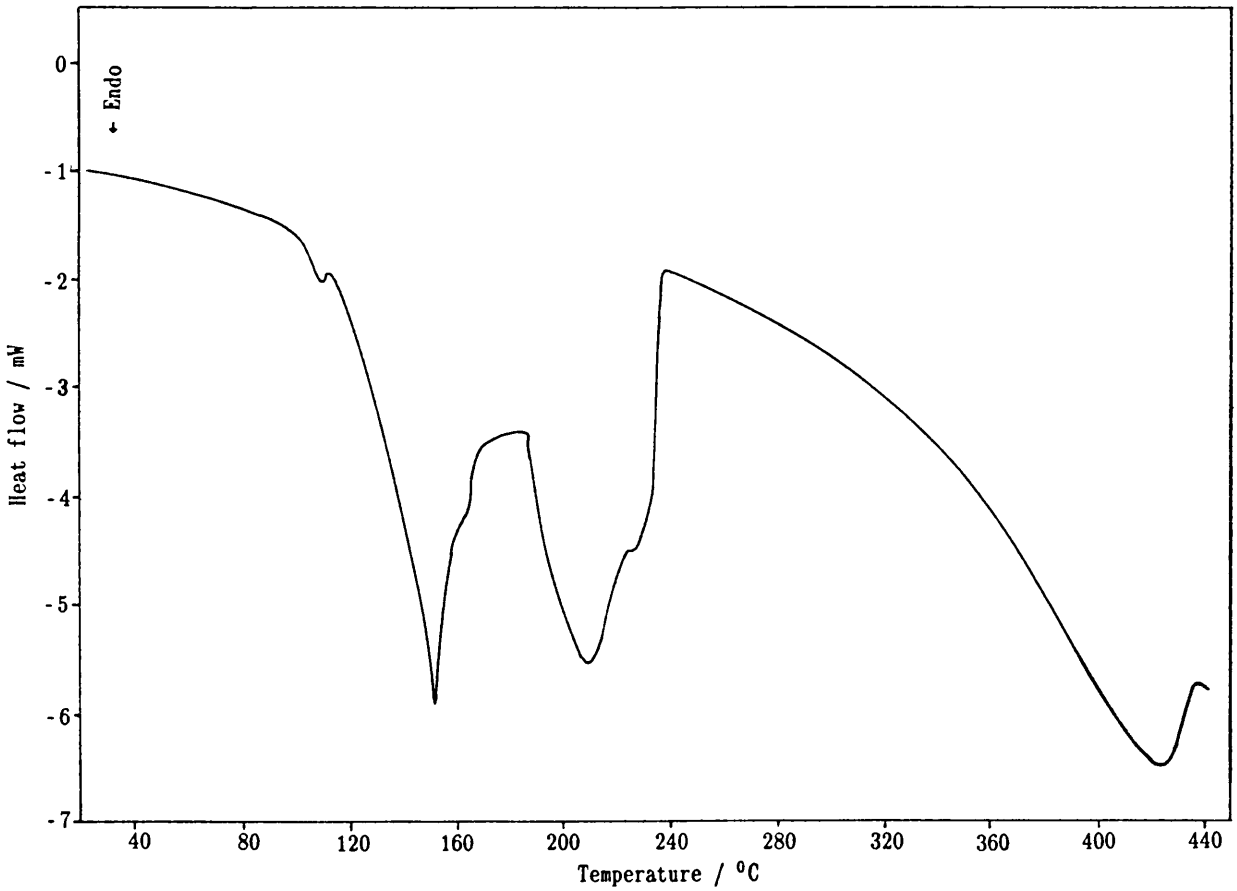

complexes. The structure of $CoCl_2(\alpha\text{-pic})$ is built up by removing α-picoline from the tetrahedral monomer in order to form a chain structure, with chlorine atoms forming bridges between cobalt atoms. Thus, by converting the chains to infinite planes, the structure of anhydrous cobalt(II) chloride is obtained.

The DSC studies performed in sealed pans show an endothermic peak at approximately $170,8^0C$, with an average enthalpy value of 38,2 kJ mol^{-1} (Figure 35). This peak can be assigned to the conversion of $CoCl_2 2(\alpha\text{-pic})$ to $CoCl_2(\alpha\text{-pic})$. This reaction occurs at a higher temperature than the temperature observed in the open pans. This could be due to the high pressure built up in the sealed pans when the α-picoline molecules are evolved. It is therefore not possible to obtain a reproducible peak for the formation of $CoCl_2$ but an exothermic peak is observed at approximately 360^0C.

In some of the DSC curves a small peak, corresponding to varying low enthalpy changes of approximately 6 kJ mol^{-1}, appeared in the temperature range 50 to 75^0C. This peak had no significant effect on the peak observed at $170,8^0C$.

Thus, the DSC studies performed in the sealed pans revealed a separation of reactions (1) and (2) and the formation of the unstable intermediate $CoCl_2(\alpha\text{-pic})$, which was previously seen and which could not be obtained in the open sample pans, was observed.

Figure 35. The DSC trace of $CoCl_2 2(\alpha\text{-pic})$ obtained in sealed sample pans at $5^0C\ min^{-1}$.

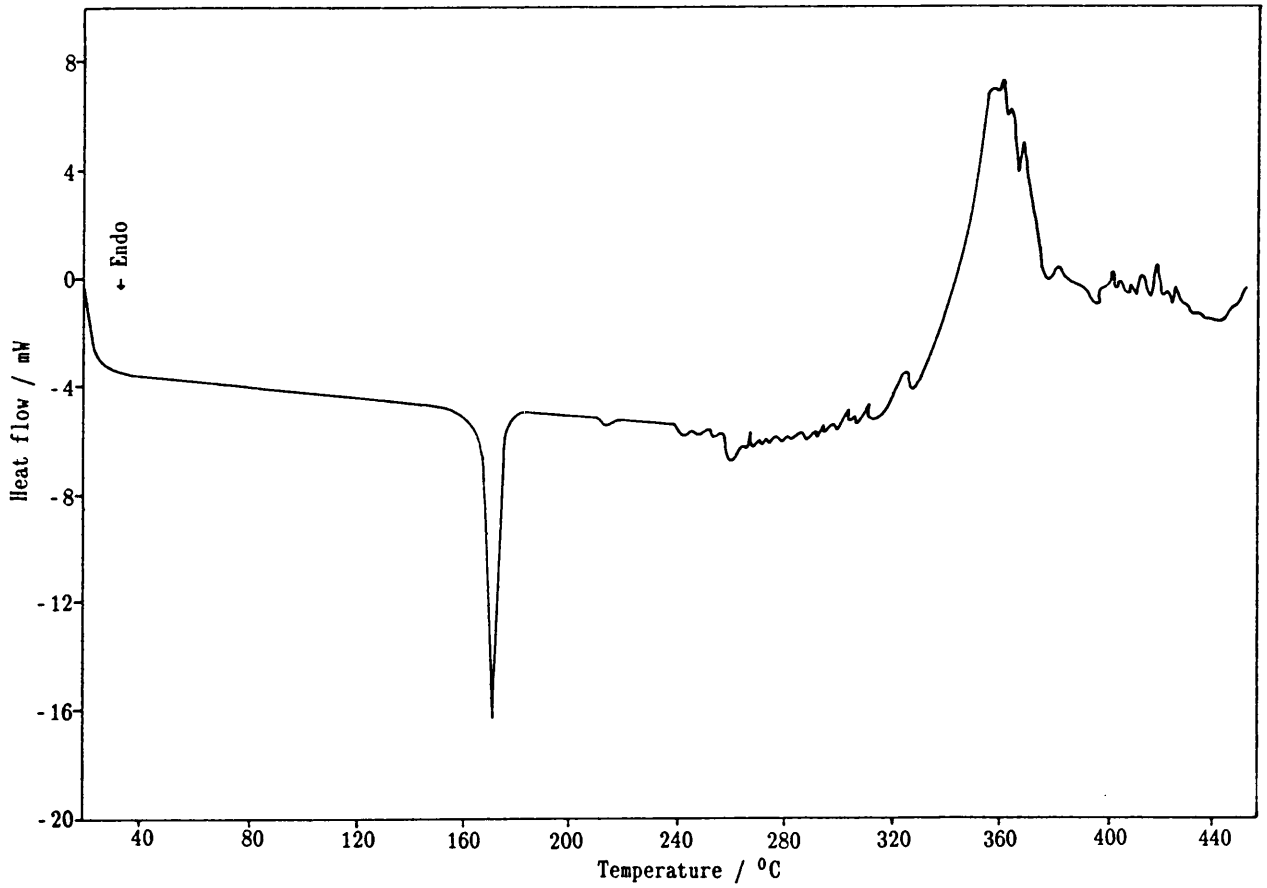

8.3 SOLUTION CHEMISTRY

H. King [1] reported the thermodynamic constants for

$CoX_2 2L$ tet. + $2L \rightleftharpoons CoX_2 4L$ oct.

where L = pyridine or α-picoline;
and X = Cl, Br, I, OCN, SCN or SeCN.

No precise values were given for the α-picoline complexes since the equilibrium lies far to the left. This study was, however, only concerned with the formation of $CoCl_2 2(\alpha\text{-pic})$ in non-aqueous media. The results obtained for the $CoCl_2/\alpha$-picoline system in acetone are summarised in Table 22.

Table 22. Thermodynamic quantities obtained for the reaction of $CoCl_2$ (0,0100 mol dm^{-3}) with α-pic (1,00 mol dm^{-3}) in acetone.

$\log \beta_1$	= 3,840
$\log \beta_2$	= 8,296
ΔG_{0-1}	= -21,90 kJ mol^{-1}
ΔG_{0-2}	= -47,32 kJ mol^{-1}
ΔH^0_{0-1}	= -27,47 kJ mol^{-1}
ΔH^0_{0-2}	= -46,17 kJ mol^{-1}
ΔS^0_{0-1}	= -18,69 J $mol^{-1} K^{-1}$
ΔS^0_{0-2}	= +3,859 J $mol^{-1} K^{-1}$

The formation reactions of $CoCl_2 2(\alpha\text{-pic})$ and $CoCl_2(\alpha\text{-pic})$ are enthalpy driven and, in addition, the formation of $CoCl_2 2(\alpha\text{-pic})$ is entropy driven. The enthalpy of formation for $CoCl_2 2(\alpha\text{-pic})$ is approximately twice as great as that for $CoCl_2(\alpha\text{-pic})$.

The distribution diagram is given in Figure 36. The percentage formation of $CoCl_2(\alpha\text{-pic})$ reaches a maximum of only 19,3% at a mole ratio of 1:1. All the species were present for most of the titration.

Figure 36. The distribution diagram for the $CoCl_2$/α-picoline system in acetone.

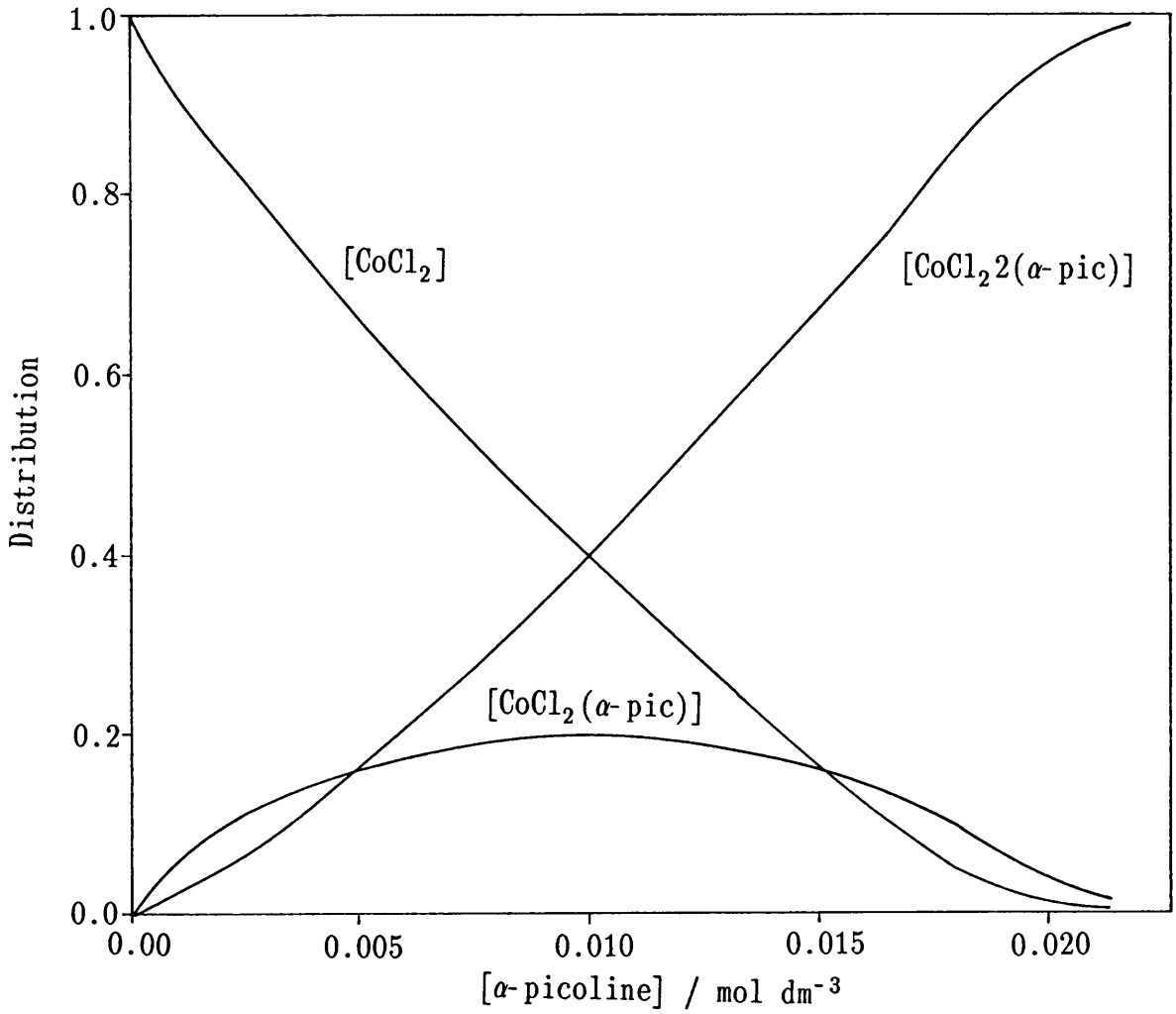

8.4 DISCUSSION

The decomposition of $CoCl_2 2(\alpha\text{-pic})$ reveals two processes which occur simultaneously. This is similar to the decomposition of $CoCl_2 2(quin)$. Only the kinetic studies performed on the first part of the dynamic curve (up to approximately 160^0C) yield significant results. The induction period of the second reaction may be assigned to the formation of mixed complexes, where the deceleratory period represents the formation of $CoCl_2$. Thus, kinetic analysis performed on the dynamic curve is only significant when the reactions are well separated. Kinetic analysis is, however, useful as it leads to the identification of mixed complexes.

Valuable information about the cobalt and α-picoline bonds was obtained. The DSC studies indicated that the second α-picoline is released more easily than the first, as was expected from the analysis of the dynamic curve. Thus, a stronger interaction exist between $CoCl_2(\alpha\text{-pic})$ and α-picoline than between $CoCl_2$ and α-picoline.

Solution chemistry studies show that the enthalpy of formation for the reaction

$$CoCl_2(\alpha\text{-pic}) + (\alpha\text{-pic}) \rightleftharpoons CoCl_2 2(\alpha\text{-pic})$$

is $(-46{,}17 + 27{,}47)$ kJ $mol^{-1} = -18{,}70$ kJ mol^{-1}. This reflects a strong interaction between $CoCl_2$ and α-picoline. The different

bonding strength results obtained from the solution and the solid state studies may be attributed to the occurence of simultaneous reactions in the solid state.

CHAPTER 9

THE SOLID STATE AND SOLUTION CHEMISTRY OF $CoCl_2$2(β-pic)

9.1 INTRODUCTION

An important part of this investigation was to study the effect of the methyl substituent, of the pyridine ring, on the kinetic results obtained from the analysis of the TG curves and also the strength of the metal-donor-N bond, therefore β- and γ-picoline complexes were included.

Paper-like $CoCl_2$4(γ-pic) crystals were prepared. These crystals had an extremely low density and it was therefore not possible to obtain reproducible TG data. Liptay [80] reported that γ-picoline does not constitute a steric hindrance. It is therefore anticipated that the composition of $CoCl_2$4(γ-pic) and its thermal decomposition are similar to those of the analogous pyridine complex. Higher decomposition temperatures were reported for $CoCl_2$4(γ-pic) than for other picoline complexes. This is due to the electron density increasing effect of the methyl-group.

The conversion of the tetrakisligandcobalt(II) halide complexes to the bisligandcobalt(II) derivatives occurs in the solid state at low temperatures and without melting [78]. This process is initiated by washing the tetrakisligand cobalt(II) complex with a suitable solvent. Both $CoCl_2$4(py) and

$CoCl_2 4(\beta\text{-pic})$ can be converted to $CoCl_2 2(py)$ and $CoCl_2 2(\beta\text{-pic})$ by washing the complexes with diethyl ether. $CoCl_2 4(\gamma\text{-pic})$ is, however, not decomposed easily by solvents, but forms $CoCl_2 2(\gamma\text{-pic})$ if it is heated.

Blue shiny single crystals were obtained after washing the complex $CoCl_2 4(\beta\text{-pic})$ several times with diethyl ether. Allan [78] reported pink $CoCl_2 4(\beta\text{-pic})$ crystals and blue $CoCl_2 2(\beta\text{-pic})$ crystals which were obtained under conditions similar to those described in Section 3.2. It was therefore assumed that all the $CoCl_2 4(\beta\text{-pic})$ was converted to $CoCl_2 2(\beta\text{-pic})$. Liptay [80] reported mixed complexes for the thermal decomposition of the complex $CoCl_2 4(\beta\text{-pic})$. It therefore seems that uncertainty exists for the composition and stiochiometry of the complex $CoCl_2 2(\beta\text{-pic})$, when it is obtained by thermogravimetrical and preparational methods.

According to Allan [78] the scheme of decomposition is

$$3CoCl_2 4(\beta\text{-pic}) \rightarrow 3CoCl_2 2(\beta\text{-pic}) \rightarrow Co_3Cl_6 2(\beta\text{-pic}) \rightarrow 3CoCl_2$$

Liptay [80] reported a similar decomposition scheme but did not include the formation of the intermediate $Co_3Cl_6 2(\beta\text{-pic})$.

9.2 SOLID STATE CHEMISTRY RESULTS

9.2.1 Dynamic results

The heating rate was an important factor in determining the thermal decomposition of the complex $CoCl_2 2(\beta\text{-pic})$ as illustrated in Figure 37.

Different mass losses were obtained at different heating rates. Koch [15] discussed the effect of heating rate on thermal decomposition reactions. According to him, heating rates may be seen as a kind of energy regulator. In isothermal studies, it is found that a correlation between the time dependence of the exponential activation energy and the rate constant exists. In non-isothermal studies, the heating rate has nearly the same significance of the time constant of a growth function. Furthermore, the relative activation energy depends on the heating rate(q) and is given by

$$d\alpha/f(\alpha) = (Z/q)\ \exp(-E_a/RT)$$

In addition, a change in heating rate resulted in a shift in the decomposition temperature as shown in Figure 37. In general, the conclusion may be drawn that when the heating rate is increased, the total reaction curve is displaced to higher temperatures.

Figure 37. Dynamic curves obtained for $CoCl_2 2(\beta\text{-pic})$ at different heating rates.

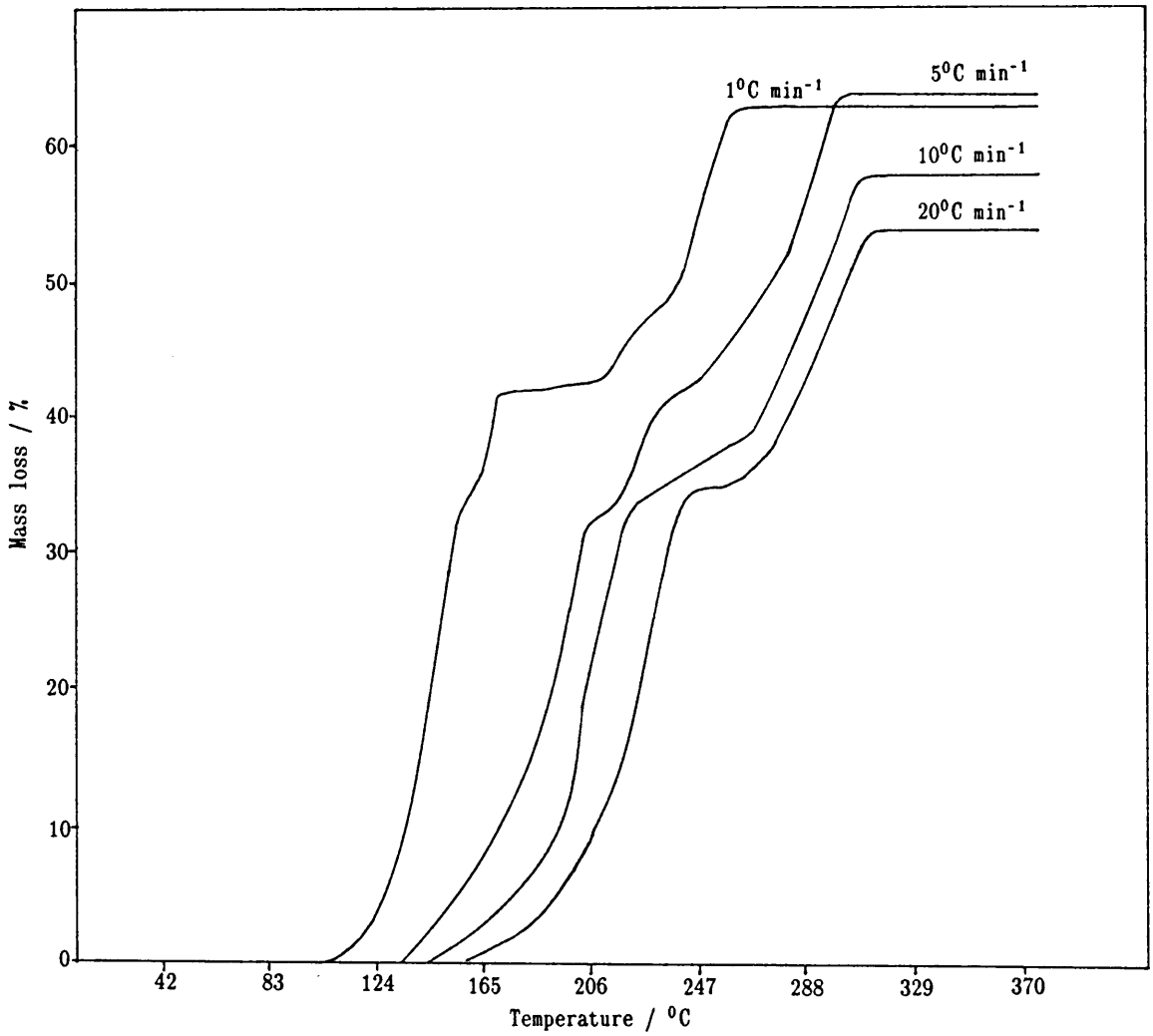

Furthermore, low heating rates yield more intermediates (steps) at different mass losses. Thus, low heating rates are useful in the study of consecutive or independent reactions. Heating rates of 1 and 5^{0}C min^{-1} yielded similar mass losses and were therefore selected as adequate heating rates for the separation of consecutive steps.

The different mass losses may be due to the formation of mixed complexes, the formation of which is dependent on the heating rate. At high heating rates (10 and 20 ^{0}C min^{-1}) the possible scheme of decomposition is

$$CoCl_2 2(\beta\text{-pic}) \rightarrow CoCl_2(\beta\text{-pic}) + (\beta\text{-pic}) \quad (1)$$

$$\rightarrow CoCl_2 + 2(\beta\text{-pic}) \quad (2)$$

The calculated theoretical mass losses for the first and the second reactions are 29,5% and 58,9%, respectively.

At low heating rates (1 and 5^{0}C min^{-1}) additional plateaus are observed. Two possible schemes may apply.

Firstly, if it is assumed that only $CoCl_2 2(\beta\text{-pic})$ is present, then the scheme of decomposition is

$3CoCl_2 2(\beta\text{-pic}) \rightarrow 3CoCl_2(\beta\text{-pic}) + 3(\beta\text{-pic})$

(theor. mass loss = 29,5%)

$\rightarrow Co_3Cl_6 2(\beta\text{-pic}) + 4(\beta\text{-pic})$

(theor. mass loss = 39,3%)

$\rightarrow 3CoCl_2 + 6(\beta\text{-pic})$

(theor. mass loss = 58,9%)

Secondly, if mixed complexes of $CoCl_2 4(\beta\text{-pic})$ and $CoCl_2 2(\beta\text{-pic})$ are present, the following additional decomposition reactions may occur:

$3CoCl_2 4(\beta\text{-pic}) \rightarrow 3CoCl_2 2(\beta\text{-pic}) + 6(\beta\text{-pic})$

(theor. mass loss = 37,1%)

$\rightarrow 3CoCl_2(\beta\text{-pic}) + 9(\beta\text{-pic})$

(theor. mass loss = 55,6%)

$\rightarrow Co_3Cl_6 2(\beta\text{-pic}) + 10(\beta\text{-pic})$

(theor. mass loss = 61,8%)

$\rightarrow 3CoCl_2 + 12(\beta\text{-pic})$

(theor. mass loss = 74,1%)

The final product was always the blue anhydrous $CoCl_2$ crystals, which changed autocatalytically to pink crystals in the presence of moist air. Therefore, it may be assumed that large quantities of $CoCl_2 4(\beta\text{-pic})$ is absent because at the final mass loss of approximately 63%, the intermediate $Co_3Cl_6 2(\beta\text{-pic})$ would have formed. If trace amounts of the complex $CoCl_2 4(\beta\text{-pic})$ are present, isothermal studies may reveal their existence.

Another factor that influences the thermal decomposition reactions is grain size [14]. Depending on the grain shape, grains of various materials can be subdivided into two main groups. The first group consists of grains which are approximately isometric or equiaxial (including spherical, multiface grains). The second group consists of non-isometric or non-equiaxial grains, such as fibrous or angular and planar (plate-like) crystals. The $CoCl_2 2(\beta\text{-pic})$ crystals obtained are plate-like and therefore belong to the second group. The non-isotropic nature of grains of powdered materials affects spatial arrangement and this leads to anisotropy. The grain shape of powders determines their properties to a large extent and may seriously affect the properties, including thermal properties, of the resulting product.

The electron microscopy studies (Section 9.2.3) revealed a large number of active points, which may be impurities, on the surface of the grains of the crystalline product. Negligible amounts of impurities in crystalline materials can have a considerable effect on the strength of the lattice of the solid [84-87] and on the surface energy [88] and properties [85,86,89,90] of the solid. Therefore, it is not permissible to ignore even small quantities of impurities when analysing a process occuring in crystalline materials. Both intraparticle and interparticle impurities are found. Surface impurities, which are an important sub-group of the latter, form very thin layers which may affect the processes of mechanical deformation, sintering, recrystallization and chemical conversion of crystalline materials.

9.2.2 Isothermal results

A suitable preheating rate was determined for the isothermal studies on the basis of the effect of heating rate on the decomposition reaction as indicated by the dynamic studies. It was therefore decided to heat the sample at $10^0C\ min^{-1}$ to a temperature approximately 20^0C below the preselected isothermal temperature and then to decrease the heating rate to $2^0C\ min^{-1}$ until the required temperature was reached.

Two successive reactions are observed over the temperature range 126^0C to 140^0C (Figure 38).

Two kinetic rate equations are needed to describe the shape of the α-time curve because one kinetic equation cannot describe the whole α-range. The first part of the reaction, up to a mass loss of approximately 29%, is best described by the contracting area model, $kt = 1 - (1 - \alpha)^{\frac{1}{2}}$, for $0,04 < \alpha < 0,74$.

The mass loss corresponds to the following decomposition reaction:

$$CoCl_2 2(\beta\text{-pic}) \rightarrow CoCl_2(\beta\text{-pic}) + (\beta\text{-pic})$$

An activation energy of 152,9 kJ mol^{-1} and a ln Z value of 40,61 were calculated.

Figure 38. The isothermal curve obtained for $CoCl_2 2(\beta\text{-pic})$ at a constant temperature of 140^0C.

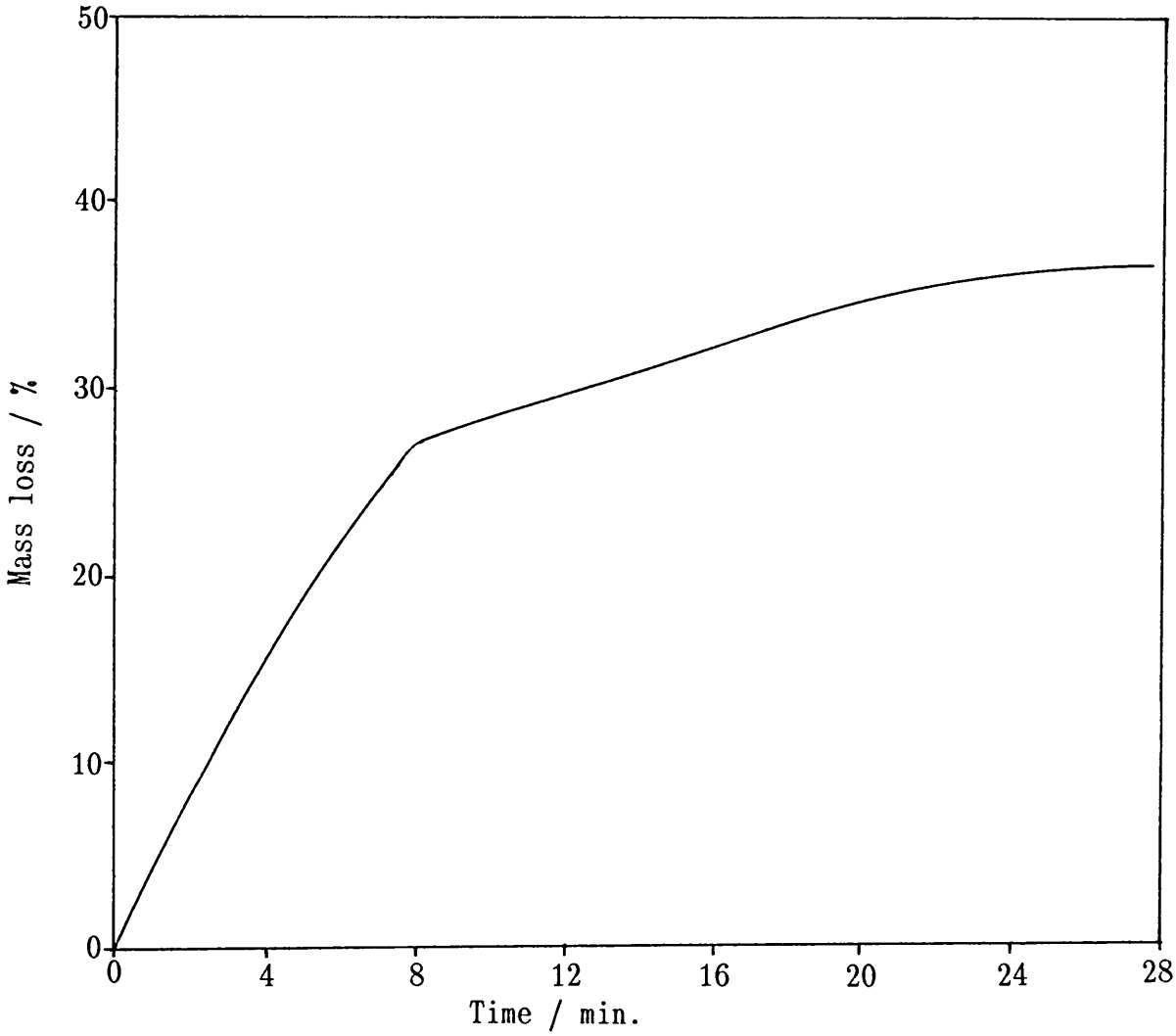

The second part of the decomposition reaction in the temperature range 126^0C to 140^0C, may result from two possible reactions. Firstly, if it is assumed that $CoCl_2 4(\beta\text{-pic})$ is absent, then the decomposition scheme is

$$3CoCl_2(\beta\text{-pic}) \rightarrow Co_3Cl_6 2(\beta\text{-pic}) + (\beta\text{-pic})$$

The calculated theoretical mass loss for the overall decomposition of $CoCl_2 2(\beta\text{-pic})$ to $Co_3Cl_6 2(\beta\text{-pic})$ is 39,3%, which compares well with the experimentally obtained mass loss of 38,8%.

Liptay [80] reported the decomposition peaks of $CoCl_2 4(\beta\text{-pic})$ at a temperature of 130^0C and higher decomposition temperatures of 230^0C and 290^0C for $CoCl_2 2(\beta\text{-pic})$ and therefore a second alternative was considered. This alternative is, if trace amounts of $CoCl_2 4(\beta\text{-pic})$ are present, the following decomposition reaction is possible:

$$CoCl_2 4(\beta\text{-pic}) \rightarrow CoCl_2 2(\beta\text{-pic}) + 2(\beta\text{-pic})$$

The calculated mass loss (37,1%) also agrees well with the experimental mass loss calculated mass loss of 38,8%.

Considering the kinetic analysis of the second part of the curve, the isothermal curves conform to the contracting volume model, $kt = 1 - (1 - \alpha)^{0.33}$, for $0,76 < \alpha < 0,99$.

Values of $E_a = 144,2$ kJ mol^{-1} and $\ln Z = 36,87$ were calculated. A

poor Arrhenius fit, with a standard error of 0,441 and the coefficient of correlation of 0,861, was obtained.

The final decomposition product was light blue and remained blue on standing in air. This product is therefore not $CoCl_2$. The decomposition process was also accompanied by melting. Allan [78] reported the melting of $CoCl_2 2(\beta\text{-pic})$ at 144^0C. In addition to the observations of Liptay [80], Allan [78] recorded the temperature of decomposition of $CoCl_2 2(\beta\text{-pic})$ at 110^0C and the intermediate $Co_3Cl_6 2(\beta\text{-pic})$ at 230^0C. These studies suggest that if any $CoCl_2 4(\beta\text{-pic})$ was present, it would have been converted to $CoCl_2 2(\beta\text{-pic})$, during the decomposition reaction.

The decomposition reaction studied in the temperature range 207^0C to 214^0C is characterised by an induction period and a decelerator period (Figure 39). The studies were performed by heating the decomposition product obtained in the temperature range 126^0C to 140^0C, to the preselected temperature at a low constant heating rate.

Light blue crystals, which turned pink on standing in air for a few minutes were obtained. Thus, the final decomposition product was anhydrous $CoCl_2$. An average experimental mass loss of 35% was obtained. If it is assumed that $Co_3Cl_6 2(\beta\text{-pic})$ was the major product from the previous selected isothermal temperature range, the following decomposition reaction is applicable:

Figure 39. The isotherm obtained for $CoCl_2 2(\beta\text{-pic})$ at a constant temperature of 207^0C.

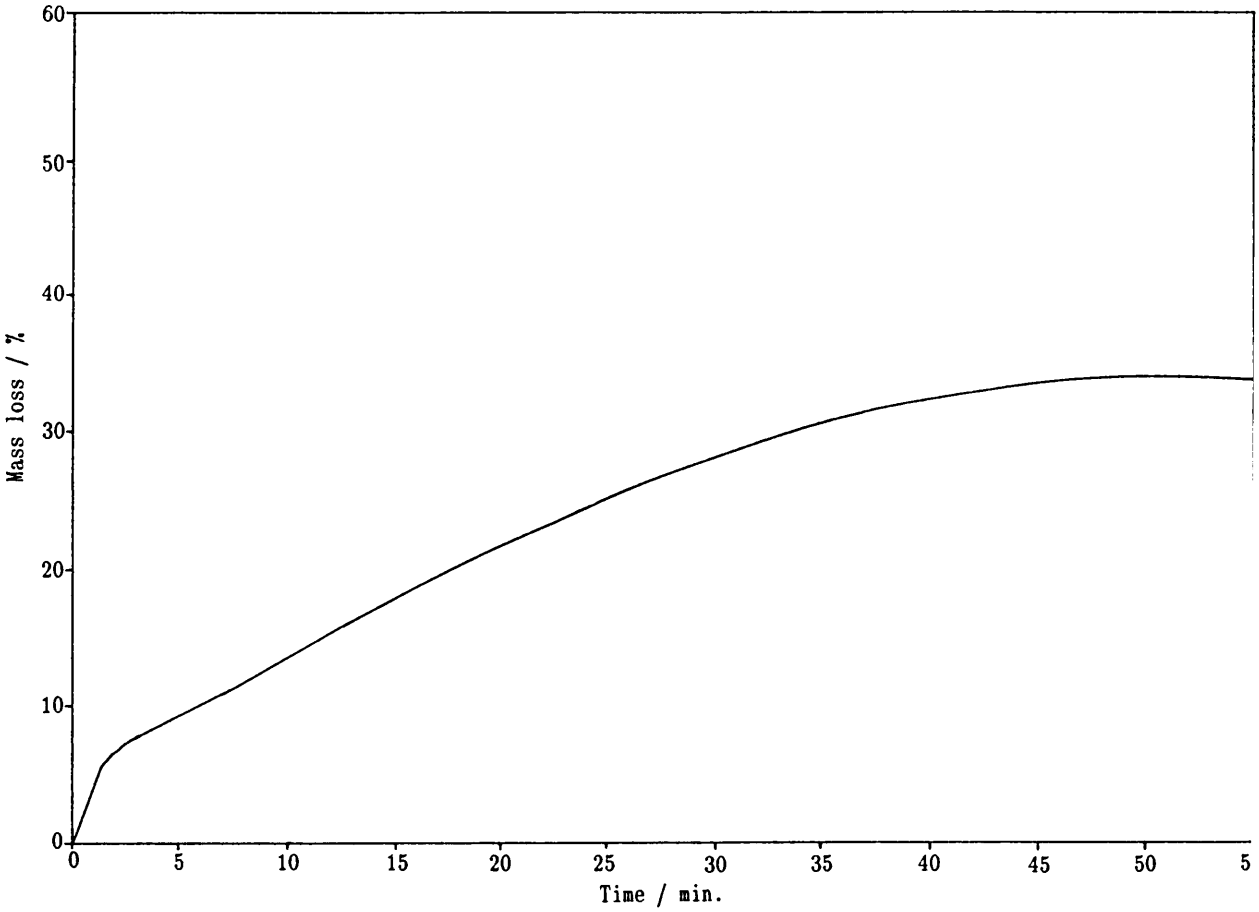

$Co_3Cl_6 2(\beta\text{-pic}) \rightarrow 3CoCl_2 + 2(\beta\text{-pic})$

with a theoretical mass loss of 32,3%.

However, Liptay [80] reported the formation of $CoCl_2$ at a higher temperature of 333^0C (obtained from the dynamic curve). The different temperatures may be attributed to the method of determining the decomposition temperatures. Experimentally, it is often found that the decomposition temperatures obtained from the isothermal studies differ from the values obtained from the dynamic studies.

The induction period as well as the decelatory period conforms to the contracting area model. The parameters calculated for the induction period were E_a = 203,8 kJ mol^{-1} and ln Z = 47,11 and the parameters calculated for the decelatory period were E_a = 178,8 kJ mol^{-1} and ln Z = 38,04.

Additional experimental methods would have been valuable in the identification of the certain intermediates. However, X-ray powder diffraction patterns for the cobalt(II) chloride pyridine-related complexes could not be obtained.

In conclusion, an explanation of the decomposition process of the starting material $CoCl_2 2(\beta\text{-pic})$ involves the assumption that trace amounts of $CoCl_2 4(\beta\text{-pic})$ are absent and therefore

$$3CoCl_2 2(\beta\text{-pic}) \rightarrow 3CoCl_2(\beta\text{-pic}) + 3(\beta\text{-pic})$$
$$\rightarrow Co_3Cl_6 2(\beta\text{-pic}) + 4(\beta\text{-pic})$$
$$\rightarrow 3CoCl_2 + 6(\beta\text{-pic})$$

Thus in addition to the intermediates found by Allan [78], the intermediate $CoCl_2(\beta\text{-pic})$ was also obtained. The presence of the $CoCl_2 4(\beta\text{-pic})$ is of small importance, since if any is present it would be converted to $CoCl_2 2(\beta\text{-pic})$ before the decomposition and the melting of $CoCl_2 2(\beta\text{-pic})$ is initiated.

9.2.3 Electron microscopy results

Micrographs were obtained during the initial stages of decomposition, in order to visualise the melting process and the thermal decomposition on the surface.

Microcraph 18 represents crystals of $CoCl_2 2(\beta\text{-pic})$ before decomposition. The crystals reveal the stacking of plate-like crystals. Impurities, which are possible active points, are visible on the surface (Micrograph 19).

The initial decomposition reaction (0,5%) of $CoCl_2 2(\beta\text{-pic})$ to $CoCl_2(\beta\text{-pic})$ (temperature 155^0C), results in decomposition on the surface (Micrograph 20). Almost abnormal growth is observed. This decomposition on the surface of the single crystals corresponds with the isothermal results. The reaction is described by the contracting area model, which is a deceleratory process and implies rapid nucleation and decomposition on the surface of the

Micrograph 18. The single crystals of $CoCl_2 2(\beta\text{-pic})$ before decomposition. (Magnification x400).

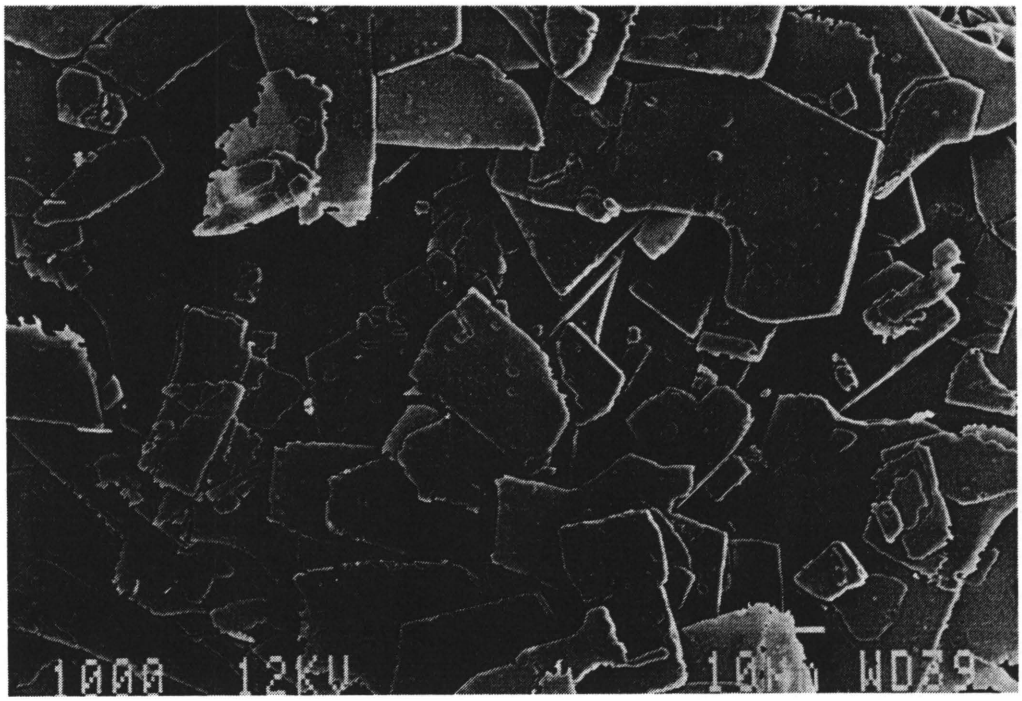

Micrograph 19. The surface of the undecomposed $CoCl_2 2(\beta\text{-pic})$ crystals. (Magnification x2500).

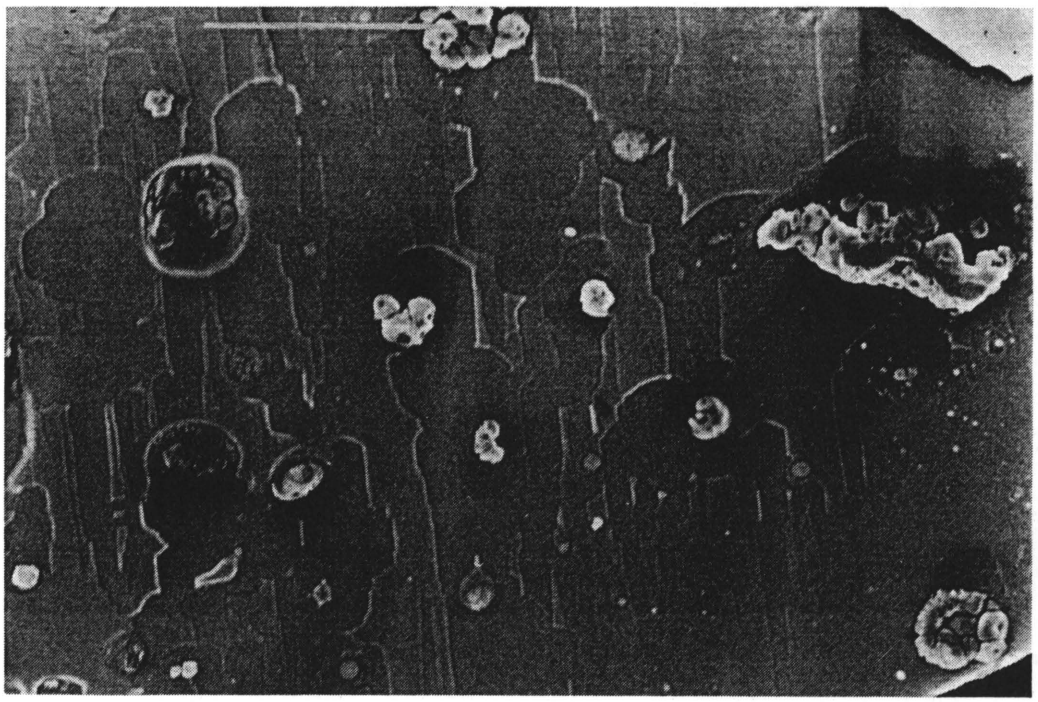

Micrograph 20. The single crystals obtained from the initial decomposition reaction (0.5%) of $CoCl_2 2(\beta\text{-pic})$. (Magnification x400).

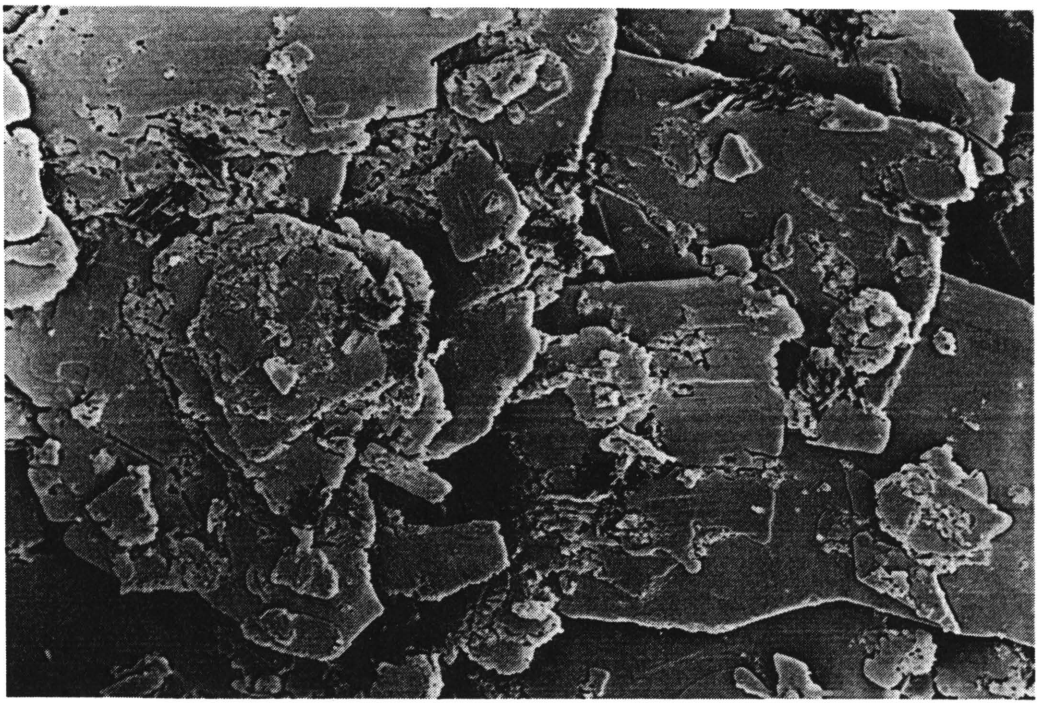

Micrograph 21. The needle crystals of the decomposition intermediate, $Co_3Cl_6 2(\beta\text{-pic})$. (Magnification x200).

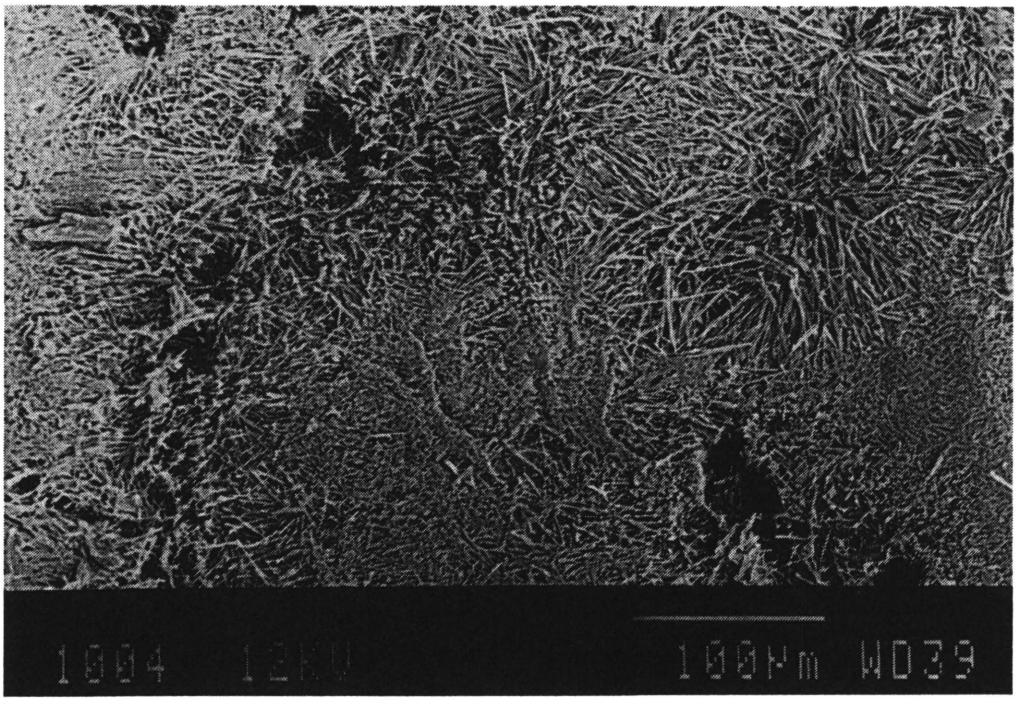

crystals. The growth and decomposition is irregular and without preference. Melting is already visible at this early stage of decomposition.

Micrograph 21 represents the intermediate $Co_3Cl_6 2(\beta\text{-pic})$. At this stage the melting process is complete and needle type crystals are formed.

Thus, the final decomposition product, $CoCl_2$, is again crystalline. Further decomposition revealed a surface similar to the surface observed in Micrograph 21, but shows an increase in the decomposition area.

9.2.4 The DSC results

The studies were performed in open sample pans only. A very large negative slope was obtained (Figure 40). This may be attributed to excessive endothermic reactions which occur simultaneously. Due to the difficulty in choosing a baseline, enthalpy calculations were not performed. The first small peak at approximately 100^0C may be assigned to the melting of $CoCl_2 2(\beta\text{-pic})$ and to structural changes. The second small peak as well as the well defined endothermic peak may be attributed to the loss of more than one β-picoline, i.e. to the formation of $Co_3Cl_6 2(\beta\text{-pic})$. The endothermic peak at 350^0C may be assigned to the formation of the final decomposition product, $CoCl_2$.

Figure 40. The DSC trace observed for $CoCl_2 2(\beta\text{-pic})$ in open sample pans.

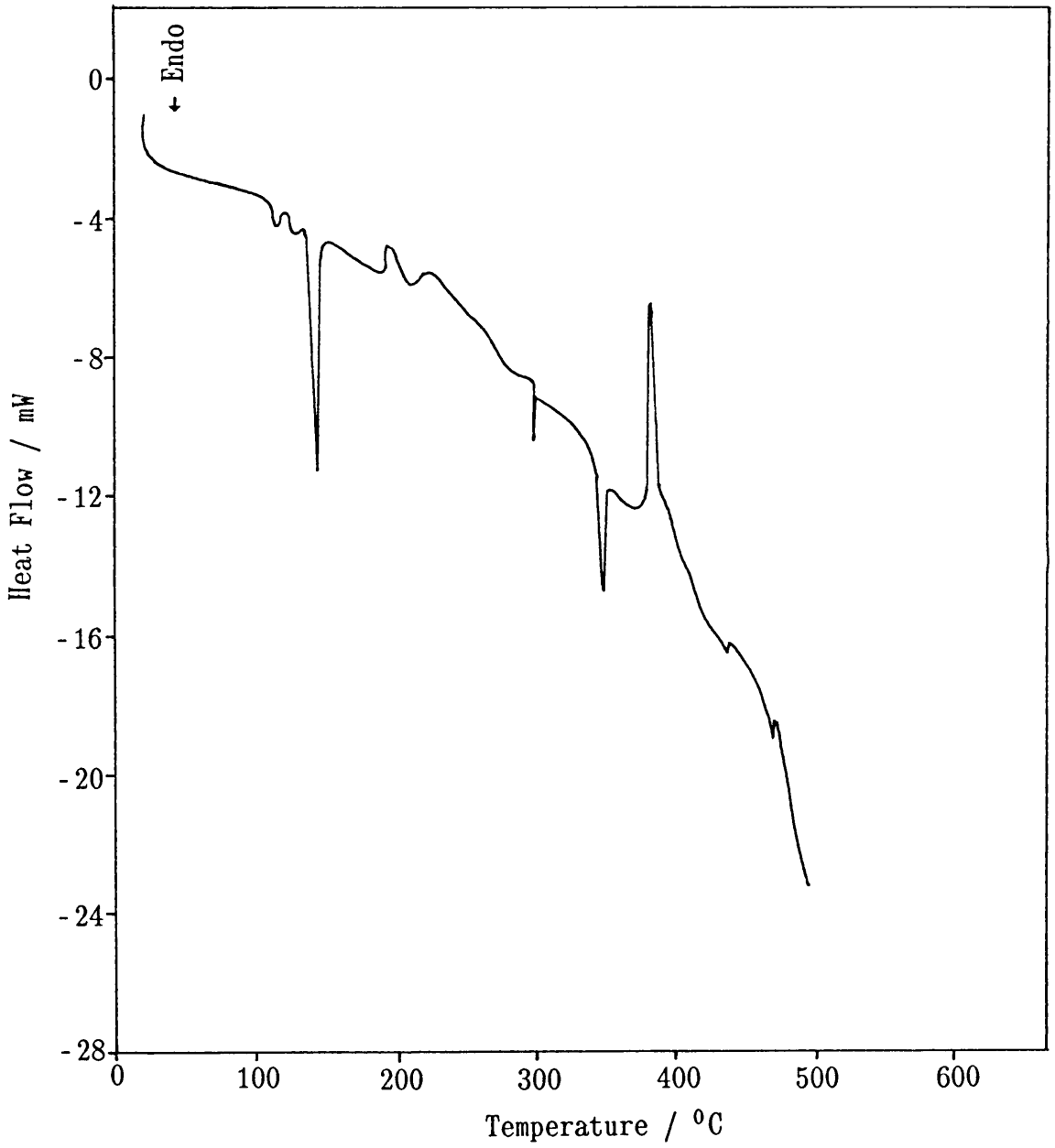

According to Allan [78] the scheme of thermal decomposition is similar to that of $CoCl_2 2(py)$. Thus

$$CoCl_2 2(\beta\text{-pic})tet. \rightarrow CoCl_2(\beta\text{-pic})oct. \rightarrow Co_3Cl_6 2(\beta\text{-pic})oct. \rightarrow CoCl_2 oct.$$

Chain structures in which chlorine atoms act as bridge between two or three cobalt atoms, are obtained for $CoCl_2(\beta\text{-pic})$ and $Co_3Cl_6 2(\beta\text{-pic})$. Finally, $CoCl_2$, which consists of an infinite plane, is formed. All the above complexes were blue.

9.3 SOLUTION CHEMISTRY RESULTS

The thermodynamic quantities obtained for the complex-formation reaction of $CoCl_2$ (0,0100 mol dm^{-3}) with β-picoline (1,00 mol dm^{-3}) in acetone, are summarised in Table 23.

Table 23. Thermodynamic quantities for the $CoCl_2/\beta$-pic system.

$\log \beta_1$	= 3,642
$\log \beta_2$	= 8,195
ΔG_{0-1}	= -20,78 kJ mol^{-1}
ΔG_{0-2}	= -46,75 kJ mol^{-1}
ΔH^0_{0-1}	= -46,12 kJ mol^{-1}
ΔH^0_{0-2}	= -61,24 kJ mol^{-1}
ΔS^0_{0-1}	= -85,03 J $mol^{-1} K^{-1}$
ΔS^0_{0-2}	= -48,62 J $mol^{-1} K^{-1}$

The formation of $CoCl_2(\beta\text{-pic})$ and of $CoCl_2 2(\beta\text{-pic})$ are both enthalpy driven. The enthalpy of formation for $CoCl_2 2(\beta\text{-pic})$ is approximately one and a half times greater than the enthalpy of formation of $CoCl_2(\beta\text{-pic})$. A stronger interaction exists between $CoCl_2$ and β-picoline than between $CoCl_2(\beta\text{-pic})$ and β-picoline.

The enthalpy of formation for the reaction

$$CoCl_2(\beta\text{-pic}) + (\beta\text{-pic}) \rightarrow CoCl_2 2(\beta\text{-pic})$$

is then $(-61{,}24 + 46{,}12)$ kJ $mol^{-1} = -15{,}12$ kJ mol^{-1}.

The distribution diagram of the system indicates a very low degree of formation for $CoCl_2(\beta\text{-pic})$, i.e. 15,1% (Figure 41). An excellent fit between the experimental and calculated Q_r values were obtained.

Figure 41. The distribution diagram for the $CoCl_2$/β-picoline system in acetone.

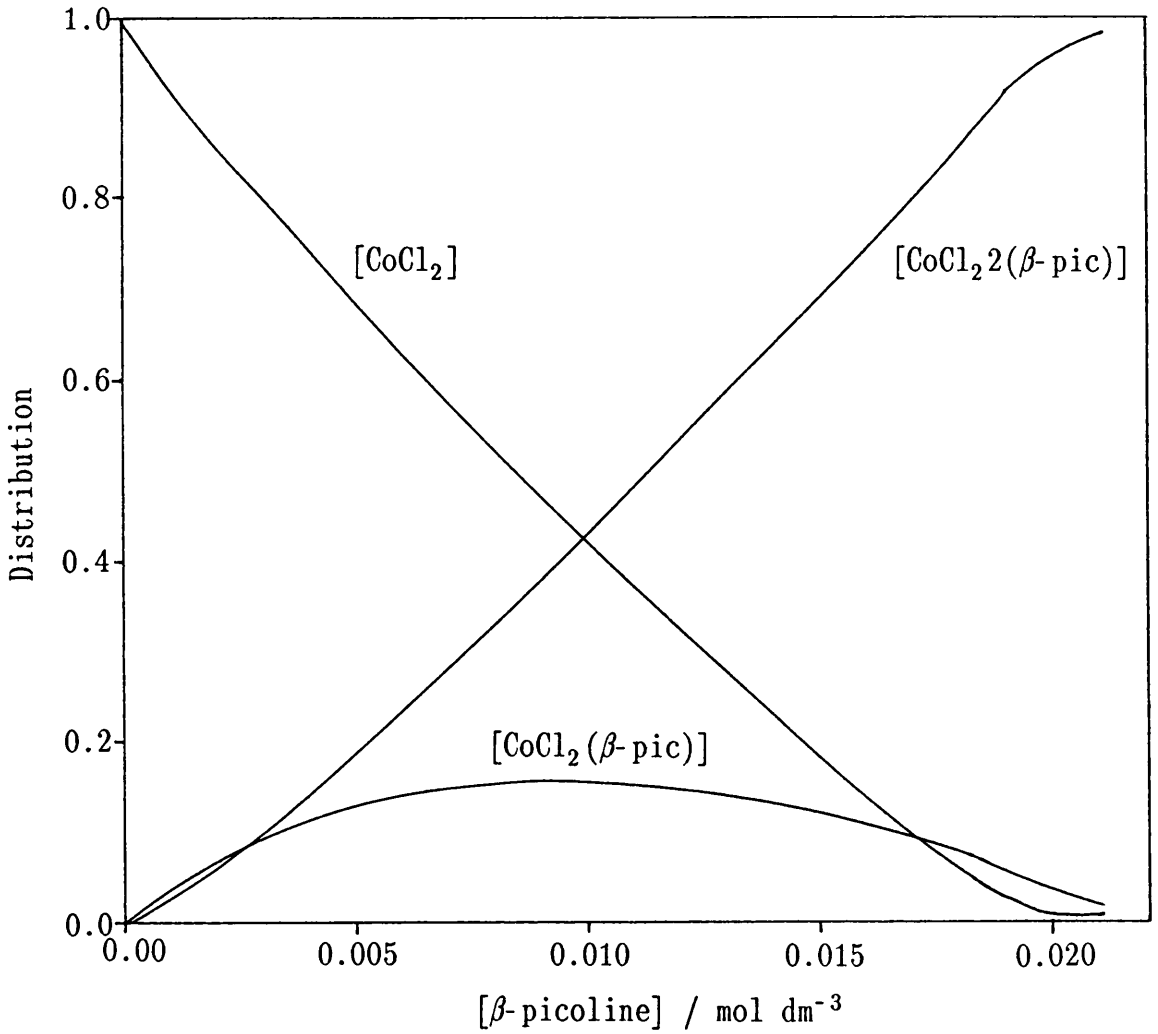

9.4 DISCUSSION

Conclusions regarding the cobalt and β-picoline bonds can be obtained from the isothermal results only. The activation energy for the decomposition reaction of $Co_3Cl_62(\beta\text{-pic})$ to $CoCl_2$ is much greater than the energy of formation of the other two intermediates. The last reaction, which involves the formation of $CoCl_2$, requires more energy than the first two reactions. Thus a stronger interaction exists between $CoCl_2$ and β-picoline than between the other intermediate complexes and β-picoline. The interactions between $CoCl_2(\beta\text{-pic})$ and β-picoline and also $Co_3Cl_62(\beta\text{-pic})$ and β-picoline are, however, more or less similar.

The solution chemistry studies also revealed a stronger interaction between $CoCl_2$ and β-picoline than between $CoCl_2(\beta\text{-pic})$ and β-picoline.

A detailed discussion of the different cobalt(II) complexes and the factors influencing the stability of the complexes as well as the strength of the metal-ligand bonds is given, in Chapter 13.

CHAPTER 10

SOLID STATE CHEMISTRY OF $CoCl_2$4(an) AND SOLUTION CHEMISTRY OF $CoCl_2$2(an)

10.1 INTRODUCTION

The thermodynamic quantities for complex formation by cobalt(II) chloride with aniline, in non-aqueous solvents, have been intensively investigated by Zhurba and Dulova [91,4-6]. A spectrophotometric method was used to study the equilibrium constants for the complex-formation reactions. The stability of the aniline complexes of $CoCl_2$ formed in non-aqueous solution depends to a significant extent on the basic nature of the solvent [6]. Solutions of $CoCl_2$ in acetone and cyclohexanone which contain aniline are extremely unstable in air [4]. The blue colour of the aniline complex of $CoCl_2$ is converted, after 10 to 15 minutes, to greenish-brown. Zhurba [91] reported low stability constants for complexes of $CoCl_2$ with amines in anhydrous methanol solution. The obvious reason is that $CoCl_2$ forms stable octahedral solvate complexes with methanol, as with other hydroxyl-containing solvents of high dielectric constant. Thus $CoCl_2$ forms octahedral solvate complexes with ethanol, which is analogous to methanol. Furthermore, hydrogen bonding, of the type N-H...O, occurs between the solvent (methanol) and the amine.

The formation of $CoCl_2$ complexes with aniline proceeds in stages, which involve the formation of 1:1 and 1:2 complexes. In view of the above, solvate complexes of $CoCl_2$ are significant in the complex-formation reaction.

The thermal decomposition of the complex $CoCl_2 2(an)$ has been reported earlier [7]. However, little is known of the dynamic TG curve, isothermal studies and various decomposition products. The exact procedure for the preparation of the complex has not been reported and the complex was prepared similarly to the previous cobalt(II) complexes (in absolute ethanol).

The thermal decomposition reaction reported is

$$CoCl_2 2(an) \rightarrow CoCl_2 + 2(an).$$

10.2 SOLID STATE CHEMISTRY RESULTS

10.2.1 Dynamic results

Several attempts were made to prepare the desired blue $CoCl_2 2(an)$ complex. When an excess of aniline solution added was to cobalt(II) chloride dissolved in ethanol a mixed blue-purple complex resulted. This complex was very unstable and the colour changed to purple, even under dry conditions.

$NiCl_2 2(an)2(EtOH)$ is formed when aniline is reacted with nickel(II) chloride in absolute ethanol [8]. Cobalt(II) chloride

may be considered to be analogous in many ways to nickel(II) chloride. Thus, it may be assumed that the formation of the complex $CoCl_2 2(an) 2(EtOH)$ is possible.

The dynamic TG curve obtained for this possible complex is given in Figure 42.

The mass losses correspond to the calculated theoretical mass losses. Thus the scheme of decomposition involves the following three steps:

$$CoCl_2 2(an) 2(EtOH)(s) \rightarrow CoCl_2 2(an)\ (s) + 2(EtOH)\ (g) \qquad (1)$$

(theor. mass loss = 22,6%)

$$\rightarrow CoCl_2(an)\ (s) + an\ (g) + 2(EtOH)\ (g) \qquad (2)$$

(theor. mass loss = 45,4%)

$$\rightarrow CoCl_2\ (s) + 2(an)\ (g) + 2(EtOH)\ (g) \qquad (3)$$

(theor. mass loss = 68,2%)

The final decomposition product was the blue anhydrous $CoCl_2$, which turned pink on standing in air. The possibility that the complex, $CoCl_2 2(an) 2(EtOH)$, exists is consistent with the mass loss. Thus, the ligand and the solvent, ethanol, exert a strong effect on the cobalt(II) ion. Since the complex is very unstable to moisture, even in a desiccator over P_2O_5, isothermal studies were not possible.

Figure 42. The TG and DTA traces of $CoCl_2$2(an)2(EtOH) recorded at $10^0C\ min^{-1}$.

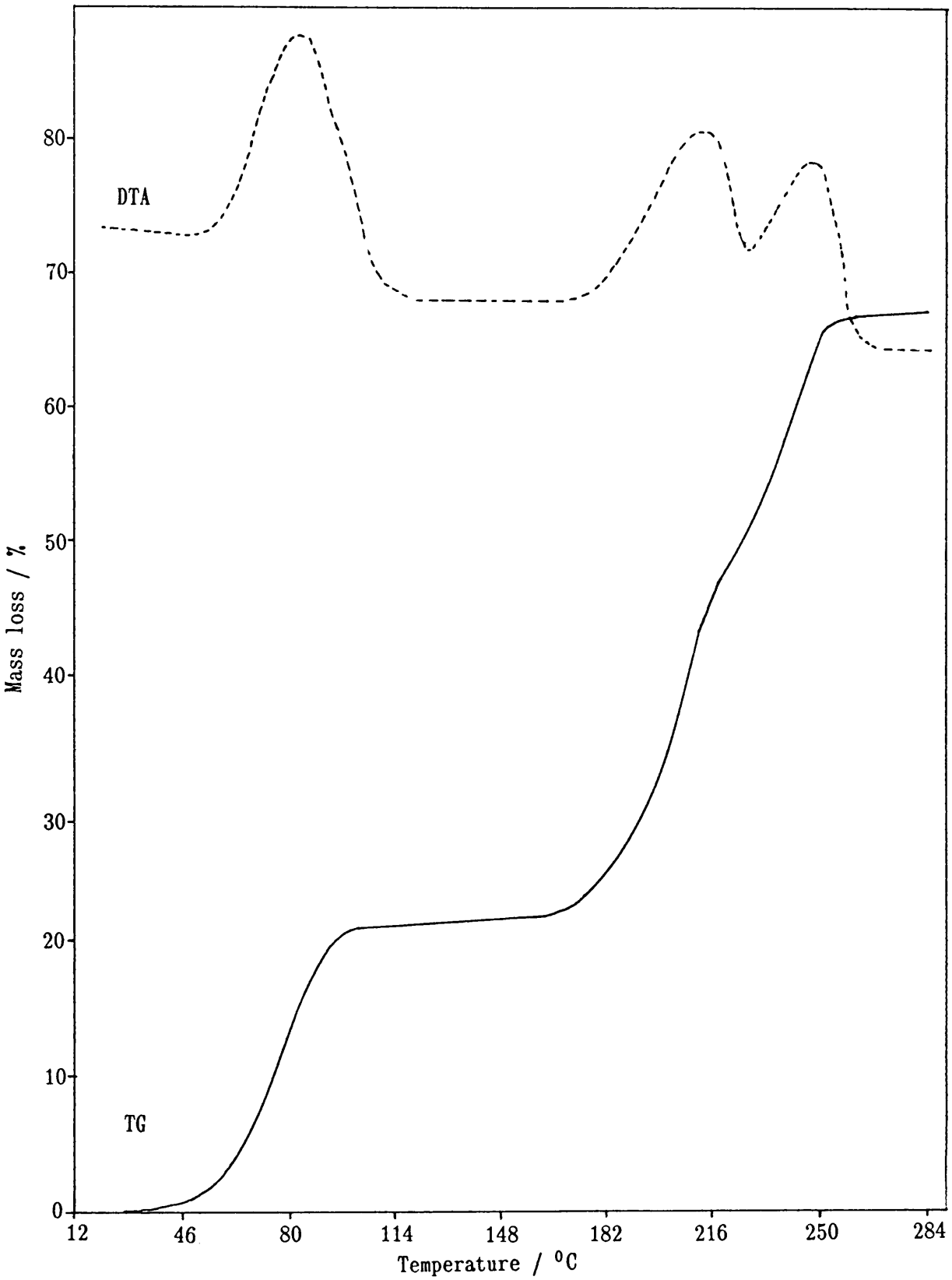

The complex $CoCl_2 2(an)$ is very unstable and forms solvated metal ligand complexes. The participation of H_2O molecules has been considered, but the mass losses do not correspond to the calculated mass losses. Thus, the interaction between the metal ion and the ligand as well as the solvent, must be considered.

Another attempt was made to prepare crystals of the aniline complex by adding an excess of aniline to a solution of cobalt(II) chloride in absolute ethanol. The blue complex was washed several times with diethyl ether. The obtained complex was stable in air and no colour change was observed on standing in air. The dynamic TG curve was recorded, from room temperature to 500^0C, at $5^0C\ min^{-1}$ (Figure 43).

The dynamic curve shows that two reactions are occuring simultaneously. The experimental mass losses correspond to the following decomposition reactions:

$$CoCl_2 4(an)\ (s) \rightarrow CoCl_2 2(an)\ (s) + 2(an)\ (g) \qquad (4)$$

(theor. mass loss = 37,1%)

$$\rightarrow CoCl_2(an)\ (s) + 3(an)\ (g) \qquad (5)$$

(theor. mass loss = 55,6%)

$$\rightarrow CoCl_2\ (s) + 4(an)\ (g) \qquad (6)$$

(theor. mass loss = 74,1%)

Figure 43. The TG and DTA curves observed for $CoCl_2 4(an)$ at $5^0C\ min^{-1}$.

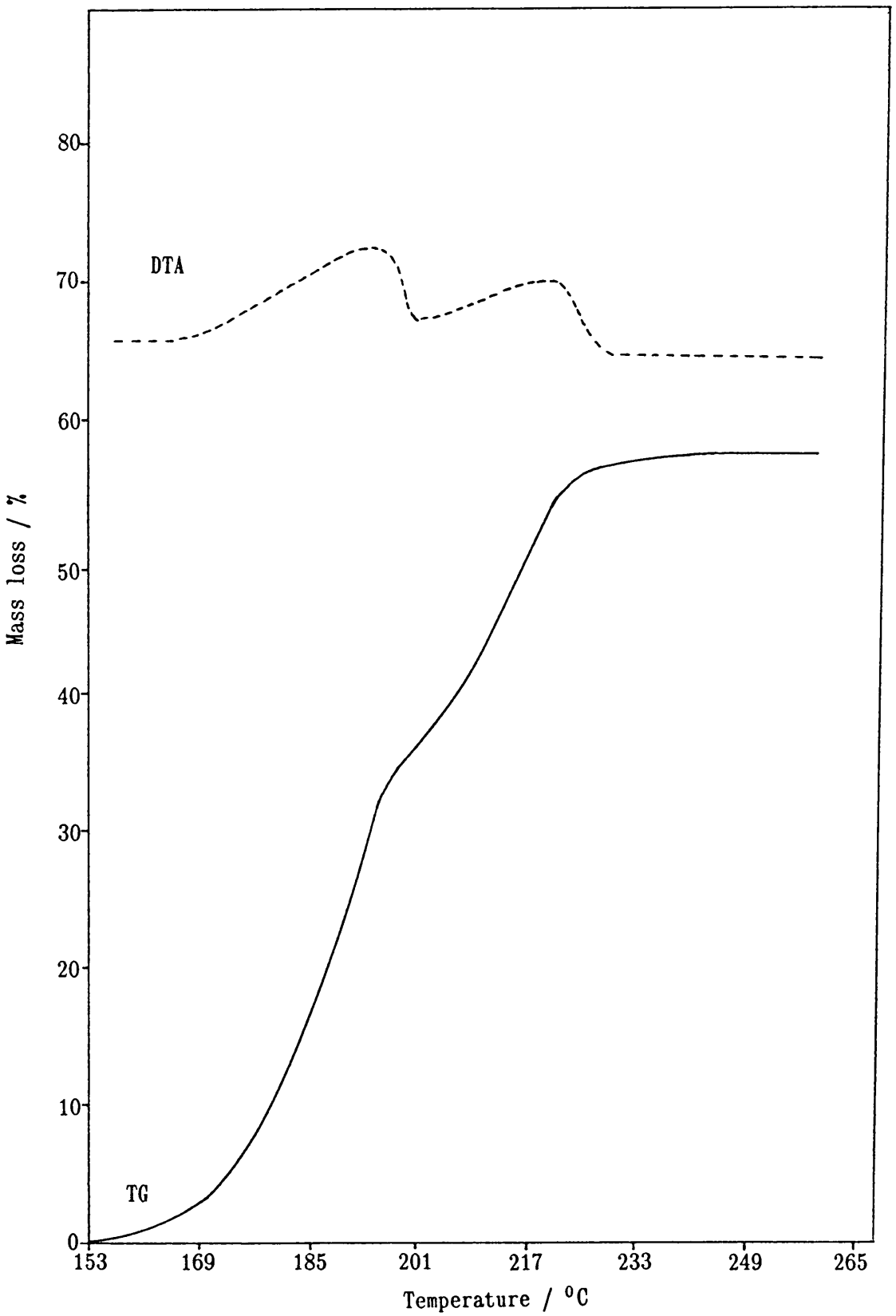

Reaction (6) was, however, not observed. The final product, $CoCl_2(an)$, was blue and became purple in the presence of moist air. Thus when excess ligand was added, the complex $CoCl_2 4(an)$ was formed. Washing the complex extremely well with diethyl ether ensured the replacement of the solvent by ligand molecules and the release of the solvent molecules. The thermal decomposition of $CoCl_2 4(an)$ has not been previously reported, but the analogous, $NiCl_2 4(an)$ formed the intermediates $NiCl_2 2(an)$, $NiCl_2(an)$ and $NiCl_2$ [92].

Kinetic analysis was performed on the dynamic TG curve obtained from the thermal decomposition of $CoCl_2 4(an)$. Reaction (4), where $CoCl_2 4(an)$ is converted to $CoCl_2 2(an)$, conforms to the contracting area model, $kt = 1 - (1 - \alpha)^{\frac{1}{2}}$, with E_a = 202,0 kJ mol^{-1} and ln Z = 50,81. The formation of $CoCl_2(an)$ (reaction 5) is also described by the contracting area model, with E_a = 245,00 kJ mol^{-1} and ln Z = 57,77. A simulated curve was obtained from these parameters, with the percentage contribution of reaction (4) = 66,7% and reaction (5) = 33,3% (Figure 44). A shift with respect to α is observed for the simulated curve. Thus, by increasing the percentage contribution of reaction (5), an improved fit was obtained (Figures 45 and 46).

Figure 44. Plots of the simulated curve (---), obtained from the dynamic analysis (reactions (1) and (2) contributes 66,7% and 33,3%, respectively), and the experimental TG curve (—).

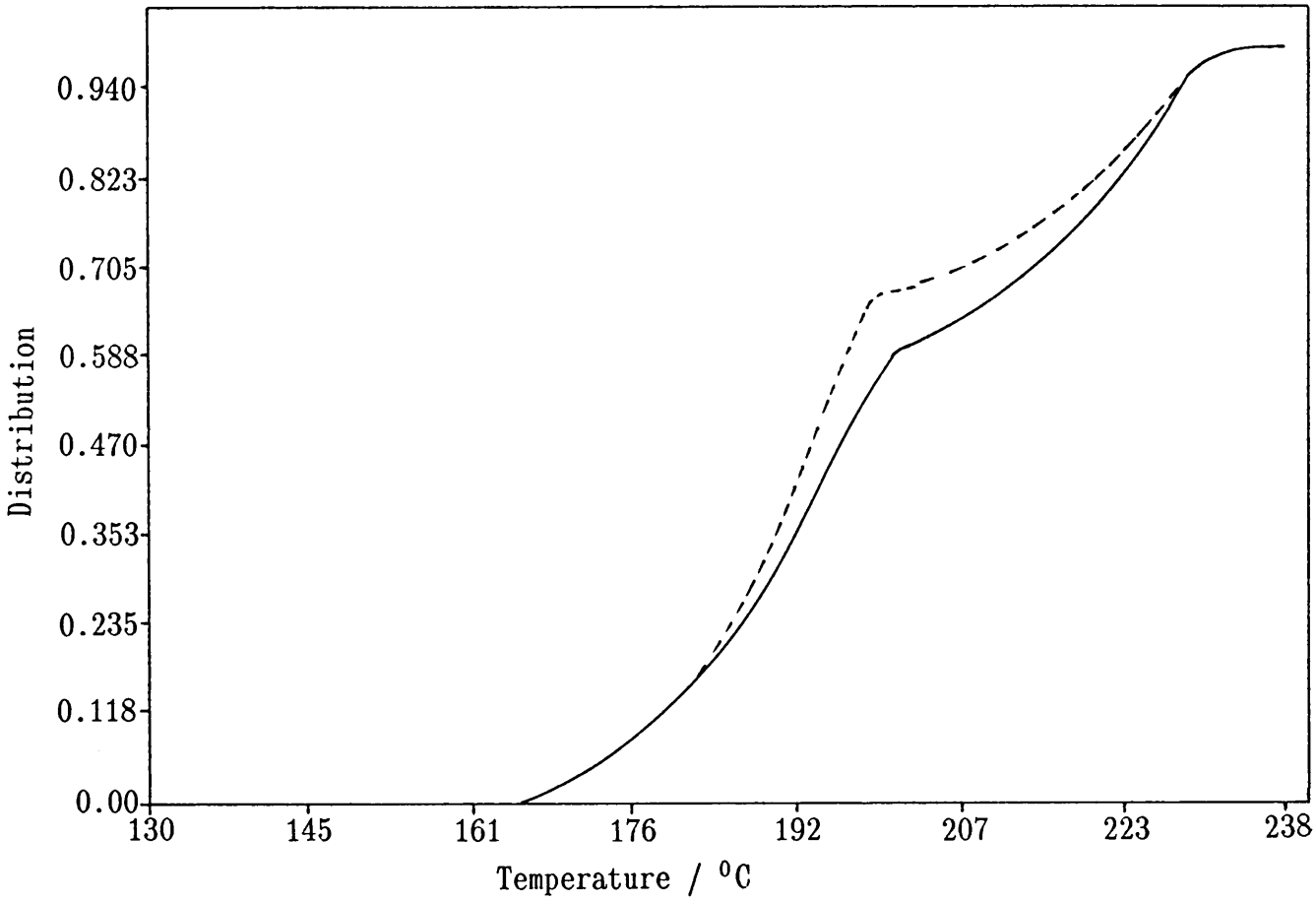

Figure 45. Plots of the simulated curve (---), obtained from the dynamic analysis (reactions (1) and (2) contributes 60,0% and 40,0%, respectively), and the experimental TG curve (—).

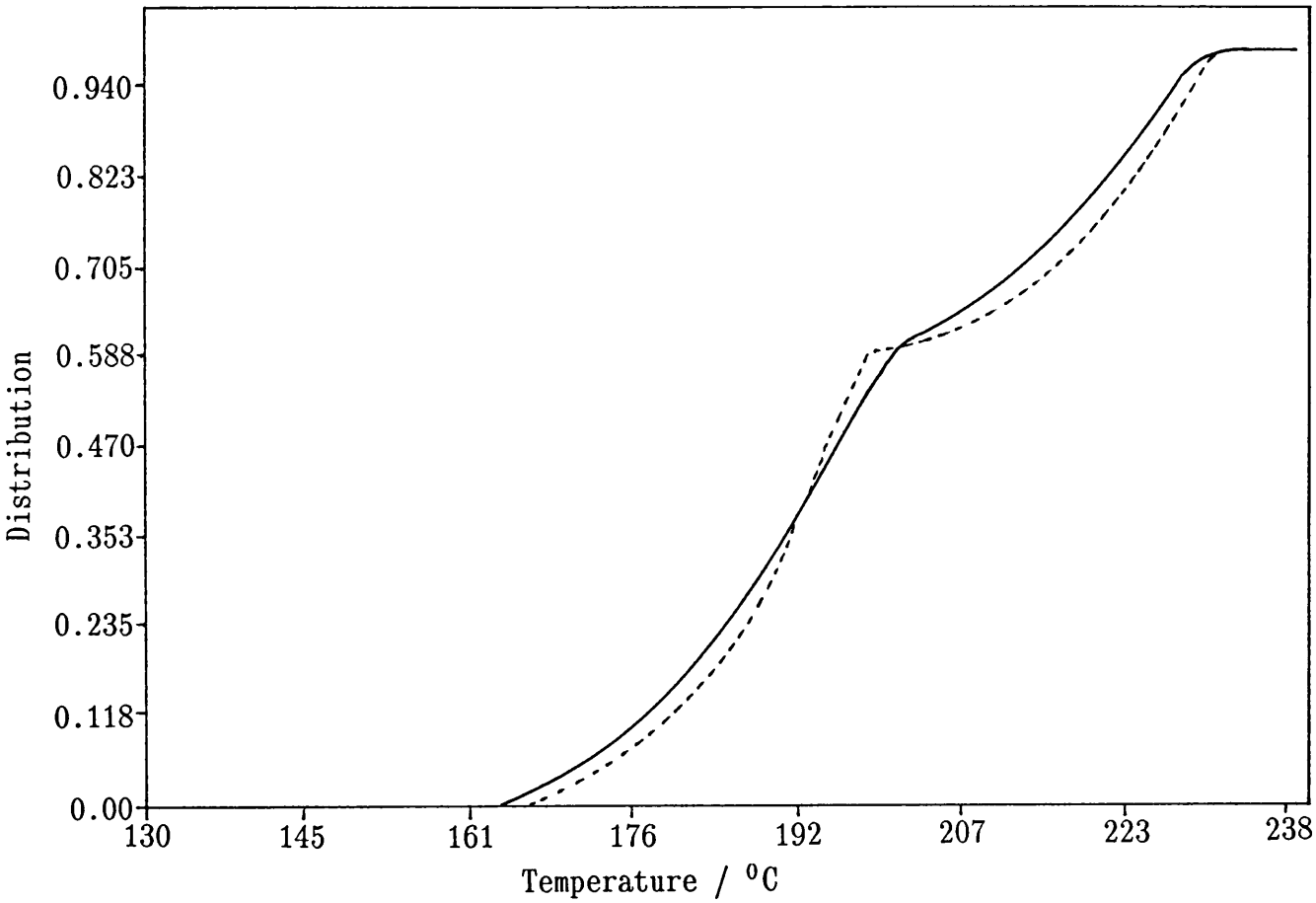

Figure 46. Plots of the simulated curve (---), obtained from the dynamic analysis (reactions (1) and (2) contributes 56,0% and 44,0%, respectively), and the experimental TG curve (—).

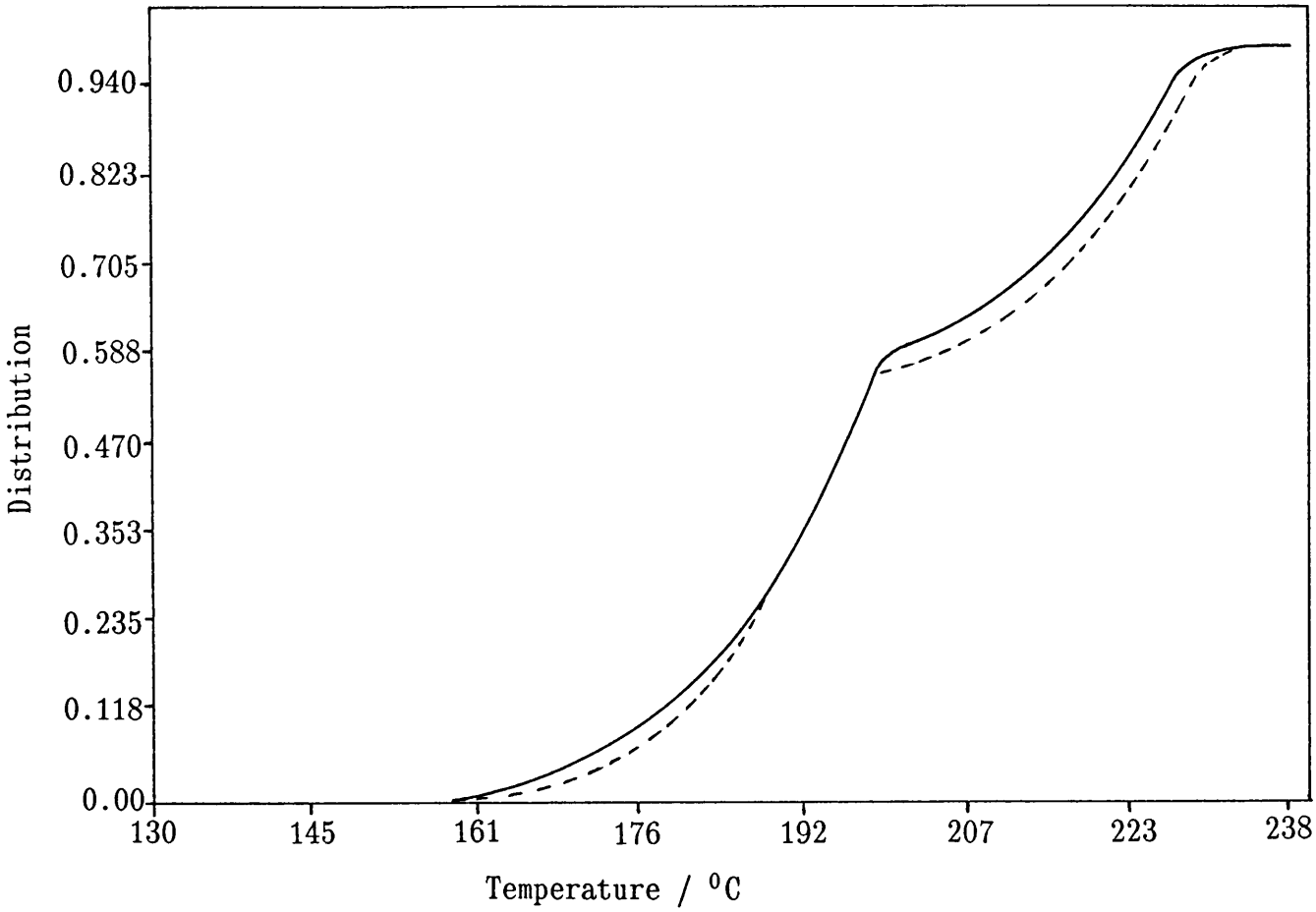

The TG curve shows that $CoCl_2$(an) is a stable intermediate up to 500^{0}C. Thus a very strong bond, which can only be broken at high temperatures, exists between $CoCl_2$ and aniline. The kinetic studies revealed a larger activation energy for the cleavage of the bond between $CoCl_2$(an) and aniline, than for the cleavage of the bond between $CoCl_2$2(an) and aniline.

10.2.2 Isothermal results

Reaction (4), the formation of $CoCl_2$2(an), was investigated in the temperature range 137^{0}C to 146^{0}C. A mass loss of 37,1% was expected, but instead the reaction continued up to a mass loss of approximately 56%. This mass loss corresponds with reaction (4) and (5), and therefore suggests the occurence of overlapping processes.

Reaction (4) consists of an induction period and a deceleratory period. The induction period, $0 < \alpha < 0{,}35$, conforms to the linear rate law with an activation energy of 205,8 kJ mol^{-1} and a ln Z value of 55,01. The deceleratory period, $0{,}35 < \alpha < 1{,}00$, conforms to the contracting area model, with E_a = 78,22 kJ mol^{-1} and ln Z = 17,36.

Reaction (5) is also described by the contracting area model, with E_a = 118,5 kJ mol^{-1} and ln Z = 27,04.

At low heating rates, dynamic curves are the equivalent of isothermal curves, thus using a heating rate of 5^{0}C min^{-1}, a

dynamic TG curve may be simulated (Figure 47). The percentage contribution of the induction period was estimated at 23,35% and the percentage contribution of the deceleratory period of reaction (4) and reaction (5) at 43,37% and 33,27%, respectively. A very poor fit was obtained. The differences in temperatures may be attributed to the low isothermal temperatures at which reaction (5) occurs. Due to this, large differences between the results of the kinetic analysis of the dynamic and isothermal curves, are observed.

Figure 47. Plots of the simulated curve (---), obtained from the isothermal studies, and the experimental TG curve (—).

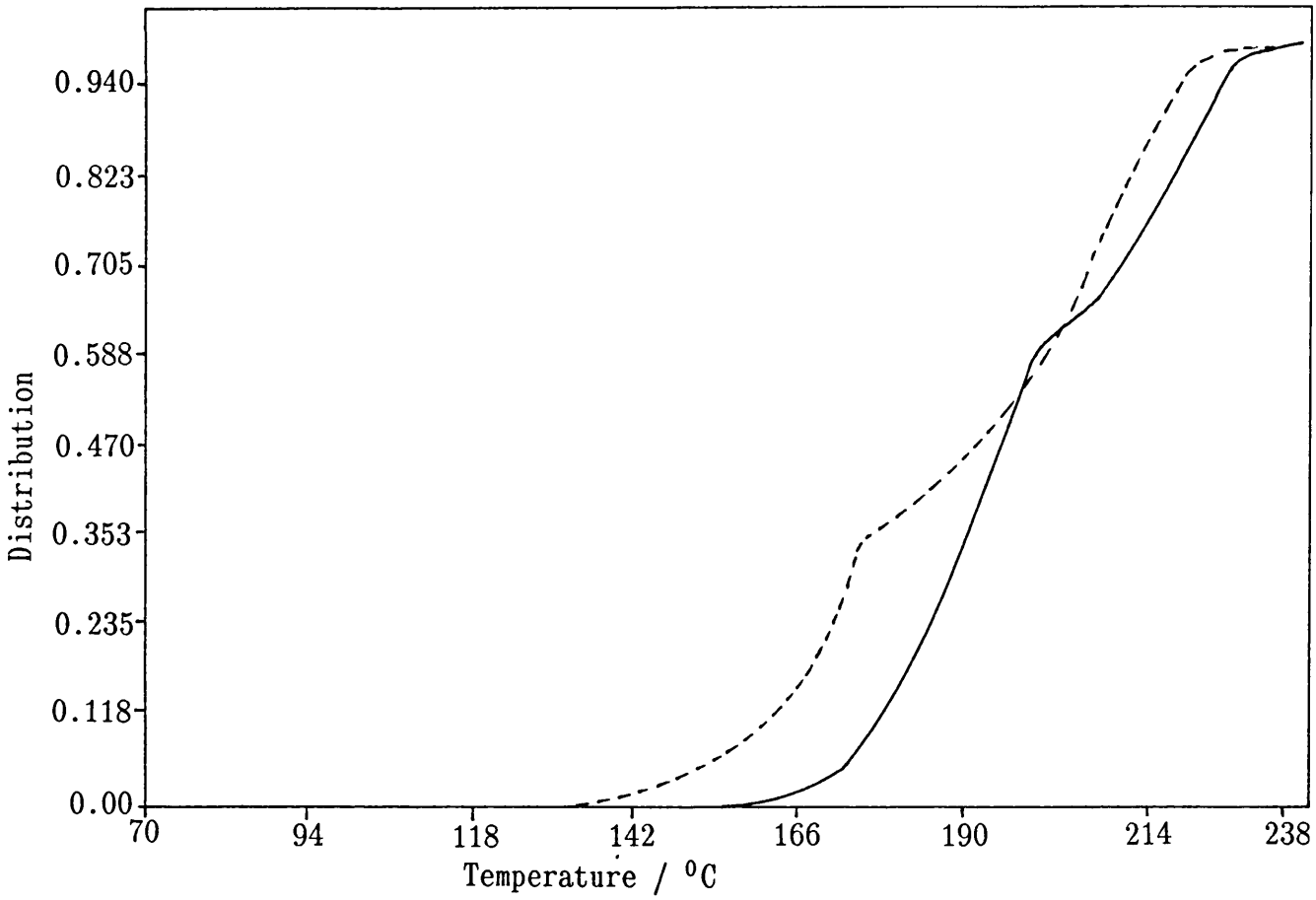

10.2.3 DSC results

The DSC studies were performed on the complex $CoCl_2 4(an)$ in open sample pans and recorded at $5^0C\ min^{-1}$. Figure 48 represents the DSC trace, with reactions (4) and (5) occuring simultaneously.

The large endothermic conversion of $CoCl_2 4(an)$ to $CoCl_2(an)$ results in an enthalpy value of 407,8 kJ mol^{-1} at the peak maxima of $212,8^0C$ and $238,6^0C$. A small peak is observed at a peak maximum of $122,6^0C$. An enthalpy value of 11,18 kJ mol^{-1} was obtained by integration. The enthalpy value is of small significance compared with the value obtained for reactions (4) and (5). The presence of trace amounts of water or solvent may be the reason for the small peak at 112^0C. However, no trace amounts of water were observed in the TG curve. Beech [7] reported an enthalpy value of 148,5 kJ mol^{-1} at peak maxima of 252^0C and 277^0C for the conversion of $CoCl_2 2(an)$ to $CoCl_2$. The enthalpy values reported by Beech for the other ligands pyridine and quinoline differ appreciably from those reported in the previous chapters of this thesis.

The scheme of decomposition, based on structural assignments, is

$CoCl_2 4(an)$ oct. → $CoCl_2 2(an)$ tet. → $CoCl_2(an)$ oct. → $CoCl_2$ oct.

Figure 48. The DSC trace observed for $CoCl_2 4(an)$ at $5^0C\ min^{-1}$.

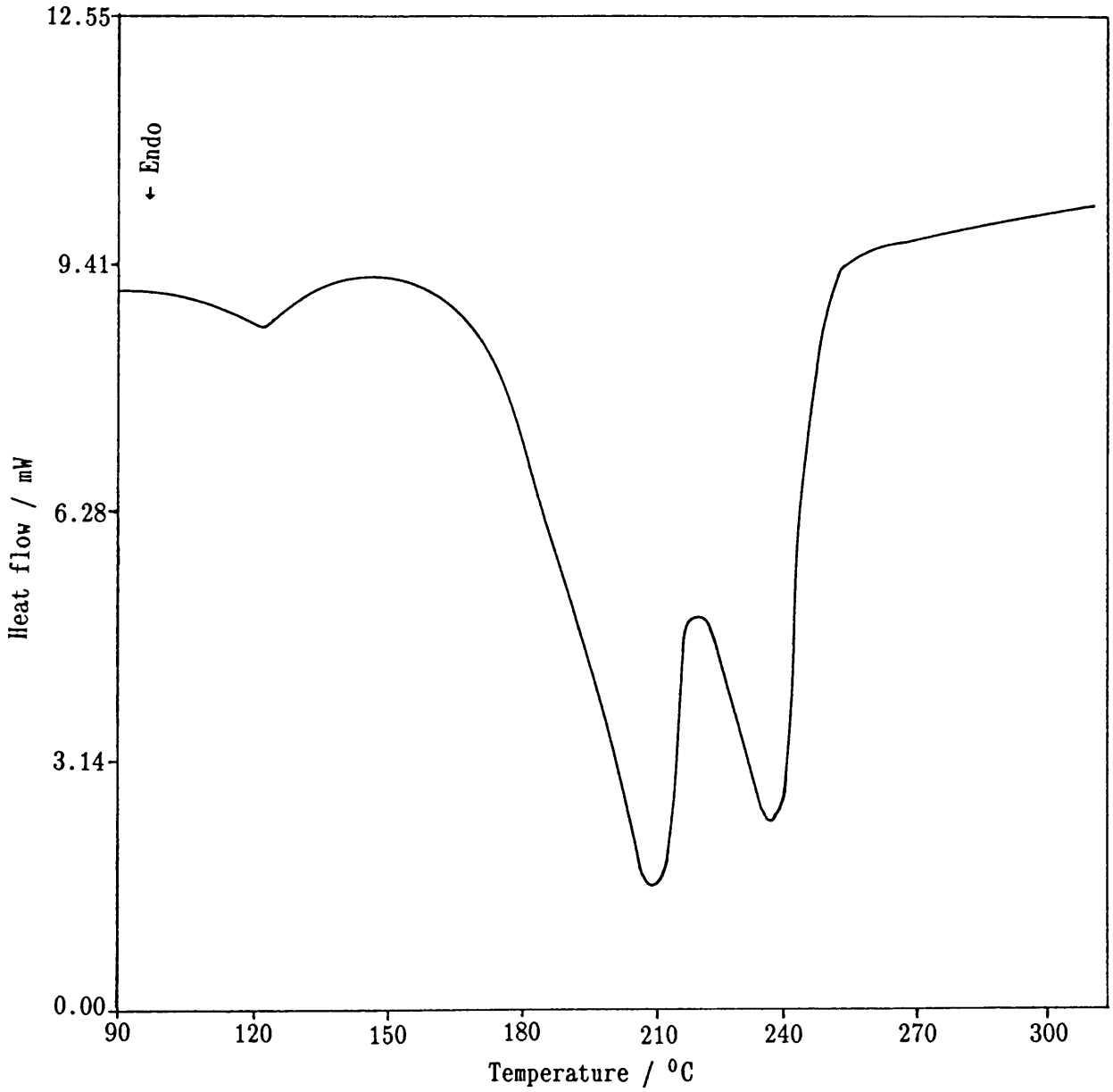

10.3 SOLUTION CHEMISTRY RESULTS

The effect of divalent cation impurities on the thermal decomposition of sodium azide has been reported by Job [20]. Therefore, the study of impurities has been extended to solution chemistry. The first part of this section describes the complexation of aniline, which has not been distilled, with cobalt(II) chloride in non-aqueous solvents. In the second part of this study, the aniline was distilled and the fraction bioling at 165^0C to 168^0C was collected. The aniline solution was covered with aluminium foil and kept in the dark.

(a) Complex formation by $CoCl_2$ with aniline, which has not been distilled, in acetone

The titration curve of 0,0100 mol dm^{-3} $CoCl_2$ with 1,00 mol dm^{-3} aniline showed a flattening at a mole ratio of $CoCl_2$:aniline of 1:3. According to the literature [4], a 1:2 complex forms. The following reactions were postulated:

$$CoCl_2 2S + (an) \rightleftharpoons CoCl_2(an)S + S$$
$$CoCl_2(an)S + (an) \rightleftharpoons CoCl_2 2(an) + S$$

where S represents the solvent molecules.

The thermodynamic quantities were calculated for a 1:2 and 1:3 system and are summarised in Table 24. Zhurba [91,4-7], using spectrophotometric data, reported lower overall formation constants for the formation of the 1:2 complex. The total

Table 24. The thermodynamic quantities for the $CoCl_2$/an system in acetone. $[CoCl_2]_i$ = 0,0100 mol dm^{-3} and $[an]_i$ = 1,00 mol dm^{-3}.

Thermodynamic quantities	1:2 complex formation	1:3 complex formation
$\log \beta_1$	4,666	4,25
$\log \beta_2$	7,031	9,20
$\log \beta_3$	——	-11,58
ΔG_{0-1} (kJ mol^{-1})	-26,62	-24,25
ΔG_{0-2} (kJ mol^{-1})	-40,11	-52,50
ΔG_{0-3} (kJ mol^{-1})	——	-66,07
ΔH^0_{0-1} (kJ mol^{-1})	-7,095	-13,56
ΔH^0_{0-2} (kJ mol^{-1})	-15,46	-12,70
ΔH^0_{0-3} (kJ mol^{-1})	——	-16,85
ΔS^0_{0-1} (J $mol^{-1}K^{-1}$)	65,52	35,87
ΔS^0_{0-2} (J $mol^{-1}K^{-1}$)	82,72	133,56
ΔS^0_{0-3} (J $mol^{-1}K^{-1}$)	——	165,17

enthalpy value of -28,6 kJ mol^{-1}, is, however, more in agreement with the total value of -22,6 kJ mol^{-1} obtained in this study. The enthalpy of formation of $CoCl_2 2(an)$ is more than twice as great as the enthalpy of formation of $CoCl_2(an)$. Zhurba [5,6] reported a decrease in entropy. He attributed this to the solvent effect of acetone, which influences the rupture of the N-H...O bonds in the complex formation process. Positive entropy values were, however, obtained and this is probably due to the formation of N-H...O bonds with aniline and the small ability of acetone to form compounds with cobalt(II) chloride.

The distribution diagram (Figure 49) of the formation of the 1:2 complex, reveals that formation of the complex $CoCl_2(an)$ is dominant up to a percentage of 87,5%. The formation of $CoCl_2(an)$ reaches a maximum at a ratio of approximately 1:1.

During the initial stages of the titration, a significant amount of $CoCl_2 2(an)$ is present. Only after the complex $CoCl_2(an)$ reaches a maximum, does the formation of $CoCl_2 2(an)$ become significant. A poor fit was obtained between the experimental and calculated Q_r values.

The titration curve, flattens at a mole ratio of 1:3. The thermodynamic quantities for the 1:3 complex-formation reaction are summarised in Table 24. The enthalpies of formation for all three complexes are more or less the same. However, the changes in entropy increase with an increase in the number of complex formation products. The thermodynamic constants obtained, showed

Figure 49. The distribution diagram obtained for the 1:2 cobalt(II) chloride-aniline complex. (Aniline not distilled).

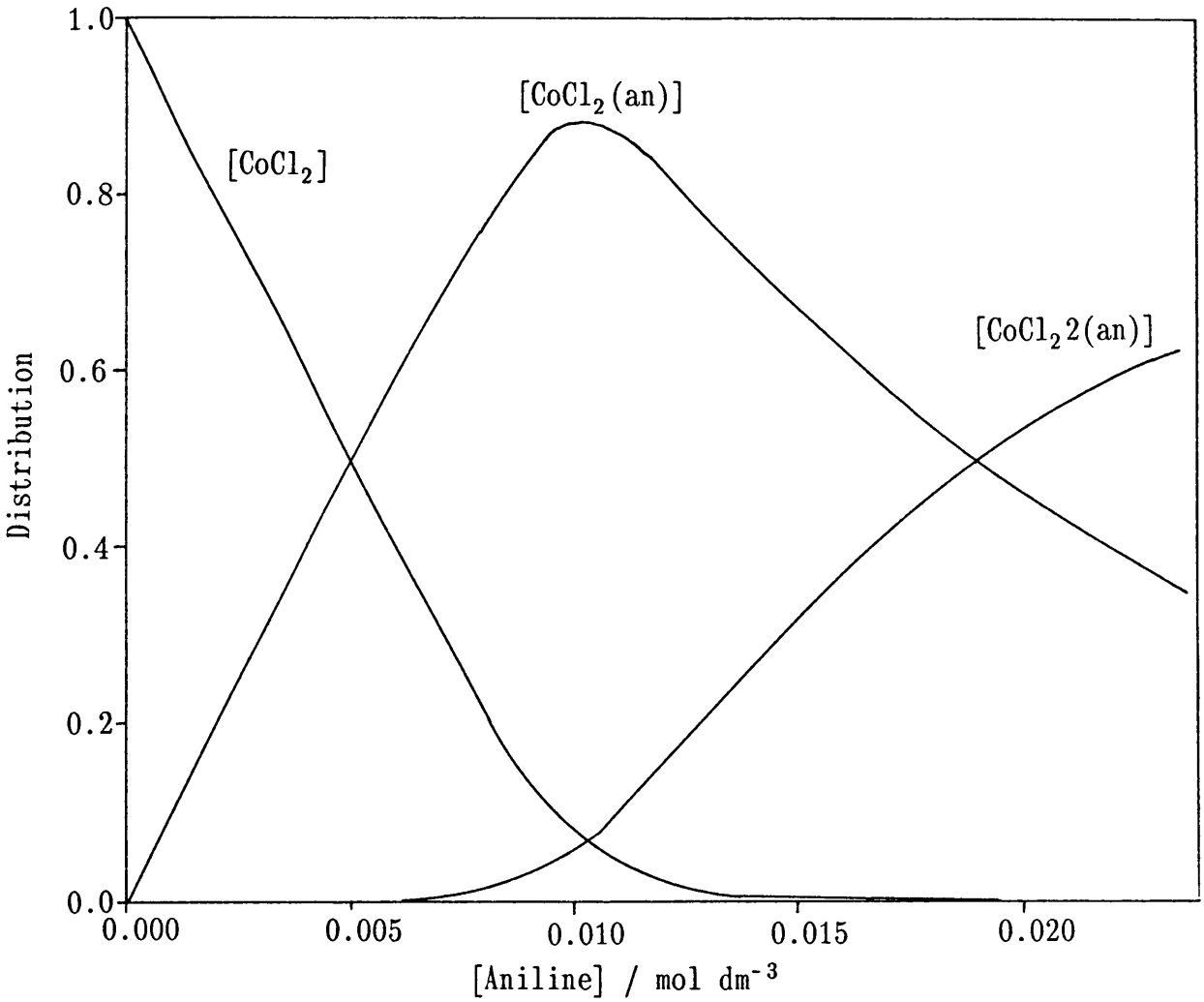

an improved fit, if plotted against the experimental titration curve. However, the distribution diagram indicates a large deviation at a mole ratio of approximately 1:3 (Figure 50). If the formation of a 1:3 complex is possible, then it must also be observed in the distribution curve. A large deviation is observed at a mole ratio of 1:3, which rules out the possibility of a 1:3 complex-formation reaction.

The distribution diagram suggests that a high degree of formation of $CoCl_2$2(an) occurs at a mole ratio of 1:3 and that the formation of $CoCl_2$3(an) increases tremendously at a mole ratio of 1:3. Although an improved fit was obtained for the 1:3 complex formation reaction, the formation of a 1:3 complex is most improbable, as seen from the distribution diagram. This supports the fact mentioned by Christensen [54] that thermodynamic constants, although they may give small minimum errors, do not always describe the system correctly. The impurities in the aniline solution may give complex-formation reactions, which lead to incorrect results. Another possible explanation is that a equilibrium, in addition to the two equilibria between the metal and the ligand, exists. This might lead to the slow formation of $CoCl_2$2(an) at a mole ratio of only 1:3.

Figure 50. The distribution diagram obtained for the 1:3 cobalt(II) chloride-aniline complex. (Aniline not distilled).

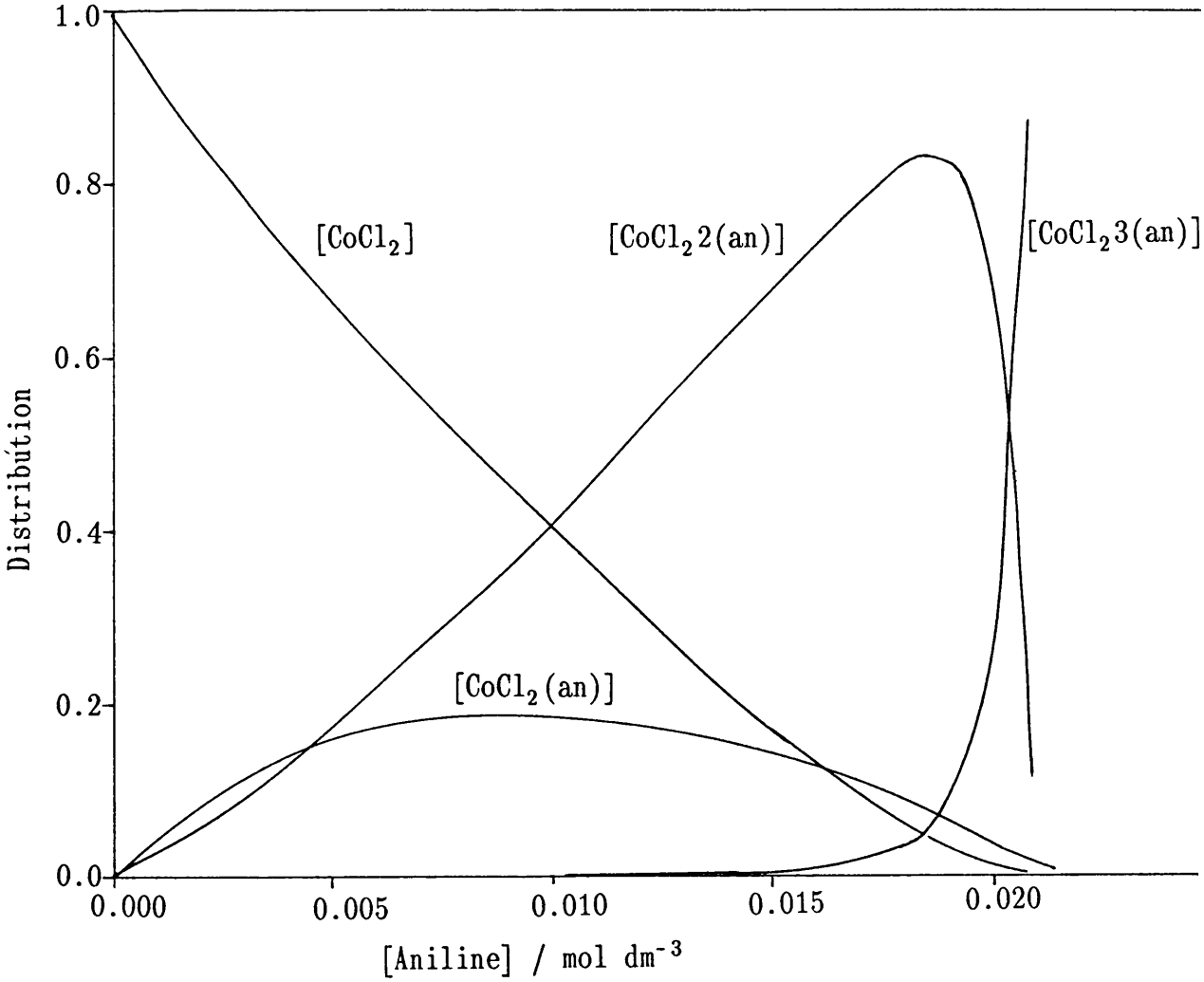

(b) Complex formation of $CoCl_2$ with distilled aniline in acetone

Similarly to Section (a), the titration curve showed a flattening at a mole ratio of 1:3. The thermodynamic constants for a 1:2 and a 1:3 complex formation reaction are summarised in Table 25.

Table 25. The thermodynamic quantities for the $CoCl_2$/an system in acetone. $[CoCl_2]_i$ = 0,0100 mol dm^{-3} and distilled $[an]_i$ = 1,00 mol dm^{-3}.

Thermodynamic quantities	1:2 complex formation	1:3 complex formation
log β_1	4,665	5,03
log β_2	8,304	8,85
log β_3	——	10,87
ΔG_{0-1} (kJ mol^{-1})	-26,61	-28,69
ΔG_{0-2} (kJ mol^{-1})	-47,37	-50,50
ΔG_{0-3} (kJ mol^{-1})	——	-62,01
ΔH^0_{0-1} (kJ mol^{-1})	-18,82	-19,00
ΔH^0_{0-2} (kJ mol^{-1})	-28,08	-26,54
ΔH^0_{0-3} (kJ mol^{-1})	——	-34,39
ΔS^0_{0-1} (J $mol^{-1}K^{-1}$)	26,14	32,52
ΔS^0_{0-2} (J $mol^{-1}K^{-1}$)	64,73	80,40
ΔS^0_{0-3} (J $mol^{-1}K^{-1}$)	——	92,68

Consider the formation of the 1:2 complex; the enthalpy of formation of $CoCl_2 2(an)$ is more than one and a half times greater than the enthalpy of formation of $CoCl_2(an)$. Similarly to Section (a), both reactions are enthalpy driven, with an increase in the change in enthalpy as the titration proceeds. A poor fit was obtained between the experimental and calculated Q_r values with the distribution diagram (Figure 51) revealing a 63% degree of formation for $CoCl_2(an)$ at a mole ratio of approximately 1:1. All three species are present for most of the time during the titration.

Consider the possibility of three equilibria being present during the titration. The thermodynamic constants are summarised in Table 25. The enthalpy of formation for the complex $CoCl_2 n(an)$ increases with an increase in n. The formation reactions of $CoCl_2(an)$, $CoCl_2 2(an)$ and $CoCl_2 3(an)$ are all enthalpy driven. The entropy and thus the amount of disorder increases as the titration proceeds. The values obtained for the thermodynamic constants for the 1:2 complex and the first two parameters for the 1:3 complex formation are close. Again, an improved fit was obtained between the experimental and calculated Q_r values. The distribution diagram reveals abnormal changes at a mole ratio of 1:3 (Figure 52) and again rules out the existence of 1:3 complex-formation.

Figure 51. The distribution diagram obtained for the 1:2 cobalt(II) chloride-aniline complex. (Aniline distilled).

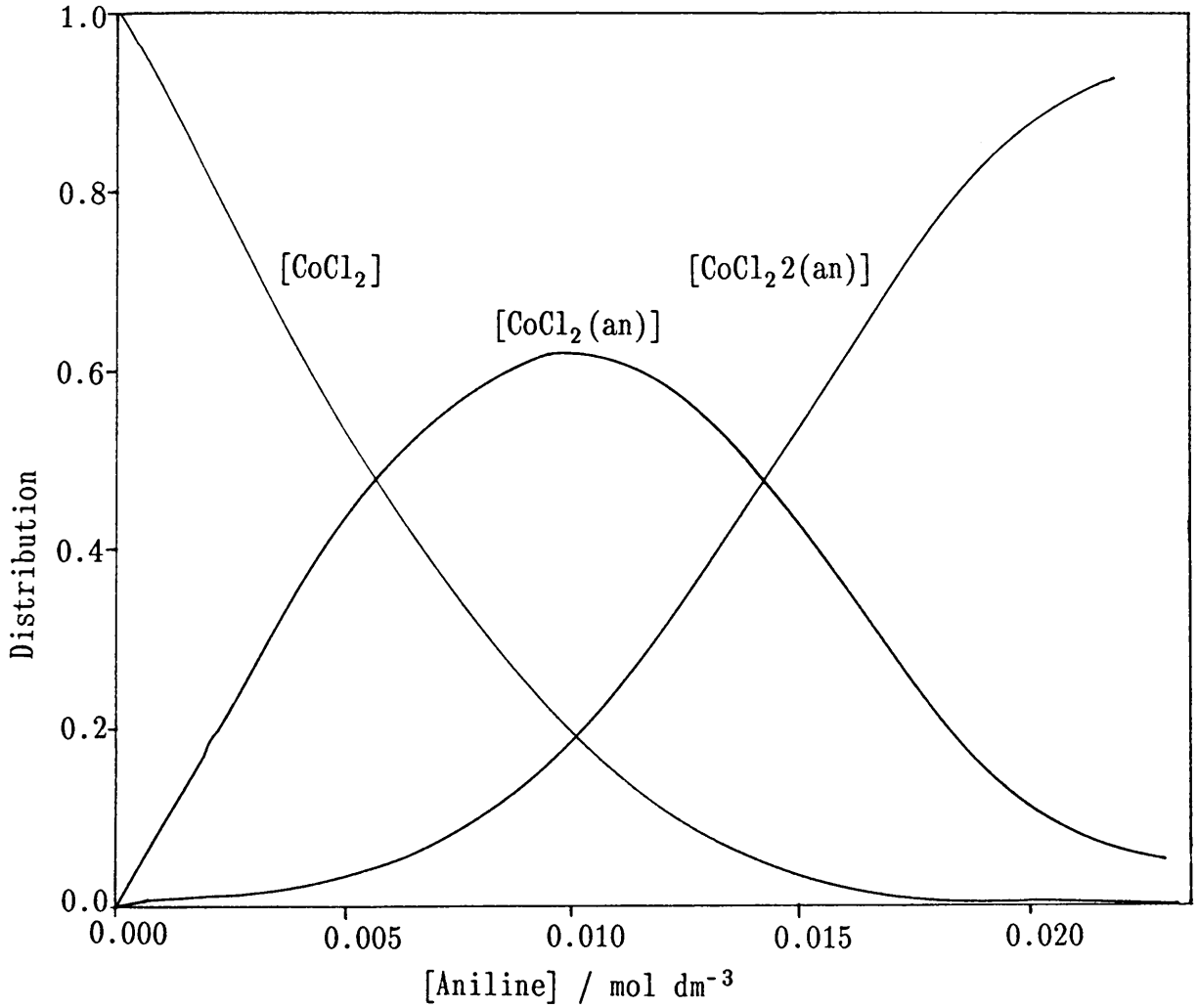

Figure 52. The distribution diagram obtained for the 1:3 cobalt(II) chloride-aniline complex. (Aniline distilled).

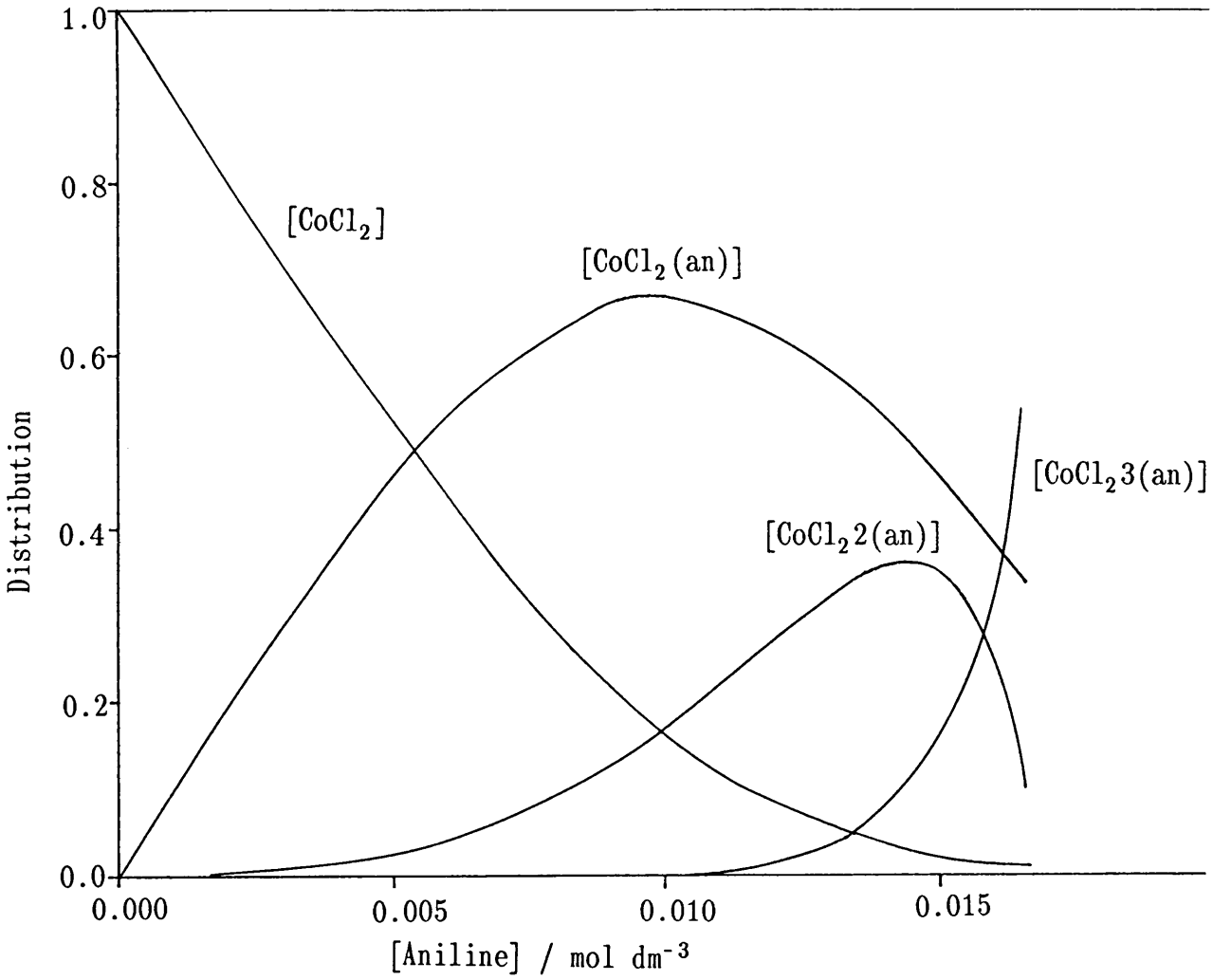

The $CoCl_2$(an) complex (Figures 51 and 52) is dominant during the titration. If $CoCl_2$3(an) exists as a stable complex, then it will start forming at a mole ratio of approximately 1:3. Thus the following reactions are dominant:

$$CoCl_2S + (an) \rightarrow CoCl_2S(an)$$
$$CoCl_2S(an) + (an) \rightarrow CoCl_2 2(an) + 2S$$

Thus, the formation of $CoCl_2$2(an) is dominant up to a mole ratio of 1:3. It is followed by the formation of $CoCl_2$3(an) at a mole ratio of 1:3. Presumbly the complex $CoCl_2$4(an) will also form if excess ligand is added. The titration curve always showed a small slope at a mole ratio of approximately 1:3, which is not due to dilution of the metal ion, but possibly due to the presence and the formation of small quantities of $CoCl_2$3(an), followed by the formation of $CoCl_2$4(an). The solid state results revealed the complex $CoCl_2$3(an) to be an unstable intermediate, with a weak interaction between $CoCl_2$2(an) and aniline. Thus, it seems that although the titration curve flattens at a mole ratio of 1:3, only the slow complex-formation reaction of the 1:2 complex occurs.

10.4 DISCUSSION

The basicity of the pyridine-related ligands was reported in Chapter 1. The low pK_a value for aniline led to the assumption of low enthalpy values. However, high values were obtained. This effect can not be explained in terms of electron delocalisation,

since aniline lacks suitable π-acceptor orbitals. A possible reason may be that in the aniline complex there is a closer approach of the bonding nitrogen because the bulky phenyl group, which is one atom removed from the cobalt atom, causes less steric repulsion.

The impurities had a significant effect on the formation of $CoCl_2 2(an)$ in acetone. Due to the impurities the degree of formation of $CoCl_2(an)$ was larger in distilled aniline. Thus the impurities suppressed the formation of $CoCl_2 2(an)$. The impurities also resulted in significant differences in the enthalpy values.

The solid state results indicated a stronger interaction between $CoCl_2(an)$ and aniline than between $CoCl_2 2(an)$ and aniline (isothermal and dynamic).

Furthermore, the solution chemistry results revealed that the equilibrium of the solvate complex is significant, resulting in the slow formation of $CoCl_2 2(an)$ at a mole ratio of 1:3. The formation of the complex $CoCl_2 2(an)$ is dominant at this mole ratio. The results indicate a stronger interaction between $CoCl_2$ and aniline than between $CoCl_2(an)$ and aniline. The complex-formation reaction of $CoCl_2(an)$ was, however, not investigated.

CHAPTER 11

THE THERMAL ANALYSIS OF $MnCl_2$2(py) AND $NiCl_2$2(py)

11.1 INTRODUCTION

Pyridine, which is a π-bonding ligand, very readily forms complexes with transition metals. In many of these complexes, which contain a π-bonding ligand, the metal atoms are in a low positive, zero, or negative formal oxidation state. In addition these complexes are characterised by the normal σ-bond, L → M, but also by an additional π-bond, M → L, which results from the back donation of electrons from the d-orbitals of the metal to the π^*-antibonding orbitals of the ligand. Furthermore, pyridine is an interesting non-aqueous solvent, since it is a good base (pK_b = 8,81), and has a low dielectric constant (ϵ = 12,3). Rosenthal [94] evaluated the spectrochemical parameters obtained from complexes of transition metal ions with pyridine.

The thermal decomposition of a metal complex is usually initiated by the splitting of a coordinate bond. The decomposition temperature may be used in order to characterise the strength of this bond [95]. The thermal decomposition of the complex of cobalt(II) with pyridine has been reported in Chapter 6. The thermal decomposition involved the initial liberation of pyridine, arising from the splitting of the metal-pyridine-nitrogen bond. Therefore, an investigation of the thermal

decomposition of metal-pyridine complexes type may furnish information on the factors influencing the strength of the metal-pyridine-nitrogen bond. With this end in view, the study was extended to manganese(II) and nickel(II) complexes. Comparative data were therefore obtained by investigating, under identical conditions, the thermal behaviour of these complexes.

11.2 THERMOGRAVIMETRIC RESULTS

11.2.1 Dynamic results

The white-pink $MnCl_2 2(py)$ crystals decompose over the temperature range 103^0C to 256^0C, according to the following decomposition reactions:

$$MnCl_2 2(py)\ (s) \rightarrow MnCl_2(py)\ (s) + (py)\ (g) \qquad (1)$$

$$MnCl_2 2(py)\ (s) \rightarrow MnCl_2\ (s) + 2(py)\ (g) \qquad (2)$$

Experimentally mass losses of 27,6% (theor. mass loss = 27,8%) and 55,2% (theor. mass loss = 55,7%) were obtained for reactions (1) and (2), respectively. The TG curve indicated two successive reactions, with the complex $MnCl_2(py)$ existing as a stable intermediate over the temperature range 140^0C to 150^0C and with $MnCl_2$, stable over the temperature range 250^0C to 450^0C, as the final decomposition product. The liberation of a fraction of pyridine, which shows the existence of the intermediate, $Mn_3Cl_6 2(py)$, was reported previously [8,79,80]. However, a heating rate of $1^0C\ min^{-1}$ could not provide the thermodynamic

evidence (TG and DTA) for the existence of the complex $Mn_3Cl_6 2(py)$. Thus, according to Beech, Liptay and Brown the following additional decomposition reaction occurs:

$$3MnCl_2(py)\ (s) \rightarrow Mn_3Cl_6 2(py)\ (s) + (py)\ (g) \qquad (3)$$

Pale yellow crystals, in agreement with Allan [96], were obtained for the complex $NiCl_2 2(py)$. In contrast Majumdar [92] reported the colour of the complex $NiCl_2 2(py)$ as light blue, which is, in fact, the colour of the complex $NiCl_2 4(py)$. The TG trace, recorded at $1^0C\ min^{-1}$, shows two successive reactions occuring over the temperature range 114^0C to 261^0C. It revealed the existence of the stable intermediate, $NiCl_2(py)$ over the temperature range 160^0C to 187^0C and the decomposition product $NiCl_2$, which is stable over the temperature range 260^0C to 397^0C. The final decomposition product was NiO at a temperature of approximately 593^0C and this corresponds with the mass loss for the reaction of $NiCl_2 2(py)$ to NiO (experimentally found = 74,0% and theoretical = 74,0%). A scheme similar to the thermal decomposition scheme of $MnCl_2 2(py)$ was obtained and therefore

$$NiCl_2 2(py)\ (s) \rightarrow NiCl_2(py)\ (s) + (py)\ (g) \qquad (4)$$

$$NiCl_2 2(py)\ (s) \rightarrow NiCl_2\ (s) + 2(py)\ (g) \qquad (5)$$

This is in accordance with the previous investigations [8,92,96,97]. Additionally, Murgulescu [98] and Liptay [80] claimed the existence of the complex $Ni_3Cl_6 2(py)$. However, this distinct complex was not detected by the thermogravimetric

analysis.

Kinetic analysis was performed on the dynamic curves of $NiCl_2 2(py)$ and $MnCl_2 2(py)$ (Table 26).

Table 26. The results from the kinetic analyses of the TG curves for $NiCl_2 2(py)$ and $MnCl_2 2(py)$ recorded at $1^0C\ min^{-1}$.

Decomposition reaction	Kinetic equation	E_a ($kJ\ mol^{-1}$)	ln Z ($ln\ min^{-1}$)
$MnCl_2 2(py) \rightarrow MnCl_2(py) + py$	$1-(1-\alpha)^{\frac{1}{2}}$	129,00	34,94
$MnCl_2(py) \rightarrow MnCl_2 + py$	$1-(1-\alpha)^{\frac{1}{2}}$	116,00	23,80
$NiCl_2 2(py) \rightarrow NiCl_2(py) + py$	$1-(1-\alpha)^{\frac{1}{2}}$	161,00	42,64
$NiCl_2(py) \rightarrow NiCl_2 + (py)$	$1-(1-\alpha)^{\frac{1}{3}}$	133,00	26,72

The contracting area model described all the decomposition reactions except the decomposition reaction of $NiCl_2(py)$ to $NiCl_2$, which conforms to the contracting volume model. Larger activation energies and frequency factors were obtained for the thermal decomposition of $NiCl_2 2(py)$. According to the stability series established by Irving and Williams [99], Ni > Co > Mn. The low activation energies and frequency factors obtained for the complex $MnCl_2 2(py)$, may be attributed to the lower initial temperature of decomposition and the position of Mn in the stability series. The combination of the parameters obtained, the heating rate ($1^0C\ min^{-1}$) and the percentage contribution of the specific reaction in terms of the total decomposition reaction, resulted in the simulated dynamic curves for the complexes. Excellent fits were obtained for both complexes (Figure 53 and 54).

Figure 53. Plots of the simulated curve (---), obtained from the analysis of the dynamic curve, and the experimental curve (—) for $NiCl_2 2(py)$.

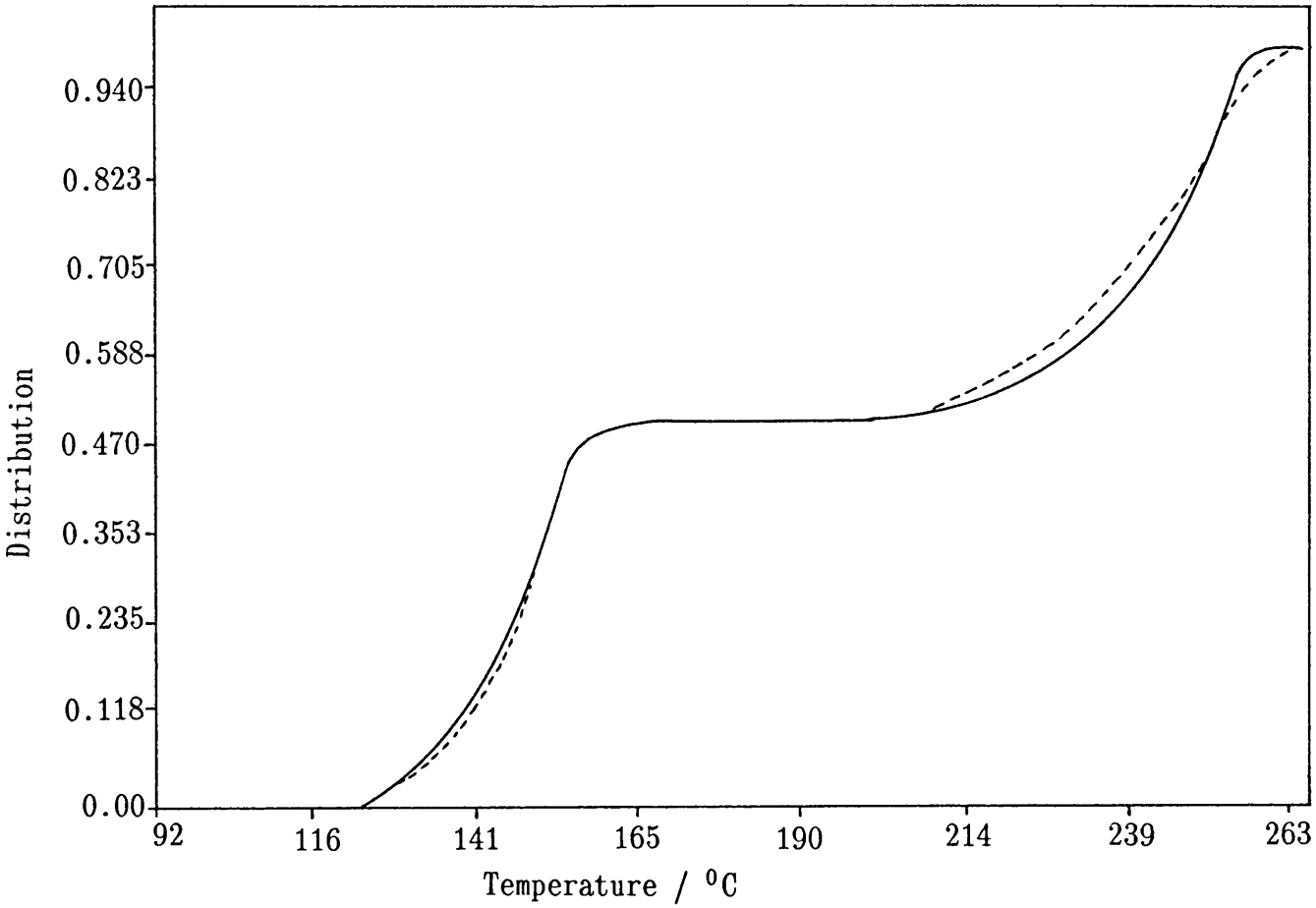

Figure 54. Plots of the simulated curve (---), obtained from the analysis of the dynamic curve, and the experimental curve (—) for $MnCl_2 2(py)$.

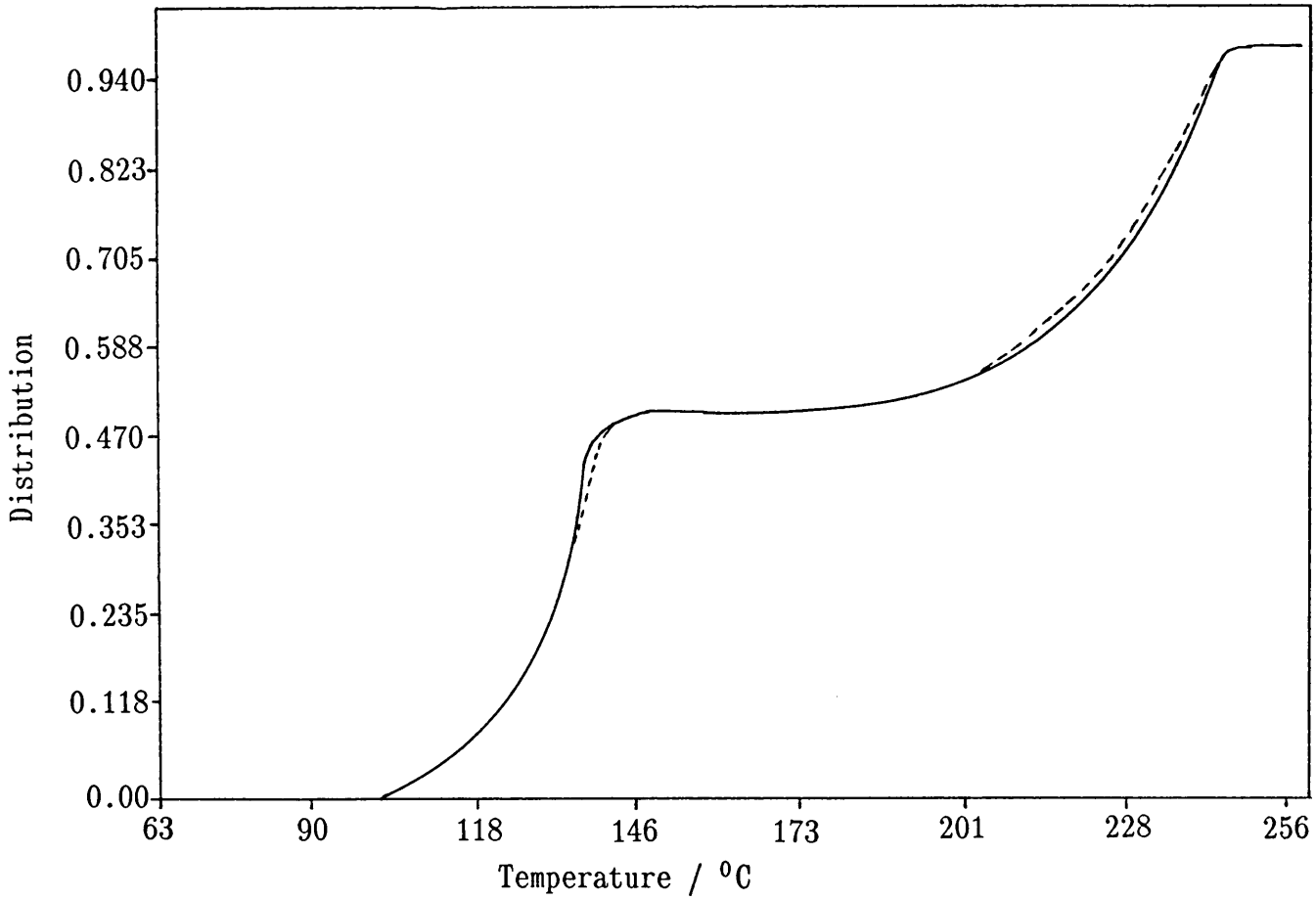

11.2.2 Isothermal results

The isothermal studies performed on the complexes $NiCl_2 2(py)$ and $MnCl_2 2(py)$, gave the following results:

In the temperature range 116^0C to 123^0C the conversion of $MnCl_2 2(py)$ to $MnCl_2(py)$ conforms to the contracting area model, $1-(1-\alpha)^{\frac{1}{2}} = kt$, for $0,09 < \alpha < 0,99$. The values, $E_a = 204,41$ kJ mol^{-1} and ln Z = 58,51 were calculated. The average mass loss obtained was 27,5% (theoretical mass loss = 27,8%).

The conversion of $MnCl_2(py)$ to $MnCl_2$ was studied over the temperature range 184^0C to 194^0C and is described by the contracting area model, over the whole α-range. The values of $E_a = 107,76$ kJ mol^{-1} and ln Z = 21,32 were obtained. Experimentally a mass loss of 37,8% was observed, which compares well with the theoretical mass loss of 38,5%.

The temperature range 144^0C to 152^0C involves the conversion of $NiCl_2 2(py)$ to $NiCl_2(py)$ and conforms to the contracting area model, over the whole α-range, with $E_a = 125,5$ kJ mol^{-1} and ln Z = 32,47. Experimentally a mass loss of 27,0% was obtained (theoretical mass loss = 27,5%).

The temperature range 212^0C to 222^0C, involves in the formation of $NiCl_2$ and is described by the contracting volume model $1-(1-\alpha)^{\frac{1}{3}} = kt$, for $0,04 < \alpha < 0,93$. The parameters, $E_a = 183,6$ kJ mol^{-1} and ln Z = 39,13 were determined. A mass loss of 37,3%

was found (theoretical mass loss = 37,9%).

By assuming a heating rate of $1^0C\ min^{-1}$, the kinetic parameters were combined to simulate a dynamic curve. A few deviations were observed, when the curve was compared to the experimental dynamic curves (Figures 55 and 56).

Although each decomposition reaction for Mn and Ni conforms to the same rate equation (dynamic and isothermal), large differences are observed for the E_a and ln Z values. Both the manganese and nickel complexes revealed an increase in the ratio E_a to ln Z for the second reaction

$$MCl_2(py)\ (s) \rightarrow MCl_2\ (s) + (py)\ (g)$$

where M = manganese or nickel.

This reveals the complex $MCl_2(py)$ to be a very stable intermediate, when compared to the complex $MCl_2 2(py)$. The existence of $Mn_3Cl_6 2(py)$ and of $Ni_3Cl_6 2(py)$ was ruled out by the isothermal studies.

Figure 55. Plots of the simulated curve (---), obtained from the analysis of the isothermal curves, and the experimental curve (—) for $NiCl_2 2(py)$.

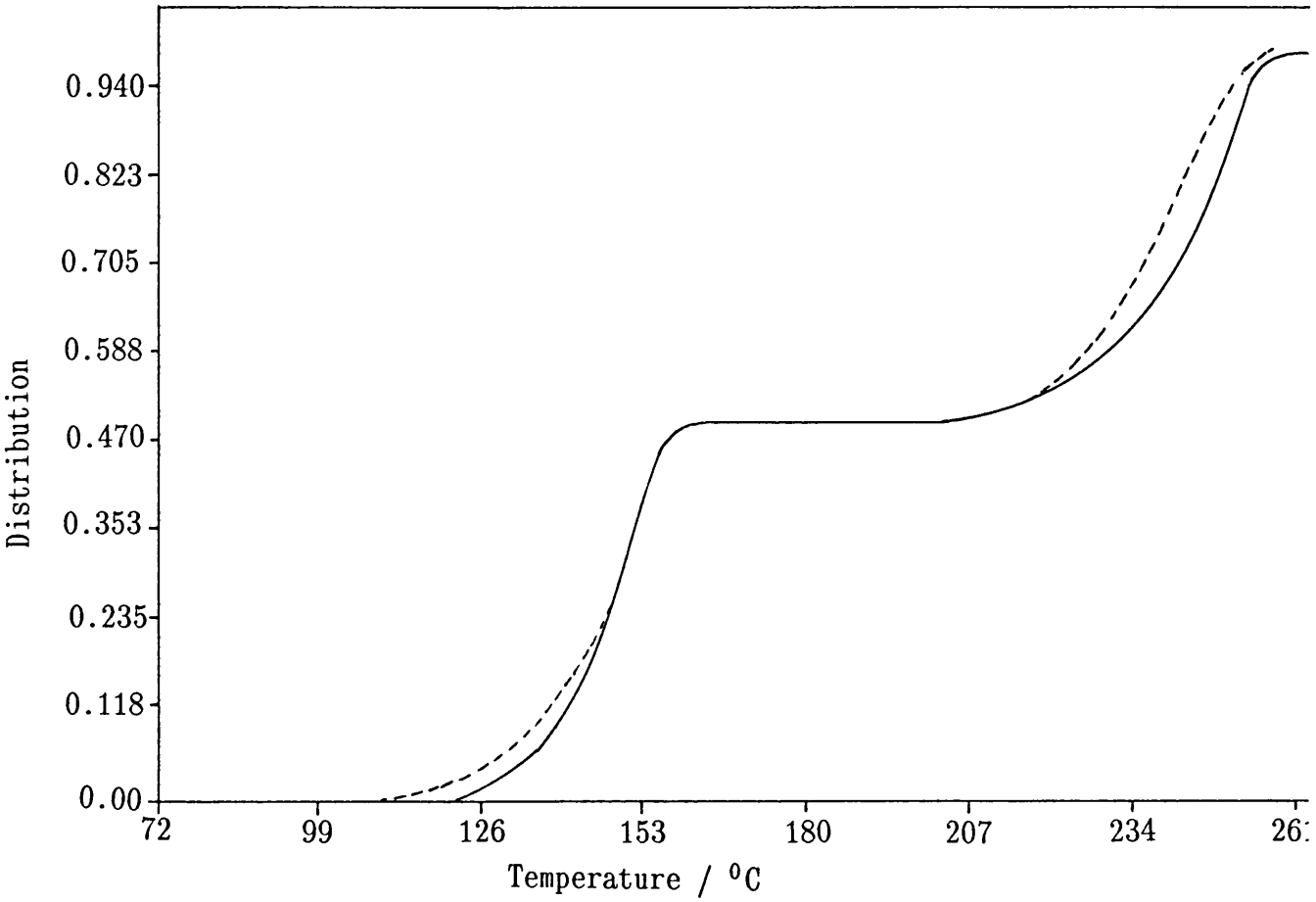

Figure 56. Plots of the simulated curve (---), obtained from the analysis of the isothermal curves, and the experimental curve (—) for $MnCl_2 2(py)$.

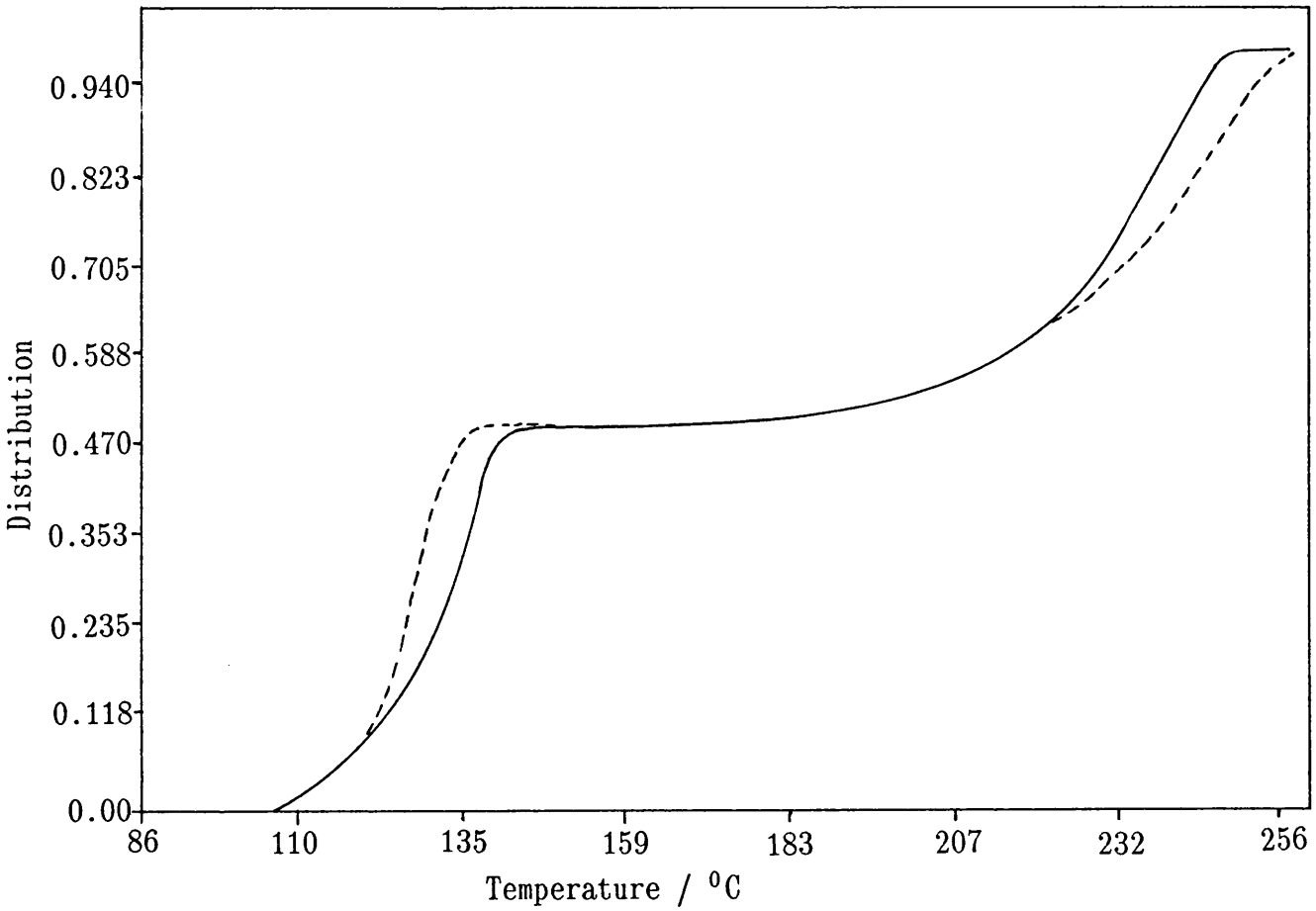

11.2.3 DSC results

The DSC studies were performed in open sample pans and the heating rate was $5^0C\ min^{-1}$. The DSC traces for $MnCl_2 2(py)$ and $NiCl_2 2(py)$ are shown in Figures 57 and 58, respectively.

The dynamic and isothermal studies showed the presence of two decomposition reactions for both complexes, thus leading to the anticipitation of two peaks in the DSC studies. However, three peaks, using DCS studies, were observed for both complexes, thus an additional decomposition reaction occurs. The first peak, at approximately 170^0C, may be assigned to the evolution of pyridine from the complexes $MnCl_2 2(py)$ and $NiCl_2 2(py)$. The second and third peaks represent two reactions occuring simultaneously. The additional peak (second peak) observed at 240^0C for $MnCl_2 2(py)$ and at approximately 280^0C for $NiCl_2 2(py)$ provides evidence, which could not be obtained from the dynamic and isothermal studies, for the existence of $Mn_3Cl_6 2(py)$ and $Ni_3Cl_6 2(py)$. The third peak represents the formation of $MnCl_2$ and $NiCl_2$.

Figure 57. The DSC trace recorded for $MnCl_2 2(py)$ at $5^0C\ min^{-1}$.

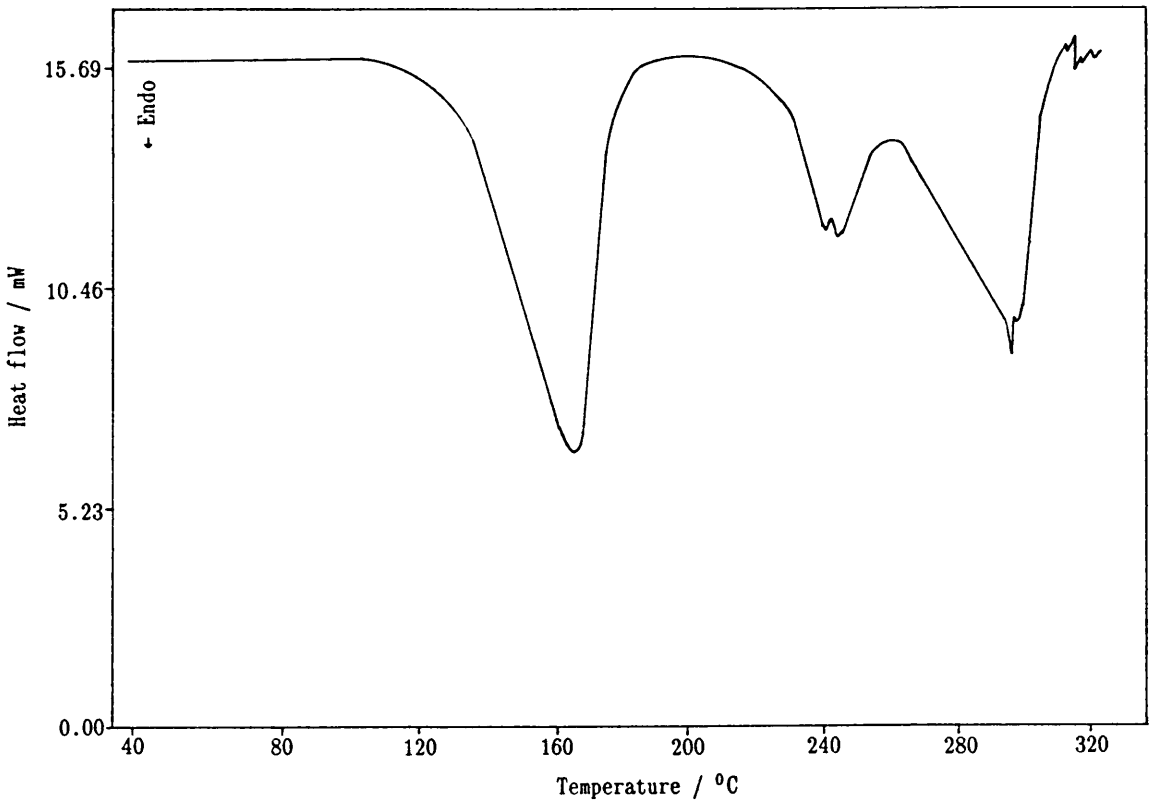

Figure 58. The DSC trace recorded for $NiCl_2 2(py)$ at $5^0C\ min^{-1}$.

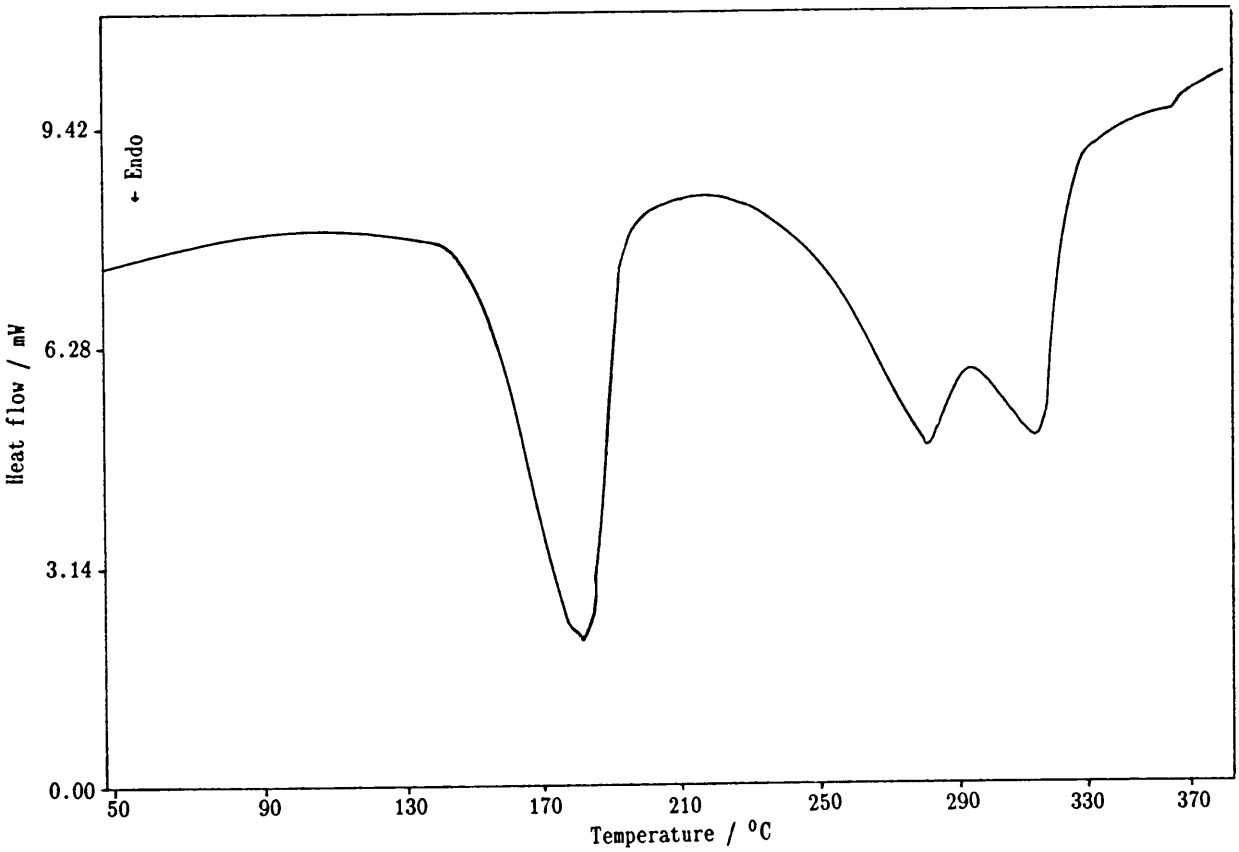

Clark [100] recorded far-infrared spectra of certain metal halide complexes with pyridine. Metal-ligand and metal-halogen stretching vibrations were assigned. His study described the relationship between metal-halogen vibrations and stereochemistry. The complexes $MnCl_2 2(py)$ and $NiCl_2 2(py)$ were found to be polymeric octahedral complexes, but poorly resolved bands were observed in the region 200-260 cm^{-1}. Hence, interpretation of the spectra was not possible. When considering a series of complexes in which the complexes have the same anion, similar structures and ligand evolution as the decomposition reaction, the metal-ligand bond-stretching frequency, which is not obtainable, would have been a useful indication of thermal stability within a series.

The structural assignments show that the scheme of decomposition for $MnCl_2 2(py)$ is

$3MnCl_2 2(py)$ oct. → $3MnCl_2(py)$ oct. → $Mn_3Cl_6 2(py)$ oct.→
$3MnCl_2$ oct.

The structural scheme of decomposition for $NiCl_2 2(py)$ is similar.

The enthalpies of formation, including the values reported by Beech [8], are summarised in Table 27. The onset temperatures and peak temperatures agree well with the values obtained by Beech. However, the enthalpies of formation differ by a factor of approximately two. The extremely high heating rates of $16^0C\ min^{-1}$, used by Beech, may contribute to the different values.

The enthalpy of formation for the first reaction is larger for nickel than for manganese. This is in accordance with the stability series of the transition elements. A similar increase is also observed for the second reaction.

Table 27. The enthalpies of formation for $MnCl_2 2(py)$ and $NiCl_2 2(py)$. The values in brackets represent the values observed by Beech.

Decomposition reaction	ΔH (kJ mol^{-1})	T_i^* (^0C)	T_p^* (^0C)
$MnCl_2 2(py) \rightarrow$ $MnCl_2(py)+py$	110,72 (62,50)	141,3 (137)	163,2 (187)
$MnCl_2(py) \rightarrow$ $MnCl_2+py$	123,42 (57,74)	249,9 (247)	294,2 (327)
$NiCl_2 2(py) \rightarrow$ $NiCl_2(py)+py$	111,82 (65,27)	157,9 (157)	178,9 (197)
$NiCl_2(py) \rightarrow$ $NiCl_2+(py)$	141,62 (71,3)	252,2 (272)	280,8 (337)

where T_i^* = onset temperature;

and T_p^* = temperature at peak maximum.

11.4 CONCLUSIONS

The dynamic and isothermal studies performed on $MnCl_2 2(py)$ and $NiCl_2 2(py)$ resulted in the determination of the decomposition reactions, which involve the formation of the stable intermediates, $MnCl_2(py)$ and $NiCl_2(py)$ and the final decomposition products, $MnCl_2$ and $NiCl_2$. The DSC traces revealed the formation of $Mn_3Cl_6 2(py)$ and $Ni_3Cl_6 2(py)$ as very unstable intermediates and thus the fractional liberation of pyridine which coincides with the formation of $MnCl_2$ and $NiCl_2$.

In Chapter 6 the dynamic, isothermal and DSC studies revealed the decomposition of $CoCl_2 2(py)$ as follows:

$3CoCl_2 2(py)$ oct. → $3CoCl_2 2(py)$ tet. → $3CoCl_2(py)$ oct. → $Co_3Cl_6 2(py)$ oct. → $3CoCl_2$ oct.

Thus, the formation of the distinct $Co_3Cl_6 2(py)$ complex as a stable intermediate is observed. It is not possible to compare the enthalpies of formation for the cobalt, manganese and nickel complexes, since the decomposition of $CoCl_2 2(py)$ is accompanied by the structural conversion of the octahedral to the tetrahedral complex and the formation of $Co_3Cl_6 2(py)$ as a stable intermediate. However, much lower enthalpies of formation were observed for the decomposition of $CoCl_2 2(py)$. This does not fit in with the position of Co in the stability series of the first row transition elements. The complexes of nickel and manganese comply with the series, when taking into consideration the lower initial

temperature of decomposition and lower activation energy values observed for the manganese complex.

Considering the results obtained from the analysis of the dynamic curves the following, can be conducted: Higher activation energies and frequency factors were obtained for the decomposition of $NiCl_2 2(py)$, than for $MnCl_2 2(py)$, which implies a stronger interaction between the metal and the ligand. Except for the first part of the decomposition reaction, similar results were obtained from the analysis of the isothermal curves.

The DSC studies revealed a higher peak maximum for $NiCl_2 2(py)$ for the loss of the first pyridine. Thus a stronger bond exists between $NiCl_2(py)$ and pyridine than between $MnCl_2(py)$ and pyridine. In contrast, the liberation of the last pyridine is observed at a higher peak temperature for $MnCl_2(py)$. Therefore the Mn-pyridine (N) bond is stronger than the Ni-pyridine (N) bond.

The enthalpies for the liberation of the first pyridine by $MnCl_2 2(py)$ and $NiCl_2 2(py)$ are similar. A larger enthalpy value was calculated for the decomposition of $NiCl_2(py)$ (liberation of the second pyridine), which suggests a larger bonding strength between $NiCl_2(py)$ and pyridine.

Thus, thermal analysis of different metal complexes supplies valuable information regarding the M-L bond strength in the different metal complexes.

CHAPTER 12

THE THERMAL DECOMPOSITION OF MANGANESE AND NICKEL COMPLEXES CONTAINING PYRIDINE-RELATED LIGANDS

12.1 INTRODUCTION

The complexes formed by pyridine and substituted pyridine derivatives with cobalt(II) chloride have been reported in Chapters 6, 8 and 9. In the previous chapter the metal-pyridine (N) bonds for the transition metals, nickel and manganese, were investigated. The effect of the methyl substituent on the metal-donor-N bond was determined by investigating the picoline complexes of cobalt(II) chloride. In general, the β- or γ-methyl groups increase the stability of the complex, as determined from the temperatures of the decomposition peaks. Thus, the electron-repelling methyl group increases the electron density at the N-donor atom, and this increases the covalency of the metal-donor-N bond. According to Liptay [80], the decomposition temperatures show that the electron-repelling effect of the methyl group is more important for the γ-position than for the β-position. However, the temperatures of decomposition for $CoCl_2 2(\beta\text{-pic})$ could not be obtained in this study, due to the melting of the complex.

The position of the substituent also influences the composition and the stability of the complex on account of the different

degrees of steric hindrance. This explains the fact that the methyl group of α-picoline, which is adjacent to the N-donor atom, prevents the formation of the tetrapyridine derivative and gives rise to the lower decomposition temperature of $CoCl_2 2(\alpha\text{-pic})$ (153,2^{0}C) when compared to that of $CoCl_2 2(py)$ (160,2^{0}C).

Another factor influencing the stability of complexes is the type of metal ion. In general, nickel forms tetrapicoline derivatives with α- and β-picoline, rather than dipicoline derivatives. This can be attributed to the size of the metal ion. The nickel-ligand interaction is weak and determines the coordination number of the metal-halide complex.

In order to obtain comparative data with respect to steric hindrance and the influence of the metal ion, the study was extended to include metal complexes (nickel and manganese) containing α-, β- and γ-picoline.

12.2 SOLID STATE CHEMISTRY RESULTS

12.2.1 Dynamic studies

The complexes of $MnCl_2 2(\alpha\text{-pic})$ and $NiCl_2 2(\alpha\text{-pic})$ could not be prepared successfully, due to their low temperatures of decomposition (approximately 60^{0}C) and their instability.

White, paper-like crystals, with an extremely low density, were

obtained in the preparation of $MnCl_2 2(\beta\text{-pic})$. The dynamic trace of the initial prepared complex revealed a number of H_2O molecules coordinated to the metal complex. The crystals were vacuum dried for approximately 48 hours. The percentage of water could not be reduced to less than 2,5% (with reference to the total mass loss). Thus, when the loss of water is included, $MnCl_2 2(\beta\text{-pic})$ decomposes over the temperature range 37^0C to 282^0C, according to the following reactions:

$$MnCl_2 2(\beta\text{-pic}) \ (s) \rightarrow MnCl_2(\beta\text{-pic}) \ (s) + (\beta\text{-pic}) \ (g) \qquad (1)$$

$$3MnCl_2(\beta\text{-pic}) \ (s) \rightarrow Mn_3Cl_6 2(\beta\text{-pic}) \ (s) + (\beta\text{-pic}) \ (g) \qquad (2)$$

$$Mn_3Cl_6 2(\beta\text{-pic}) \ (s) \rightarrow 3MnCl_2 \ (s) + 2(\beta\text{-pic}) \ (g) \qquad (3)$$

Mass losses of 30,10% (theoretical mass loss = 29,8%) and 41,0% (theoretical mass loss = 39,8%) were obtained for reactions (1) and (1)+(2), respectively. A mass loss of 61,9% was found experimentally for reactions (1)+(2)+(3) (theoretical mass loss = 59,7%). The scheme of thermal decomposition is in agreement with previous reports [8,79].

The kinetic results of the dynamic curve of $MnCl_2 2(\beta\text{-pic})$ are summarised in Table 28.

Table 28. The kinetic results obtained from the dynamic curve of $MnCl_2 2(\beta\text{-pic})$ recorded at $3^0C\ min^{-1}$.

Decomposition reaction	Rate equation	E_a ($kJ\ mol^{-1}$)	ln Z ($ln\ min^{-1}$)
H_2O loss	$1-(1-\alpha)^{\frac{1}{3}}$	151,0	53,64
1	$1-(1-\alpha)^{\frac{1}{3}}$	100,0	27,42
2	$1-(1-\alpha)^{\frac{1}{3}}$	155,0	37,67
3	$1-(1-\alpha)^{\frac{1}{2}}$	140,0	28,87

An excellent fit was obtained between the simulated and dynamic curves (Figure 59).

Figure 59. Plots of the simulated curve (---), obtained from the analysis of the dynamic curve, and the experimental dynamic curve (—) for $MnCl_2 2(\beta\text{-pic})$.

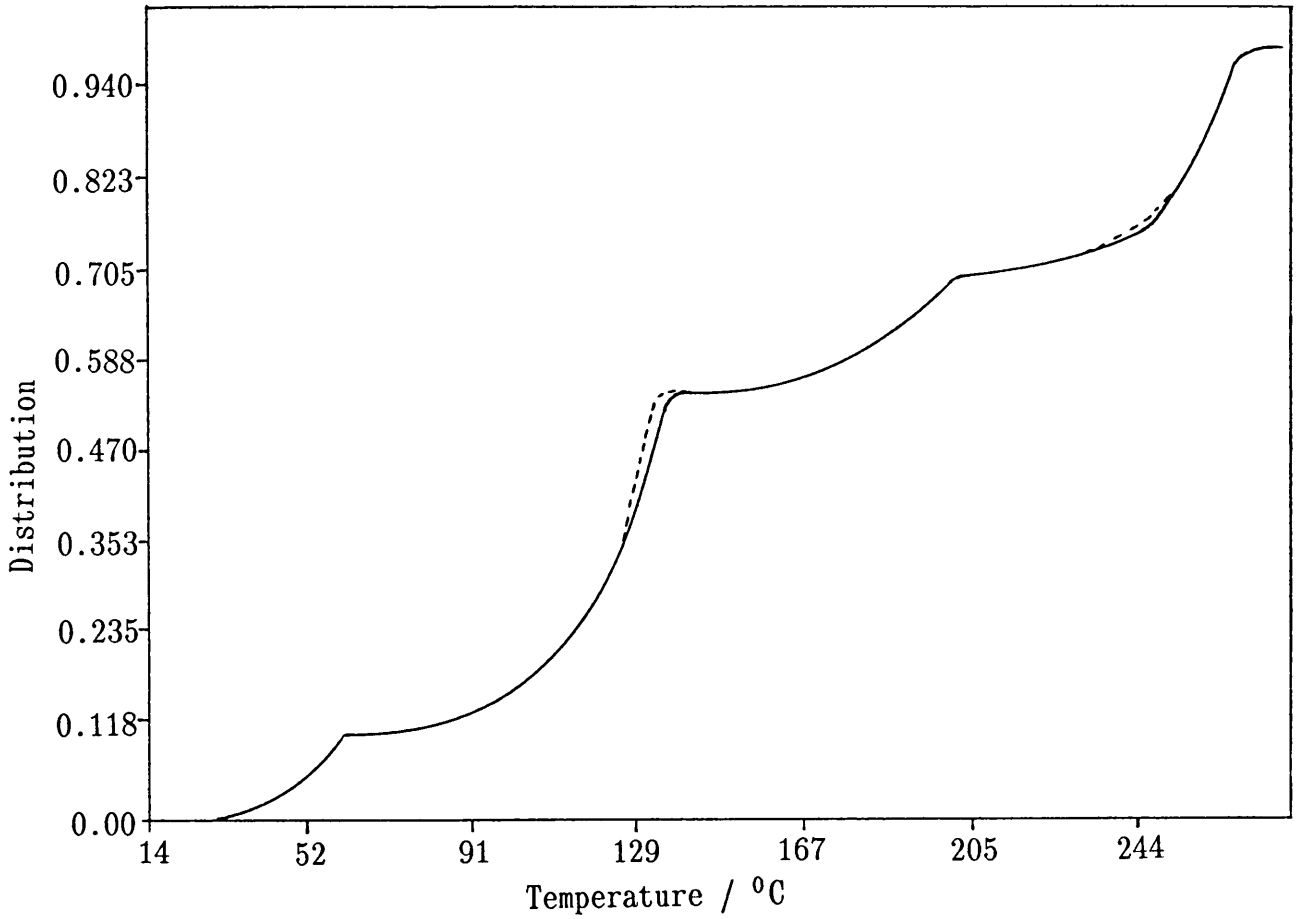

The white crystals of $MnCl_2 2(\gamma\text{-pic})$ decompose over the temperature range 94^0C to 283^0C, according to the following reactions:

$$MnCl_2 2(\gamma\text{-pic})\ (s) \rightarrow MnCl_2(\gamma\text{-pic})\ (s) + (\gamma\text{-pic})\ (g) \qquad (4)$$

$$MnCl_2(\gamma\text{-pic})\ (s) \rightarrow MnCl_2\ (s) + (\gamma\text{-pic})\ (g) \qquad (5)$$

Mass losses of 30,0% (theoretical mass loss = 29,8%) and 59,8% (theoretical mass loss = 59,7%) were obtained for reactions (4) and (4)+(5), respectively. Beech [8] reported the formation of $Mn_3Cl_6 2(\gamma\text{-pic})$ as an additional stable intermediate. However, a heating rate of $1^0C\ min^{-1}$ did not reveal the presence of this intermediate.

A kinetic study was performed on the dynamic curve of the complex $MnCl_2 2(\gamma\text{-pic})$. Both reactions conform to the contracting area model. Activation energies of 109,00 kJ mol^{-1} and 90,00 kJ mol^{-1} were calculated for reactions (4) and (5), respectively. The ln Z values for reactions (4) and (5) were 29,06 and 16,11, respectively. The fit between the simulated and experimental curves is shown in Figure 60.

Figure 60. Plots of the simulated curve (---), obtained from the analysis of the dynamic curve, and the experimental curve (—) for $MnCl_2 2(\gamma\text{-pic})$.

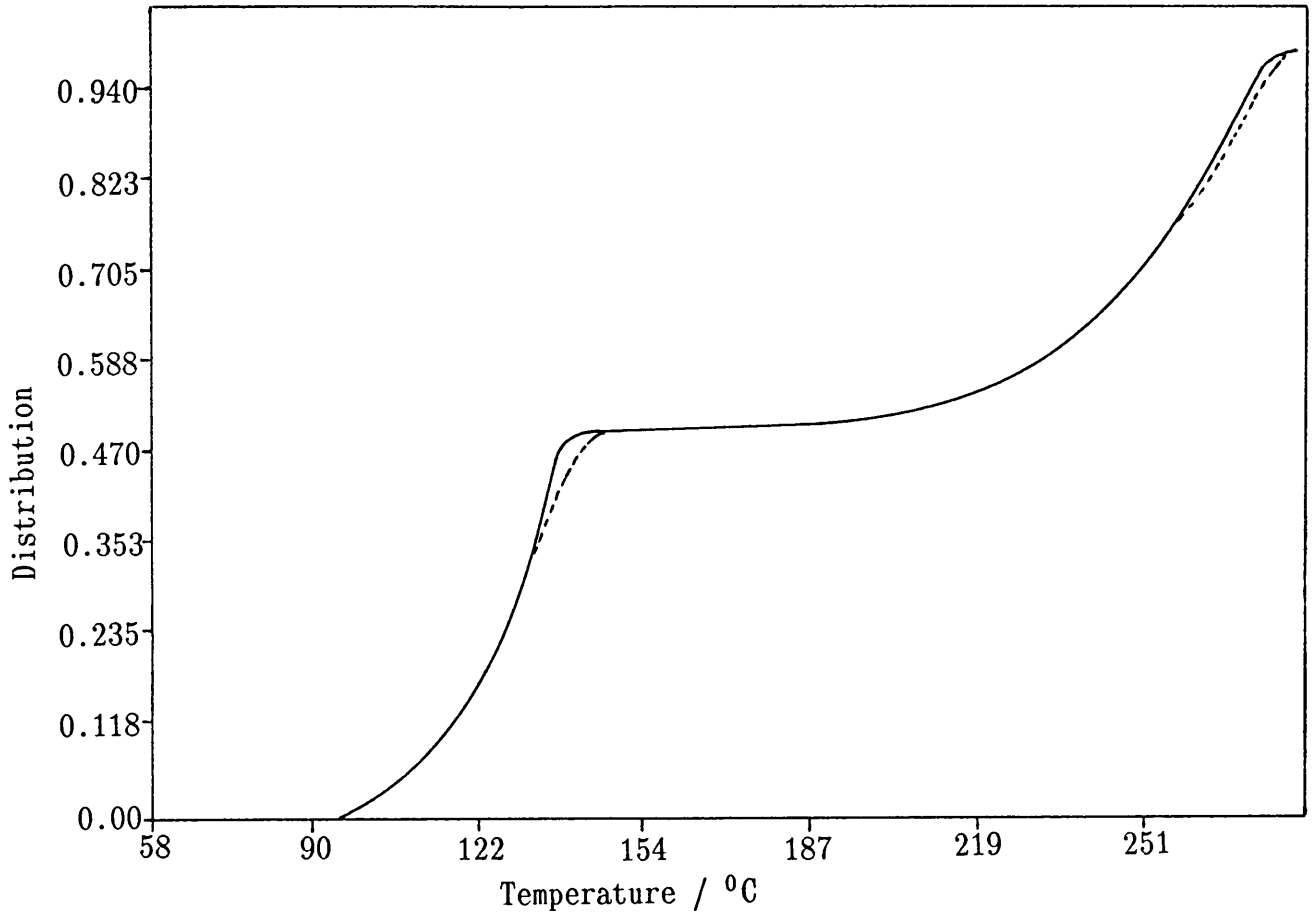

The size of the nickel ion led to an increase in the coordination number. Therefore, pale yellow $NiCl_2 4(\beta\text{-pic})$ and $NiCl_2 4(\gamma\text{-pic})$ complexes were obtained.

The complex, $NiCl_2 4(\beta\text{-pic})$, decomposes over the temperature range 75^0C to 275^0C, according to the following dissociation reactions:

$$NiCl_2 4(\beta\text{-pic})\ (s) \rightarrow NiCl_2 2(\beta\text{-pic})\ (s) + 2(\beta\text{-pic})\ (g) \qquad (6)$$

$$NiCl_2 2(\beta\text{-pic})\ (s) \rightarrow NiCl_2(\beta\text{-pic})\ (s) + (\beta\text{-pic})\ (g) \qquad (7)$$

$$NiCl_2(\beta\text{-pic})\ (s) \rightarrow NiCl_2\ (s) + (\beta\text{-pic})\ (g) \qquad (8)$$

The mass losses obtained compare extremely well with the calculated mass losses. The reactions determined by the mass losses are in agreement with previous reports [92,96], but G. Beech [8] observed the additional intermediate $Ni_3Cl_6 2(\beta\text{-pic})$.

Kinetic analysis was carried out on the dynamic curve recorded at $3^0C\ min^{-1}$. Due to the low density of the complex, only reactions (6) and (7) were investigated. The contracting area model described both reactions. The following parameters were obtained: E_a = 128,00 kJ mol^{-1} and ln Z = 38,99 for reaction (6) and E_a = 182,00 kJ mol^{-1} and ln Z = 50,10 for reaction (7). When proceeding from $NiCl_2 4(\beta\text{-pic})$ to $NiCl_2 2(\beta\text{-pic})$, a definite increase in activation energy and frequency factor is observed. Reaction (6) is accompanied by the loss of two β-picolines, and therefore more energy is required for the liberation of the folowing β-picoline. Thus, a stronger interaction exists between the nickel and the β-picoline in the octahedral complex

$NiCl_2 2(\beta\text{-pic})$, than in the distorted octahedral complex $NiCl_2 4(\beta\text{-pic})$. An excellent fit is obtained between the simulated and experimental curves (Figure 61).

Figure 61. Plots of the simulated curve (---) ,obtained from the kinetic analysis of the dynamic curve, and the experimental curve (—) for $NiCl_2 4(\beta\text{-pic})$.

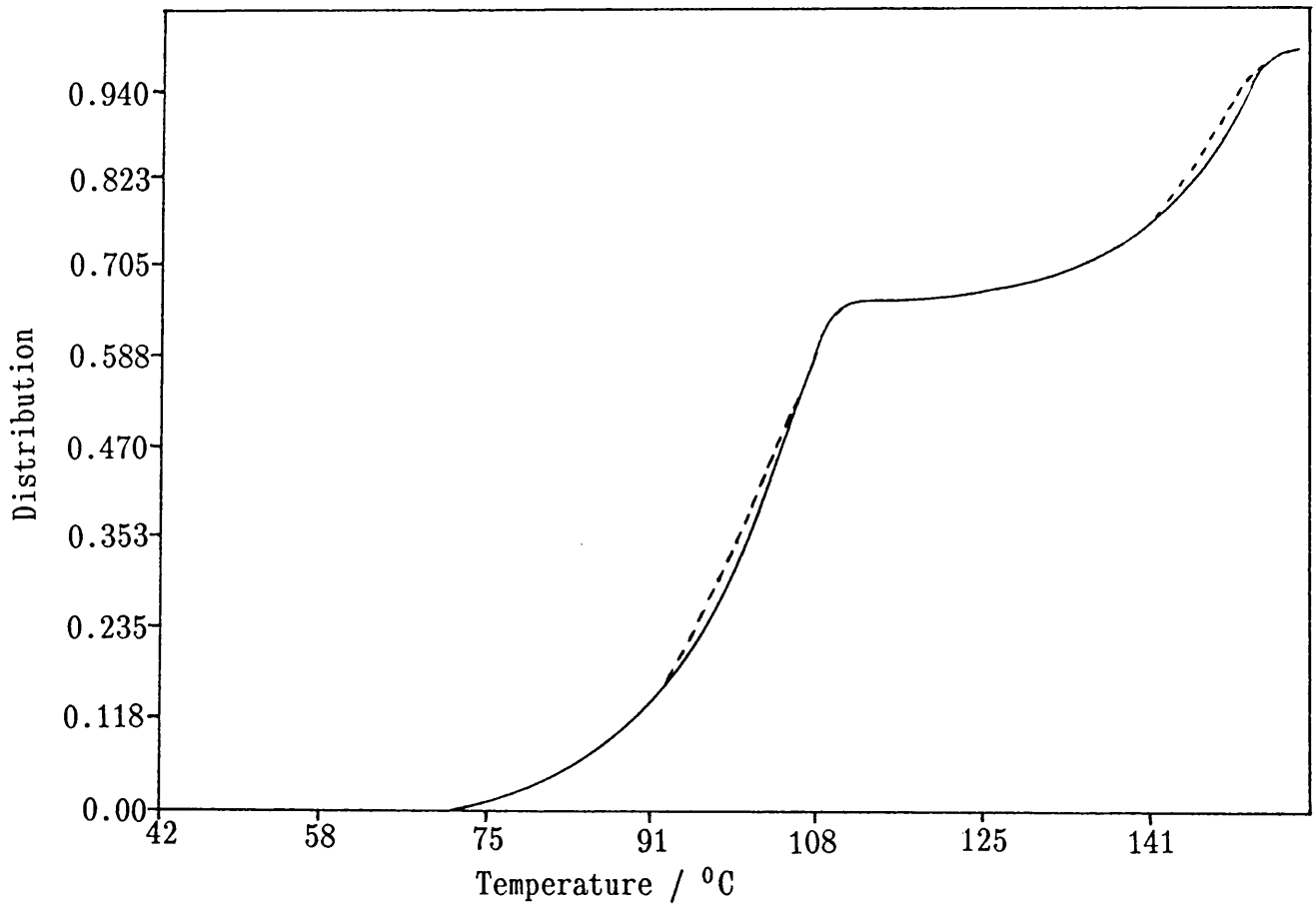

The white complex $NiCl_2 4(\gamma\text{-pic})$ decomposes over the temperature range 95^0C to 293^0C and the reaction is accompanied by the sintering of the sample. An external sign of sintering in any crystal is a reduction in external dimensions (shrinkage) [14]. This results in a corresponding reduction in porosity and an increase in the apparent density. Thus, the essence of sintering is the filling of free spaces inside the grains so that the area of the entire surface of the grains diminishes and the surface of contact increases. The shrinkage of the crystals indicates the possibility that the rate equation for the contracting area or volume model is valid.

The complex $NiCl_2 4(\gamma\text{-pic})$ releases the ligand γ-picoline most readily and the scheme of decomposition is

$$NiCl_2 4(\gamma\text{-pic})\ (s) \rightarrow NiCl_2(\gamma\text{-pic})\ (s) + 3(\gamma\text{-pic})\ (g) \qquad (9)$$

$$NiCl_2(\gamma\text{-pic})\ (s) \rightarrow NiCl_2\ (s) + (\gamma\text{-pic})\ (g) \qquad (10)$$

Mass losses of 55,5% (theoretical mass loss = 55,6%) and 74,9% (theoretical mass loss = 74,2%) were obtained for reactions (9) and (9)+(10), respectively. The dissociation reactions were reported by several authors [8,92,96].

The results obtained for the kinetic analysis of the complex $NiCl_2 4(\gamma\text{-pic})$ are summarised in Table 29. Reaction (10) revealed an induction and deceleratory period, and it was therefore not possible to fit a single rate equation over the whole α-range. In addition, it was found that the contracting area model described

both periods.

Considering reaction (10), the induction period may be the result of the formation of $Ni_3Cl_6 2(\gamma\text{-pic})$. However, a lower mass loss of 58,6% was obtained, compared to the calculated value of 61,8%.

An exceptionally high increase in the activation energy and frequency factor is observed for the formation of $NiCl_2$. This indicates the existence of a strong interaction between nickel and γ-picoline in the complex $NiCl_2(\gamma\text{-pic})$, similarly to $NiCl_2 2(\beta\text{-pic})$.

Table 29. Kinetic parameters obtained for $NiCl_2 4(\gamma\text{-pic})$ from the analysis of the dynamic curve ($3^0C\ min^{-1}$). All the reactions conform to the contracting area model.

Decomposition reaction	% contribution	E_a (kJ mol^{-1})	ln Z (ln min^{-1})
9	74,1	90,00	22,94
10			
induction	4,10	93,00	19,68
deceleratory	21,8	226,00	47,02

A perfect fit between the simulated and experimental data is observed (Figure 62).

Figure 62. Plots of the simulated curve (---) ,obtained from the kinetic analysis of the dynamic curve, and the experimental curve (—) for $NiCl_2 4(\gamma\text{-pic})$.

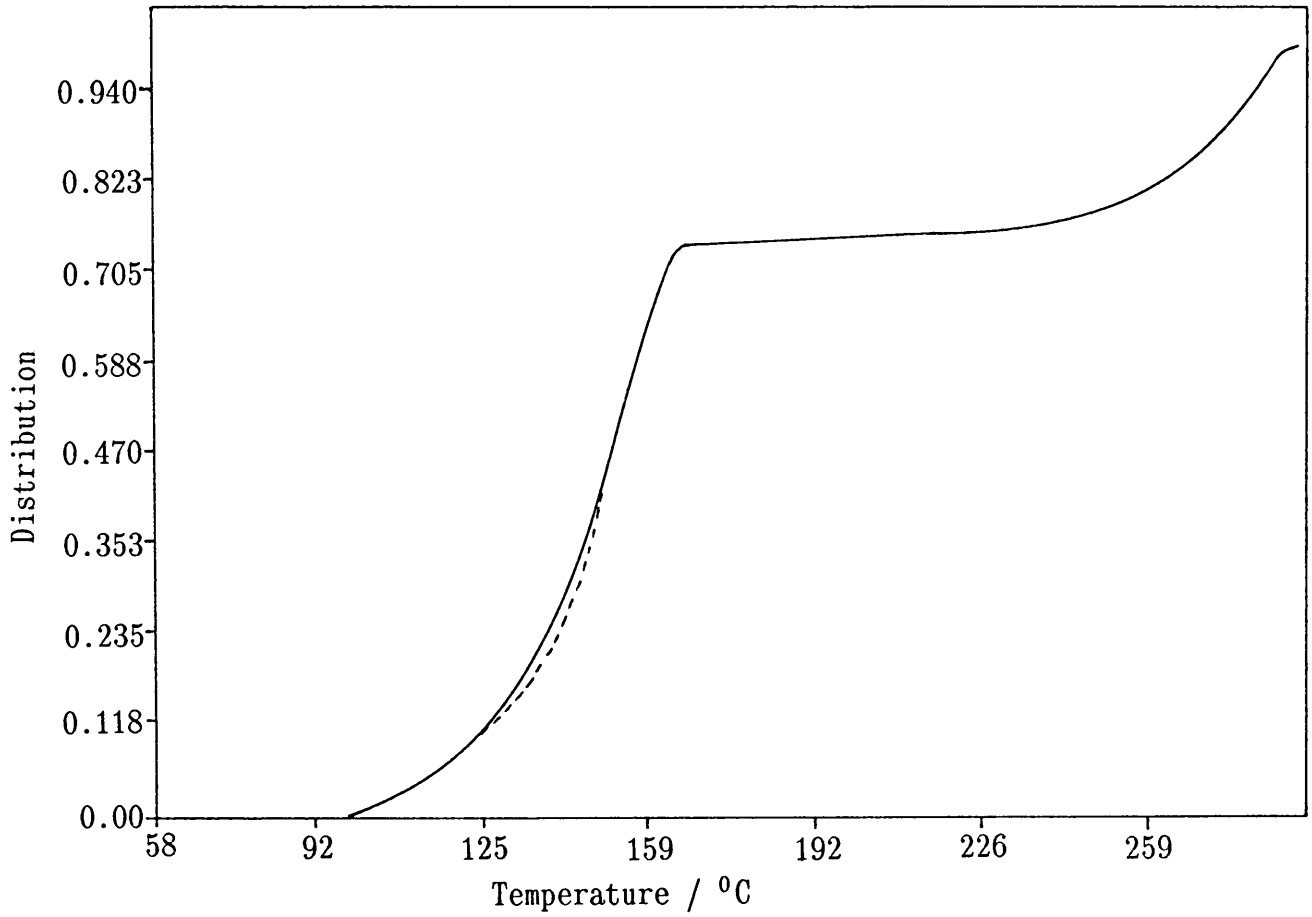

12.2.2 Isothermal results

The isothermal curves of some nickel and manganese complexes were not reproducible, due to the low densities of the complexes.

The following results were obtained from the isothermal studies performed on $MnCl_2 2(\gamma\text{-pic})$: Reaction (4) (formation of $MnCl_2(\gamma\text{-pic})$) was studied over the temperature range 95^0C to 102^0C. This decomposition reaction conforms to the contracting area model for $0,07 < \alpha < 0,99$. Values of E_a = 81,52 kJ mol^{-1} and ln Z = 20,84 were determined.

Reaction (5) (formation of $MnCl_2$) was investigated over the temperature range 184^0C to 192^0C. This reaction is again described by the contracting area model for $0,10 < \alpha < 0,90$ and has E_a = 96,50 kJ mol^{-1} and ln Z = 17,07.

The simulated curve revealed in Figure 63 was obtained, by assuming a heating rate of 1^0C min^{-1}. Although the same rate equations were applicable, a poor fit was obtained for the last part of the decomposition reaction.

Figure 63. Plots of the simulated curve (---), obtained from the isothermal results, and the experimental curve (—) for $MnCl_2 2(\gamma\text{-pic})$.

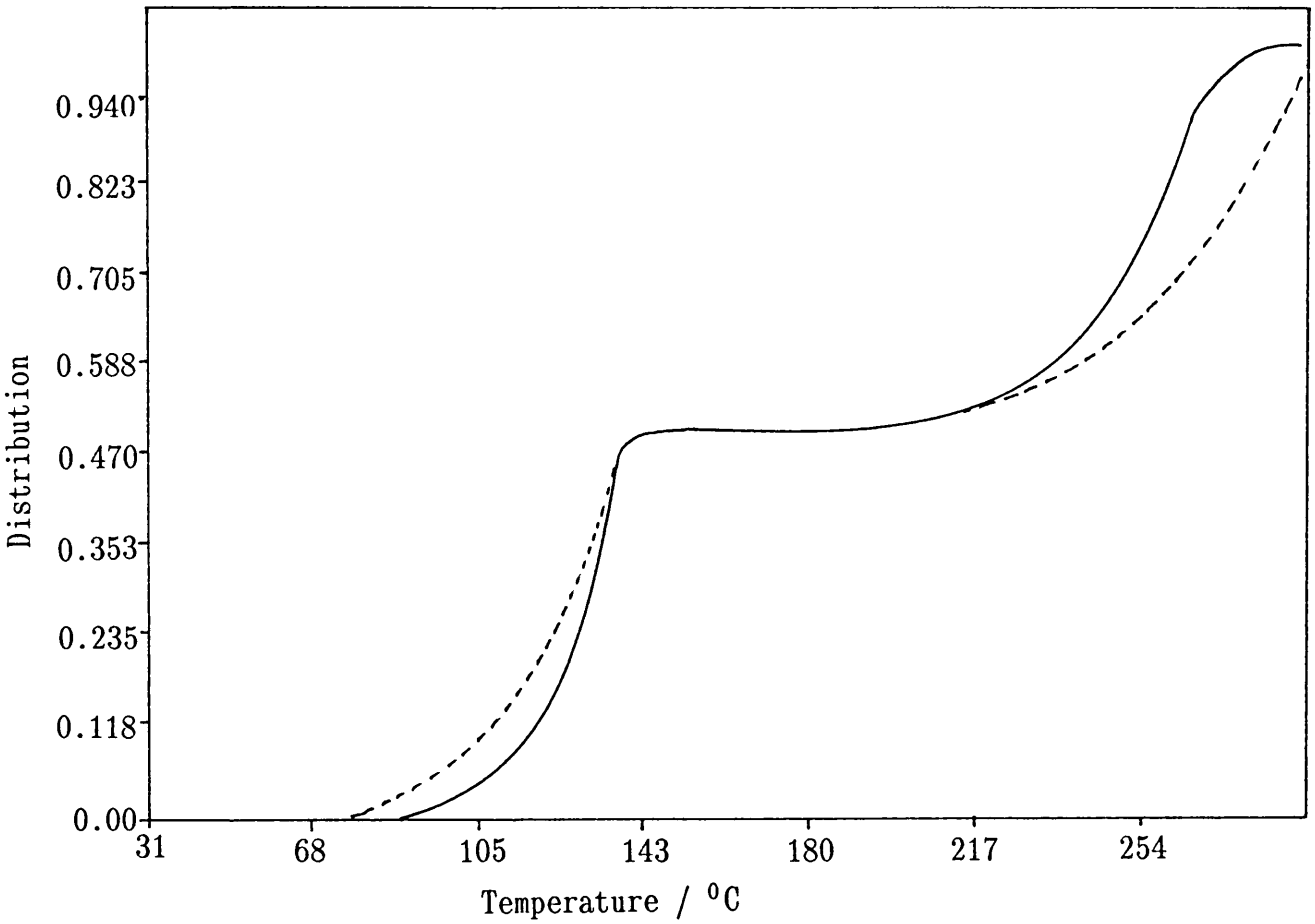

The complex $NiCl_2 4(\beta\text{-pic})$ decomposes to $NiCl_2 2(\beta\text{-pic})$ over the temperature range 74^0C to 83^0C, according to the linear rate law, $kt = \alpha$, for $0,02 < \alpha < 0,90$ with $E_a = 95,76$ kJ mol^{-1} and $\ln Z = 28,42$. Reaction (7) (formation of $NiCl_2(\beta\text{-pic})$) was studied in the temperature range 104^0C to 126^0C and conforms to the contracting area model for $0,06 < \alpha < 0,99$, with $E_a = 87,95$ kJ mol^{-1} and $\ln Z = 22,54$. A very poor fit was obtained with these parameters when a heating rate of 3^0C min^{-1} was assumed (Figure 64). It is of interest to note that, for reaction (6), the kinetic rate equation obtained from the isothermal studies differs from that obtained from the analysis of the dynamic curve.

In the temperature range 97^0C to 110^0C, the complex $NiCl_2 4(\gamma\text{-pic})$ decomposes to $NiCl_2(\gamma\text{-pic})$ according to the contracting area model, over the whole α-range and has values of $E_a = 63,89$ kJ mol^{-1} and $\ln Z = 14,63$. Reaction (10) (formation of $NiCl_2$) was investigated in the temperature range 215^0C to 222^0C. It was not possible to fit a single rate equation over the whole α-range at different temperatures. This may be attributed to the possible formation of the intermediate $Ni_3Cl_6 2(\gamma\text{-pic})$.

Figure 64. Plots of the simulated curve (---), obtained from the isothermal results, and the experimental curve (—) for $NiCl_2 4(\beta\text{-pic})$.

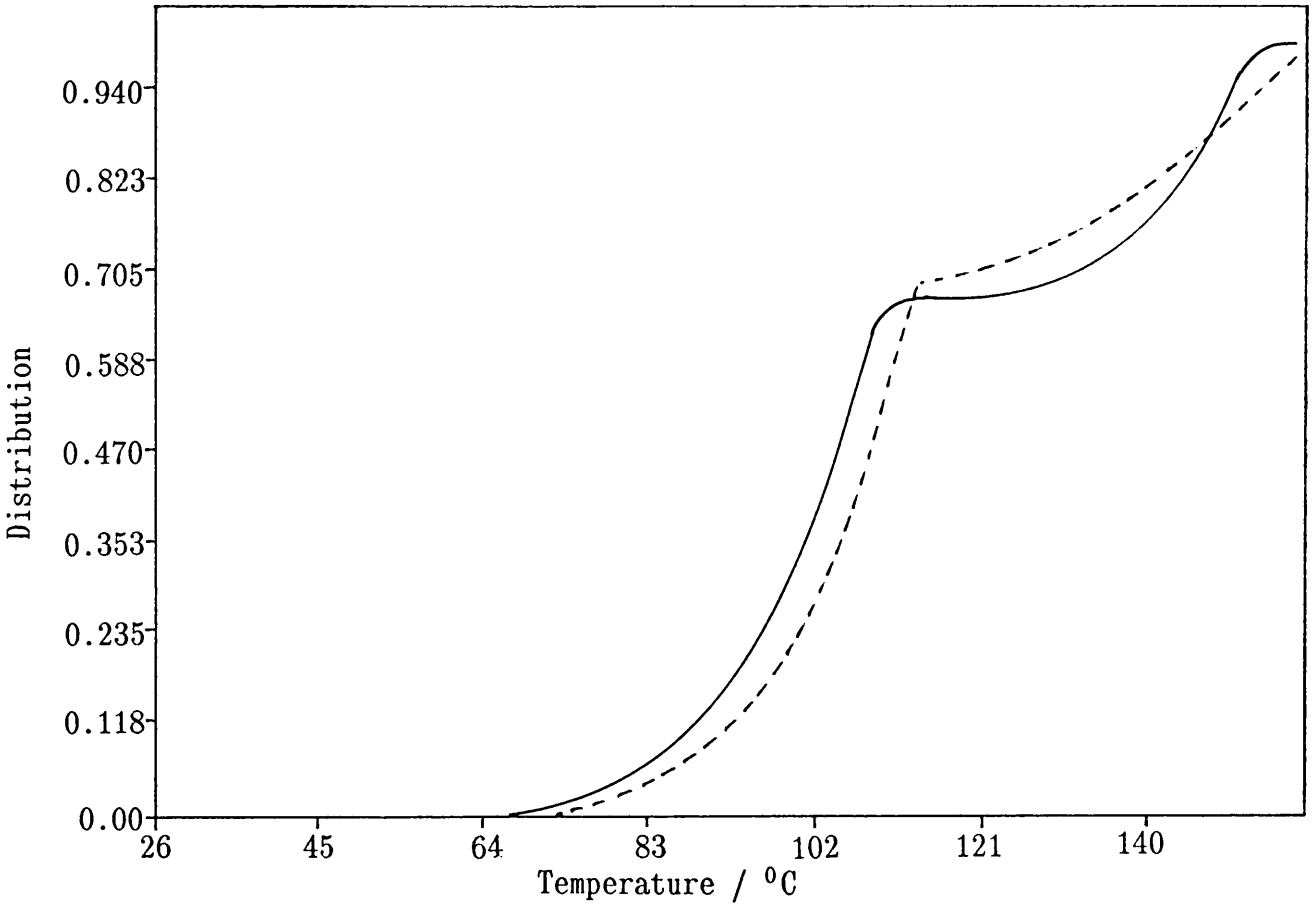

12.2.3 Electron microscopy studies

Micrograph 22 shows the single crystals of $NiCl_2 4(\beta\text{-pic})$ before decomposition. The crystals are mostly uniform in appearance and square.

The decomposition intermediate, $NiCl_2 2(\beta\text{-pic})$ shows decomposition on the surface of the crystals (Micrograph 23) and breakage of the crystal network is also observed.

The final decomposition intermediate, $NiCl_2$, reveals complete decomposition on the surface but remained intact (Micrographs 24 and 25).

12.2.4 DSC results

The studies were performed in open sample pans. The enthalpies of formation and the peak maxima are reported for $MnCl_2 2(\beta\text{-pic})$, $MnCl_2 2(\gamma\text{-pic})$, $NiCl_2 4(\beta\text{-pic})$ and $NiCl_2 4(\gamma\text{-pic})$ (Table 30).

The DSC traces recorded for the complexes are shown in Figures 65 to 68.

Micrograph 22. The single crystals of $NiCl_2$4(β-pic) before decomposition. (Magnification x300).

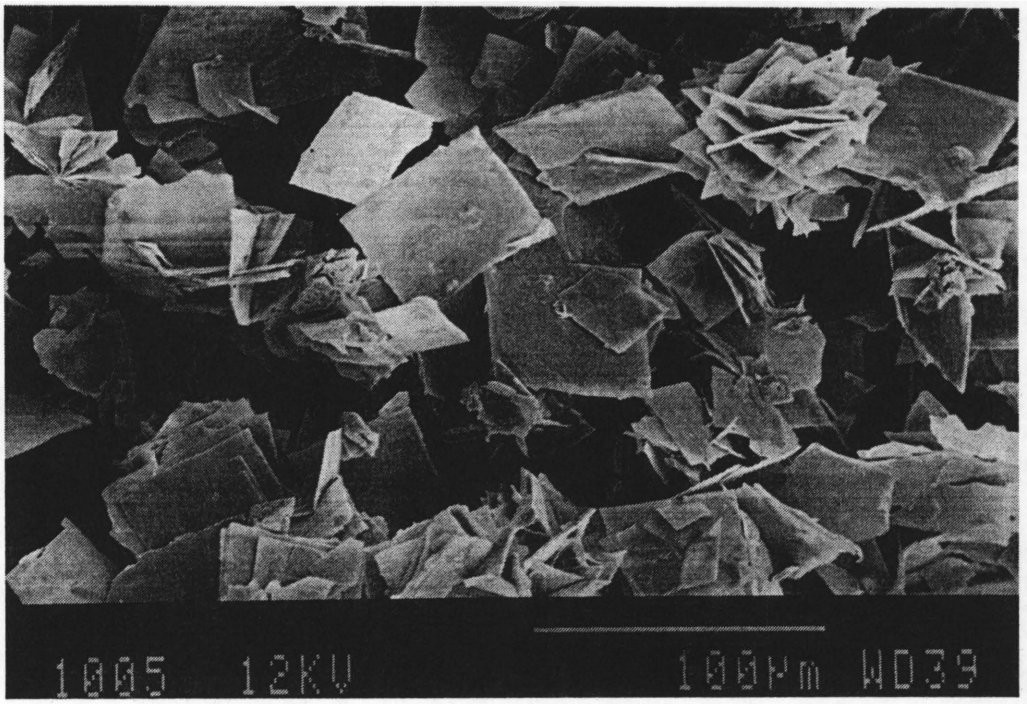

Micrograph 23. The crystals of the decomposition intermediate, $NiCl_2$2(β-pic). (Magnification x3000).

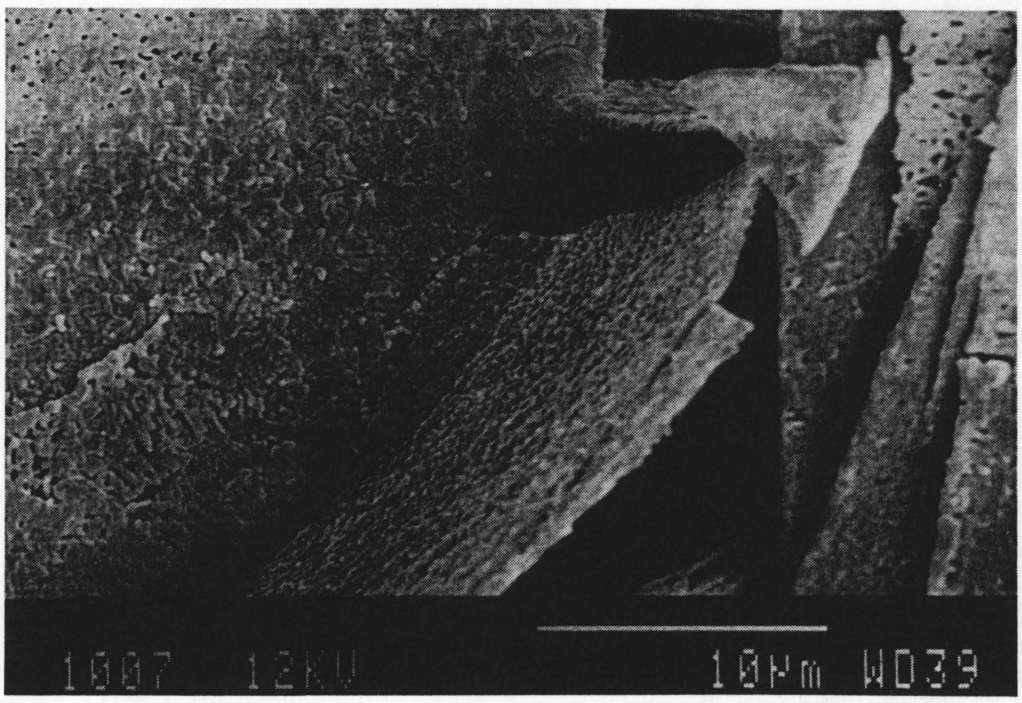

Micrograph 24. The single crystals of the final decomposition product, $NiCl_2$. (Magnification x400).

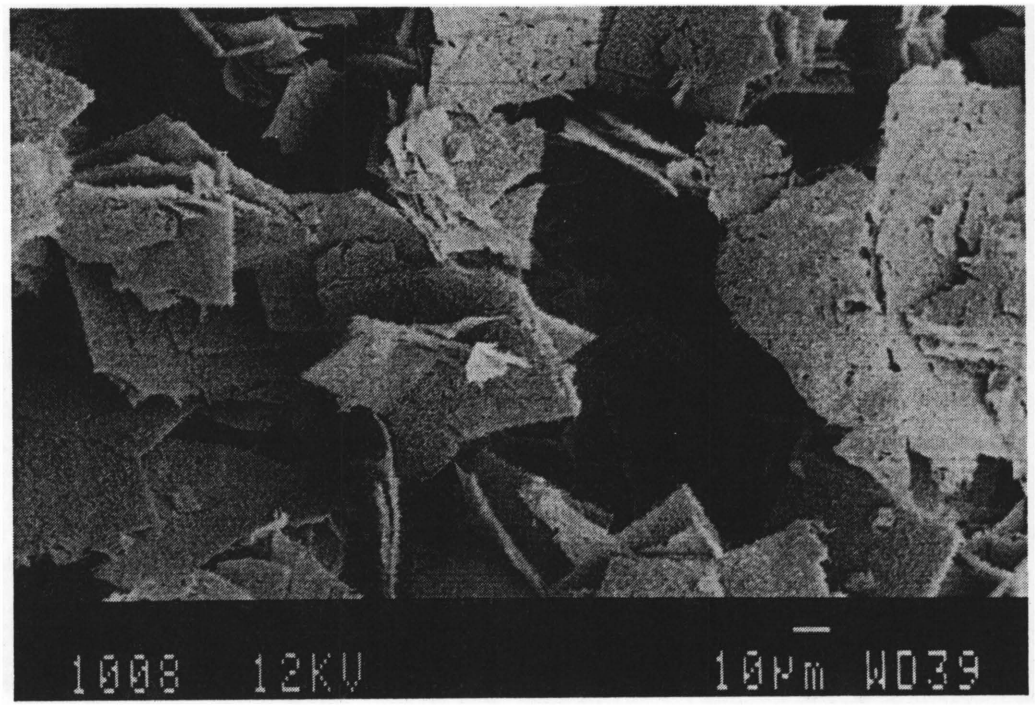

Micrograph 25. The surface of the final decomposition product, $NiCl_2$. (Magnification x3000).

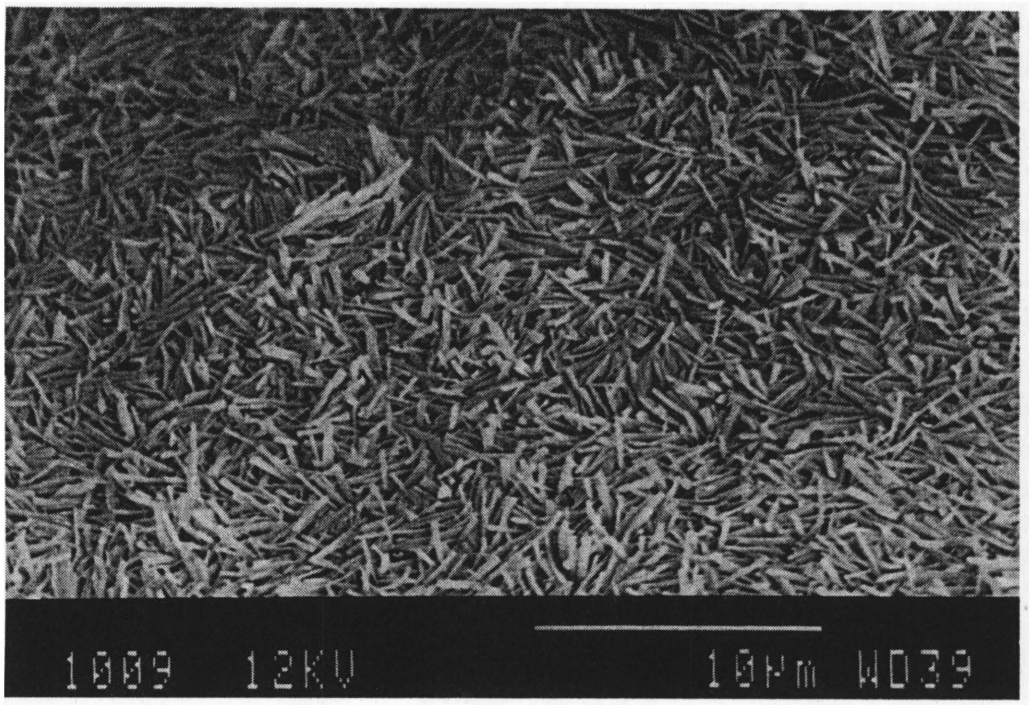

Table 30. Enthalpies of formation and decomposition temperatures obtained for some picoline complexes. The values in brackets represent the values reported by Beech [8].

Decomposition reaction	T_i (^0C)	T_p (^0C)	ΔH (kJ mol^{-1})
1	118,5	136,8	100,16
	(117)	(177)	(56,9)
2+3	191,2	204+288	27,74
	(207+272)	(237+342)	(77,4)
4	143,5	169,8	113,24
	(107)	(167)	63,18
5	238,0	317,9	131,65
	(227)	(267+342)	(81,2)
6	107,4	122,5	203,8
	(117)	(157)	(107)
7	152,4	166,9	89,92
	(172)	(217)	(58,2)
8	243,9	251,6	34,66
	(237)	(277)	(82,4)
9	136,8	170,2	386,2
	(132)	(197)	(192)
10	266,8	297,0	140,8
	(262)	(332)	(87,0)

Figure 65. The DSC trace recorded for $MnCl_2 2(\beta\text{-pic})$ at $3^0C\ min^{-1}$.

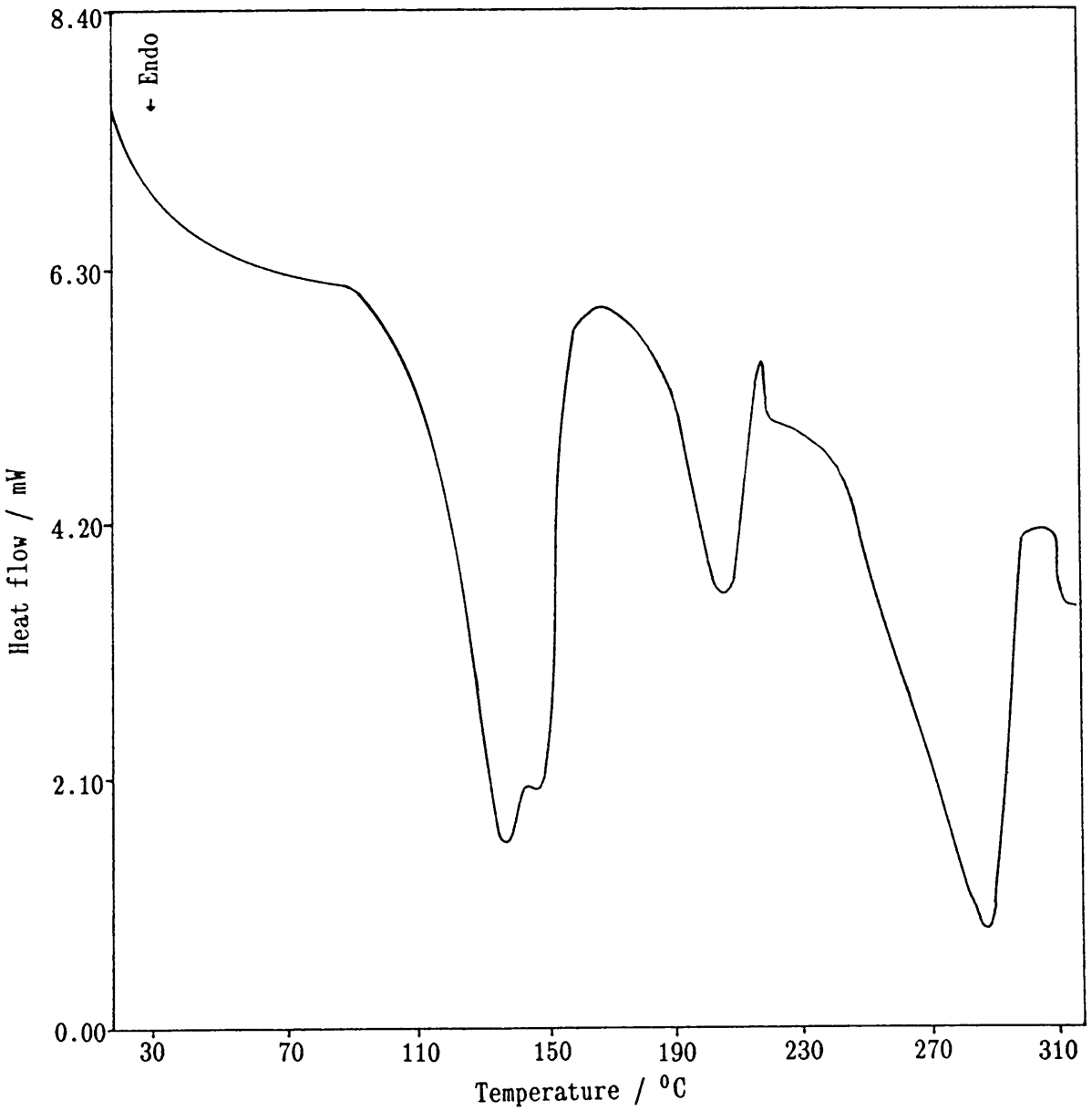

Figure 66. The DSC trace recorded for $MnCl_2 2(\gamma\text{-pic})$ at $5^0C\ min^{-1}$.

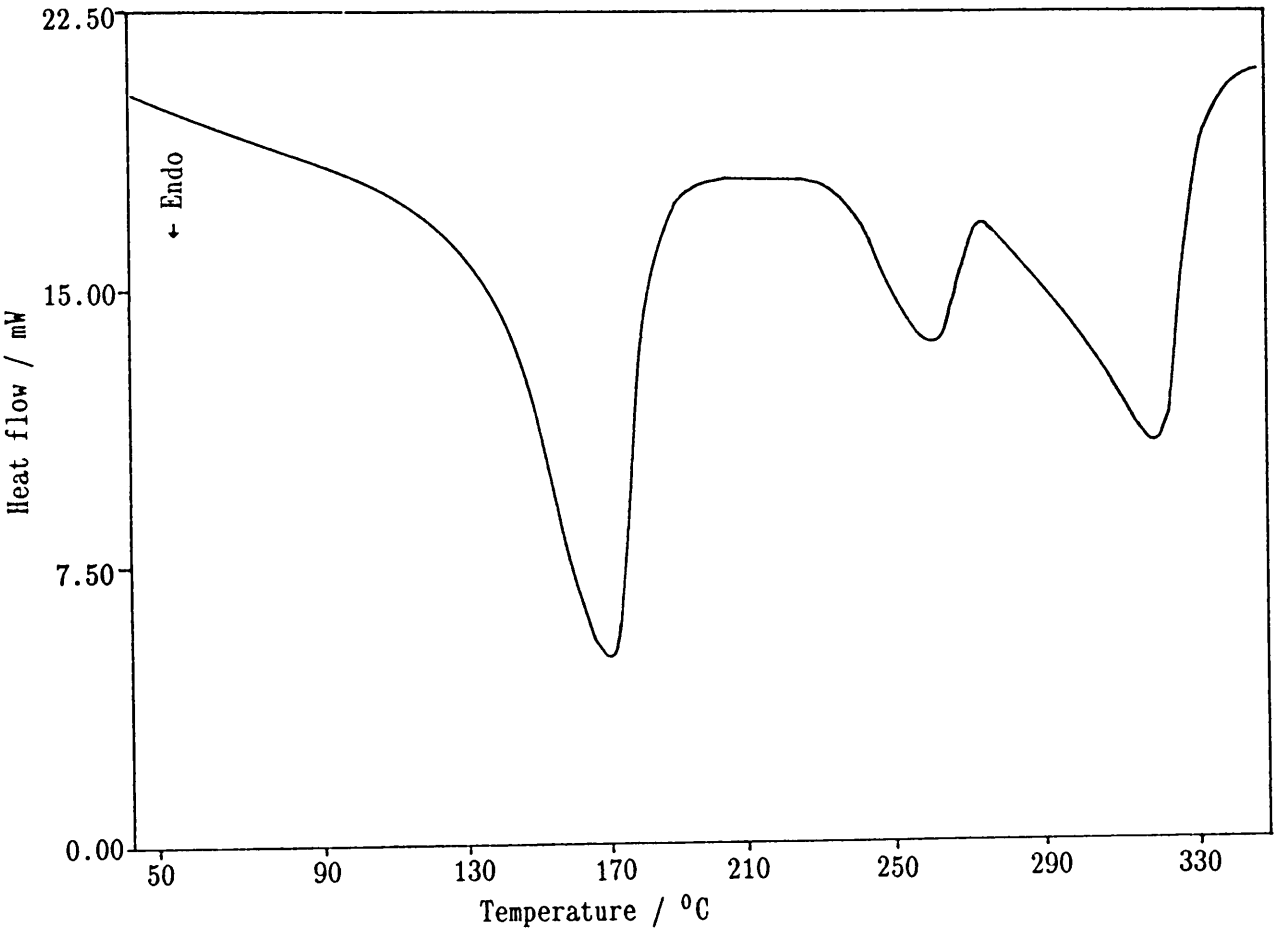

Figure 67. The DSC trace recorded for $NiCl_2 4(\beta\text{-pic})$ at $5^0C\ min^{-1}$.

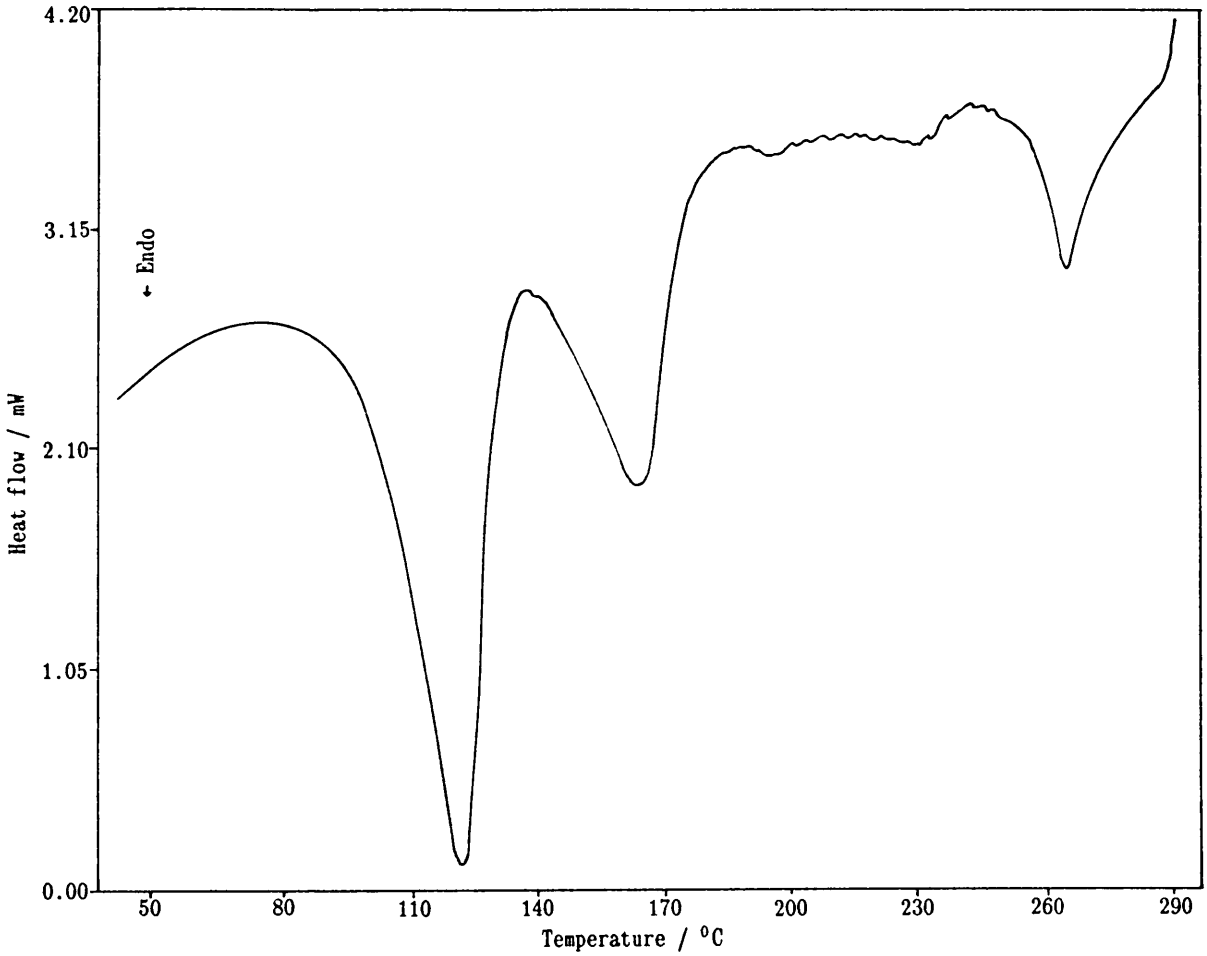

Figure 68. The DSC trace recorded for $NiCl_2 2(\gamma\text{-pic})$ at $5^0C\ min^{-1}$.

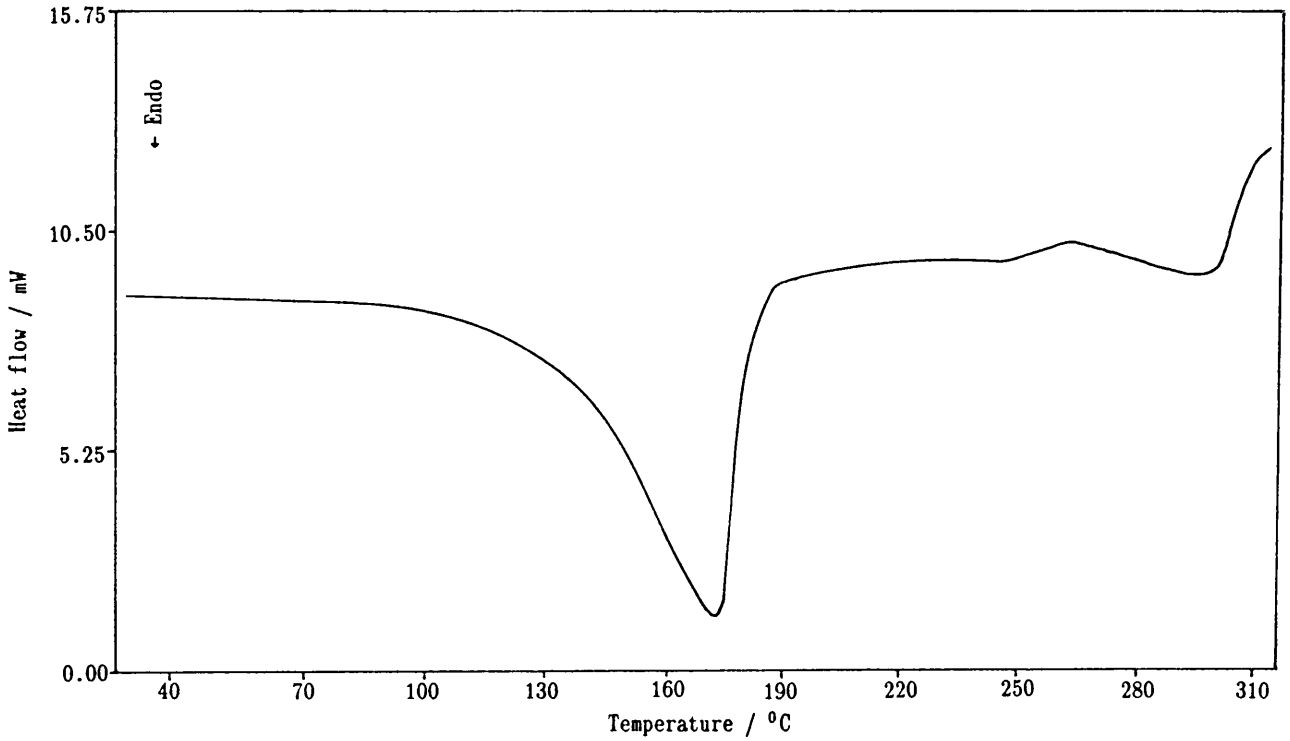

For manganese the decomposition temperatures of $MnCl_2$2(β-pic) and $MnCl_2$(β-pic) are lower than the decomposition temperatures of $MnCl_2$2(γ-pic) and $MnCl_2$(γ-pic). This implies that a stronger interaction exists between manganese and γ-picoline than between manganese and β-picoline. This was expected, since the methyl group in the γ-position should cause less steric hindrance on the metal than the methyl group in the β-position. This stronger interaction between the metal and the γ-picoline was also observed for the nickel ion. Thus, the γ-methyl group increases the stability of the complex by increasing the covalency of the metal-donor N bond. This is in agreement with the observations made by Liptay [80].

It is difficult to draw conclusions with respect to the different metal-β-picoline and metal-γ-picoline complex, since nickel forms tetrapicoline derivatives. However, considering the reactions by which $NiCl_2$ and $MnCl_2$ are formed the following is observed:
In general higher decomposition temperatures are observed for manganese than for nickel. This is due to the size of the nickel ion which results in a weaker interaction between the nickel and picoline, than that between manganese and picoline.

12.3 CONCLUSIONS

It is known that in metal complexes, thermal decomposition begins with the splitting of a coordinate bond and that the temperature of decomposition can be used to characterise the strength of the metal-ligand bond. In this chapter, the effects of both the metal

and the pyridine-related ligands were reported. The results obtained were in agreement with the previous reports.

It was observed that the methyl group in the γ-position increased the stability of the metal complex and resulted in higher decomposition temperatures.

Due to the size of the nickel ion, a weaker interaction between nickel and picoline was observed and this again resulted in lower decomposition temperatures.

CHAPTER 13

CONCLUSIONS

13.1 INTRODUCTION

Several authors have reported the effect of bonding strength and the coordination of different ligands by metal ions. May [101] investigated the coordination equilibria of bis(2,4-pentanediono) copper(II) with eight different pyridine ligands. He reported that the complexes were relatively weak and that there was no correlation of the stability constant with the electron-releasing or electron-withdrawing nature of the substituents. The heats of formation decreased, however, as the electron-withdrawing power of the substituents increased. May suggested that there was no correlation between the ligand base strength and complex stability in very weak complexes. These complexes showed the relative importance of solvation and steric effects, rather than electronic effects.

The primary aim of this study was to draw comparisons between the different cobalt(II) chloride complexes, which contain the ligands pyridine, aniline, quinoline, and α-, β- and γ-picoline. Other transition metal complexes were, however, also included in this study. Certain trends were observed for the different complexes and these will be considered with respect to the solid state and solution chemistry of the complexes.

13.2 COMPARISONS OF COMLEXES IN THE SOLID STATE

13.2.1 Thermogravimetric analysis

As stated previously, the temperature at which a complex starts to decompose reflects, to a certain extent, the stability of the complex. The onset temperatures of decomposition are given in Table 31.

Table 31. Temperatures of onset of decomposition for certain cobalt, nickel and manganese complexes.

Complex	T_i (°C)	pK_a of ligands
$MnCl_2$2(γ-pic)	94	5,98
$NiCl_2$4(γ-pic)	95	5,98
$CoCl_2$2(α-pic)	108	5,96
$MnCl_2$2(β-pic)	37	5,63
$NiCl_2$4(β-pic)	75	5,63
$NiCl_2$2(β-pic)	113	5,63
$CoCl_2$2(β-pic)	138	5,63
$MnCl_2$2(py)	103	5,22
$CoCl_2$2(py)	121	5,22
$NiCl_2$2(py)	160	5,22
$CoCl_2$2(quin)	170	4,85
$CoCl_2$2(an)	200	4,58

The stability of a complex is influenced by the balance of several factors, viz. the basicity of the ligands, the charge densities in the pyridine ring and the steric effect of the methyl group on the metal-ligand bond.

Considering only the basicity of the ligands, higher pK_a values represent weaker metal-ligand-N bonds and thus lower onset temperatures of decomposition can be expected. According to Table 31, the cobalt complexes comply with this prediction. This influence of the basicity of the ligands on the stability of the complexes is also observed for the manganese complexes, except for the complex $MnCl_2 2(\beta\text{-pic})$, which has water molecules coordinated to the complex. The tetrapicoline nickel complexes do not, however, comply with this trend, and it is therefore anticipated that an additional factor influences the stability of these complexes. It is difficult to compare the nickel complexes with the cobalt and manganese complexes because the liberation of the γ-picoline ligand occurs very easily and the onset temperature for $NiCl_2 2(\gamma\text{-pic})$ can therefore not be determined accurately.

By considering the effect of substituents on the pyridine ring, the following conclusions can be made:
The $CoCl_2$ complexes show a weaker metal-ligand bond for the α-picoline complex, than for the pyridine complex. This is most probably due to the steric effect of the methyl group in the α-position. The higher onset temperature of decomposition observed for $CoCl_2 2(\beta\text{-pic})$, in comparison to the pyridine and

α-picoline complexes, may be attributed to the increase in stability caused by the excess charge on the 2, 4 and 6 positions in the pyridine ring which inhibits the π-bonding. By comparing the decomposition temperatures of the complexes, $CoCl_2$2(quin) and $CoCl_2$2(py), it can be seen that the quinoline complex decomposes at a higher temperature. This increase in the temperature of decomposition may be due to the more extensive electron delocalisation in quinoline. However, by comparing $CoCl_2$2(an) and $CoCl_2$2(py), it can be seen the aniline complex decomposes at a lower temperature. This deviation from the expected value may be attributed to the bulky phenol group, being one atom removed from the small sized cobalt(II) ion, which allows a closer approach of the bonding nitrogen atom.

The γ-picoline complexes of manganese and nickel, in comparison with the β-picoline complexes, show an increase in the onset temperatures of decomposition. The ligand γ-picoline, when compared to the ligand α-picoline, does not show steric hindrance. The electron-repelling methyl group increases the electron density at the N-donor atom, and thus increases the covalency of the metal-donor-N bond. Thus, in general, the presence of the γ-methyl group increases the stability of the complex. These results are in agreement with the observations reported by Liptay [80].

13.2.2 Kinetic analysis

Kinetic analyses were performed on the isothermal and dynamic TG

curves for all the complexes. Most of the reactions were consistent with the contracting area model and certain conclusions with respect to the factors influencing the stability of the complexes may therefore be drawn. The decomposition reactions of the cobalt(II) chloride complexes which conform to the contracting area model, as found by the kinetic analysis of the dynamic TG curve, are given in Table 32. The values in brackets are the values obtained from the kinetic analysis of the isothermal curves. There is a relationship between the activation energy and the frequency factor, which can be expressed as

$$k = Z \exp(-E_a/RT)$$

This equation led to the investigation of the ratio of E_a to ln Z, which was obtained from the kinetic results of the isothermal and dynamic TG curves. The ratio of E_a to ln Z obtained from the isothermal reaction should be similar to that obtained from the dynamic TG curves, for the same reaction.

Table 32. Decomposition reactions of the cobalt(II) chloride complexes which conform to the contracting area model. The values in brackets are obtained from the isothermal curves.

Decomposition reaction	E_a (kJ mol^{-1})	ln Z (ln min^{-1})	E_a/ln Z
$CoCl_2 2(py) \rightarrow CoCl_2(py)$	99,00	25,82	3,834
+ (py)	(64,6)	(14,6)	(4,42)
$3CoCl_2(py) \rightarrow Co_3Cl_6 2(py)$	217,0	51,97	4,175
+ (py)	(95,9)	(20,9)	(4,59)
$Co_3Cl_6 2(py) \rightarrow 3CoCl_2$	194,0	40,50	4,790
+ 2(py)	(97,1)	(18,3)	(5,31)
$CoCl_2 2(quin) \rightarrow CoCl_2(quin)$	135,0	31,21	4,325
+ (quin)	(107,7)	(23,69)	(4,546)
$CoCl_2(quin) \rightarrow CoCl_2$	192,0	40,52	4,738
+ (quin)	(69,3)	(11,92)	(5,814)
$CoCl_2 2(\alpha\text{-pic}) \rightarrow CoCl_2(\alpha\text{-pic})$	116,0	29,82	3,890
+ (α-pic)	(117,7)	(30,73)	(3,830)
$CoCl_2(\alpha\text{-pic}) \rightarrow CoCl_2$	198,00	47,39	4,178
+ (α-pic)	(72,87)	(14,92)	(4,884)
$CoCl_2 4(an) \rightarrow CoCl_2 2(an)$	202,0	50,81	3,976
+ 2(an)	(78,22)	(17,36)	(4,506)
$CoCl_2 2(an) \rightarrow CoCl_2(an)$	245,0	57,77	4,241
+ (an)	(118,5)	(27,04)	(4,382)

Consider the conversion of $CoCl_2 2L$ to $CoCl_2 L$. If L = α-picoline is compared to L = pyridine, then higher E_a and ln Z values are observed for L = α-picoline. This is most probably due to the high basicity of α-picoline and the steric effect of the methyl group in the α-position. Higher E_a and ln Z values are also observed for L = aniline and quinoline, if compared to L = pyridine. This increase in stability is in agreement with the observations reported in Section 13.2.1.

It is generally found that the ratio of E_a to ln Z obtained from the analysis of the isothermal curves is higher, than the ratio obtained from the analysis of the dynamic TG curve. The same trends are, however, observed for the ratios obtained from both the isothermal curves and the dynamic curves.

The decomposition reactions of nickel and manganese complexes, which are consistent with the contracting area model, are summarised in Tables 33 and 34, respectively.

Table 33. Decomposition reactions of the nickel(II) chloride complexes which conform to the contracting area model. The values in brackets are obtained from the isothermal curves.

Decomposition reaction	E_a (kJ mol^{-1})	ln Z (ln min^{-1})	E_a/ln Z
$NiCl_2 2(py) \rightarrow NiCl_2(py)$	161,00	42,62	3,778
$+ (py)$	(125,5)	(32,47)	(3,865)
$NiCl_2 4(\beta\text{-pic}) \rightarrow NiCl_2 2(\beta\text{-pic})$	128,00	38,99	3,283
$+ 2(\beta\text{-pic})$	(---)	(---)	(---)
$NiCl_2 2(\beta\text{-pic}) \rightarrow NiCl_2(\beta\text{-pic})$	182,00	50,10	3,633
$+ (\beta\text{-pic})$	(87,95)	(22,54)	(3,902)
$NiCl_2 4(\gamma\text{-pic}) \rightarrow NiCl_2(\gamma\text{-pic})$	90,00	22,94	3,923
$+ 3(\gamma\text{-pic})$	(63,89)	(14,63)	(4,367)
$NiCl_2(\gamma\text{-pic}) \rightarrow NiCl_2$	226,0	47,02	4,806
$+ (\gamma\text{-pic})$	(---)	(---)	(---)

Table 34. Decomposition reactions of the manganese(II) chloride complexes which conform to the contracting area model. The values in brackets are obtained from the isothermal curves.

Decomposition reaction	E_a (kJ mol^{-1})	ln Z (ln min^{-1})	E_a/ln Z
$MnCl_2 2(py) \rightarrow MnCl_2(py)$	129,00	34,94	3,692
+ (py)	(204,41)	(58,51)	(3,494)
$MnCl_2(py) \rightarrow MnCl_2$	116,00	23,80	4,874
+ (py)	(107,76)	(21,32)	(5,054)
$Mn_3Cl_6 2(\beta\text{-pic}) \rightarrow 3MnCl_2$	140,00	28,87	4,849
+ 2(β-pic)	(---)	(---)	(---)
$MnCl_2 2(\gamma\text{-pic}) \rightarrow MnCl_2(\gamma\text{-pic})$	109,00	29,06	3,751
+ (γ-pic)	(---)	(---)	(---)
$MnCl_2(\gamma\text{-pic}) \rightarrow MnCl_2$	90,00	16,11	5,587
+ (γ-pic)	(---)	(---)	(---)

By considering the results obtained from the analysis of the dynamic TG curves the following conclusions can be made:
The decomposition reaction of $NiCl_2 2(\beta\text{-pic})$ to $NiCl_2(\beta\text{-pic})$, when compared to the decomposition of $NiCl_2 2(py)$, shows higher E_a and ln Z values. This may be attributed to the electron density effect of the methyl group in the β-position. A lower activation energy and frequency factor was obtained for the decomposition of the $NiCl_2 4(\gamma\text{-pic})$ complex (which involves the liberation of 3 γ-picoline molecules), than for the decomposition of $NiCl_2 2(py)$, and this is mainly due to the decrease in the steric effect of the methyl group in the γ-position. An increase in the stability of the γ-picoline complexes, compared to the pyridine complexes, was expected but this stability was not found as shown by the E_a and ln Z values. The ratio of E_a to ln Z shows an increase and this may reflect the increase in stability of the complexes when going from pyridine to γ-picoline. Thus, in some instances, consideration of the ratio of E_a to ln Z, rather than the single values of E_a and ln Z, may lead to more significant conclusions. Considering only the E_a and ln Z values may thus lead to incorrect assumptions.

$NiCl_2 2(py)$ and $MnCl_2 2(py)$ were compared in Chapter 11.

The results were similar to those for the cobalt(II) chloride complexes and the same trends, with respect to an increase and decrease in the ratio of E_a to ln Z, were observed for the analysis of the isothermal and dynamic TG curves.

It was found for all the reactions where both the isothermal and dynamic TG studies were performed, that the results obtained from the dynamic TG curve represented the experimental TG curve the best, if separate reactions occured.

13.2.3 DSC results

Only the DSC studies perormed in the open pans will be considered. The enthalpies of formation and the temperature at peak maxima for the various decomposition reactions are given in Table 35.

The temperature at the peak maximum reflects to a certain extent the stability of the complex. The decomposition temperatures are given in Table 35. The following conclusions can be made for the cobalt(II) complexes:

The complex $CoCl_2 2(\alpha\text{-pic})$ has the lowest decomposition temperature. The low stability of this complex is due to the steric effect of the methyl group in the α-position and the high pK_a value of the ligand α-picoline. High temperatures of decomposition are found for $CoCl_2 4(an)$ and $CoCl_2 2(quin)$ and this expected increase in the temperature of decomposition is in agreement with the results discussed in the previous sections.

Table 35. DSC results for the various decomposition reactions.

Decomposition reaction	T_p (^0C)	ΔH (kJ mol^{-1})
$CoCl_2 2(py) \rightarrow CoCl_2(py)$	160,2	66,8
$3CoCl_2(py) \rightarrow Co_3Cl_6 2(py) \rightarrow 3CoCl_2$	217+283	22,8+55,4
$CoCl_2 2(quin) \rightarrow CoCl_2$	228+287	214,0
$CoCl_2 2(\alpha\text{-pic}) \rightarrow CoCl_2$	153+208	155,0
$CoCl_2 4(an) \rightarrow CoCl_2(an)$	213+239	407,8
$MnCl_2 2(py) \rightarrow MnCl_2(py)$	163,1	110,7
$MnCl_2(py) \rightarrow MnCl_2$	294,2	123,4
$MnCl_2 2(\beta\text{-pic}) \rightarrow MnCl_2(\beta\text{-pic})$	136,8	100,2
$MnCl_2(\beta\text{-pic}) \rightarrow MnCl_2$	204,4	27,74
$MnCl_2 2(\gamma\text{-pic}) \rightarrow MnCl_2(\gamma\text{-pic})$	169,8	113,2
$MnCl_2(\gamma\text{-pic}) \rightarrow MnCl_2$	317,9	131,6
$NiCl_2 2(py) \rightarrow NiCl_2(py)$	178,8	111,8
$NiCl_2(py) \rightarrow NiCl_2$	280,8	141,6
$NiCl_2 4(\gamma\text{-pic}) \rightarrow NiCl_2(\gamma\text{-pic})$	170,2	386,2
$NiCl_2(\gamma\text{-pic}) \rightarrow NiCl_2$	297,0	140,8
$NiCl_2 4(\beta\text{-pic}) \rightarrow NiCl_2 2(\beta\text{-pic})$	122,5	203,8
$NiCl_2 2(\beta\text{-pic}) \rightarrow NiCl_2(\beta\text{-pic})$	166,9	89,92
$NiCl_2(\beta\text{-pic}) \rightarrow NiCl_2$	251,6	34,66

The manganese and nickel complexes are difficult to compare due to the presence of water in the β-picoline complex and formation of tetrapicoline complexes of nickel. A higher decomposition temperature is, however, found for $MnCl_2 2(\gamma\text{-pic})$, than for $MnCl_2 2(py)$. This increase in the stability of the γ-picoline complex was also observed previously.

The stability series is, Ni > Co > Mn [99]. The decomposition temperatures show, however, that the metal pyridine complexes reflect the following order: Co > Mn > Ni. This deviation from the order expected for the stability series was discussed in Chapter 11.

It is found in general that the heats of dissociation show the same trends as those observed for the decomposition temperature at peak maximum. It is of interest to note that the enthalpies recorded for the conversion of $NiCl_2(\beta\text{-pic})$ and $MnCl_2(\beta\text{-pic})$ to $NiCl_2$ and $MnCl_2$, respectively, are very low in comparison with the decomposition reactions of corresponding γ-picoline complexes. The excess charge on the 2, 4 and 6 positions is, therefore, still very dominant in the β-picoline complexes and increases the stability of the complexes. Thus, it is again found that the factors influencing the stability of complexes are, the basicity of the ligands, the different charge densities in the pyridine ring and the steric effects of the methyl substituents on the metal-ligand bond.

13.3 COMPARISONS OF COMPLEXES IN SOLUTION

The complex-formation reactions of cobalt(II) chloride with different pyridine-related ligands in solution were investigated. The overall formation constants and the enthalpies of formation are given in Table 36.

Table 36. Log β_i and ΔH_i values reported for the complex-formation reactions of cobalt(II)chloride in acetone.

Ligand	$\log\beta_1$	$\log\beta_2$	ΔH^0_{0-1}	ΔH^0_{0-2}
			(kJ mol^{-1})	
pyridine	4,919	8,407	-37,47	-79,81
quinoline	4,255	8,570	-30,20	-41,50
α-picoline	3,840	8,296	-27,47	-46,17
β-picoline	3,642	8,195	-46,12	-61,24
aniline	4,665	8,304	-18,82	-28,08

The electron-donor power of the ligands decreases in the following order:

α-picoline > β-picoline > pyridine > quinoline > aniline.

If the overall stability constants is considered, then for the $CoCl_2L$ complexes the following order of stability is observed:

pyridine > aniline > quinoline > α-picoline > β-picoline

while for the $CoCl_2 2L$ complexes the following order is found: quinoline > pyridine > aniline > α-picoline > β-picoline.

Thus, the formation of the complexes is not consistent with the electron-donor power of the ligands. Steric effects and the basicity of the ligands contribute to the stability of the complexes and these effects may overpower the electronic effects. May [101] made similar observations for the formation of weak complexes of copper(II) with pyridine-related ligands.

The heat of formation supplies information on the bonding strength of metal complexes. Thus, by considering the heat of formation to approximate the bond energy of the new coordinate bond the following orders can be obtained for $CoCl_2 L$ and $CoCl_2 2L$, respectively:
β-picoline > pyridine > quinoline > α-picoline > aniline;
and pyridine > β-picoline > α-picoline > quinoline > aniline.

These series show that the steric effect of the methyl group in the α-position is dominant, especially in the $CoCl_2 L$ complexes, but to a lesser extent in the $CoCl_2 2L$ complexes, and this gives rise to a weak metal-ligand bond. In contrast, the methyl group in the β-position increases the character of the metal-ligand bond and thus favours π-bonding in the complex. Extremely low values for the complex-formation of $CoCl_2$(an) and $CoCl_2 2$(an) are obtained. This may be attributed to the very low pK_a value of the ligand aniline as well as the closer approach of the bonding nitrogen atom in aniline.

Thus, the same factors which influence the stability of the complexes in the solid state, are also found in solution. A delicate balance exists between the previously mentioned factors, which contribute to the strength of the different metal-ligand bonds. This is found both in solid state and in solution. These factors were also observed by several authors, as reported in the previous chapters.

REFERENCES

1. H.C.A. King, E.Körös and S.M. Nelson, J. Chem. Soc., (1963) 5449.
2. V.A. Logachev and V.I. Dulova, Russian J. Inorg. Chem., 16 (1971) 145.
3. V.A. Logachev, V.I. Dulova and N.R. Molchanova, Russian J. Inorg. Chem.,18 (1973) 1361.
4. T.V. Zhurba and V.I. Dulova, Russian J. Inorg. Chem., 15 (1970) 140.
5. T.V. Zhurba and V.I. Dulova, Russian J. Inorg. Chem., 16 (1971) 1168.
6. T.V. Zhurba and V.I. Dulova, Russian J. Inorg. Chem., 16 (1971) 1309.
7. G. Beech, C.T. Mortimer and E.G. Tyler, J. Chem. Soc.(A), (1967) 925.
8. G. Beech, C.T. Mortimer and E.G. Tyler, J. Chem. Soc.(A), (1967) 1111.
9. J.R. Allan, D.H. Brown, R.H. Nuttall and D.W.A. Sharp, J. Inorg. Nucl. Chem., 27 (1965) 1305.
10. D.A. Young, "Decomposition of Solids", Pergamon Press, Oxford, (1966).
11. C.N.R. Rao, "Modern Aspects of Solid State Chemistry", Plenum Press, New York-London, (1970).
12. N.B. Hannay, "Treatise on Solid State Chemistry", Plenum Press, New York-London, 5 (1976) 193.

13. G. Busch and H. Schade, "Lectures on Solid State Physics", Pergamon Press, U.K. etc., 79 (1976).
14. P.P. Budnikov and A.M. Ginstling, "Principles of Solid State Chemistry, Reactions in solids", Maclaren and Sons Ltd., London, (1968).
15. E. Koch, "Non-isothermal reaction analysis", Academic Press, London, (1977).
16. J.H. de Boer, "Reactivity of Solids", Elsevier, Amsterdam, (1961) 1.
17. J.A. Hedvall, "Solid State Chemistry", Elsevier, Amsterdam, (1966).
18. I. Tamm, Phys. Z. S.S.S.R., 1 (1932) 733.
19. M.E. Brown, CHEMSA, (1979) 74.
20. J.L. Job and W.J. Mc Gill, Joern. S.A. Chem. Inst., 22 (1969) 139.
21. S.Z. Roginsky, "Adsorption and Katalyse an inhomogenen Oberflächen, Akademie Verlag", Berlin, (1958).
22. A. Wischin, Proc. Roy. Soc.(A), 172 (1939) 314.
23. C. Bagdassarian, Acta Physicochim, URSS, 20 (1945) 441.
24. A.R. Allnatt and P.W.M. Jacobs, Con. J. Chem., 46 (1968) 111.
25. W.E. Garner, "The Chemistry of Solid State", Butterworth, London, (1955).
26. K.E.J. Barrett, "Analytical Calorimetry", Plenum Press, London, (1968) 279.
27. P.K. Gallagher and D.W. Johnson, Thermochim. Acta, 2 (1971) 413.

28. P.K. Gallagher and D.W. Johnson, Thermochim. Acta, 6 (1973) 67.

29. M. Avrami, J. Chem. Phys., 7 (1939) 1103, 8 (1940) 212, 9 (1941) 177.

30. B.V. Erofeev, Compt. Rend. Akad. Sci. U.R.S.S., 52 (1946) 511.

31. E.G. Prout and F.C. Tompkins, Trans. Faraday Soc., 40 (1944) 488.

32. C.D. Doyle, J. Appl. Polymer Sci., 5 (1961) 285.

33. J. Zsakó, J. Phys. Chem., 72 (1968) 2406.

34. J. Šesták, Silikaty, 11 (1967) 153.

35. V. Šatava, Silikaty, 5 (1961) 68.

36. J. Šesták and G. Berggren, Thermochim. Acta, 3 (1970) 1.

37. S. Roginsky and E. Schulz, Z. Phys. Chem., A138 (1928) 21.

38. K.L. Mampel, Z. Phys. Chem., A187 (1940) 235.

39. P.W.M. Jacobs and F.C. Tompkins, "Chemistry of the Solid State", W.E. Garner, Ed. Butterworth and Co. Ltd., London, (1955) 184.

40. G.F. Hüttig, Monatsh. Chem., 85 (1954) 365.

41. E.A. Prodan and M.M. Pavlyuchenko, "Heterogeneous Chemical Reactions", M.M. Pavlyuchenko and E.A. Prodan, Ed., Nauka i tekhnika, Minsk., U.S.S.R., (1965) 20.

42. G.M. Lewis, Z. Phys. Chem., 52 (1905) 310.

43. H.H. Horowitz and G. Metzger, Anal. Chem., 35 (1963) 1464.

44. T. Ozawa, Bull. Chem. Soc. Jap., 38 (1965) 1881.

45. V. Šatava and F. Škvara, J. Am. Ceram. Soc., 52 (1969) 591.

46. I. Akahira, Table No.3, Sci. Papers Inst. Phys. Chem. Res. (Tokyo), (1929) 181.

47. J.H. Sharp, G.W. Brindley and B.N.N. Achar, J. Am. Ceram. Soc., 49 (1966) 379.

48. V. Šatava, J. Therm. Anal., 5 (1973) 217.

49. J. Proks, Chem. Zvesti, Bratislava, 20 (1966) 697.

50. H.S. Britton, S.J. Gregg and G.W. Winsor, Trans. Faraday Soc., 48 (1952) 63.

51. U. Haber, J. Rosický and S. Škramovsky, Silikaty, Prague 7 (1963) 170.

52. J. Bjerrum, "Metal Amine Formation in Aqueous Solution", P. Haase & Son, Copenhagen, (1957).

53. J.J. Christensen, J. Ruckman, D.J. Eatough and R.M. Izatt, Thermochim. Acta, 3 (1972) 203.

54. J.J. Christensen, D.J. Eatough and R.M. Izatt, Thermochim. Acta, 3 (1972) 219.

55. J.J. Christensen, L.D. Hansen, J.A. Partridge and R.M. Izatt, J. Phys. Chem., 70 (1966) 2003.

56. J.J. Christensen, L.D. Hansen, J.H. Rytting and R.M. Izatt, J. Am. Chem. Soc., 88 (1966) 2641.

57. J.J. Christensen, D.O. Tolman, D.P. Wrathall and R.M. Izatt, J. Phys. Chem., 71 (1967) 3001.

58. J.J. Christensen, D.P. Wrathall and R.M. Izatt, Anal. Chem., 40 (1968) 175.

59. J.J. Christensen, J.O. Oscarson, D.P. Wrathall and R.M. Izatt, Anal. Chem., 40 (1968) 1713.

60. F.D. Rossini, "Experimental Thermochemistry", Interscience, New York, 1 (1956) 30.

61. L.G. Sillén, Acta Chem. Scand., 16 (1962) 159.

62. P. Paoletti, A. Vacca and D. Arenare, J. Phys. Chem., 70 (1966) 193.

63. J.J. Christensen, D.J. Eatough, R.L. Snow and R.M. Izatt, J. Phys. Chem., 72 (1968) 1208.

64. C.P.J. van Vuuren, M.C. de Lange and P.P. Stander, Thermochim. Acta, 114 (1987) 295.

65. W.C. Davidon, "Argonne National Laboratory Report ANL 5990, Rev. 2", Argonne, I 11 (1966).

66. L.R. Ocone, J.R. Soulen and B.P. Block, J. Inorg. Nucl. Chem., 15 (1960) 76.

67. J.J. Christensen, J.H. Rytting and R.M. Izatt, J.Chem. Soc.(A), (1969) 861.

68. S. Cabani and P. Gianni, J. Chem. Soc.(A), (1968) 547.

69. H.C. Smit, L. Meites and G. Kateman, Anal. Chim. Acta, 153 (1983) 121.

70. O. Popovych and R.P.T. Tomkins, "Non-aqueous Solution Chemistry", J. Wiley & Sons, Inc., (1981).

71. V. Gutmann, "Coordination Chemistry in Non-Aqueous Solutions", Springer, New York, (1968).

72. J.S. Fritz, Anal. Chem., 26 (1954) 1701.

73. W.J. Mackellar and D.B. Rorabacher, J. Amer. Chem. Soc., (1971) 4379.
D.B. Rorabacher and F.R. Shu, Inorg. Chem., 11 (1972) 1496.

74. R.J. Baltisberger, C.L. Knudson and M.F. Anderson, Inorg. Chem., 13 (1974) 2354.

75. J.W. Akitt, J.C.S. Dalton, (1974) 175.

76. L. Sacconi, P. Paoletti and M. Ciampolini, J. Chem. Soc., (1964) 5046.

77. N.S. Gill, R.S. Nyholm and G.A. Barclay etc., J. Inorg. Nucl. Chem., 18 (1961) 88.

78. J.R. Allan, D.H. Brown and R.H. Nuttall, J. Inorg. Nucl. Chem., 26 (1964) 1895.

79. P.B. Bowman and L.B. Rogers, J. Inorg. Nucl. Chem., 28 (1966) 2215.

80. G. Liptay, K. Burger and É. Mocsári-Fülöp, J. Therm. Anal., 2 (1970) 25.

81. W.W. Wendlandt, Chemist Analyst, 53 (1964) 71.

82. D.H.Brown. R.H. Nuttall and D.W.A. Sharp, J. Inorg. Nucl. Chem., 26 (1964) 1151.

83. D.P. Graddon and E.C. Watton, Aust. J. Chem., 18 (1965) 507.

84. G.B. Bokii, "Introduction to crystal chemistry", Moscow University, Moscow, (1954).

85. A. Ries, "Chemistry of crystals containing defects", Foreign Literature Press, Moscow, (1956).

86. G. Buckley, "Crystal growth", Foreign Literature Press, Moscow, (1954).

87. V.D. Kuznetsov, "Crystals and crystallization", GTTI, Moscow, (1954).

88. V.D. Kuznetsov, "Surface energy of solids", GTTI, Moscow, (1954).

89. H.K. Adam, "Physics and Chemistry of surfaces", Tekh. Theor. Lit., Moscow-Leningrad, (1947).

90. N. E. Pestov, "Physicochemical properties of granular and powdered chemical products", Academy of Sciences, USSR, Moscow-Leningrad, (1947).

91. T.V. Zhurba and V.I. Dulova, Russ. J. Inorg. Chem., 15 (6) (1970) 878.

92. A.K. Majumdar and A.K. Mukherjee, J.Inorg. Nucl. Chem., 26 (1964) 2177.

93. H.C. Brown, D.H. Mc Daniel and O. Häfliger, "Determination of Organic Structures by Physical Methods", ed. Braude and Nachod, Academic Press, New York, (1955).

94. M.R. Rosenthal and R.S. Drago, Inorg. Chem., 4 (1965) 840.

95. G. Liptay, K. Burger and E. Papp-Molnár, J. Inorg. Nucl. Chem., 31 (1969) 247.

96. J.R. Allan, D.H. Brown, R.H. Nuttall and D.W.A. Sharp, J. Inorg. Nucl. Chem., 27 (1965) 1529.

97. D.H. Brown, R.H. Nuttall and D.W.A. Sharp, J. Inorg. Nucl. Chem., 25 (1963) 1067.

98. I.G. Murgulescu, E. Segal and D. Fătu, J. Inorg. Nucl. Chem., 27 (1965) 2677.

99. H. Irving and R.J.P. Williams, J. Chem. Soc., (1953) 3192.

100. R.J.H. Clark and C.S. Williams, Inorg. Chem., 4 (1965) 350.

101. W.R. May and M.M. Jones, J. Inorg. Nucl. Chem., 25 (1963) 507.